

FUNDAMENTAL UNDERSTANDING OF A HIGH PERFORMANCE POLYMER  
FOR ORGANIC PHOTOVOLTAICS AND NEW MATERIAL DEVELOPMENT  
BY RATIONAL MOLECULAR ENGINEERING

Wentao Li

A dissertation submitted to the faculty of the University of North Carolina at Chapel Hill  
in partial fulfillment of the requirements for the degree of Doctor of Philosophy  
in the Department of Chemistry.

Chapel Hill  
2015

Approved by:

Maurice Brookhart

James Cahoon

Jeffrey Johnson

David Nicewicz

Wei You

© 2015  
Wentao Li  
ALL RIGHTS RESERVED

## ABSTRACT

Wentao Li: Fundamental Understanding of a High Performance Polymer for Organic Photovoltaics and New Material Development by Rational Molecular Engineering  
(Under the direction of Wei You)

Organic photovoltaics are a promising renewable energy technology. Development of novel materials and device architecture for further enhancing their efficiency requires fundamental understanding of the impact of chemical structures on photovoltaic properties. Given that device characteristics depend on many parameters, deriving structure-property relationships has been very challenging.

Among many high performance polymers for organic photovoltaics, poly(benzodithiophene-*alt*-dithienyl difluorobenzotriazole) (PBnDT-FTAZ) is a very special one, due to its extremely efficient conversion of photons to observed current density. Although its absorption range is narrow with a band gap of  $\sim 2.0$  eV, the power conversion efficiency of its bulk heterojunction solar cell based on phenyl-C61-butyric acid methyl ester (PC<sub>61</sub>BM) breaches 7%. In this dissertation, we conclude two fundamental reasons to account for the exceptional device performance of PBnDT-FTAZ by comprehensive investigation into morphology and device physics. On one hand, the molecular weight determines the morphology in the non-crystalline region. An appropriate molecular weight helps to achieve a small domain size, thus a shorter exciton diffusion path together with larger interfacial areas in the PBnDT-FTAZ:PC<sub>61</sub>BM bulk heterojunction, leading to improved short circuit current density. On the other hand, fluorination introduces better backbone stacking in the crystalline region, leading to significantly

improved hole mobility, which reduces bimolecular recombination and directly accounts for the observed high fill factor in the OPV device. Overall, two important structure-property relationships regarding the molecular weight and the degree of fluorination of PBnDT-FTAZ are elucidated.

In order to extend the absorption range and to further enhance the device performance of benzotriazole based polymers, we developed a general yet versatile synthetic approach towards a diverse set of triazole based conjugated molecules bearing various electron accepting abilities. The structural differences of as-synthesized three new triazole acceptors have a significant impact on the optoelectronic properties of conjugated polymers incorporating these triazoles. Bulk heterojunction solar cells based on one of these new polymers feature a high open circuit voltage of  $\sim 1$  V and a notable efficiency of 8.4% with an active layer thickness around 300 nm.

## ACKNOWLEDGEMENTS

First and foremost, I would like to thank my advisor, Professor Wei You, for his incredible patience during my graduate research. When I started to synthesize PBnDT-FTAZ on May 3<sup>rd</sup>, 2011, neither of us anticipated that I would have to spend 700 days to fully reproduce a polymerization result. During this long puzzle solving process, Wei never even complained. Instead, he stayed focused on the underlying scientific questions and constantly provided me with numerous useful tips. I am truly grateful to Wei's invaluable mentoring in regard to research methodology, experiment, presentation and writing over past five years. His work ethic will always inspire me to be a diligent and devoted researcher.

I would like to thank my predecessors in synthetic lab for their guidance and suggestions. Dr. Huaxing Zhou taught me all his experimental procedures and tricks. Dr. Samuel Price showed me how organic chemistry could be applied into material synthesis. Dr. Rycel Uy answered my every trivial question in lab. I would thank my collaborators inside You group, Dr. Liqiang Yang and Dr. Liang Yan, not only for fabricating my polymers into working solar cell devices, but also for tutoring me elementary semiconductor physics. I also thank multiple collaborators in other disciplines who helped us gain deeper understanding into OPVs, especially Dr. Harald Ade and Dr. John Tumbleston at North Carolina State University for their X-ray scattering study on film morphology, and Dr. Steve Albrecht and Dr. Dieter Neher at University of Potsdam, Germany, for their device physics works.

I thank Professor Maurice Brookhart, Professor James Cahoon, Professor David Nicewicz, and Professor Jeffery Johnson for serving on my final defense committee. I also acknowledge Professor Valery Ashby for her previous committee work in my preliminary defense.

I want to thank my undergraduate research advisor, Professor Weidong He, at University of Science and Technology of China, for generously providing me an individual research project and kindly tolerating my destructions in his office and lab. His knowledge in living polymerization and polymer physics fostered my strong interest in polymeric materials.

Many thanks to my friends in Class 2010, UNC Chemistry, my past and previous You group colleagues, friendly staffs inside/outside of the Department of Chemistry, and all my other friends at Chapel Hill, for helping me to adapt myself into a new country and new culture quickly and comfortably. Many heartwarming details definitely make my experience at UNC memorable, and will always remind me to be a considerate person.

Finally, I thank my family for their love and support along the way. Special thanks to my wife, Mengmeng, who has borne with my careless and dull mind for five years. Keeping a long-distance relationship is never easy. Your support and accompaniment made my past five years much more enjoyable and meaningful.

## TABLE OF CONTENTS

<b>LIST OF TABLES .....</b>	<b>xi</b>
<b>LIST OF FIGURES .....</b>	<b>xii</b>
<b>LIST OF SCHEMES AND CHARTS .....</b>	<b>xv</b>
<b>LIST OF EQUATIONS .....</b>	<b>xvi</b>
<b>LIST OF ABBREVIATIONS AND SYMBOLS .....</b>	<b>xvii</b>
<b>CHAPTER 1</b>	
<b>INTRODUCTION TO ORGANIC PHOTOVOLTAICS .....</b>	<b>1</b>
1.1 Performance parameters of photovoltaics.....	3
1.2 Device structure of an organic solar cell.....	5
1.3 Working mechanism of organic photovoltaics .....	6
1.3.1 Exciton generation .....	7
1.3.2 Charge separation.....	8
1.3.3 Charge transport.....	10
1.3.4 Charge collection .....	11
1.4 General design rules of polymers for organic photovoltaics .....	12
1.5 A unique polymer: pbndt- ftaz.....	15

## **CHAPTER 2**

<b>CONTRASTING N-ALKYLATION SELECTIVITIES OF BENZOTRIAZOLE IN THF AND DMF.....</b>	<b>18</b>
2.1 Introduction.....	18
2.2 Optimization of N2-alkylation yield.....	20
2.3 Opposite N-selectivity in THF and DMF .....	22
2.4 Ion aggregate postulation.....	24
2.5 Optimization of N1-alkylation yield.....	26
2.6 Conclusion .....	27

## **CHAPTER 3**

<b>CONTROLLING MOLECULAR WEIGHT OF PBN DT-FTAZ AND UNDERSTANDING ITS SIGNIFICANT IMPACT ON PHOTOVOLTAIC PROPERTIES .....</b>	<b>28</b>
3.1 Introduction.....	28
3.2 Stoichiometry in polymerization.....	29
3.3 Photovoltaic performance and electrochemical properties .....	33
3.4 Morphology impact of polymer molecular weight .....	37
3.5 Discussion and conclusion.....	43
3.7 Experimental Section .....	45

## **CHAPTER 4**

<b>MOBILITY-CONTROLLED PERFORMANCE OF THICK SOLAR CELLS BASED ON PBN DT-FTAZ.....</b>	<b>47</b>
---	-----------



4.1 Introduction.....	47
4.2 Design and synthesis of PBnDT-(X)TAZ.....	50
4.3 Photovoltaic device performance.....	55
4.4 Morphology and Molecular Texture .....	57
4.5 Factors Influencing Fill Factor.....	61
4.8 Experimental Section .....	73
 <b>CHAPTER 5</b>	
<b>A GENERAL APPROACH TOWARDS ELECTRON DEFICIENT TRIAZOLE UNITS TO CONSTRUCT CONJUGATED POLYMERS FOR SOLAR CELLS .....</b>	<b>76</b>
5.1 Introduction.....	76
5.2 Synthesis and discussion.....	80
5.3 Optical and electrochemical properties.....	92
5.4 Photovoltaic Device Performance.....	95
5.5 Conclusion .....	99
 <b>CHAPTER 6</b>	
<b>CONCLUSIONS AND FUTURE DIRECTIONS .....</b>	<b>101</b>
6.1 Conclusions .....	101
6.2 Future directions .....	103
6.2.1 Polydispersity effect.....	103
6.2.2 Further study on fluorination effect .....	104

6.2.3 Enriching triazole acceptor library.....	105
6.2.4 Bridging the gap between small molecules and polymers .....	107
6.2.5 Future directions in OPV field .....	108
<b>APPENDIX I: GENERAL METHODS .....</b>	<b>113</b>
<b>APPENDIX II: DETERMINING N-ALKYLATION SELECTIVITY OF BENZOTRIAZOLE BY <sup>1</sup>H-NMR SPECTRA IN CHAPTER 2 .....</b>	<b>117</b>
<b>APPENDIX III: NMR SPECTRA OF INTERMEDIATES, MONOMERS AND POLYMERS IN CHAPTER 5 .....</b>	<b>134</b>
<b>REFERENCES.....</b>	<b>149</b>

## LIST OF TABLES

<b>Table 2.1</b>	Effect of solvent and temperature on yield and selectivity.....	21
<b>Table 2.2</b>	Effect of alkyl and leaving group on selectivity.....	22
<b>Table 2.3</b>	Solvent effect on N2-selectivity.....	23
<b>Table 2.4</b>	Crown ether effect on alkylation N2-selectivity.....	26
<b>Table 2.5</b>	N2-selectivity and conversion in a series of THF/DMF mixed solvents.....	27
<b>Table 3.1</b>	Controlling the molecular weight of PBnDT-FTAZ via tuning stoichiometric ratio.....	32
<b>Table 3.2</b>	Average photovoltaic performance and hole mobility of PBnDT-FTAZ:PC <sub>61</sub> BM devices with different molecular weights.....	34
<b>Table 3.3</b>	Polymerization yields and energy levels <sup>[a]</sup> of PBnDT-FTAZ polymers based on different molecular weights.....	36
<b>Table 3.4</b>	Relative composition variations, domain spacing and anisotropy measured by R-SoXS along with power conversion efficiency.....	38
<b>Table 4.1</b>	PBnDT-(X)TAZ: chemical composition, molecular weight and photovoltaic device properties.....	53
<b>Table 4.2</b>	Estimated HOMO energy levels according to CV measurement.....	55
<b>Table 5.1</b>	Molecular weight and dispersity, absorption onset and energy levels of PBnDT-TAZ polymers.....	93
<b>Table 5.2</b>	Highest performance of four triazole-based polymers with PEDOT:PSS as hole transport layer.....	96
<b>Table 5.3</b>	Active Layer thickness, photovoltaic performance and hole mobility of TAZ polymers.....	96
<b>Table 5.4</b>	Thickness dependence of PBnDT-PyCNTAZ device performance.....	99

## LIST OF FIGURES

<b>Figure 1.1</b>	<i>J-V</i> curve of an organic solar cell with performance parameters.....	4
<b>Figure 1.2</b>	Schematic illustration of a typical organic solar cell in normal architecture.....	5
<b>Figure 1.3</b>	Schematic illustration of bulk heterojunction active layer in an organic solar cell with charge transport channel depicted.....	6
<b>Figure 1.4</b>	Working mechanism of BHJ organic solar cell: four steps of charge transfer process.....	7
<b>Figure 1.5</b>	Chemical structures of PBnDT-HTAZ and PBnDT-FTAZ, and their OPV performance in BHJ solar cells with PC <sub>61</sub> BM.....	16
<b>Figure 1.6</b>	Contour plot of calculated efficiency as a function of band gap and LUMO level based on Schurrer's model.....	17
<b>Figure 3.1</b>	Correlation of actual <i>M<sub>n</sub></i> measured by GPC and calculated <i>M<sub>n</sub></i> by the Carothers Equation.....	32
<b>Figure 3.2</b>	(a) Current density vs. voltage curves and (b) Incident photon to current efficiency (IPCE) curves of PBnDT-FTAZ: PC <sub>61</sub> BM devices with molecular weight ranging from 10 kg/mol to 60 kg/mol.....	34
<b>Figure 3.3</b>	UV-visible absorption spectra of pure polymers in dichlorobenzene solution (left) and pure polymer film on glass substrate (right).....	35
<b>Figure 3.4</b>	UV-visible absorption spectra of the polymer:PC <sub>61</sub> BM blends (i.e., the active layers) on glass/ITO/PEDOT:PSS substrates.....	36
<b>Figure 3.5</b>	(a) GIWAXS out-of-plane and in-plane 20 ° sector averages along with circular averaged data of the five blend films. (b) Lorentz corrected R-SoXS scattering profiles for 284.1 eV for the five blend films.....	39
<b>Figure 3.6</b>	Two dimensional (2D) GIWAXS data for blend polymer films and neat polymer films of five polymers.....	46
<b>Figure 3.7</b>	(a) 2-D R-SoXS scattering data for the 40k polymer based blend film. (b) Perpendicular and parallel sector averages with respect to electric field polarization for all blend samples.....	46
<b>Figure 4.1</b>	GPC Curves of PBnDT-(X)TAZ polymers.....	53
<b>Figure 4.2</b>	UV-Vis absorption of PBnDT-(X)TAZ polymers in thin films.....	54
<b>Figure 4.3</b>	Cyclic voltammograms of PBnDT-(X)TAZ polymer thin films.....	54

<b>Figure 4.4</b>	(a) J-V curves for the BHJ devices of ~350 nm thick films based on all five copolymers of PBnDT-(X)TAZ under 1 sun, AM 1.5G condition. (b) EQE for the same devices in (a). (c) The change of $J_{sc}$ and $V_{oc}$ with increased amount of F substitution. (d) The increase of fill factor tracks the increase of overall device efficiency as more F substituents are incorporated into the copolymer.....	56
<b>Figure 4.5</b>	Field dependent EQE. EQE for different applied voltages ranging from +0.5V to -3V as indicated in the left plot.....	57
<b>Figure 4.6</b>	(a) P-SoXS circular average profiles at 284.1 eV. (b) Sector averaged profiles representing P-SoXS data perpendicular and parallel to the electric field polarization.....	59
<b>Figure 4.7</b>	GIWAXS data of blend films on glass/ITO/PEDOT:PSS device substrates .....	61
<b>Figure 4.8</b>	Upper panel: the external generation efficiency (EGE) with offset for clarity as a function of applied pre-bias measured with TDCF at excitation wavelength of 530 nm. Lower panel: The EQE measured at 530 nm and normalized to -2 V as function of voltage for all five blends.....	64
<b>Figure 4.9</b>	(a) The measured number of collected charges ( $Q_{coll}$ ) and the corresponding bimolecular recombination (BMR) fit with increasing delay time between laser pulse and extraction voltage for the F50 sample at 0.7 V pre-bias. (b) The BMR coefficient deduced from BMR fits as shown in (a) at conditions close to the respective open circuit for all five blends.....	66
<b>Figure 4.10</b>	Charge carrier mobilities of electrons and holes together with the effective extraction mobility as a function of fluorine substitution.....	68
<b>Figure 4.11</b>	BMR coefficient.....	74
<b>Figure 4.12</b>	Hole mobility derived from the hole only device.....	74
<b>Figure 4.13</b>	Carrier density and effective extraction mobility measured with BACE.....	75
<b>Figure 5.1</b>	High <i>N</i> -2 selectivity shown in $^1\text{H}$ -NMR of crude product of <i>NH</i> -1,2,3-triazole alkylation. Methylene peaks are assigned to marked <i>N</i> -alkyl isomers and starting material.....	91
<b>Figure 5.2</b>	Normalized film absorptions of PBnDT-TAZ polymers spun cast from their <i>o</i> -dichlorobenzene (ODCB) solution; inset shows the color variations of their ODCB solution (0.15 mg/mL).....	94
<b>Figure 5.3</b>	Energy level diagram of PBnDT-TAZ polymers and PC <sub>61</sub> BM.....	94
<b>Figure 5.4</b>	<i>J</i> -V curves of BHJ device based on four TAZ polymers with CuSCN as hole transport layer under 1 sun, AM 1.5G condition.....	97

<b>Figure 5.5</b>	Incident photon to current efficiency (IPCE) of BHJ device based on four TAZ polymers with CuSCN as hole transport layer under 1 sun, AM 1.5G condition.....	97
-------------------	--	----

## LIST OF SCHEMES AND CHARTS

<b>Scheme 2.1</b>	Benzotriazole alkylation isomerism and characteristic NMR peaks.....	20
<b>Scheme 3.1</b>	Polymerization scheme of PBnDT-FTAZ.....	29
<b>Scheme 4.1</b>	Synthesis of the set of PBnDT-(X)TAZ with various amount of F substitution.....	51
<b>Chart 5.1</b>	General Structure of Triazole Based Acceptors.....	77
<b>Scheme 5.1</b>	Synthetic strategies of popular acceptor units for organic photovoltaics.....	79
<b>Scheme 5.2</b>	Syntheses of three <i>m</i> -TAZ acceptors from a 1,4-diketone intermediate and related PBnDT-TAZ polymers.....	80
<b>Scheme 6.1</b>	Proposed molecules to enrich triazole acceptor library.....	106
<b>Scheme 6.2</b>	ADMET polymerization of small molecules with photovoltaic perform.....	107
<b>Scheme 6.3</b>	A representative polymer displaying dramatically enhanced OPV performance from 1.6% to 10% upon morphology improvement.....	110

## LIST OF EQUATIONS

Equation 1.1.....	4
Equation 1.2.....	4
Equation 3.1.....	30
Equation 3.2.....	30



## LIST OF ABBREVIATIONS AND SYMBOLS

$\eta$	power conversion efficiency
$J_{rec}$	recombination current density
BACE	bias enhanced charge extraction
BG	band gap
BHJ	bulk heterojunction
BMR	bimolecular recombination
BnDT	benzodithiophene
CNTAZ	poly(benzodithiophene- <i>alt</i> -dithienyl benzotriazole-5,6-dicarbonitrile)
CT	charge transfer
CV	cyclic voltammetry
$\bar{D}$	polydispersity index
DPP	diketopyrrolopyrrole
DTBT	dithienyl benzothiadiazole
DTfBT	difluorinated dithienyl benzothiadiazole
DTPyT	dithienyl thiadiazolopyridine
EGE	external generation efficiency
EQE	external quantum efficiency
$FF$	fill factor
FTAZ	difluoro benzotriazole
GIWAXS	grazing incidence wide angle X-ray scattering
GPC	gel permeation chromatography
GRIM	Grignard metathesis
HMPA	hexamethylphosphoramide
HOMO	highest occupied molecular orbital
HTL	hole transport layer
IP	ionization potential

IPCE	incident photon to current efficiency
ITO	indium tin oxide
$J_{sc}$	short circuit current density
LUMO	lowest unoccupied molecular orbital
$M_n$	number average molecular weight
$M_{PP}$	maximum power point
MW	molecular weight
$M_w$	weight average molecular weight
NBS	N-bromosuccinimide
NGR	non-geminate recombination
NMR	nuclear magnetic resonance
ODCB	<i>o</i> -dichlorobenzene
OFET	organic field-effect transistor
OPV	organic photovoltaics
$p$	polymerization degree
P3HT	poly(3-hexyl thiophene)
PBnDT-FTAZ	poly(benzidithiophene- <i>alt</i> -difluoro dithienyl benzotriazole)
PBnDT-HTAZ	poly(benzidithiophene- <i>alt</i> - dithienyl benzotriazole)
PC <sub>61</sub> BM	phenyl-C61-butyric acid methyl ester
PCE	power conversion efficiency
PEDOT:PSS	poly(3,4-ethylenedioxythiophene) poly(styrenesulfonate)
PrzTAZ	poly(benzodithiophene- <i>alt</i> -dithienyl triazolopyridazine)
P-SoXS	polarized resonance soft X-ray scattering
PyCNTAZ	poly(benzodithiophene- <i>alt</i> -dithienyl 6-cyano triazolopyridine)
$Q_{coll}$	amount of collected charges after delay
$Q_{pre}$	amount of charges collected during delay
$Q_{tot}$	amount of extractable charges
$r$	stoichiometry ratio between two monomers

RPM	round per minute
RSoXS	resonance soft X-ray scattering
SCLC	space charge limited current
STXM	scanning transmission X-ray microscopy
TA	transient absorption
TAZ	benzotriazole
TDCF	time-delayed collection field
TPD	thienopyrrolo-dione
TSI	total scattering intensity
$V_{\text{coll}}$	collection bias
$V_{\text{oc}}$	open circuit voltage
$V_{\text{pre}}$	prebias during short laser pulse before charge collection
$d$	film thickness
$e$	elementary charge
$n$	charge carrier density at steady state
$\gamma$	recombination coefficient

## CHAPTER 1

### INTRODUCTION TO ORGANIC PHOTOVOLTAICS

Sustaining and advancing human civilization has been heavily relying on massive consumption of fossil fuels since the Industrial Revolution. For instance, the annual coal consumption in the United States rapidly increased from 0.2 quadrillion British thermal unit (Btu) in 1850 to 15.5 quadrillion Btu in 1920, and coal has remained as one of the primary energy sources thereafter.<sup>1</sup> Fossil fuels certainly have many advantages as the energy source: they are readily available from coal mines or oil fields, easy to be transported at low cost, and able to produce large amount of energy upon combustion. However, two severe issues concerning the massive usage of fossil fuels have emerged after decades of combustion of coal, oil and natural gas. First, it takes millions of years for buried organic materials to be converted into combustible fossil fuels; therefore, in a foreseeable future, fossil fuel is a non-renewable energy source. In fact, it is estimated that coal would be the only remaining fossil fuel after 2042, which could also be completely depleted another 70 years later.<sup>2</sup> Second, the combustion of fossil fuels generates large amounts of carbon dioxide, a greenhouse gas that significantly contributes to global warming, and multiple air pollutants including nitrogen oxides, sulfur oxides and particulates. For all these reasons, a transition from these fossil fuels to renewable and environmentally benign energy sources is rather a *must* than an *option*.

Among various alternative energy sources (e.g., solar, wind, geothermal, hydraulic), solar energy attracts much attention because it has a number of unique advantages. In most areas on

the Earth, the Sun provides infinite energy supply through continuous light radiation in the daytime. By directly converting sunlight into electricity, solar panels do not generate any waste; these solar cells do not have moving parts to convert light into electricity, thus they are noise-free. Moreover, the manufacturing cost for mainstream solar panels (e.g., Si, CdSe, and CIGS) has been continuously falling down; combined with the installation cost, the total cost for producing the electricity with these solar cells have been rapidly approaching the “grid parity”. Well-developed, residential-use solar panels are already available from solar panel distributors, and have been adopted by numerous homes across the globe.

Issues remain, though. Take Si solar cells for example. After years of research and development, Si solar cells have reached very high power conversion efficiency in the lab (~25%);<sup>3</sup> however, some significant drawbacks still hinder the wider application of Si solar cells. First, the manufacturing process of a monocrystalline Si solar cell requires much energy input, for example, melting polycrystalline silicon at 1425 °C. As a result, the Si solar cell’ energy payback time, i.e., the time a photovoltaic system needs to generate the same amount of energy that was consumed during its manufacturing, is one of the longest among all photovoltaic technologies.<sup>4</sup> Second, the manufacturing process of Si photovoltaic panels generates undesirable wastes, including particulates, silicon waste solid, and other hazardous chemicals. Third, a monocrystalline Si solar cell is extremely brittle. They are very sensitive to mechanical constraints, which puts some limits on where these Si cells can be used, and also introduces additional failure mechanism (e.g., broken cells).

To address these three issues with Si photovoltaics, i.e., high energy cost, substantial amount of waste during production and poor mechanical flexibility, organic photovoltaics (OPVs) are being developed as an alternative to Si solar cells. The mature industrial-scale synthesis of

polymers (and small molecules) is expected to cut down both manufacturing costs and generated waste. By taking advantage of good solubility of structurally tailored polymers, the active layer in OPV devices can be solution-processed; furthermore, large-area films can be easily prepared by casting this solution onto substrates in a roll-to-roll fashion, effectively reducing the fabrication cost. Paired with a soft substrate and mechanically robust electrodes, the entire photovoltaic device incorporating a polymer thin film can be flexible, expanding the application of such OPV devices in new areas, for example, wearable electronics.

However, compared with well-studied Si photovoltaics, OPV devices usually exhibit a much less competitive efficiency (~6% at sub-module level), and many fundamental questions remain to be answered. This chapter will briefly introduce performance parameters of a photovoltaic device (OPV included) and the basic device structure of an organic solar cell. The working mechanism of OPV will be next discussed, together with the electrochemical and morphological requirements for conjugated polymers to be used in the OPV device. After a summary of the design rules of conjugated polymers for OPV, this chapter will be finished by introducing a special conjugated polymer that has unique and intriguing properties.

## 1.1 Performance parameters of photovoltaics

The power conversion efficiency (i.e., PCE, or  $\eta$ ) of all solar cells, regardless of the working component (i.e., Si, CdSe, CIGS, or organics), is determined by three parameters: the open circuit voltage ( $V_{oc}$ ), the short circuit current ( $J_{sc}$ ) and the fill factor ( $FF$ ).

$V_{oc}$  and  $J_{sc}$  are the *maximum* output voltage and current that a solar cell is able to produce, respectively. However, under the working condition, the voltage and current are closely related,

and there exists a maximum power point ( $M_{PP}$ ) on current density vs. voltage curve ( $J$ - $V$  curve). The efficiency is defined as the ratio of the maximum power output to the solar power input (equation 1.1), and the  $FF$  is defined as the ratio of the maximum power output to the product of  $V_{oc}$  and  $J_{sc}$  (equation 1.2), i.e., the area ratio between two rectangles in Figure 1.1.<sup>5</sup>

$$\eta = \frac{P_{max}}{P_{in}} = \frac{J_{sc} \cdot V_{oc} \cdot FF}{P_{in}} \quad (1.1)$$

$$FF = \frac{P_{max}}{J_{sc} \cdot V_{oc}} \quad (1.2)$$

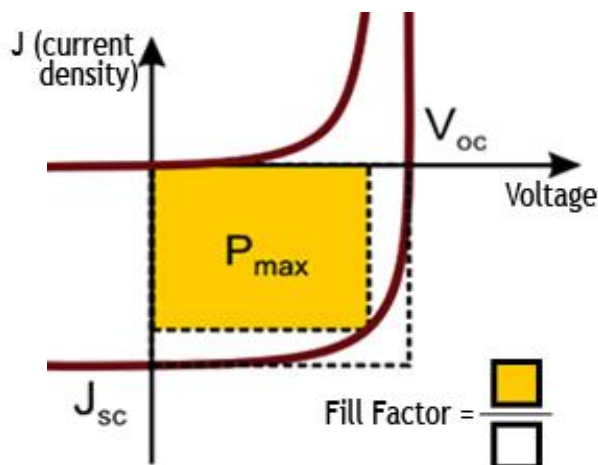


**Figure 1.1** A representative  $J$ - $V$  curve of an organic solar cell with performance parameters. (Adapted from reference 3.)

In organic solar cells, the relationship among these three parameters ( $J_{sc}$ ,  $V_{oc}$  and  $FF$ ) are rather convoluted. Change in any one of them is usually accompanied by certain impacts on the other two. Although progress in understanding the physical origins of all three parameters and their relationships has been made in the past decade through both computational modelling and experimental device physics studies, a though discussion on these topics is beyond the scope of this dissertation. Instead, we will qualitatively describe how chemical modifications of conjugated polymers and morphological variations of the active layer would affect the device

performance, and attempt to introduce some independent structure-property relationships of conjugated polymers used in OPV devices.

## 1.2 Device structure of an organic solar cell

In a normal device architecture (*vs.* inverted device architecture), an organic solar cell has its charge generation part, i.e., the active layer, sandwiched between the anode (e.g., transparent indium tin oxide (ITO)) and the cathode (e.g., calcium/aluminum double metal layer) (Figure 1.2).<sup>6</sup> Bearing different work functions, these two electrodes form a built-in electrical field to provide driving force for charge carriers generated in the active layer to the right electrode. In most cases, a layer of poly(3,4-ethylenedioxythiophene) poly(styrenesulfonate) (PEDOT:PSS) is applied between ITO and the active layer to adjust the work function of anode for better hole transport. Recently, some optional electron transport layers (ETL) were also developed to be applied between the cathode and the active layer, with functions similar to that of PEDOT:PSS layer.<sup>7</sup>

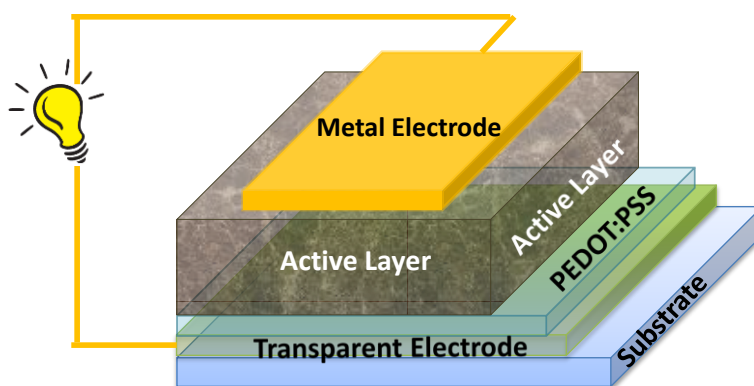


**Figure 1.2** Schematic illustration of a typical organic solar cell in conventional architecture. (Reprinted from reference 7 with permission. Copyright 2012 American Chemical Society)



The active layer, where the sunlight is converted to electricity, directly determines the performance of organic photovoltaics. The most effective active layer configuration so far is bulk heterojunction (BHJ), which is essentially a physical blend of *p*-type, electron-donating organic semiconductors, i.e., conjugated polymers, and *n*-type electron-accepting organic semiconductors, i.e., fullerenes derivatives.<sup>8</sup> These two components form an interpenetrating network with large interfacial area between the polymer and the fullerene, and building hole/electron transport pathways at the same time. A schematic illustration of BHJ, in the context of a conventional device architecture, is shown in Figure 1.3.<sup>9</sup> Therefore, it is crucial for BHJ active layer to adopt a favorable morphology in order to achieve a high PCE.

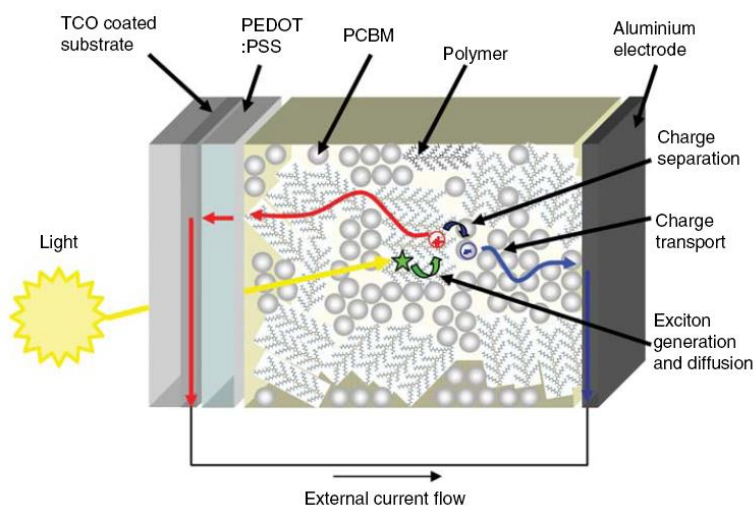


**Figure 1.3** Schematic illustration of bulk heterojunction active layer in an organic solar cell with charge transport channel depicted. (Reprinted from reference 9 with permission. Copyright 2008 Material Research Society)

### 1.3 Working mechanism of organic photovoltaics

With the help of the built-in field provided by the electrodes and sufficient interfacial area provided by the BHJ, the OPV device converts sunlight into electricity via four steps:

exciton generation, charge separation, charge diffusion, and charge collection (Figure 1.4). We will briefly describe the physical process, including possible losses, in each step, and derive corresponding requirements for polymer and BHJ morphology to facilitate different charge transfer processes at various interfaces and length scales.

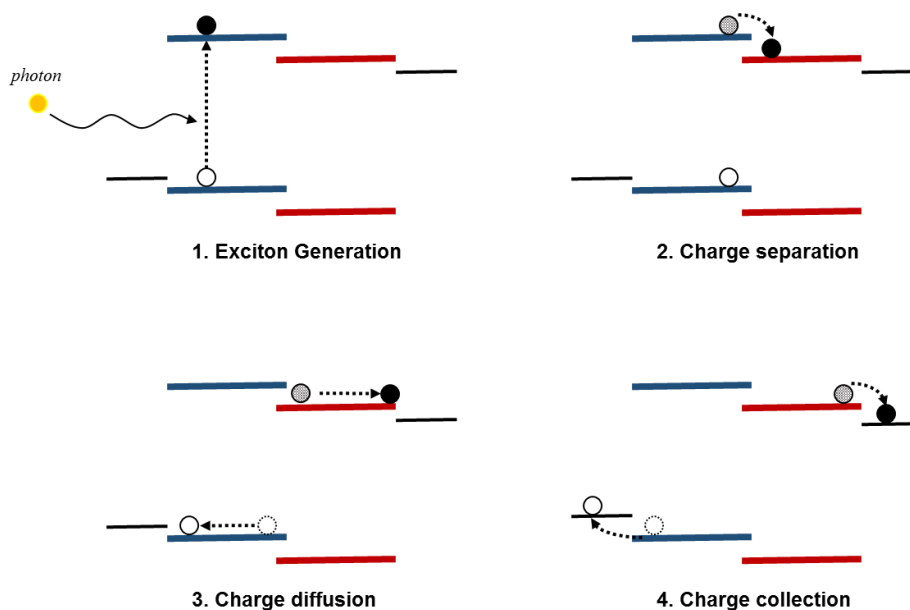


**Figure 1.4** Working mechanism of BHJ organic solar cell: Four steps of charge transfer process.

### 1.3.1 Exciton generation

When the incident photon possesses an energy larger than the band gap of the light-absorbing *p*-type polymer, the photon will be absorbed and an electron on the polymer's highest occupied molecular orbital (HOMO) will be excited to higher energy levels, leaving a hole in the polymer's HOMO level. Please note that the *n*-type fullerenes also absorb light and generate excitons, however, to a much less extent when compared with the primary light absorber – the *p*-type polymer. For simplicity, we will only discuss the fate of exciton generated by the *p*-type

polymers in the following discussion. Depending on the energy of incident photon, the electron can be excited to different states, but most of them will finally thermalize to the lowest unoccupied molecular orbital (LUMO) to form a Coulombically bound electron and hole pair, with the electron on the LUMO and the hole on the HOMO. This electron/hole pair is usually referred to as the exciton.

Because excitons are only generated by those incident photons with the wavelength smaller than the absorption onset of polymer, a more red-shifted absorption profile of polymer would thus utilize a wider range of the sunlight, and could in principle generate more excitons for subsequent steps. Thus, a small band gap is usually desirable for polymers to absorb more sunlight and to maximize the exciton generation.

However, an inevitable loss mechanism exists in this exciton generation step: excited electrons have to thermalize to the LUMO level to form excitons. This means that the extra energy that is greater than the band gap of the polymer will be released as the thermal energy. This thermalization loss accounts for the most energy loss in a single junction solar cell. Together with the absorption loss from un-utilized photons that have less energy than the band gap of the polymer, this thermalization loss largely sets the Shockley-Queisser limit of a single junction solar cell to 33%.<sup>10</sup>

### **1.3.2 Charge separation**

The generated excitons on polymers will then diffuse to the *p-n* junction interface, i.e., the interface between *p*-type polymers and *n*-type fullerene derivatives (usually phenyl-C<sub>61</sub>-butyric acid methyl ester (PC<sub>61</sub>BM), to form a charge transfer state. The LUMO offset between the fullerene and the polymer provides a driving force to overcome the Coulombic attraction

within the charge transfer state, and facilitates the electron transfer from polymer's LUMO to fullerene's LUMO, leaving the hole still on polymer's HOMO and forming a charge separation state.

In this step, the exciton generated by light absorption is converted into one free electron on PC<sub>61</sub>BM and one free hole on polymer. Since this is the key step converting absorbed sunlight into free charges, it is crucial for organic solar cells to optimize this step to achieve high efficiency. Five requirements are usually considered to promote this charge separation step.

1) Since the exciton diffusion length is believed to be around 10 nm,<sup>11</sup> a proper domain size with an average diameter of 20 – 30 nm would be favorable for the excitons to survive from the diffusion process. Recent experimental results also indicate that a smaller domain size effectively enhances the charge separation efficiency (and overall efficiency) even though the energy levels and band gap of the conjugated polymer are not ideal.<sup>12</sup>

2) The polymer and PC<sub>61</sub>BM must be well intermixed to form sufficient interfacial areas in order to ensure high probability of charge separation. Ideally, the miscibility between polymer and PC<sub>61</sub>BM should be high enough to form enough interfacial area for exciton to split, but also low enough to form pure domains for charge transport (*vide infra*).

3) At the polymer:PC<sub>61</sub>BM interface, polymer backbone should be facing the fullerene with its  $\pi$ -plane (“face-on”) instead of interacting the fullerene with the edge of backbone (“edge-on”) or with the polymer chain end (“end-on”). This “face-on” conformation has been experimentally proved to benefit the exciton splitting at the molecular interface.<sup>13</sup>

4) According the Marcus theory, the LUMO offset between polymer and PC<sub>61</sub>BM should be similar to the reorganization energy of the electron transfer. Too large or too small a driving force would raise the transition state energy and decrease electron transfer rate. Thus,

appropriate LUMO-LUMO pairing between the polymer and the fullerene derivative is necessary to achieve a high efficiency of charge separation.<sup>14</sup> It is usually accepted that a minimum LUMO offset of 0.3 eV is needed to ensure exciton splitting.<sup>15</sup>

5) A partial charge-separated state on the polymer would be helpful to promote the exciton to fully split at the interface. Most often, a strong dipole pointing from the electron-rich unit to the electron-deficient unit of the polymer backbone helps to form a partial charge-separated state, and fluorination at the latter position is proved to be effective in increasing this dipole moment.<sup>16,17</sup> Correspondingly, the PC<sub>61</sub>BM should be adjacent to the electron-deficient unit of the polymer backbone, such that the partially separated electrons can be readily accepted by PC<sub>61</sub>BM. On the contrary, when the electron-deficient unit is hindered from PC<sub>61</sub>BM by bulky side chains, the charge separation efficiency would drop.<sup>18</sup>

Efficiency loss in this charge separation step mainly comes from the geminate recombination between unseparated electron and hole pairs (i.e., the charge transfer state can relax back to the ground state). Nevertheless, geminate recombination is still being actively investigated. Fortunately, the loss due to geminate recombination is often negligible when compared with the thermalization loss (*vide supra*) and the non-geminate recombination loss (*vide infra*); therefore the geminate recombination loss will not be further discussed in following chapters.

### 1.3.3 Charge transport

Under the built-in field, separated electrons and holes can transport from the polymer:PC<sub>61</sub>BM interface to the cathode and anode, respectively. Naturally, a comparable transport rate (i.e., carrier mobility) between electrons and holes is desirable.<sup>19</sup>

In most cases, because PC<sub>61</sub>BM domain is more crystalline than the polymer domain, the electron mobility is faster than the hole mobility. Therefore, the hole mobility typically becomes the limiting factor. The hole mobility in the BHJ blend includes three components: 1) hole transport along the polymer backbone; 2) hole transport among adjacent  $\pi$  planes in the same polymer domain; 3) hole transport between adjacent polymer domains. Therefore, to improve the hole mobility requires close  $\pi$ - $\pi$  stacking of polymer backbone, pristine crystalline domain of polymers, and good connectivity among crystalline domains.

The third major loss mechanism of OPV, non-geminate recombination, other than the thermalization loss and light absorption loss, occurs in the charge transport step. When the charge transport is not efficient enough to remove all separated charges, for example, due to a low hole mobility, free electrons and holes could accumulate in each domain and recombine at the polymer:PC<sub>61</sub>BM interface. A bimolecular recombination model is usually applied to simplify the non-geminate recombination process, in which the recombination current density is proportional to the square of charge carrier density under steady state.<sup>20</sup>

#### **1.3.4 Charge collection**

The end of the light-to-electricity process involves the free electrons and holes being collected by the cathode and anode, respectively. Thus, a proper energy level matching between polymer and the anode, and that between the fullerene and the cathode, are required to minimize the loss during the charge collection. Similarly to the charge separation step, a “face-on” orientation of polymer backbone to the electrode and a strong dipole at the electrode interface<sup>21</sup> are also favorable. Optimization of this step usually involves with surface modification to achieve the Ohmic contact, which is out of this dissertation’s scope.

## 1.4 General design rules of polymers for organic photovoltaics

Given the specific working mechanism of OPV as discussed above, we can conclude the general design rules of conjugated polymers to achieve highly efficient organic solar cells. Please note that as the understanding of OPV working mechanism has been gradually deepened in the past two decades, the design rationale of polymers has also been continuously improved over the time. Thus we try to summarize the design rationale of conjugated polymers for BHJ solar cells from a historical perspective.

1) Recognizing the limited light absorption of poly(3-hexylthiophene) (P3HT) due to its band gap of 1.9 eV, the community initially focused on designing new conjugated polymers to extend the absorption range of P3HT. This was done by introducing the concept of “donor-acceptor” (D-A) alternating copolymers, i.e., electron-rich moiety and electron-deficient moiety alternatively bound along the conjugated polymer backbone. This design strategy was to directly address the first step in the working mechanism of OPV: exciton generation. Numerous low band gap D-A polymers were synthesized to absorb more incident lights, and to further improve  $J_{sc}$ .

On the other hand,  $V_{oc}$  is mainly determined by the energy difference between free electrons and holes, which depends on the difference between PC<sub>61</sub>BM's LUMO level and polymer's HOMO level. Therefore, a high  $V_{oc}$  would require a deep HOMO level of the polymer. However, further lowering the HOMO level of the polymer would lead to a larger band gap, which would diminish the light absorbing ability of the polymer. Therefore, a trade-off exists: a deep HOMO is preferable to achieve a high  $V_{oc}$ , but the  $J_{sc}$  would be “sacrificed” due to a large band gap; on the other hand, a high HOMO would lead to a smaller band gap, benefiting  $J_{sc}$ , but the  $V_{oc}$  would inevitably become smaller. In 2006, Scharber et al. elegantly summarized this

trade-off, indicating that there exists an optimal HOMO level that could strike a balance between  $J_{sc}$  and  $V_{oc}$  to maximize the efficiency of organic solar cells.<sup>15</sup> Thereafter, much effort was made to synthesize polymers that would target the optimal HOMO and LUMO levels.

Perhaps the most noteworthy D-A polymers that were able to achieve high energy conversion efficiency numbers were the PTB series, first published by Luping Yu's group in 2009.<sup>22</sup> Soon after, benefiting from previous establishments in the chemical structure-band gap correlation of conjugated polymers,<sup>23</sup> many high-performing D-A polymers with desirable energy levels and band gaps were synthesized from 2009 to 2011, reaching efficiency numbers of 6%-7%, including three contributions from our research group.<sup>24-26</sup> Most of these polymers were designed under the guidance of Scharber's calculation.

2) Quite successful as Scharber's model was, many "seemingly promising" polymers would turn out to be low performing, even these polymer fitted into the Scharber's model very well. Some polymers, although possessing near-optimal energy levels and band gaps, generated poor current in their OPV device. Detailed investigation into these polymers usually revealed similar reasons: poor hole transport, either because of weak  $\pi$ - $\pi$  stacking of polymers or an "edge-on" orientation of polymer backbones to the electrode. Thus, in the second stage of polymer design, the community focused on the hole transport properties of polymers, i.e., the charge transport step in the working mechanism of OPV, in addition to the Scharber's model.

An emphasis was put on the morphology in the crystalline region of the BHJ active layer, since the crystalline domain directly determines hole mobility. Grazing incidence wide angle X-ray scattering (GIWAXS) was widely applied to examine the backbone orientation and  $\pi$ - $\pi$  stacking strength. In this stage (roughly 2012 until now), in order to achieve high mobility polymers, the OPV community borrowed some design rationale in another important research



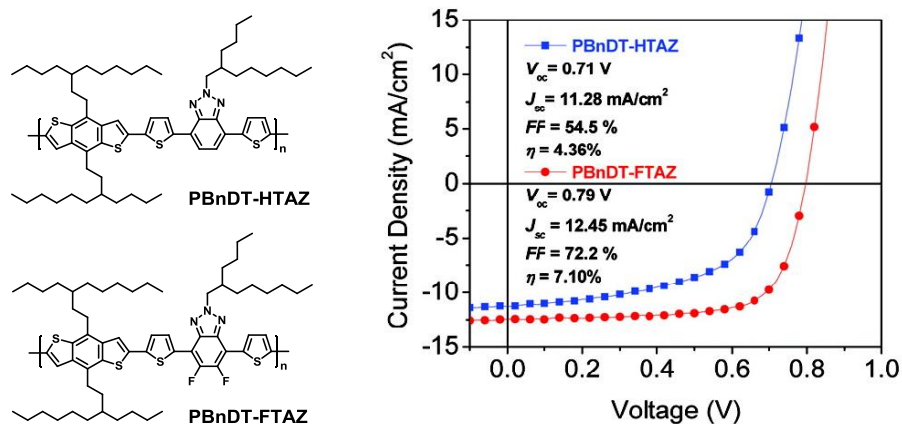
area within organic electronics: organic field-effect transistor (OFET). In fact, a number of building blocks, discovered in the OFET field, which were able to achieve high mobility have been adopted into the design of conjugated polymers for OPV.

3) More recently, the OPV community started to appreciate the importance of sub-mesoscale morphology in the BHJ active layer. Complimentary to GIWAXS, resonant soft X-ray scattering (RSoXS) reveals the morphology in weakly crystalline region by providing the scattering contrast on the 10 nm scale.<sup>27</sup> RSoXS characterizes domain spacing and domain purity, in addition to the backbone orientation at the polymer:PC<sub>61</sub>BM molecular interface. These important parameters are closely related to the key step of the OPV working mechanism: charge separation.<sup>28-31</sup> On the other hand, time-resolved spectroscopy, especially transient absorption (TA), sheds light on the charge separation kinetics on the femtosecond (fs) scale. The fate of generated excitons at polymer:PC<sub>61</sub>BM interface can thus be tracked and compared with hypothesized polymer design rationale. For example, the effect of dipole moment on charge separation has been investigated by TA.<sup>17</sup>

With a deeper understanding of the OPV operating mechanism, enabled by many new investigating tools, and the enriched structure-property relationships, designing conjugated polymers to achieve higher efficiencies of OPV devices becomes more complex and convoluted. In addition to the appropriate energy levels, band gap and a high hole mobility, the “ideal” polymers would also require favorable BHJ morphology, including minimal domain size, appropriate domain purity, “face-on” molecular orientation to PC<sub>61</sub>BM, docking position for fullerene near acceptor moiety, etc.

## 1.5 A unique polymer: PBnDT-FTAZ

In early 2011, our research group synthesized two structurally similar polymers for OPV (structures shown in Figure 1.5).<sup>32</sup> Surprisingly, the fluorinated polymer introduced an all-around



improvement of  $J_{sc}$ ,  $V_{oc}$ , and  $FF$ . Although structurally, poly(benzodithiophene-*alt*-dithienodifluorobenzotriazole) (PBnDT-FTAZ) merely replaced two hydrogen atoms in the repeating unit of poly(benzodithiophene-*alt*-dithienobenzotriazole) (PBnDT-HTAZ) with two fluorine atoms, the PCE of the former was significantly higher than that of the latter (7.1% vs. 4.4%), approaching the world-record high efficiency at the time.

**Figure 1.5** Chemical structures of PBnDT-HTAZ and PBnDT-FTAZ, and their OPV performance in BHJ solar cells with PC<sub>61</sub>BM. (Reprinted from reference 32 with permission. Copyright 2012 American Chemical Society.)

This high efficiency, especially the high  $J_{sc}$ , was unexpected, because the band gap of PBnDT-FTAZ was much larger than the ideal value in the Scharber's model (2.0 eV vs. 1.5 eV). In fact, PBnDT-FTAZ probably possesses the largest band gap among all high performing polymers with efficiencies above 6%. Its absorption range is only up to 620 nm, thus almost half of the visible light is not utilized at all. Therefore, why PBnDT-FTAZ was able to achieve a high

current from its narrow absorption range became interesting. In addition, the high *FF* (over 70%) of its OPV device was also very intriguing.

Interestingly, fluorination of PBnDT-HTAZ into PBnDT-FTAZ did not significantly change the HOMO and LUMO levels, according to the experimental results.<sup>32</sup> In fact, if we fit the LUMO level and the band gap of these two polymers into the Scharber's model, the predicted efficiency of PBnDT-HTAZ actually matches well with the experimental result (Figure 1.6). Therefore, it is the fluorine substituent that would largely account for the drastic performance improvement for PBnDT-FTAZ.

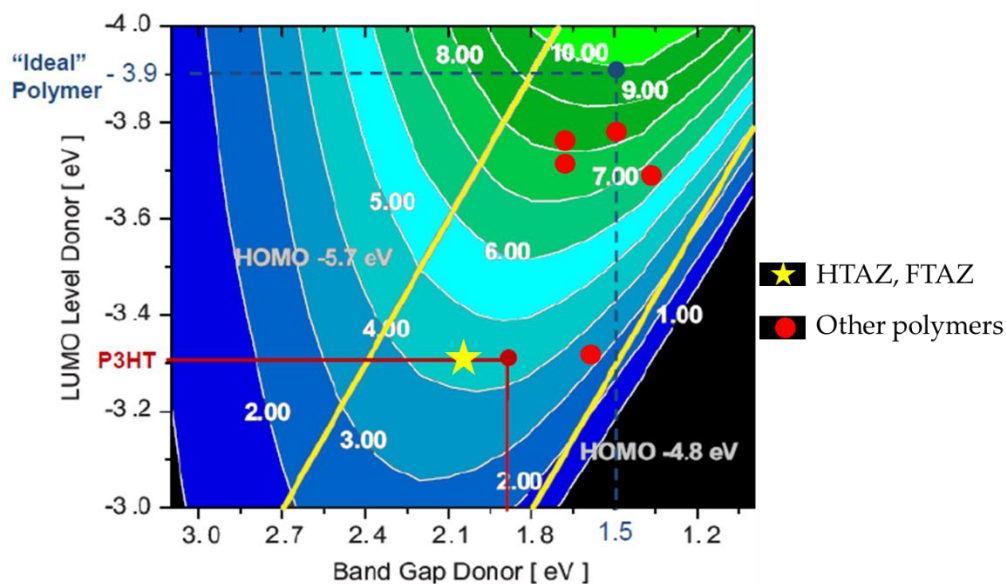


**Figure 1.6** Contour plot of calculated OPV efficiency as a function of band gap and LUMO level based on Scharber's model published in reference 13. PBnDT-HTAZ and PBnDT-FTAZ are labeled as yellow star while other high performing polymers are labeled as red dots.

This intriguing behavior of PBnDT-FTAZ (vs. PBnDT-HTAZ) thus inspired us to conduct a comprehensive investigation to answer “why PBnDT-FTAZ is so unique”. In the following Chapters, we will first unveil the fundamental reasons for this unexpectedly high

efficiency of PBnDT-FTAZ. During the investigation into this specific polymer, we identified two important structure-property relationships of conjugated polymers, and correlated the chemical modification to OPV device performance via BHJ morphology. Furthermore, based on our further fundamental understanding of PBnDT-FTAZ polymer and its OPV devices, we synthesized a new series of triazole (TAZ) based polymers through a general and versatile synthetic strategy. Pleasingly, OPV performance of one of these new polymers exceeds that of PBnDT-FTAZ, and opens a gate to even higher efficiencies via chemical modifications.

## CHAPTER 2

### CONTRASTING N-ALKYLATION SELECTIVITIES OF BENZOTRIAZOLE IN THF AND DMF

#### 2.1 Introduction

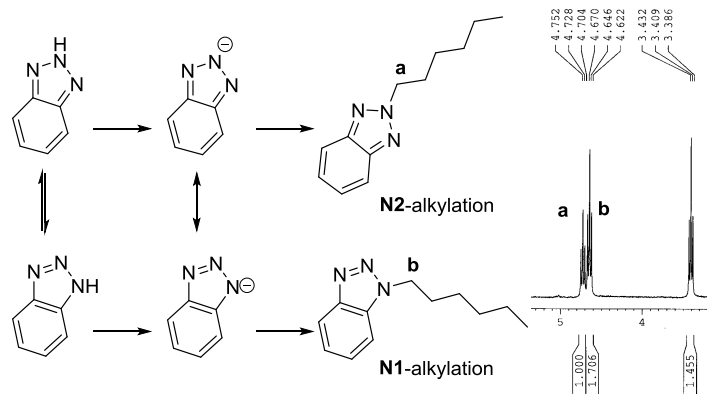
The acceptor unit of PBnDT-FTAZ, benzotriazole, has been used as a unique building block in the design of donor-acceptor conjugated polymers since its first such application was reported in 2004.<sup>33</sup> One notable feature of benzotriazole is that the necessary alkylation can occur on the N2 position of the benzotriazole (i.e., N2-alkylation). Such a “centered” alkylation pattern not only helps to solubilize resulting polymers, but also minimizes the steric hindrance between adjacent repeat units. Therefore, a more planar conjugated backbone is usually obtained by benzotriazole, which is beneficial for charge transport (e.g., high mobility), a desirable feature for organic photovoltaics (OPV).<sup>32,34-38</sup> PBnDT-FTAZ itself is a persuading example. The higher mobility of PBnDT-FTAZ than that of the archetypical poly(3-hexyl thiophene) (P3HT) partly accounts for former’s higher efficiency over 7% than the typically obtained 4% for P3HT based solar cells. In addition to its use in the design and synthesis of novel materials, benzotriazole has also been applied in synthetic chemistry. For example, Katritzky *et al.* have developed benzotriazole into a useful synthetic auxiliary for alkoxy-, alkylthio-, amino- and amido-alkylation, where benzotriazole serves as a weak nucleophile and a good leaving group.<sup>39-41</sup>

However, the yield of the desirable N2-alkylation is typically low in reported syntheses,<sup>42-45</sup> which significantly impedes efficient utilization of this unique building block. For example, Katritzky *et al.* reported a method to noticeably improve the overall yield of N-alkylation of benzotriazole; however, the N2-alkylation observed by NMR was only to be 20% - 55%, depending upon the alkyl halide.<sup>45</sup> In our original report of PBnDT-FTAZ, the yield of N2-alkylating the 5,6-difluorobenzotriazole was only around 17%, severely limiting large-scale syntheses of this promising monomer (FTAZ) and related polymers.<sup>32</sup> This low yield of N2-alkylation is largely due to the fact that the inherent tautomerization of the benzotriazole leads to two competing alkylations (N1 vs. N2 in Scheme 1). To promote the N2-functionalization of benzotriazole, Reynolds *et al.* introduced steric hindrance such as bromine or thiophene on 4/7 position of the benzotriazole and effectively improved N2-selectivity.<sup>37</sup> Alternatively, Shi *et al.* discovered that reacting benzotriazole with an alcohol under standard Mitsunobu condition favors the formation of the kinetic product (N2-substitution).<sup>46</sup> Successful as they are, these new approaches either suffer from multi-step syntheses of specific substrates, or only show high N2-selectivity with a few sterically hindered alkyls. In this chapter, we describe our own optimization of the alkylation of benzotriazole. We discover that for this simple S<sub>N</sub>2 reaction, the yield can be significantly improved in polar, aprotic solvents. Furthermore, these polar solvents favor the N2-alkylation whereas ether solvents significantly promote the N1-alkylation. We postulate that this reverse regioselectivity in ether is likely due to the formation of ion aggregates, similar to those found in solutions of enolates.

## 2.2 Optimization of N2-alkylation yield

In a typical benzotriazole alkylation *via* the S<sub>N</sub>2 mechanism, the triazole moiety is first deprotonated by a base. The benzotriazole anion serves as the nucleophile to attack the substrate, e.g., primary alkyl bromides (Scheme 2.1). In this scenario the selectivity and yield of the alkylation are solely determined in the second step, an S<sub>N</sub>2 reaction. Therefore, our study was focused on factors that govern the S<sub>N</sub>2 reaction, including solvent, temperature, leaving group and the substrate (i.e., the alkyl chain). We used <sup>1</sup>H-NMR spectra of the crude product after careful work-up to determine the selectivity and to estimate the conversion of each reaction. Selectivity and conversion were calculated according to equation 2.1 and 2.2, respectively, based on the integration of characteristic methylene peaks corresponding to these two isomers (N1 vs. N2) and the residual alkyl bromide (Figure S1).

**Scheme 2.1** Benzotriazole alkylation isomerism and characteristic NMR peaks



$$N2 \text{ selectivity} = \frac{I_a}{I_a + I_b} \times 100\% \quad (2.1)$$

$$\text{conversion} = \frac{1.2(I_a + I_b)}{I_a + I_b + I_c} \quad (2.2)$$

We first explored the effect of solvent and temperature, because they typically exert the most influence on the rate of the S<sub>N</sub>2 reaction. Methanol appeared to be the most popular solvent in existing literature.<sup>42-44</sup> However, the rate of S<sub>N</sub>2 reaction is usually limited in protic solvents, because the nucleophile is highly solvated *via* hydrogen bonding with protic solvent molecules. To improve the reaction rate (and the yield), we first attempted a common polar, aprotic solvent, DMF. The isolated yield in methanol is as low as literature reported; however, the isolated yields in DMF are significantly improved (Table 2.1). Interestingly, both solvents (methanol and DMF) facilitate the formation of the N2-product with little dependence on temperature (i.e., ~ 60% N2-selectivity in all studied cases). To summarize, a polar, aprotic solvent such as DMF greatly improves the yield of the alkylation of benzotriazole, with N-2 product being the dominant isomer. Also, a lower temperature appears to afford slightly higher yield of the N2 product. Finally, Table 2.1 shows that the isolated yield of the N2 isomer is very similar to the N2 selectivity estimated by <sup>1</sup>H-NMR, which indicates the conversion calculated by <sup>1</sup>H-NMR is a good estimate. Therefore, we will use the conversion and selectivity determined by <sup>1</sup>H-NMR in the following discussion for convenience without loss of meaningful comparison.

**Table 2.1** Effect of solvent and temperature on yield and selectivity

Solvent	T( °C)	NMR conversion	NMR N2-selectivity	isolated N2-yield <sup>b</sup>
MeOH	65	118%	62%	21%
DMF	0	111%	61%	64%
DMF	r.t.	112%	58%	58%
DMF	60	117%	55%	57%

<sup>a</sup> The reactions were performed with 1 mmol benzotriazole, 1.2 mmol (20% excess) hexyl bromide and 2.0 mmol potassium carbonate in 40 mL of solvent.

<sup>b</sup>The average isolated yield of N2-hexyl benzotriazole of three identical reactions (after column separation).



### 2.3 Opposite N-selectivity in THF and DMF

Table 2.2 summarizes the effect of leaving group and alkyl chain identity on the selectivity of this alkylation. As suggested by the previous discussion, all reactions were conducted in DMF at room temperature. First, no appreciable conversion was observed for the reaction with *t*-butyl bromide (entry 6), which supports the assumption that the alkylation proceeds via an S<sub>N</sub>2 mechanism. In general, both length and bulkiness of alkyl chains have minimal effects on the N2- selectivity (entries 1 through 5). N2-selectivity is lower with chloride/iodide leaving groups (entries 7 and 8). However, one exception comes from methyl iodide (entry 9), where a noticeably higher N2-selectivity (76%) was observed.

**Table 2.2** Effect of alkyl and leaving group on selectivity<sup>a</sup>

entry	Alkyl	leaving group	N2-selectivity
1	hexyl	bromide	69%
2	2-ethylhexyl	bromide	67%
3	2-butyloctyl	bromide	66%
4	<i>n</i> -butyl	bromide	55%
5	<i>s</i> -butyl	bromide	62%
6	<i>t</i> -butyl	bromide	N/A
7	hexyl	chloride	58%
8	hexyl	iodide	54%
9	methyl	iodide	76%

<sup>a</sup> The reactions were performed with 1 mmol of benzotriazole, 1.2 mmol of alkyl halide and 2.0 mmol of potassium carbonate in 40 mL of DMF at r.t. N/A denotes that no reaction was observed by NMR.

Attempting to further increase the yield and the N2-selectivity, we then investigated several common polar, aprotic solvents of various polarities. As shown in Table 2.3, similar N2-selectivity values around 70% were observed when solvents of similarly strong polarity as DMF were used, such as NMP and DMAc. Though DMSO is usually considered to be a more polar solvent than aforementioned ones, the alkylation with DMSO as the solvent does not show much N2-preference (*vide infra*). Surprisingly, for the reaction conducted in THF, a very low N2-selectivity (22%) was observed, together with a significantly low conversion. Interestingly, other ether solvents show similarly suppressed N2-selectivity. For example, the N2-selectivity for the reaction in dimethoxyethane is only 31%. When dioxane was adopted as the solvent, the N2-selectivity was even lower than that in THF. Additionally, no reaction was observed for ethyl ether as the solvent, since its low polarity does not favor the S<sub>N</sub>2 reaction.

**Table 2.3** Solvent effect on N2-selectivity<sup>a</sup>

entry	Solvent	N2-selectivity	conversion
1	DMF	57%	>99%
2	NMP	71%	>99%
3	DMAc	62%	>99%
4	DMSO	53%	>99%
5	THF	28%	43%
6	Dioxane	25%	2.2%
7	DME	31%	2.5%
8	Ethyl Ether	N/A	N/A

<sup>a</sup>The reactions were performed with 1.0 mmol of benzotriazole, 1.2 mmol of hexyl bromide and 2.0 mmol of K<sub>2</sub>CO<sub>3</sub> in 40 mL of solvent at r.t. N/A in selectivity denotes no product was observed on NMR.

## 2.4 Ion aggregate postulation

This opposite selectivity of benzotriazole alkylation in THF vs. DMF is quite analogous to that of enolate alkylation where two competing reaction pathways also exist, O-alkylation and C-alkylation.<sup>47</sup> When the enolate alkylation occurs in polar, aprotic solvents, such as hexamethylphosphoramide (HMPA), the negative charge of enolate anion is mainly located on the oxygen. Thus O-alkylation dominates the reaction. However, when the same enolate alkylation is conducted in THF, the oxygen anion of enolate participates in the formation of ion aggregates, together with metal cations and solvent molecules. As a result, only  $\alpha$  carbon is available for alkylation, leading to C-alkylation as the major reaction pathway. The structures of these enolate ion aggregates in THF have been well studied via UV-absorption and X-ray diffraction by Streitwieser *et al.*<sup>48-53</sup> and Williard *et al.*,<sup>54-57</sup> respectively. In addition, similar ion aggregates formed by various molecules<sup>58-63</sup> in other ether solvents have been reported.<sup>64</sup>

Herein we postulate that the observed different selectivity between N1-alkylation and N2-alkylation of benzotriazole in different solvents is also subject to this ion aggregate mechanism. We propose that in DMF and other polar, aprotic solvents, free benzotriazole anions are generated after complete deprotonation. Statistically, assuming equal charge densities at all three nitrogens, the ratio of N-2 anion vs. N-1 anion would be 1:2 (i.e., 33% probability of N-2 anion), which should lead to a 33% of N-2 selectivity. However, Table 2.3 shows the *opposite*: the N2-selectivity in DMF, NMP, and DMAc is typically above 65%. In fact, this preference of N2-product over N1-product for benzotriazole in polar, aprotic solvents is in good agreement with an earlier study on the tautomerism of 1,2,3-triazole, where Albert and Taylor predicted that the 2-H tautomer is preferred by a factor of two.<sup>65</sup> It was believed that the 1-H tautomer would suffer from an additional repulsion between the lone electron pairs on two adjacent  $sp^2$ -nitrogens.

Structurally similar to 1,2,3-triazole, the benzotriazole likely prefers the 2-H tautomer as well, which would lead to the dominance of N2-anion in polar, aprotic solvents and explain the N2-selectivity around 67%.

On the other hand, in THF and other ether solvents, the deprotonated benzotriazole could form ion aggregates with potassium cations and ether molecules, similar to the formation of enolate based ion aggregates in THF. In this scenario, the formation of ion aggregates by the dominant N2-anion would leave the N1-position of the N2-anion for the alkylation, whereas the N1-anion incorporated into the ion aggregates would subject the N2-position to the alkylation. Therefore, this very likely formation of ion aggregates would essentially *reverse* the N2-selectivity observed in polar, aprotic solvents where “free” anions are prevalent. In addition, the reaction rate would significantly slow down because of the low polarity of ether solvents and the additional step of “breaking apart” these ion aggregates before forming the alkylated product. Thus low conversion was observed in these ether solvents.

While DMF and THF show clear regioselectivity, conducting the same reaction in DMSO does not particularly prefer N2- or N1-alkylation. This is likely because the oxygen atom in DMSO has more  $sp^3$  character than that in DMF and more  $sp^2$  character than that in THF. This intermediate hybridization of oxygen in DMSO could result in only partial formation of ion aggregates. This partial formation of ion aggregates would not only explain the low selectivity in DMSO, but would also account for the higher conversion in DMSO than that in THF.

To offer more evidence to support the proposed formation of ion aggregates in ether solvents, we designed a simple experiment as follows. Because potassium cations can be easily trapped by 18-crown-6, adding 18-crown-6 into the reaction mixture would deplete these potassium cations that are required for the formation of ion aggregates. Therefore, the amount of

ion aggregates would dramatically decrease after adding a sufficient amount of 18-crown-6. As Table 2.4 shows, the 2-selectivity from the alkylation in DMF changes little in the presence of 18-crown-6, suggesting that the crown ether does not affect the  $S_N2$  reaction. However in THF, addition of crown ether increases the N2-selectivity from 22% to 45% and improves the conversion significantly, from 2.6% to 89% (see NMR spectra in SI). Both observations can be ascribed to the suppression of ion aggregate formation due to the sequestration of free potassium cations with 18-crown-6.

**Table 2.4** Crown ether effect on alkylation N2-selectivity <sup>a</sup>

Condition	DMF	THF
without 18-crown-6	68%	22%
with 18-crown-6	64%	45%

<sup>a</sup> The reaction were performed with 1.0 mmol of benzotriazole, 1.2 mmol of hexyl bromide and 2.0 mmol of  $K_2CO_3$  in 50 mL of solvent at r.t., with or without 2.0 mmol of 18-crown-6.

## 2.5 Optimization of N1-alkylation yield

Although N1-selectivity is preferred in THF, the conversion of this alkylation is too low to synthesize N1-alkyl benzotriazole in meaningful scale. To remedy the extremely low conversion in THF, we attempted to add DMF into the THF-based reaction to improve the polarity of the solvent system. Table 2.6 presents the 2-selectivities and conversions in a series of DMF/THF mixed solvents. Very encouragingly, a mere 5% DMF in THF can improve the conversion to 62%, while still achieving the high N1-selectivity observed in pure THF. Such a small amount of DMF might loosen the ion aggregates, expediting the reaction. However, further increases in the percentage of DMF in the mixed solvent could prevent the formation of ion aggregates completely and diminish the N1-selectivity, as indicated by Table 2.5.

**Table 2.5** N2-selectivity and conversion in a series of THF/DMF mixed solvents <sup>a</sup>

DMF (V%)	N2-selectivity	Conversion
0	24%	10%
5	29%	62%
20	46%	113%
50	53%	113%
80	53%	114%
95	58%	111%
100	60%	115%

<sup>a</sup> The reactions were performed with 1.0 mmol of benzotriazole, 1.2 mmol of hexyl bromide and 2.0 mmol of K<sub>2</sub>CO<sub>3</sub> in 50mL of mixed solvent at r.t.

## 2.6 Conclusion

In summary, we successfully improved the isolated yield of N2-alkylated benzotriazole to 64% by optimizing the reaction conditions of a simple S<sub>N</sub>2 reaction, very close to the theoretically predicted upper limit of 67%. Further, we observed opposite N1- and N2-selectivity for the alkylation of benzotriazole in DMF and THF, which could be explained by the formation of ion aggregates of the deprotonated 2-H benzotriazole tautomers, potassium cations and ether solvent molecules. This hypothesis was supported by a few experimental observations. We believe the disclosed mechanism through our experimental design will help design strategies to optimize the desirable isomers in other compounds of similar tautomerism. Finally, the much improved yield of the desirable N2-alkylated benzotriazole will significantly increase the accessibility of this unique building block for constructing novel materials for various applications.

## CHAPTER 3

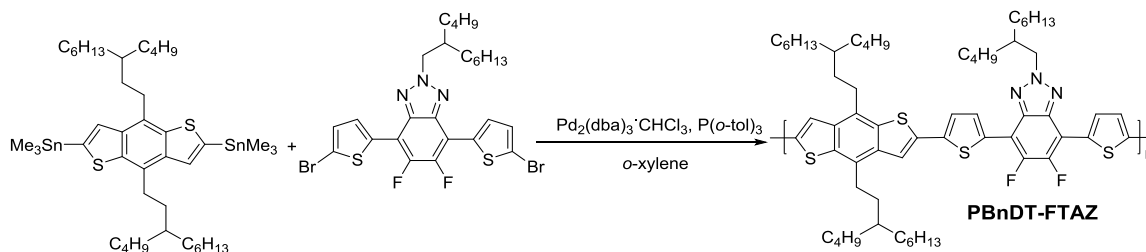
# CONTROLLING MOLECULAR WEIGHT OF PBNDT-FTAZ AND UNDERSTANDING ITS SIGNIFICANT IMPACT ON PHOTOVOLTAIC PROPERTIES

### 3.1 Introduction

Since its inception,<sup>32</sup> PBnDT-FTAZ has received significant attention<sup>66</sup> because it is an intriguing material with many outstanding features that need to be further explained. For example, with a medium band gap of 2.0 V, PBnDT-FTAZ can still generate over 7% power conversion efficiency with a noticeably high fill factor of over 70% in BHJ cells with a relatively thick film (200 – 300 nm).<sup>32</sup> Furthermore, the high performance of PBnDT-FTAZ based BHJ cells are not very sensitive to the morphology of the active layer.<sup>67</sup> However, during our own reproduction of PBnDT-FTAZ (Scheme 3.1),<sup>32</sup> we discovered that the molecular weight has a significant impact on the device performance.

Indeed, for any conjugated polymer for OPV devices, having an appropriate band gap and fine-tuned energy levels through molecular engineering of the conjugated backbone is only the first step towards the desired high PCE.<sup>6,68,69</sup> Even for conjugated polymers of an identical structure (e.g., conjugated backbone, side chain and substituents), the one having a high molecular weight usually outperforms the one of a low molecular weight when used in OPV devices, primarily through a significant increase in the  $J_{sc}$ . Such an effect of molecular weight on the OPV performance was first observed in the archetypical P3HT:PC<sub>61</sub>BM by Brabec et al.<sup>70,71</sup>

and Heeger et al.<sup>72</sup> Later, similar effects were also discovered for low band gap polymers by the Bazan group,<sup>73-74</sup> and our group,<sup>75</sup> among others.<sup>21,76</sup> As we will show in this chapter, all these interesting properties exhibited by PBnDT-FTAZ can only be obtained with polymers of a proper molecular weight. A careful study of a set of PBnDT-FTAZ with precisely controlled molecular weight (from 10 kg/mol to 60 kg/mol, calculated  $M_n$ ) reveals that the molecular weight significantly influences the morphology and structural order of PBnDT-FTAZ in its BHJ blend, all of which can be correlated with the device performance. Achieving such a deep understanding can undoubtedly facilitate the future design of high efficiency polymers for BHJ solar cells. This study details this systematic study, including the method we employed to precisely control the molecular weight of PBnDT-FTAZ.



**Scheme 3.1** Polymerization scheme of PBnDT-FTAZ.

### 3.2 Stoichiometry in polymerization

To construct a set of PBnDT-FTAZ with precisely controlled molecular weight, we decided to apply the classic Carothers equation (equation 3.1)<sup>77</sup> since the syntheses of donor-acceptor copolymers via palladium catalyzed polycondensation (e.g., Stille or Suzuki) fall into the category of classic step growth polymerization of AA/BB type monomers.<sup>77</sup> It is interesting



to note that the majority of these studies on the impact of molecular weight relied on fractionation of as synthesized polymers<sup>76</sup> or purity of the monomers<sup>21</sup> to obtain polymers of different molecular weight. These two methods are frequently adopted because it is very difficult to obtain polymers of high molecular weight via palladium (Pd) catalyzed polycondensation for any new conjugated polymers, let alone the accurate control of the molecular weight.

$$\bar{X}_n = \frac{1+r}{1+r-2rp}, (0 < r \leq 1, p \leq 1) \quad (3.1)$$

$$\bar{X}_n = \frac{1+r}{1-r}, (0 < r \leq 1, p = 1) \quad (3.2)$$

To use the Carothers equation to control the molecular weight in a predictive manner, one of the easiest approaches is to vary the stoichiometric ratio of two monomers ( $r$  in equation 3.1) while assuming the extent of reaction ( $p$ ) is unity or close to unity.<sup>77</sup> Under such an assumption, equation 3.1 is simplified into equation 3.2. However, to effectively use equation 3.2 in the case of the Stille coupling based polycondensation, one would have to optimize the reaction condition to promote the reaction to completion ( $p = 1$ ), in addition to having ultra-pure monomers (so as to precisely tune the stoichiometric ratio,  $r$ ). Indeed, we spent significant efforts in optimizing the polymerization as shown in Scheme 3.1. The key findings are summarized as follows. First, the purity of the monomers is crucial. Fortunately, both monomers in Scheme 3.1 are solid, which allowed us to purify them via multiple recrystallizations. Second, the purity of Pd catalysts needs to be ensured. In our case, the commercially available catalyst,  $\text{Pd}_2(\text{dba})_3$ , must be further purified via recrystallization into  $\text{Pd}_2(\text{dba})_3 \cdot \text{CHCl}_3$  to remove the redundant Pd nanoparticles, as reported by Ananikov et al.<sup>78</sup> These catalytically inactive Pd nanoparticles, often present in the commercially available Pd catalysts, not only significantly reduce the

desirable loading ratio of the catalyst, but also can have negative impact on the coupling reaction/polycondensation. Finally, we discovered that the use of a microwave reactor was a powerful tool to drive the reaction to completion in a very short period of time (10 to 30 min). All these findings are very general, and should be applicable to other similar Stille coupling based polymerization as well.

With carefully purified catalyst and monomers, we were able to vary the stoichiometric ratio of these two monomers to obtain PBnDT-FTAZ with the targeted molecular weight under the microwave condition. Table 3.1 summarizes the molecular weight data of our PBnDT-FTAZ polymers, together with the estimated band gap from the UV-Vis absorption onset. Please note that gel permeation chromatography (GPC), though generally accepted to estimate the molecular weight, only provides data relative to the standard (polystyrene in our case), and typically overestimates the molecular weight of conjugated polymers by a factor of 1.5 or higher relative to the true molecular weight.<sup>79,80</sup> Thus we were pleased to observe a quite linear correlation of the actual molecular weight (measured by GPC) vs. the targeted one (calculated by equation 3.2) (Figure 3.1), indicating our successful control of the molecular weight of PBnDT-FTAZ based on the Carothers equation.

**Table 3.1** Controlling the molecular weight of PBN-DT-FTAZ via tuning stoichiometric ratio

Polymer	Stoichiometric Ratio	Targeted MW (kg/mol)	$M_n^b$ (kg/mol)	$M_w^b$ (kg/mol)	Dispersity ( $\bar{D}$ ) <sup>b</sup>	Absorption onset (nm)	Band gap (eV) <sup>d</sup>
10k <sup>a</sup>	1:1.100	10	18.3	34.4	1.89	609	2.04
20k	1:1.050	20	36.5	76.6	2.10	612	2.03
40k	1:1.025	40	55.2	119	2.15	614	2.02
60k	1:1.000	60	71.4	156	2.19	615	2.02
10k/60k (1:2)			36.3 <sup>c</sup>	115 <sup>c</sup>	3.17 <sup>c</sup>	614	2.02

<sup>a</sup> “10k” is denoted for the polymer with the targeted molecular weight of 10 kg/mol, “20k” for the polymer with the targeted molecular weight of 20 kg/mol, etc.

<sup>b</sup> Determined by GPC in 1,2,4-trichlorobenzene at 150 °C

<sup>c</sup> Calculated according to GPC values.

<sup>d</sup> Measured from film absorption spectra at  $\lambda_{\max}$ .

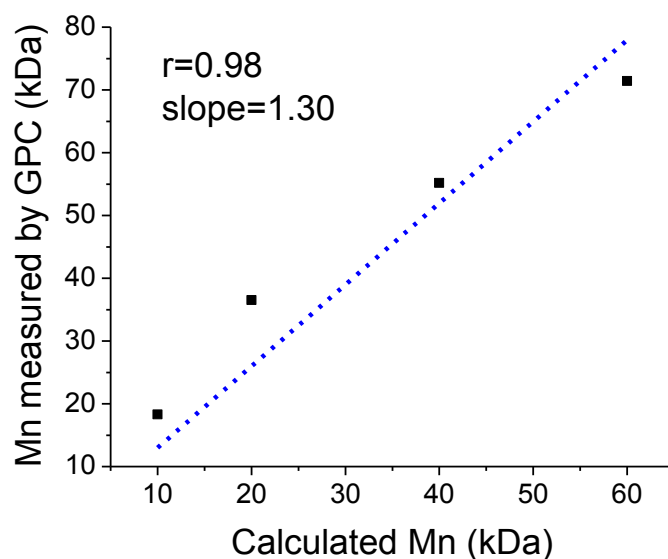


**Figure 3.1** Correlation of actual  $M_n$  measured by GPC and calculated  $M_n$  by the Carothers Equation. The near-to-unity correlation coefficient indicates good reliability of molecular weight control by stoichiometry. The slope of 1.30 reflects the fact that GPC usually overestimates the molecular weight of conjugated polymers by a certain constant.

### 3.3 Photovoltaic performance and electrochemical properties

The photovoltaic characterization of these four polymers shows a clear impact on the performance by the molecular weight (Figure 3.2 and Table 3.2). For fair comparison, devices were fabricated according to an optimized condition we reported earlier[3b] (see experimental section for details). Indeed, the highest efficiency (over 7%) is the device based on the 40k polymer, with a  $J_{sc}$  of 12.9 mA/cm<sup>2</sup>, a  $V_{oc}$  of 0.79 V, and a  $FF$  over 70%. In contrast, lower molecular weight polymers (10k and 20k) based BHJ devices offer much lower efficiency values, primarily because of the reduced  $J_{sc}$  and  $FF$  (Table 3.2). Further increasing the molecular weight beyond 40 kg/mol, for example, in the case of the 60k polymer, leads to a noticeably lower solubility in the processing solvent (trichlorobenzene). Nevertheless, the BHJ device based on the 60k polymer still shows an efficiency of 6.4%, a value slightly lower than that obtained from the device based on the 40k polymer (7.3%). To further understand the impact of molecular weight on the device performance, we mixed 10k and 60k polymers by 1:2 weight ratio to “recreate” the 40k polymer with a  $M_w$  very close to that of the as-synthesized 40k polymer (but  $M_n$  close to that of the as-synthesized 20k polymer). Interestingly, such a “recreated” 40k polymer based BHJ device offers higher efficiency (6.7%) than that of the device based on either the 10k polymer (1.4%) or the 60k polymer (6.4%). Furthermore, the incident photon to current efficiency (IPCE) data (Figure 3.2b) shows the relative contribution of the polymer and the fullerene constituents to the performance, which is clearly molecular weight dependent. For example, the 10k polymer based device shows a flat IPCE curve though at low IPCE values, indicating balanced contribution of the polymer and the fullerene to the  $J_{sc}$ . On the other hand, the largest imbalance is observed in the 60k polymer based device, which exhibits an excellent

IPCE of 70% for the polymer (near 600 nm) but a significant suppression to near 40% for the fullerene at 400 nm.

**Table 3.2** Average photovoltaic performance and hole mobility of PBnDT-FTAZ: PC<sub>61</sub>BM devices with different molecular weights

Polymer	Polymer: PC <sub>61</sub> BM	Thickness (nm)	$V_{oc}$ (V)	$J_{sc}$ (mA/cm <sup>2</sup> )	$FF$ (%)	$\eta$ (%)	Mobility (cm <sup>2</sup> /V s)
10k	1:2	230	0.71	3.61	55.5	1.4	$1.75 \pm 0.37 \times 10^{-3}$
20k	1:2	320	0.71	11.6	60.4	5.0	$3.31 \pm 0.41 \times 10^{-3}$
40k	1:2	315	0.79	12.9	71.9	7.3	$4.10 \pm 0.30 \times 10^{-3}$
60k	1:2	330	0.77	12.7	65.6	6.4	$3.03 \pm 0.30 \times 10^{-3}$
10k/60k (1:2)	0.33:0.66:2	355	0.80	12.4	66.6	6.7	$4.05 \pm 0.47 \times 10^{-3}$

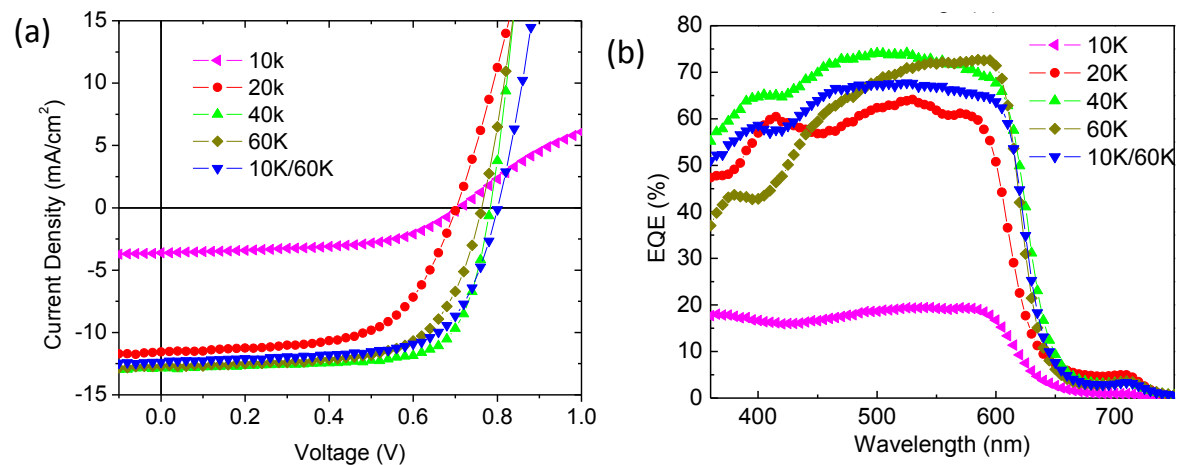


**Figure 3.2** (a) Current density vs. voltage curves and (b) Incident photon to current efficiency (IPCE) curves of PBnDT-FTAZ: PC<sub>61</sub>BM devices with molecular weight ranging from 10 kg/mol to 60 kg/mol. All polymer: PC<sub>61</sub>BM blends were prepared in trichlorobenzene (TCB) as the processing solvent.

So what cause(s) this interesting impact of molecular weight of PBnDT-FTAZ on its BHJ device performance? First, the difference in molecular weight has little impact on the absorption of PBnDT-FTAZ in solution and as thin films (Figure 3.3). When PBnDT-FTAZ is blended with PC<sub>61</sub>BM in the active layer, the blend based on the 10k polymer does show a lower absorbance in the region (500 nm to 600 nm) where PBnDT-FTAZ absorbs the most (Figure 3.4). However, this minor difference in the absorbance cannot account for the significantly lower  $J_{sc}$  as obtained from the 10k polymer based BHJ devices. Second, the measured energy levels for all studied polymers are very similar (Table 3.3), with similar band gaps as well. Therefore, a plausible explanation – the molecular weight influencing the device properties via changing the optical and electronic properties of these polymers – is essentially ruled out. Third, the charge carrier mobility (measured by Space Charge Limited Current method (SCLC) increases by a factor of two as the molecular weight increases from 10 kg/mol to 40 kg/mol (Table 3.2). However, this difference on the mobility can only *partially* account for the observed *significant* increase of the  $J_{sc}$  from the 10k polymer based BHJ devices to the 40k based devices, since the “low” hole mobility of the 10k polymer based devices,  $1.75 \times 10^{-3} \text{ cm}^2/\text{V}\cdot\text{s}$ , is sufficiently high to sustain a high  $J_{sc}$ .<sup>81</sup>

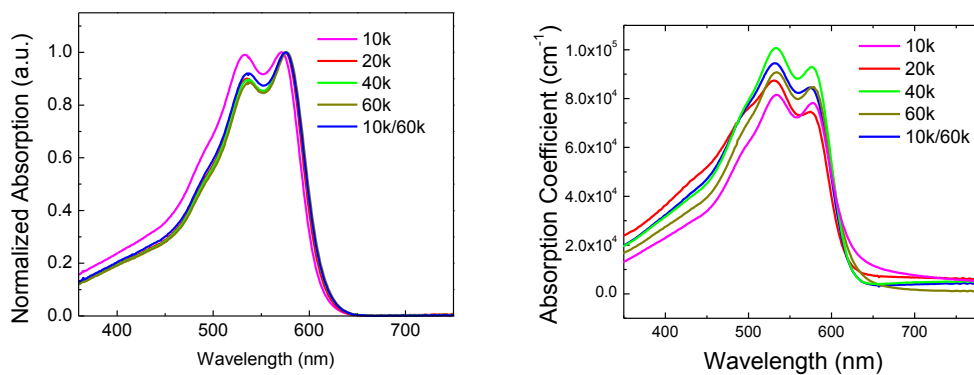


**Figure 3.3** UV-visible absorption spectra of pure polymers in dichlorobenzene solution (left) and pure polymer film on glass substrate (right).

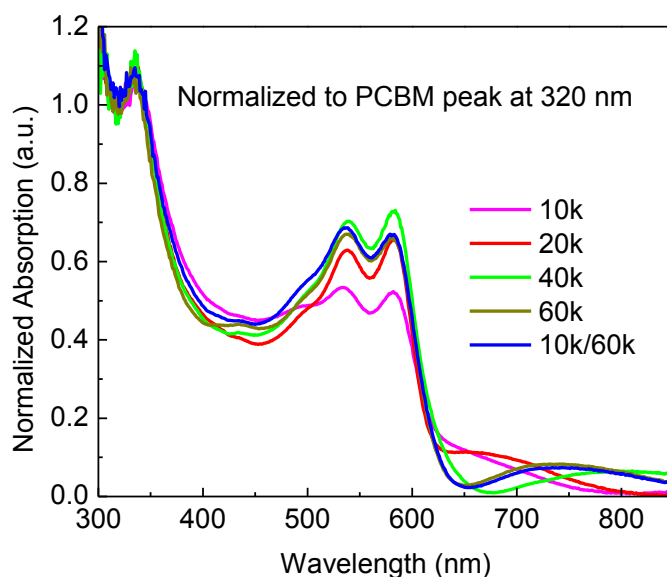


**Figure 3.4** UV-visible absorption spectra of the polymer:PC<sub>61</sub>BM blends (i.e., the active layers) on glass/ITO/PEDOT:PSS substrates. Note: Varied absorbance in transparent region (> 650 nm) is due to optical interference.

**Table 3.3** Polymerization yields and energy levels<sup>a</sup> of PBnDT-FTAZ polymers based on different molecular weights

Polymer	Yield (%)	HOMO (V)	LUMO <sup>b</sup> (V)	Band gap <sup>c</sup> (V)
10 kg/mol	97 <sup>d</sup>	− 5.46	− 3.42	2.04
20 kg/mol	56	− 5.51	− 3.48	2.03
40 kg/mol	60	− 5.59	− 3.57	2.02
60 kg/mol	70	− 5.51	− 3.49	2.02
10/60 kg/mol		− 5.58	− 3.56	2.02

<sup>a</sup> Measured by cyclic voltammetry with ferrocene/ferrocenium as the standard;

<sup>b</sup> Calculated from optical band gap (BG) using the equation LUMO=HOMO+BG;

<sup>c</sup> optical band gap calculated from the absorption onset on UV-vis spectrum;

<sup>d</sup> Only THF portion was collected for 10k polymer (see Experimental Section).

### 3.4 Morphology impact of polymer molecular weight

Further investigation of the active layer via X-ray techniques offers insights on the morphology and structure in these thin films. We employed grazing incidence wide angle X-ray scattering (GIWAXS) to probe the crystalline regions of BHJ active layers and the neat polymer reference thin films (Figure 3.6 in Experimental Section). In general, the data confirms that all five PBnDT-FTAZ polymers exhibit relatively low crystallinity (including the “recreated” 40k polymer) in the neat films and the BHJ blends, similar to what we observed before.<sup>67</sup> However, careful inspection of these data discloses subtle but distinct difference among all five BHJ blends. The lamellar stacking peak for the 10k polymer based BHJ blend has the highest intensity among all five films (Figure 3.5a), corresponding to a  $d$ -spacing of 18 Å in the (100) direction. In addition, the (010)  $\pi - \pi$  stacking is weak and does not show much intensity difference between the in-plane and out-of-plane directions. These data indicate that the low molecular weight polymer (10k) has the highest lamellar ordering among all five films, and there is no preferred orientation of “face-on” or “edge-on” with respect to the substrate. However, as the molecular weight increases, the intensity of the peak corresponding to the (100) direction decreases, implying that the film is getting even more amorphous. More importantly, higher molecular weight based blends show noticeably higher diffraction intensity of the (010)  $\pi - \pi$  stacking peak for the out-of-plane than for the in-plane direction, implying the conjugated backbone adopts more “face-on” orientation as the molecular weight increases. The “face-on” orientation, i.e.,  $\pi$  conjugated backbone lying towards the substrate/electrode, facilitates the vertical charge transport as seen in typical BHJ devices, which explains the noticeable increase of the hole mobility as the molecular weight goes beyond 10 kg/mol (Table 3.2). Finally, the diffraction pattern of the “recreated” 40k polymer is very similar to that of the pristine 40k polymer,



indicating that the ordered regions of these two BHJ films are qualitatively the same. It might thus not be coincidental that the measured hole mobility of the “recreated” 40k polymer is almost identical to that of the pristine 40k polymer, and the efficiency of the BHJ device based on the former polymer is close to that of the device based on the latter polymer. Nevertheless, given that the crystallinity (and hence the degree of ordering) of the PBnDT-FTAZ polymers is low, we caution against strong interpretations of the preferential “face-on” orientation. We also note that the diffuse halo at  $1.4 \text{ \AA}^{-1}$  due to PC<sub>61</sub>BM aggregation is essentially identical for all devices, indicating that a similarly aggregated phase of PC<sub>61</sub>BM is present in all devices.

**Table 3.4** Relative composition variations, domain spacing and anisotropy measured by R-SoXS along with power conversion efficiency.

Polymer	Relative composition variations	Domain spacing (nm)	Anisotropy Ratio at 286.2 eV	$\eta$ (%)
10k	1.00	470	0.15	.4
20k	0.95	110	0.18	.0
40k	0.83	65	0.19	.3
60k	0.78	65	0.17	.4
10k/60k (1:2)	0.68	110	0.14	.7

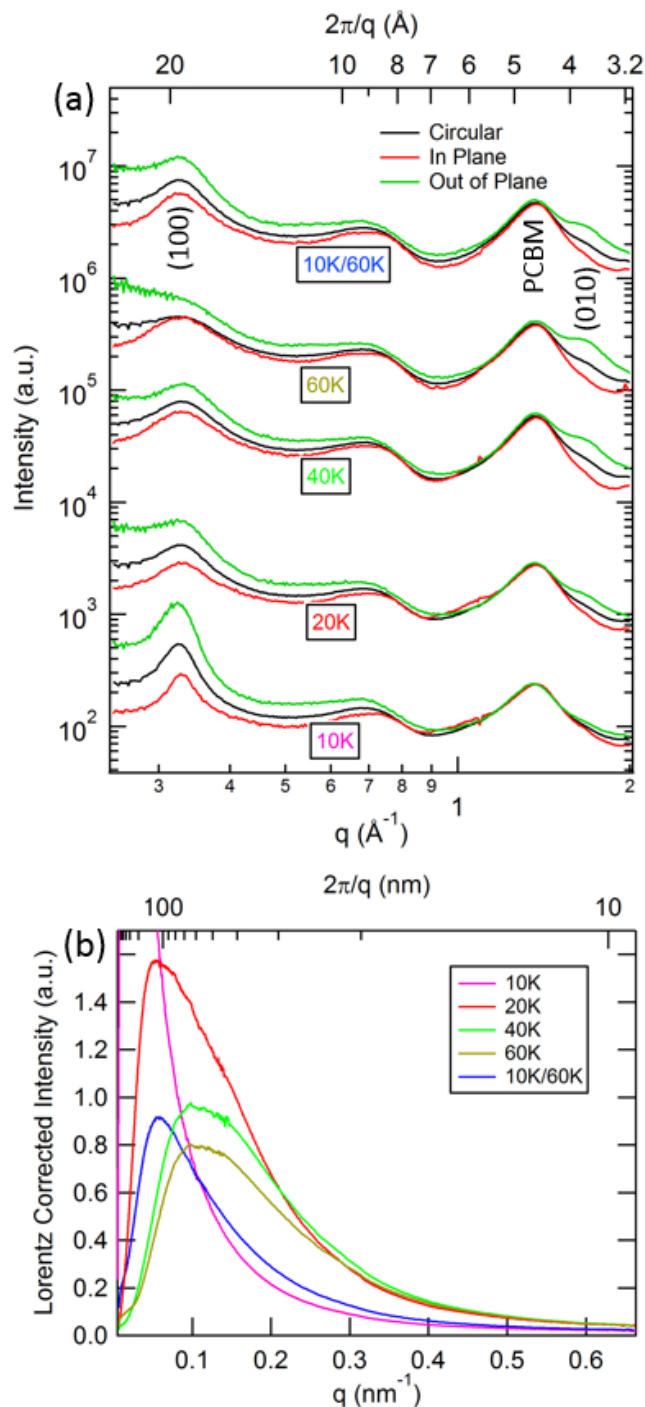


**Figure 3.5** (a) GIWAXS out-of-plane and in-plane  $20^\circ$  sector averages along with circular averaged data of the five blend films of this study. The (100) lamellar and (010) pi-pi stacking peaks are labeled along with typical signal from PC<sub>61</sub>BM. Traces have been scaled vertically for ease of view (log y-axis). (b) Lorentz corrected R-SoXS scattering profiles for 284.1 eV for the five blend films of this study. The peak scattering intensity for the 10k polymer:PC<sub>61</sub>BM blend on this scale is 8.5.

Complementary to GIWAXS, which is only sensitive to the crystalline region, resonance soft X-ray scattering (R-SoXS) probes the overall compositional morphology including the highly amorphous regions, i.e., domain size distribution, long period and relative composition variations.<sup>82</sup> R-SoXS is particularly useful to this set of samples because all five PBnDT-FTAZ polymers show relatively low crystallinity as discussed earlier. Table 3.4 summarizes the domain characteristics of all polymers in their BHJ blends from R-SoXS, with the scattering profiles plotted in Figure 3.5b. The profiles represent the spatial frequency distribution of the composition variations and do not exhibit a hierarchical morphology (as might have been indicated by a bimodal distribution) over the length scales probed. The biggest difference between devices is the long period, which represents the domain spacing between regions that exhibit the largest composition variations. The low molecular polymer (10 kg/mol) based BHJ blend shows the largest in-plane domain spacing (~470 nm confirmed with soft X-ray microscopy), almost 8 times of the domain spacing from the BHJ blend based on the 40k polymer. If we assume a volume ratio of 1:2 for the polymer-rich domain and the fullerene-rich domain based on the weight ratio of 1:2 for polymer:PC<sub>61</sub>BM in all blends, an average domain size of 157 nm ( $470 \text{ nm} \cdot 0.33$ ) for the polymer-rich domain can be estimated for the 10k polymer based blend, in stark contrast to the 22 nm for the 40k polymer based blend, which has the best BHJ device performance. Given the fact that similar domain composition variations have been determined for these two blends, the much smaller domain size in the case of the 40k polymer based BHJ blend indicates significantly more interfacial area between the polymer-rich and the PC<sub>61</sub>BM domains, and consequently a shorter average distance for excitons to travel to such interfaces. Similarly, charge extraction from mixed regions that exhibit excellent exciton quenching ability would be facilitated by shorter distances to the respective majority phase.<sup>83</sup> We note that recent

observations of fullerene miscibility in donor polymers<sup>84-88</sup> implies a minimum level of PC<sub>61</sub>BM dispersion within the rather amorphous FTAZ. Such dispersed fullerenes might be essential in splitting excitons and providing charge transport channel as shown recently in two other high performing materials systems.<sup>83,89</sup> It might thus not be necessary to achieve much smaller domain sizes and spacings as those observed here.

Polarization dependent R-SoXS can also assess the relative orientation of the backbone of the conjugated polymer (i.e., edge-on versus face-on) relative to the polymer/fullerene interface,<sup>83, 27</sup> which has been shown in bilayer devices to be critical to device performance<sup>90</sup> and has also been implicated recently in fullerene-based BHJs to play a significant role.<sup>83</sup> Here, the anisotropy parameter that describes such orderings shows the highest face-on orientation of the conjugated backbone with respect to the polymer/PC<sub>61</sub>BM interface for the 40k polymer based device (see Table 3.4 and Figure 3.6 in Experimental Section), i.e., the best performing device. However, the differences in relative face-on orientation are not very large between devices. We thus assume that exciton dissociation and charge recombination behaviors at polymer-rich/PC<sub>61</sub>BM interfaces are similar for all five samples. Therefore the interfacial area and travel distance for excitons would largely control  $J_{sc}$ . Indeed, the shorter distances and larger interface areas of the 40k polymer based device, for example, results in a four times larger  $J_{sc}$  than in the case of the 10k polymer based device (Table 3.2). Therefore, the compositional morphology in highly amorphous regions of these PBnDT-FTAZ polymers, i.e., domain size distributions and domain purity, is believed to be the leading cause for the observed molecular weight-dependence of BHJ performance (in particular  $J_{sc}$ ).

The difference of the domain spacing and composition variations of these five samples can also help understand why the “recreated” 40k polymer (i.e., the 10k/60k polymers blend)

based BHJ cell offers a very respectable efficiency value of 6.7%. This efficiency value is close to that of the device based on the pristine 40k polymer (Table 3.2), but higher than the efficiency of any other polymer based BHJ device in this study. First, the domain spacing in the “recreated” 40k polymer based BHJ blend (~ 110 nm) is surprisingly similar to that in the 20k polymer based blend (Table 3.5), and larger than the domain spacing (~ 65 nm) in the pristine 40k polymer based blend. This observation seems contradictory to the previous discovery that the crystalline region of the “recreated” 40k polymer based BHJ film is qualitatively similar to that of the pristine 40k polymer based one. However, this “unexpected” result on the domain spacing can be correlated with the fact that the calculated  $M_n$  of the “recreated” 40k polymer ( $M_w$  close to the pristine 40k polymer) is very close to that of the 20k polymer (Table 3.1). All these results might imply that domain spacing measured between polymer-rich regions is more affected by the  $M_n$  while the  $M_w$  would have a larger influence on the  $\pi$ - $\pi$  stacking in the crystalline region. Next, we want to address why the  $J_{sc}$  of the BHJ device based on the “recreated” 40k polymer is noticeably higher than that of the 20k polymer based device, but similar in value to that of the 40k polymer or 60k based devices. We believe this observation is related with the domain purity in these BHJ blends, which is likely not at a compositional equilibrium. As shown in Table 3.5, the relative domain purity (i.e., relative composition variations) of the “recreated” 40k polymer based blend is noticeably less than that of the pristine 20k polymer based one. The decreased composition variations indicates increased inter-mixing of PC<sub>61</sub>BM within the polymer-rich phase in the case of “recreated” 40k polymer based blend when compared with that in the 20k polymer based blend. The increased dispersion of PC<sub>61</sub>BM and the polymer in a mixed domain would facilitate exciton harvesting within this mixed domain and the charge transport of the electron to the polymer-rich/PC<sub>61</sub>BM-aggregate interface. Very similar observations that mixed

domains can enhance performance have been made recently in several other systems,<sup>89,91,92</sup> and the higher mixing would effectively compensate for the larger domain size (proportional to the domain spacing) in the case of “recreated” 40k polymer based blend. As a result, the obtained  $J_{sc}$  of the “recreated” 40k polymer based device is higher than that of 20k polymer based one (similar domain size but less dispersed PC<sub>61</sub>BM), and close to that of the 40k polymer based device (smaller domain size and less dispersed PC<sub>61</sub>BM). Finally, please note that the “recreated” 40k polymer is a *mixture* of the 10k polymer and the 60k polymer, thus it is not a big surprise to have PC<sub>61</sub>BM easily percolate into this mixture, leading to less pure domains with more dispersed PC<sub>61</sub>BM. Please note that the present expansion of the morphology paradigm to include mixed domains and dispersed fullerene is complex and the precise role of these factors is subject of recent and ongoing research.<sup>91,92</sup> Significantly more detailed work is also required to fully understand why the external quantum efficiency (EQE) of the fullerene but not the polymer drops with the use of the highest molecular weight polymer (e.g., 60k polymer in this study). A complete disentanglement of this complexity is outside the scope of this chapter, but our observations serve as a good motivator for further study.

### 3.5 Discussion and conclusion

A few worth-noting points emerged from this study. First, it is a viable approach to use the Carothers equation to precisely control the molecular weight of conjugated polymers, as we showed in the case of PBnDT-FTAZ. However, one has to carefully purify the reagents (e.g., monomers and the catalyst) and optimize the reaction condition (e.g., microwave heating) before adopting this methodology to the synthesis of other conjugated polymers via Pd catalyzed coupling reactions. Second, the molecular weight of conjugated polymers *does* have a significant

impact on the performance of related BHJ solar cells, based on our study and results from other studies<sup>21,70-72,74-76</sup>. Though the “optimal” molecular weight could be different for specific polymers, it appears that polymers having a molecular weight ( $M_n$ ) between 30 kg/mol and 60 kg/mol are good candidates to demonstrate the “true” photovoltaic properties of the conjugated polymer without performance being significantly “tainted” by the molecular weight.<sup>21,70-72,74-76,79</sup> Such an “optimal” molecular weight appears to be around 40 kg/mol for PBnDT-FTAZ. Third, the causes for such molecular weight impact on the photovoltaic performance could be different for different conjugated polymers. Though others have shown that the crystalline regions of polymers in these BHJ blends<sup>21,74</sup> could be the leading factor that affects the performance, we show that the compositional morphology, i.e., domain spacing and domain purity, is even more important to account for the performance of polymers having relatively low crystallinity and a high percentage of amorphous domains as in the case of PBnDT-FTAZ and some other polymers (e.g., PTB7).<sup>87</sup> It appears that PBnDT-FTAZ having a molecular weight ( $M_n$ ) of 40 kg/mol strikes a nice balance of domain spacing/size, purity and structural orientation in the crystalline region, thereby resulting in the highest efficiency of 7.3% of its BHJ device in the studied set of materials. Finally, the subtle difference between the “recreated” 40k polymer and the pristine 40k polymer (e.g., device performance, morphology and structure in BHJ blends) implies that the polydispersity, though largely neglected in the past, might play a role in affecting the device performance of conjugated polymer based solar cells. Therefore, the “precise” synthesis of conjugated polymers with controlled molecular weight and polydispersity should be one of the research priorities in the future.<sup>93-95</sup> One strategy could be extending the Grignard metathesis (GRIM) synthesis of polythiophene to other conjugated polymers. For example, recently Seferos et al. demonstrated the controlled synthesis of electron-deficient conjugated polymers via

refining nickel based catalyst.<sup>96</sup> Lastly, the observed subtle difference on the contribution of polymer and PC<sub>61</sub>BM to the EQE indicate that this materials system has not been fully optimized in the present devices. In fact, such an interesting observation should motivate studies that seek to understand the parameters that control and optimize the individual contributions from the polymer and fullerenes.

### 3.7 Experimental Section

*Polymerization with stoichiometric control:* The synthesis and purification of monomers (dibromo FTAZ and bistrimethyltin BnDT) and the purification of catalyst Pd<sub>2</sub>(dba)<sub>3</sub> were as described in previous publications. In a microwave reaction tube equipped with a stir bar was added 64.5 mg of dibromo FTAZ (0.1 mmol), calculated amount of bistrimethyltin BnDT (96.9 mg for the 10k polymer, 92.5 mg for 20k, 90.3 for 40k or 88.1 for 60k), 4.9 mg of P(*o*-tol)<sub>3</sub> and 2.0 mg of Pd<sub>2</sub>(dba)<sub>3</sub> CHCl<sub>3</sub>. After three vacuum-argon refilling cycles, 6.5 mL of anhydrous *o*-xylene was added via syringe. The tube was then planted in a CEM Discover microwave reactor to allow the polymerization for 10 minutes (300 W, 200 °C, 100 psi, 10 minutes of heating time). The resulted gel was then dissolved in hot chlorobenzene and precipitated in 120 mL of methanol. The collected precipitation was extracted in a Soxhlet extractor by ethyl acetate, hexane, THF and chloroform subsequently. The chloroform portion (10k polymer was all dissolved in THF portion) was concentrated and precipitated in 120 mL of methanol again to yield a metallic purple solid. The yield of each polymer is summarized in Table S2.



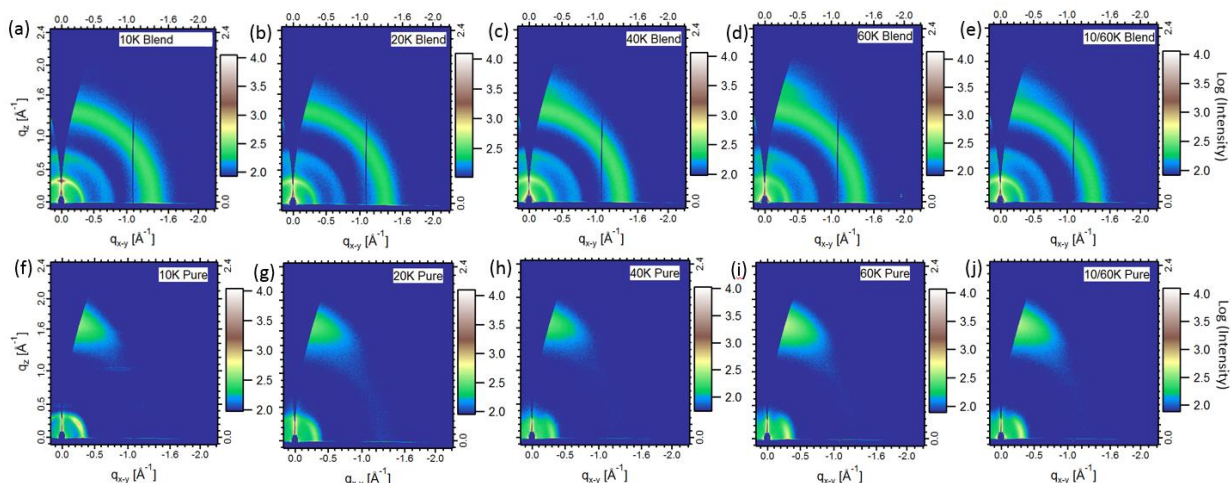


**Figure 3.6** Two dimensional (2D) GIWAXS data for blend polymer films based on (a) 10k, (b) 20k, (c) 40k, (d) 60k and (e) 10k/60k PBnDT-FTAZ polymers. Corresponding data of neat polymer films of (f) 10k, (g) 20k, (h) 40k, (i) 60k and (j) 10k/60k PBnDT-FTAZ. All films were on PEDOT:PSS Si substrates, and showed comparable features/intensities of measurements on actual devices on glass/ITO/PEDOT:PSS substrates. The 2D data have been corrected for the “missing wedge” of data along the out-of plane direction.

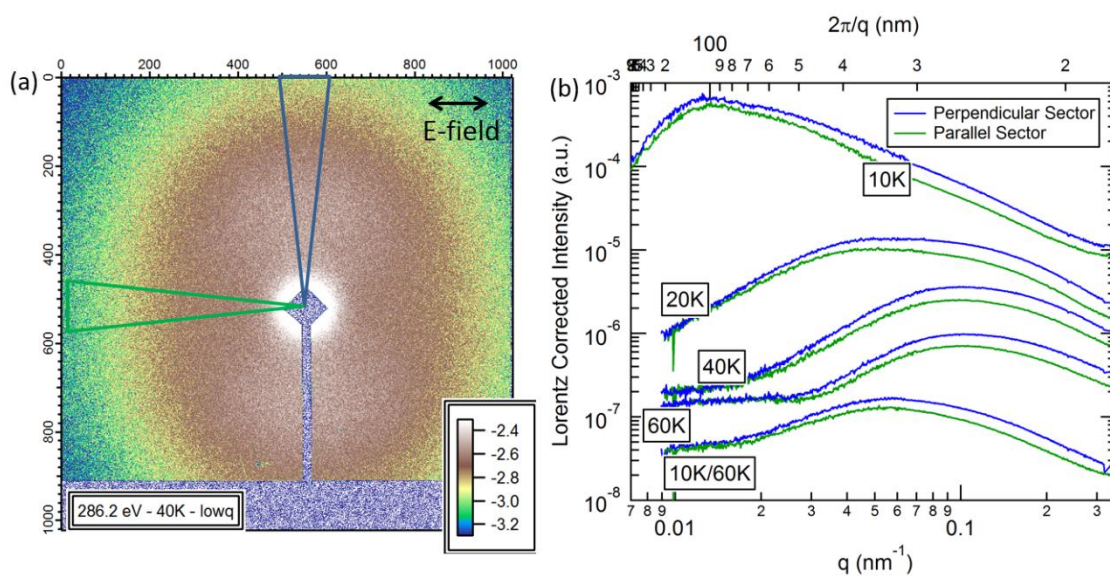


**Figure 3.7** (a) 2-D R-SoXS scattering data for the 40k polymer based blend film. (b) Perpendicular and parallel sector averages with respect to electric field polarization for all blend samples corresponding to the colored wedges in (a). Greater intensity is noted in all samples perpendicular to the electric field. Circular averages of the 2-D data are shown in the main text in Figure 3b. Two detector distances are used to achieve the  $q$ -range in (b) with the 2-D data corresponding to “low  $q$ ” shown in (a). The scattering anisotropy ratio in Table 3.4 of the main text is calculated by integrating the profiles in (b) above and taking the difference over the sum of the perpendicular and parallel sectors for each blend.

## CHAPTER 4

### Mobility-Controlled Performance of Thick Solar Cells based on PBnDT-FTAZ

#### 4.1 Introduction

Intensive research activities into polymer/fullerene BHJ devices have generated rapid and significant progress, with 10% efficiency on single junction OPV already on the horizon.<sup>97</sup> Though these impressive accomplishments have been largely driven by the design and synthesis of novel conjugated materials,<sup>25,68,98-100</sup> fundamental understanding on the complex BHJ morphology<sup>87,101,102</sup> and device physics<sup>103-105</sup> of these novel materials has provided invaluable insights into correlations of the chemical structure to device properties. However, given the fact that many factors influence the photovoltaic performance of BHJ devices, including chemistry/materials related properties (energy levels, band-gap, molecular weight, etc.), morphology and molecular texture related properties (molecular orientation, domain size and purity, etc.), and charge carrier dynamics (yield and field-dependence of charge generation, non-geminate recombination, mobility, trapping etc.), as-derived structure-property correlations are typically convoluted.<sup>106,107</sup> It has been very difficult – if possible at all – to draw simple and explicit correlations between the change in chemistry and the observed variation in device performance, let alone offer straightforward yet convincing physical causes.

The complexity of such structure – property relationships can be illustrated by the ongoing investigation on the “fluorine effect”, i.e., the device performance improvement via the fluorine substitution in conjugated polymers.<sup>26,99,108,109</sup> Indeed, a significant amount of work to

pursue the underlying reasons for this “fluorine” effect has been carried out. While early studies attributed the improvement in device efficiency upon fluorination mainly to the higher  $V_{oc}$ , which could be related to a deeper polymer HOMO,<sup>99</sup> it became clear that fluorination can also increase other photovoltaic properties (but does not always do so), such as  $J_{sc}$  and  $FF$ .<sup>25</sup> Mechanisms such as charge separation assisted by the intramolecular electrostatics,<sup>16</sup> improvements in mobility due to planarization of the backbone along with better intermolecular order,<sup>110</sup> preferential texture with respect to the substrate,<sup>109</sup> and preferential orientation of the backbone with respect to the discrete polymer/fullerene interface<sup>102</sup> have been proposed as explanations for the “F-effect”. However, relating such structural changes to device performance becomes difficult when considering that altering the chemical structure of the backbone typically affects important morphological (e.g., domain size distribution and purity) and textural parameters (e.g., molecular packing and orientation). For simplicity, we use the term morphology to describe the spatial distributions of polymer and fullerene, and texture to describe molecular packing, mosaicity, and orientation correlations. For example, typical polymer:fullerene blend systems are characterized by a significant change in domain size and purity when adding fluorine atoms to the acceptor unit of the polymer.<sup>109,111-113</sup> Importantly, these meso-scale morphological changes will affect other relevant parameters, such as the probability that a photogenerated exciton reaches the heterojunction or that free carriers recombine non-geminately.<sup>111</sup> Furthermore, as Chapter 3 indicates, the molecular weight of these conjugated polymers has a significant and only recently appreciated impact on morphology and device performance,<sup>114</sup> and is not always well controlled.<sup>115</sup> Therefore, though several studies revealed a monotonic change of some or all photovoltaic parameters with increasing fluorine content,<sup>112,116,117</sup> it turned out to be difficult to assign these chemical structure induced

performance changes to basic physical processes and causes. Finally, these studies rarely quantified all loss processes. With a limited set of measurements, one can only reach incomplete conclusions.

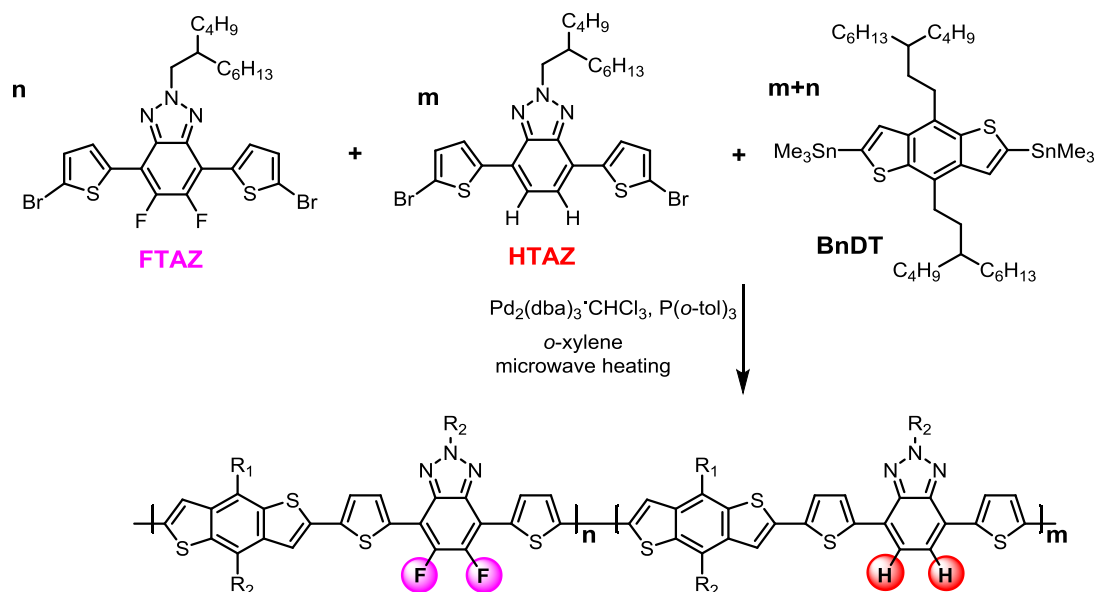
In contrast to these earlier studies where the impact of morphology and texture is significant and complicates the structure-property correlation, in this chapter we describe that, in a series of five PBnDT-FTAZ based copolymers<sup>25</sup> with a systematic increase of the F substitution and very comparable molecular weights, the morphology of the BHJ blends as well as molecular orientation relative of the polymer chains to the polymer:fullerene interface is surprisingly similar for all five polymers blended with PC<sub>61</sub>BM. However, the overall power conversion efficiency of photovoltaic devices with these five structurally closely related polymers varies by more than 80%. A comprehensive investigation reveals that almost all parameters describing photocarrier dynamics are also comparable for all five BHJ devices – except the hole mobility. In fact, the monotonically and steadily enhanced hole mobility with the increased amount of F substitution on the conjugated backbone is solely responsible for the significantly increased fill factor – the dominant impact on the overall efficiency – of ~ 350 nm thick BHJ devices of these five copolymers. Almost all other previously proposed explanations for the “F effect” are either not observed or only play very minor roles in this study. We primarily attribute the increases in mobility to improved intermolecular charge transfer due to the observed improved molecular  $\pi$ - $\pi$  stacking in the beneficial preferential face-on orientation relative to the electrodes.

Recent work has identified insufficient hole mobility as a major cause of limited device performance because inefficient hole extraction aggravates non-geminate recombination loss.<sup>106,118</sup> These effects become particularly important for thicker active layers, as

photogenerated charges need to travel a long distance towards the electrodes and because internal fields are rather low in the solar cell working regime.<sup>119,120</sup> Our discovery of this simple yet explicit correlation between charge carrier mobility and fill factor urges us to search for methods to increase the charge carrier mobility (e.g., hole mobility) by exquisite design of molecular structure and/or morphological control in the BHJ blend. Such an approach will enable high device efficiencies for active layer thickness above 300 nm, which is ideal for high absorption and ease of fabrication, particularly with an eye towards roll-to-roll or other high volume printing techniques preferred for commercialization.

## **4.2 Design and synthesis of PBnDT-(X)TAZ**

We chose PBnDT-(X)TAZ to construct the studied set of copolymers, because its hydrogen version (PBnDT-HTAZ) and the fluorinated version (PBnDT-FTAZ) have shown significant differences in important device characteristics in thick films devices.<sup>25,102</sup> The amount of fluorine (F) substitution in the PBnDT-(X)TAZ was systematically varied by adjusting the feed ratio of these two monomers (HTAZ and FTAZ) via random copolymerizations (Scheme 4.1 and Table 4.1). Since the only difference between these two monomers (HTAZ and FTAZ) are these two fluorine substituents on the central benzotriazole, and all polymers were prepared via (random) polycondensation, this set of polymers can be seen as PBnDT-HTAZ with randomly selected x% of HTAZ units – on the conjugated backbone – substituted with two F atoms (i.e., no regular pattern; 0% is the original PBnDT-HTAZ while 100% is the original PBnDT-FTAZ).



**Scheme 4.1** Synthesis of the set of PBnDT-(X)TAZ with various amount of F substitution.  $R_1$ =3-butylthio,  $R_2$ =2-butylthio.

Obtaining such a set of conjugated polymers differing only on the amount of F substitution in a random fashion is not a simple task. For example, two previous investigations<sup>115,117</sup> on a similar set of polymers based on PTB7 with different amount of F substitution (0% to 100% with 20% increment) have reached different device results and conclusions, largely because of the lack of control on the molecular weight, and even the actual F% in the copolymers significantly deviated from the expected value according to the feed ratio.<sup>115</sup> Fortunately, we recently demonstrated that with purified monomers and catalysts, the molecular weight of PBnDT-FTAZ can be almost precisely controlled via the classic Carothers equation.<sup>114</sup> Furthermore, by correlating molecular weight with device performance, we showed that a number average molecular weight ( $M_n$ ) of 40 kg/mol appears to be optimal to fully achieve the excellent photovoltaic properties of PBnDT-FTAZ.<sup>114</sup> We thus followed our previously reported procedure to carefully purify all monomers (i.e., FTAZ, HTAZ and BnDT), catalyst and other reagents, and applied the stoichiometric control to achieve similar molecular weight for this set

of PBnDT-(X)TAZ polymers. Indeed, the measured molecular weights of all four F-containing polymers (i.e., F25 through F100) are all around 40 kg/mol, except for F00 (i.e., the original PBnDT-HTAZ) which has a higher molecular weight of 71 kg/mol (Figure 4.1). Overall, there is an anti-correlation, with lower molecular weight achieved for higher F-content. This is likely due to the lower solubility of fluorinated conjugated polymers, which could retain more of the low molecular weight fraction in the final polymer during the Soxhlet extraction (thus a lower overall molecular weight). Importantly, the actual amount of F substitution in these copolymers, determined by elemental analysis, matches the calculated amount (from the feed ratio of HTAZ:FTAZ) exceedingly well (Table 4.1), a clear indication of the “randomness” of these copolymerizations. The optical and aggregation properties of these polymers are quite similar and consistent with prior observations, with the absorption coefficient increasing slightly as more F substituents were added on the conjugated backbone (Figure 4.2). In addition, the HOMO energy levels estimated from the cyclic voltammetry (CV) measurement are quite similar with less than 0.1 eV difference among all five copolymers (Figure 4.3), with the F00 (i.e., PBnDT-HTAZ) being the highest and the F100 (i.e., PBnDT-FTAZ) the lowest as previously reported (Table 4.2).

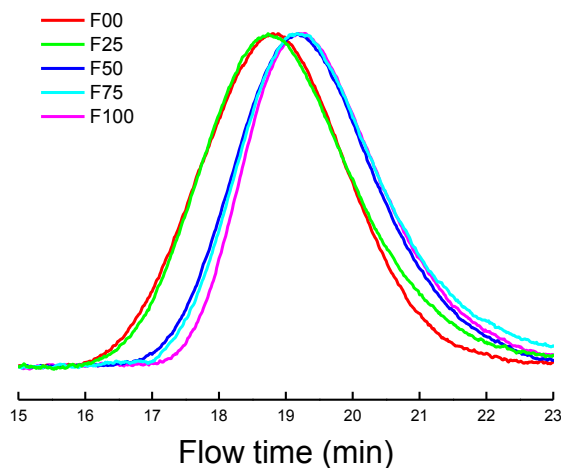


**Figure 4.1** GPC Curves of PBnDT-(X)TAZ polymers

**Table 4.1** PBnDT-(X)TAZ: chemical composition, molecular weight and photovoltaic device properties

PBnDT-(X)TAZ <sup>a</sup>	Feed ratio of HTAZ:FTAZ (wt% F) <sup>b</sup>	Actual wt% F <sup>c</sup>	$M_n$ (kg/mol)	Dispersity ( $\bar{M}$ )	$V_{oc}$ (V)	$J_{sc}$ (mA/cm <sup>2</sup> )	FF (%)	$\eta$ (%)
F00*	1:0 (0.00)	0.00	71	2.6	0.731 $\pm 0.004$	11.27 $\pm 0.48$	46.6 $\pm 0.9$	3.84 $\pm 0.16$
F25	3:1 (0.94)	0.93	59	2.9	0.742 $\pm 0.001$	12.27 $\pm 0.25$	54.3 $\pm 0.7$	4.94 $\pm 0.16$
F50	1:1 (1.86)	1.77	44	2.5	0.764 $\pm 0.002$	12.44 $\pm 0.37$	62.3 $\pm 1.0$	5.92 $\pm 0.22$
F75	1:3 (2.77)	2.45	44	2.7	0.780 $\pm 0.004$	12.21 $\pm 0.36$	64.9 $\pm 1.3$	6.18 $\pm 0.25$
F100*	0:1 (3.66)	3.35	38	2.5	0.797 $\pm 0.004$	12.75 $\pm 0.44$	70.6 $\pm 1.3$	7.17 $\pm 0.32$

<sup>a</sup> Nomenclature: “F25” represents the polymer made with a feed ratio of HTAZ:FTAZ at 3:1, thus 25% FTAZ by molar ratio in (X)TAZ. The wt% F in the polymer, however, is actually 0.93%, as given in the column entitled with “actual % F”.

<sup>b</sup> Theoretical wt% F is the calculated value based on the feed ratio of HTAZ:FTAZ;

<sup>c</sup> Actual wt% F was obtained by elemental analysis of all five samples.



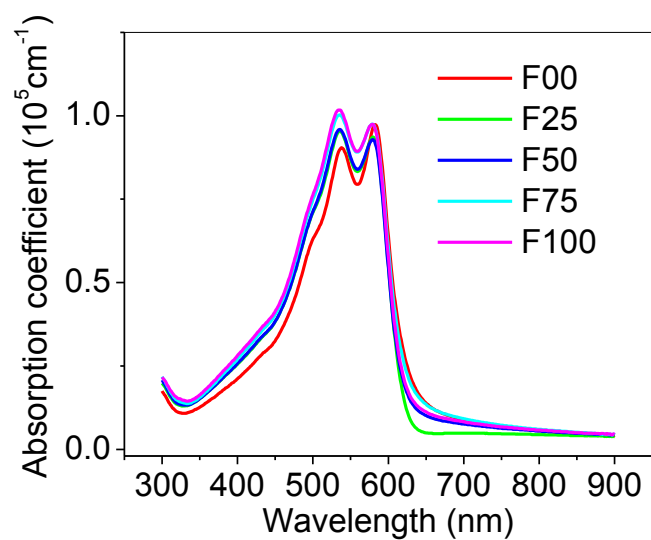


**Figure 4.2** UV-Vis absorption of PBnDT-(X)TAZ polymers in thin film

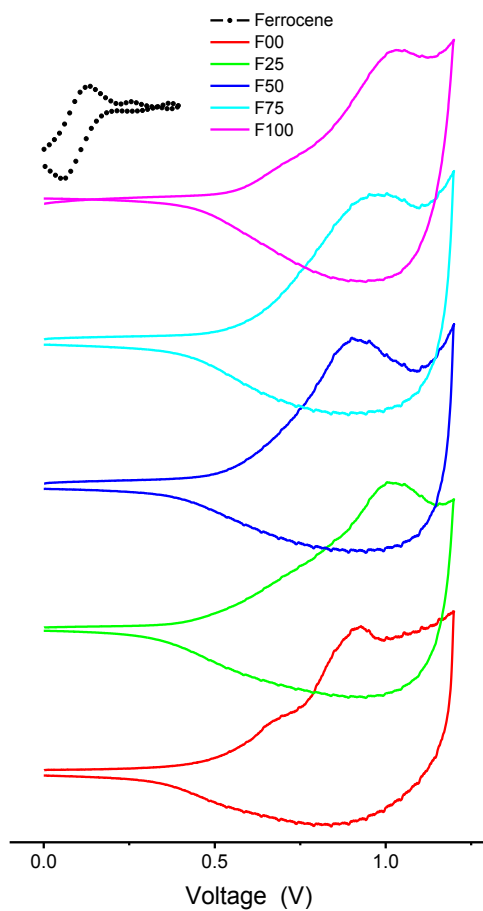


**Figure 4.3** Cyclic voltammograms of PBnDT-(X)TAZ polymer thin films

**Table 4.2** Estimated HOMO energy levels according to CV measurement

Polymer	P3HT	F00	F25	F50	F75	F100
HOMO (eV)	- 5.20	- 5.38	- 5.45	- 5.39	- 5.39	- 5.45

### 4.3 Photovoltaic device performance

Photovoltaic properties of these polymers were obtained via standard BHJ devices fabricated with identical processing condition (see experimental section) in order to minimize undesirable impact on the PV performance from other factors (e.g., morphological changes due to different solvent, current variation due to significant difference in the thickness of active layer). Here, we chose an active layer thickness of  $\sim 350$  nm, which is of significant commercial relevance, in particular, roll-to-roll printing. All thicknesses were very similar, with less than 5% difference from one copolymer to the other. Only through these rigorous controls can one draw meaningful conclusion about structure-property relationships.

Figure 4.4a displays the J-V curves under 1 sun condition (AM 1.5G,  $100 \text{ mW/cm}^2$ ) for all devices, with corresponding EQE presented in Figure 4.4b. With the data tabulated in Table 4.1, we plot the  $V_{oc}$ ,  $J_{sc}$ ,  $FF$  and the overall efficiency  $\eta$  against the amount of F substitution (%), as shown in Figure 4.4c and 4.4d. A few notable findings emerge. First, the  $V_{oc}$  almost linearly increases with the amount of F substitution. This implies that the electronic states/orbitals, particularly the HOMOs, are delocalized and averaged over many monomer units, likely due to the random nature of the F substitution. However, the difference on  $V_{oc}$  between F00 and F100 is only 0.07 V, corresponding to a less than 10% increase going from F00 to F100. Second, it appears that there is a big increase in  $J_{sc}$  when 25% of the HTAZ being substituted with FTAZ (i.e., F25), then the increase on  $J_{sc}$  due to further increasing the amount of F substitution

levels off (with a slight fluctuation). Still, going from F00 to F100, the  $J_{sc}$  only increases about 13%. Importantly, the current generated for high reverse bias almost merges for all blends (Figure 4.5), demonstrating that the dependence of  $J_{sc}$  on chemical structure is mainly coupled to the fill factor. The fill factor, not only shows a gradual increase along with the amount of F substitution, it exhibits the most significant change of all parameter with an improvement of about 50% going from F00 to F100.

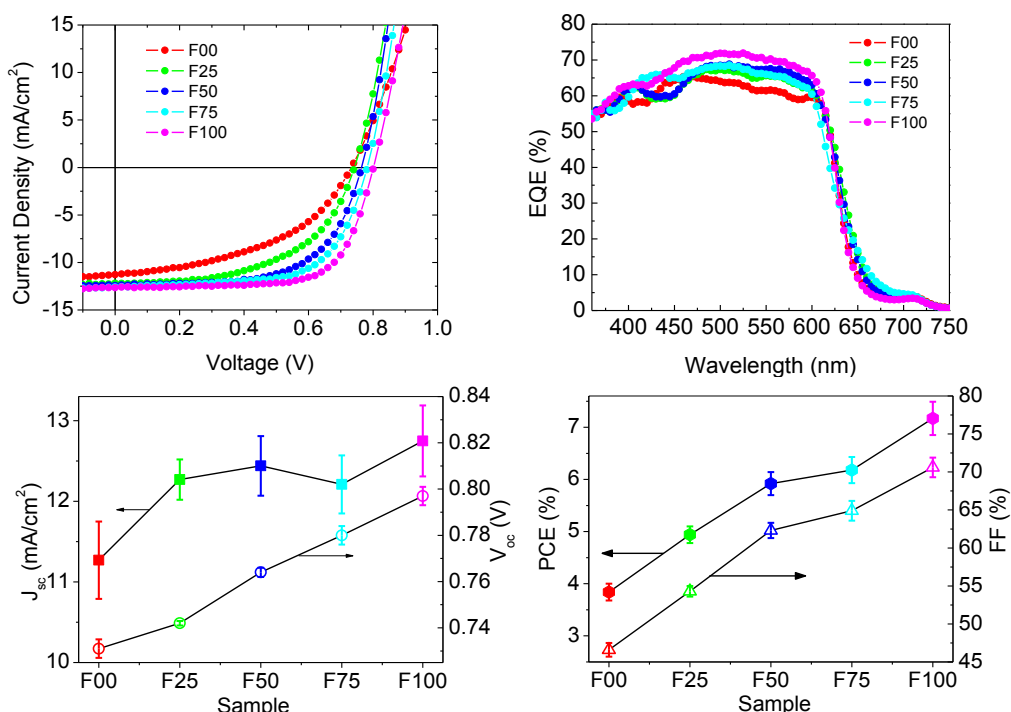


**Figure 4.4** (a) J-V curves for the BHJ devices of ~350 nm thick films based on all five copolymers of PBnDT-(X)TAZ under 1 sun, AM 1.5G condition. (b) EQE for the same devices in (a). (c) The change of  $J_{sc}$  and  $V_{oc}$  with increased amount of F substitution. (d) The increase of fill factor tracks the increase of overall device efficiency as more F substituents are incorporated into the copolymer.

Overall and synergistically, the device efficiency steadily improves as the amount of F substitution increases, resulting in an 80% enhancement from F00 (less than 4% overall energy conversion efficiency) to F100 (over 7% efficiency). Notably, the gradual increase in the device efficiency by incorporating more F substitution tracks the trend on fill factor extremely well

(Figure 4.4d), clearly reflecting that the fill factor is the dominant factor for the efficiency enhancement.

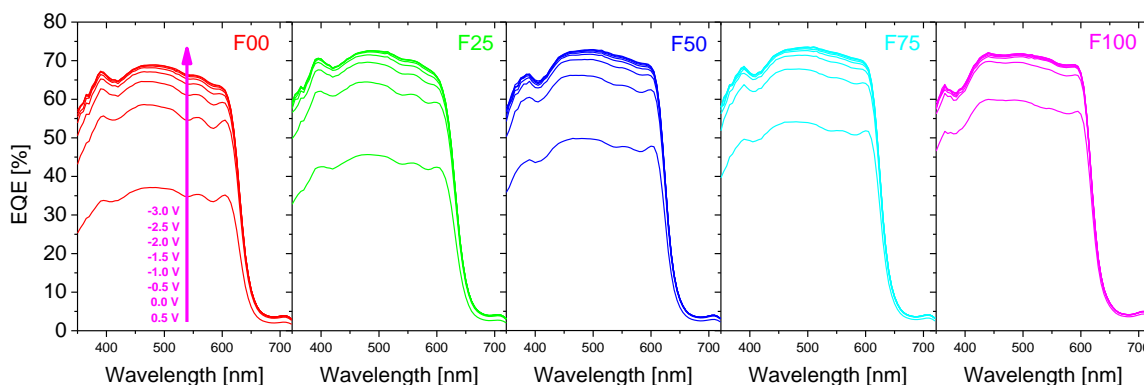


**Figure 4.5** Field dependent EQE. EQE for different applied voltages ranging from +0.5V to -3V as indicated in the left plot.

In order to understand the cause(s) responsible for the significantly improved efficiency – in particular, fill factor – a detailed investigation of the morphology and device physics is needed and was therefore undertaken.

#### 4.4 Morphology and Molecular Texture

The differences in performance described above could be due to changes in morphology with sequential fluorination of the conjugated backbone. Indeed, fluorination has been shown to modify morphology<sup>109,111</sup> and could be an important effect in this system as well. However, as shown below, similar active layer morphologies were observed for all devices in this work. First, polarized resonant soft X-ray scattering (P-SoXS) reveals that the domain spacing, domain purity, and preferential molecular orientation with respect to donor/acceptor interfaces cannot explain the performance differences described above. Figure 4.6 shows Lorentz-corrected P-SoXS scattering profiles of active layer films floated directly from measured devices. The peak in scattering intensity, or long period, corresponds to domain spacings between 55 and 65 nm.

Furthermore, the shapes of the scattering profiles are similar, indicating similar distributions of spatial frequencies of the samples. Specifically, BHJ blends based on F25 through F100 only exhibit one log normal spatial frequency distribution as shown in Figure 4.6a. Only F00 required two log normal distribution to fit the observed spatial frequency distributions. Along with domain spacing, integration of each scattering profile represents the total scattering intensity (TSI), which is proportional to the square root of the average composition variations.<sup>87</sup> Except for the F00 blend, all samples exhibit similar TSI and therefore similar average domain purities, which differ at most in a non-monotonic way by 15%. The F00 blend has domains at two length scales that are on average 35% more mixed than the other blends. The slightly different morphology for the F00 blend could be due to the higher molecular weight of the polymer in this blend. Finally, anisotropic scattering, the strength of which has been positively correlated in some systems to fill factor and  $J_{sc}$ ,<sup>102</sup> was observed for all samples in this study, and corresponds to face-on molecular orientation with respect to the D/A interfaces. The strength of molecular orientation is similar for the F25 to F100 samples with differences being less than 10%. As with the domain purity, the F00 blend is also different in regard to this structural parameter, with more random orientation relative to the D/A interface on account of the scattering anisotropy being 30% weaker and only observed for the high  $q$  peak. We note that the HTAZ used in the current study had a higher molecular weight than in the prior work by Tumbleston et al.,<sup>102</sup> in which the HTAZ exhibited nearly random molecular orientation and thus a larger difference in molecular orientation with respect to FTAZ than in the current study. The prior work also exhibited a larger difference in performance, consistent with a possible impact arising from a difference in molecular orientation as postulated by Tumbleston et al. These differences emphasize again that molecular weight can impact morphology, aggregation and texture and detailed studies of all

structural parameters and device physics are required when assessing modifications of chemical structures.

Furthermore, FTAZ has been shown to be relatively insensitive to the differences in morphology,<sup>121</sup> so long as the molecular weight is reasonably high.<sup>114</sup> It is thus unlikely that the observed relatively subtle and non-monotonic changes in these morphological parameters can explain monotonic changes in the device performance since, except for the F00 blend, the morphologies for all other four blends (F25 through F100) are very similar and the difference that are observed do not correlate to the device performance. Thus, the interpretation of trends in device data as a function of fluorination degree has to be based on parameters other than morphology or molecular orientation relative to the D/A interface.

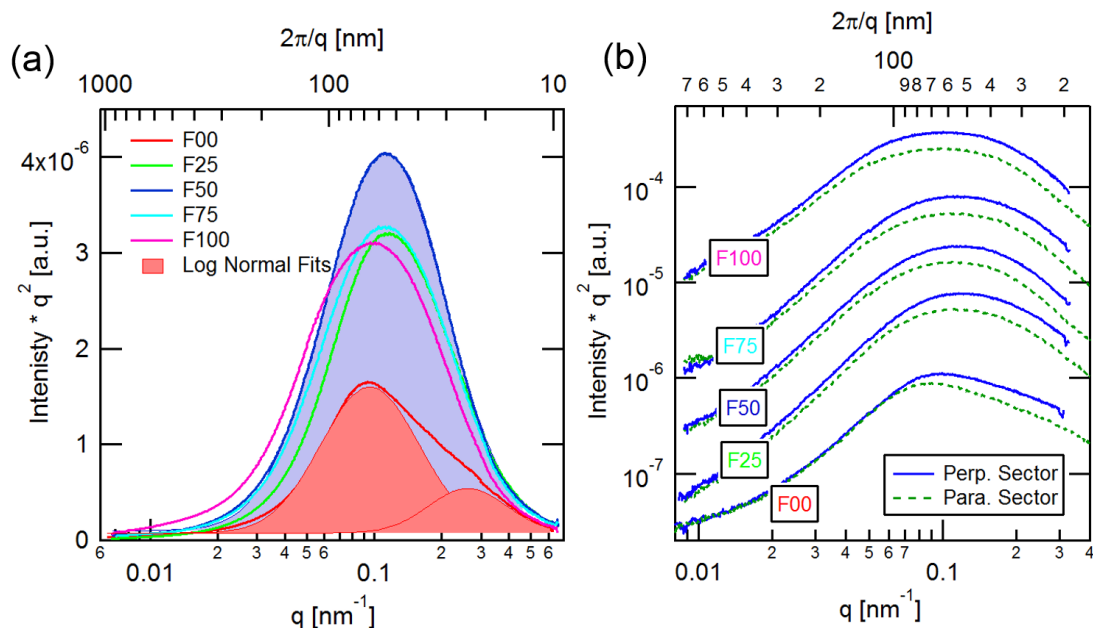


**Figure 4.6** (a) P-SoXS circular average profiles at 284.1 eV. Scattering profiles for all blends show similar intensity and shape, indicating similar distributions of spatial frequencies along with composition variations in the samples. All blends can be fitted with single log normal distributions, except for the F00 blend, which requires two for a good fit. (b) Sector averaged profiles representing P-SoXS data perpendicular and parallel to the electric field polarization. All samples show greater scattering perpendicular to the electric field, reflecting face-on preferential molecular orientation with respect to D/A interfaces.

In contrast to the P-SoXS data that assesses the mesoscale morphology and the in-plane molecular orientation relative to the D/A interface, grazing incidence wide angle X-ray scattering (GIWAXS), however, shows a clear and monotonic evolution of the texture, i.e., molecular packing and mosaicity (Figure 4.7). Even though overall, only broad (100) and (010) polymer peaks are observed, indicating short coherence length and a high degree of disorder,<sup>121,122</sup> significant evolutions can be readily observed. Figure 4.7 clearly shows that an increase in fluorination causes a significant increase in (010) intensity, particularly in the out-of-plane direction (i.e., perpendicular to the electrodes). At the same time, the (100) spacing increases and the lamellar stacking becomes increasingly in-plane. The GIWAXS data thus indicate a systematic evolution of molecular packing with increased  $\pi$ - $\pi$  stacking, and increased beneficial face-on orientation relative to the electrodes as the amount of F substitution increases. This evolution improves intermolecular hole transfer in the required direction (*vide infra*). Additionally, the GIWAXS data clearly shows a PC<sub>61</sub>BM aggregation peak at  $1.4 \text{ \AA}^{-1}$ , which would indicate that a favorable energetic landscape and good electron transport is also present for the electrons.

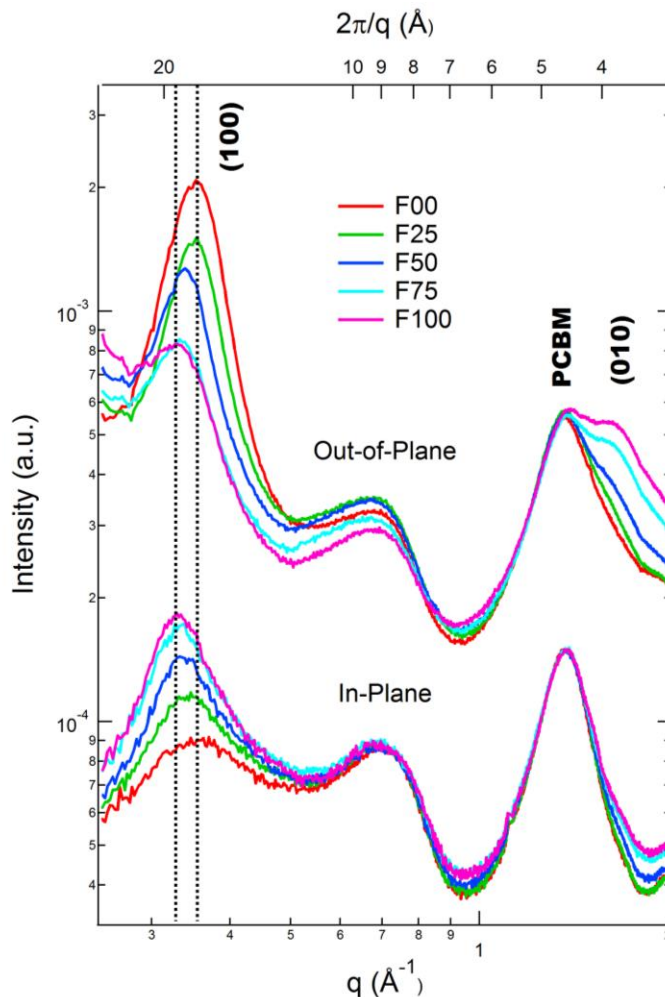


**Figure 4.7** GIWAXS data of blend films on glass/ITO/PEDOT:PSS device substrates. The (100) lamellar, PC<sub>61</sub>BM, and (010)  $\pi$ - $\pi$  stacking peaks are labeled.  $\pi$ - $\pi$  stacking intensity, face-on crystallite orientation with respect to the substrate and lamellar distance increase with more fluorine content. In-plane and out-of-plane data set offset for clarity.

#### 4.5 Factors Influencing Fill Factor

After establishing that only minor morphological differences but trending texture exist for all five blends, we turn our attention to charge carrier dynamics to understand the pronounced increase in fill factor with higher amount of fluorine. The fill factor basically depends on three fundamental processes. First, one needs to look into the *charge generation efficiency*, the



probability that an incident photon generates a free charge in given internal field. According to some studies, this process might depend on the field since the initial geminate pairs need to overcome the Coulomb attraction, causing the fill factor to deteriorate.<sup>123,124</sup> Second, one should investigate the loss due to *non-geminate recombination* (NGR), i.e., recombined free charges before being extracted. The NGR loss current density ( $J_{rec}$ ) is proportional to the recombination coefficient  $\gamma$  multiplied by the steady state carrier density  $n$  to the power of the recombination order, which is two for bimolecular recombination (BMR). Therefore, in the case of BMR, this current loss can be expressed as  $J_{rec} = e \cdot d \cdot \gamma \cdot n^2$  where  $e$  is the elementary charge and  $d$  is the device thickness. When  $\gamma$  is high, e.g., due to low domain purity, free charges are lost particularly at low internal fields close to the  $V_{oc}$ , which results in a reduced fill factor.<sup>125</sup> Third, when *charge extraction* is inefficient due to low (hole) mobilities, a higher overall steady-state carrier density  $n$  is present in the device. Therefore the probability that a carrier undergoes NGR is increased,<sup>106</sup> resulting again in a low fill factor. For any given generation current and electric field, the carrier density in the active layer scales inversely with mobility. Thus, being proportional to the product of electron and hole density, this NGR loss is very sensitive to mobility.

Recently, techniques have become available that can selectively address losses from field dependent free charge formation and NGR.<sup>123,124</sup> Time-delayed collection field (TDCF) is one of these techniques.<sup>124</sup> Within TDCF, a short laser pulse generates charge carriers at a certain applied bias (pre-bias  $V_{pre}$ ), which is selected to lie within the solar cell working regime. After 10 ns, the voltage is ramped up to a high reverse bias (i.e., collection bias  $V_{coll}$ ) to extract all generated charges, thus avoiding loss from NGR. Importantly, the delay time of 10 ns between

photogeneration and extraction ensures complete dissociation of all geminate pairs before charge extraction; and using low fluences ensures suppression of NGR losses during the short delay.

#### 4.5.1 Charge generation

The external generation efficiency (EGE) measured with TDCF at 530 nm excitation wavelength as a function of applied pre-bias for all five blends is displayed in the upper panel of Figure 4.8. As TDCF with properly selected parameters fully suppresses non-geminate losses, the EGE is a reliable measurement of how efficiently incident photons are converted into extractable free charges as a function of external bias. Figure 4.8 upper panel clearly shows that the charge generation is independent of the applied field for all five blends. As the formation of free charge was identified to proceed via the thermalized charge transfer (CT) states in a working solar cell,<sup>126</sup> the field-independent charge generation seen here hints at sufficiently delocalized and only weakly bound CT state. This can be fulfilled in the presence of aggregated PC<sub>61</sub>BM domains<sup>127</sup> together with a favorable interfacial energy landscape that stabilizes charges away from the donor:acceptor interface.<sup>105,128</sup>

To exactly quantify the efficiency of free charge generation and collection for the five blends, the EQE spectra were recorded as a function of bias (Figure 4.7). At high reverse bias, NGR losses are excluded and EQE measured under these conditions give the absolute yield of free charge formation and coincides with the EGE. Interestingly, for all five blends, the EQE at high reverse bias is very comparable around 69-73%. Especially, EQE for F00 (i.e., PBnDT-HTAZ) reduced by only 3% compared with other blends. Together with the field independent charge generation, this observation means that the absolute efficiency of charge generation is very comparable for all blends at all fields. Therefore, at reduced bias, the drop in EQE must be due to NGR as we will discuss below.

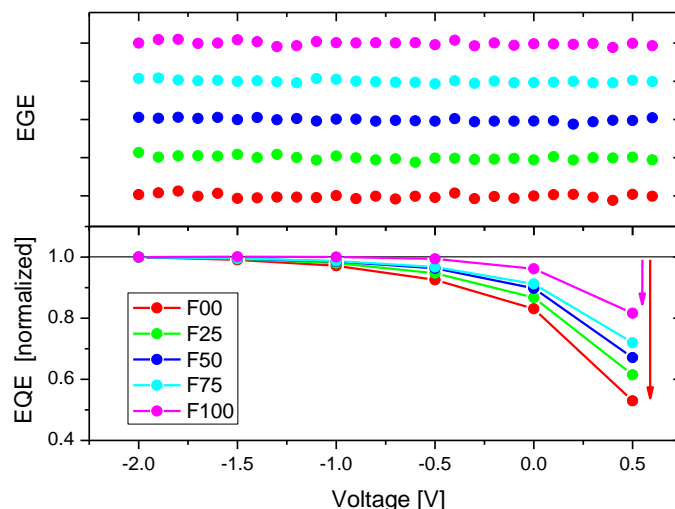


**Figure 4.8** Upper panel: the external generation efficiency (EGE) with offset for clarity as a function of applied pre-bias measured with TDCF at excitation wavelength of 530 nm. Lower panel: The EQE measured at 530 nm and normalized to  $-2$  V as function of voltage for all five blends. The arrows indicate the losses due to NGR at 0.5 V for F00 and F100.

#### 4.5.2 Non-germinate recombination

The lower panel in Figure 4.8 shows the field-dependent EQE extracted at 530 nm for direct comparison with the upper panel that displays the EGE. The EQE is normalized to a high reverse bias of  $-2$  V. In contrast to the EGE, the EQE decreases with bias between 0 and 0.5 V, which is entirely caused by NGR (the relative NGR losses at 0.5 V is indicated by the arrows in Figure 4.8). This loss is largely reduced by the increased amount of F substitution, in accordance with the increase in fill factor.

Further advance of the TDCF technique allows one to track the fate of photogenerated free carriers, by varying the delay between charge generation and the extraction of all remaining free charges. Data from these delayed extraction measurements for F50 at conditions close to the respective open circuit voltage are shown in Figure 4.9a, with the complete set of data for all five samples shown in Figure 4.11 in the experimental section. The amount of collected charge ( $Q_{\text{coll}}$ )

as a function of delay time can be fitted to a recombination model which also accounts for the number of charges that have been extracted during delay ( $Q_{\text{pre}}$ ). By definition,  $Q_{\text{coll}}$  and  $Q_{\text{pre}}$  add up to  $Q_{\text{tot}}$ , which is the total number of extractable charges. The data can be nicely described by considering only bimolecular recombination (BMR) as the dominating NGR mechanism for all blends, meaning that the current loss due to NGR depends quadratically on the carrier density and is thus very sensitive to the extraction efficiency. Figure 4.9b shows the bimolecular recombination coefficient deduced from the fits at 0.7 V for all five blends. Interestingly, although the fill factor increases almost linearly with the amount of F substitution, the BMR coefficient is virtually identical and around  $1 \times 10^{-17} \text{ m}^3/\text{s}$  for all five blends. This data essentially excludes a possible cause – a large change of the BMR coefficient – of the significantly different fill factor in this study. The very small effect of the increased fluorine substitution on the BMR coefficient in this study is consistent with the fact that the mesoscale morphologies are very similar for all five blends, but in contrast to previous results on fluorinated PCPDTBT, where the BMR coefficient was shown to decrease substantially upon fluorination.<sup>106</sup> The decrease of BMR coefficient for fluorinated PCPDTBT was attributed to the formation of larger and purer phases, in accordance with earlier interpretations from recombination experiments and simulations.<sup>129,130</sup> The weak change on the BMR coefficient found here can, therefore, be related to very similar domain size and purity among all five blends.

The data also clearly implies that there is virtually no change in bimolecular recombination rates with fluorination, which mirrors the results that the quantum efficiency of free charge generation – involving the same intermediates as NGR – is unaffected by fluorination. Thus, the average molecular overlap between the fullerene and the polymer is either very similar and independent of fluorination or not important in determining charge separation or

recombination. Therefore, this system offers a unique opportunity to directly compare the theory with the experimental results without being complicated by molecular interactions (typically postulated in other systems).

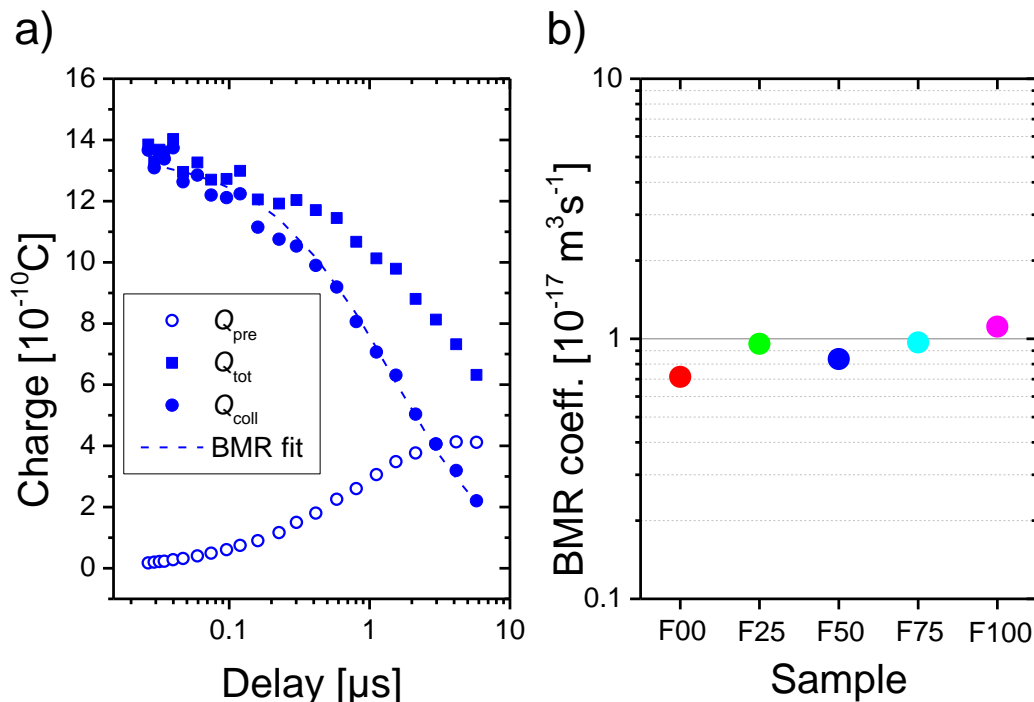


**Figure 4.9** (a) The measured number of collected charges ( $Q_{\text{coll}}$ ) and the corresponding bimolecular recombination (BMR) fit with increasing delay time between laser pulse and extraction voltage for the F50 sample at 0.7 V pre-bias. The number of charges that are extracted during delay is  $Q_{\text{pre}}$ . The sum of both,  $Q_{\text{coll}} + Q_{\text{pre}} = Q_{\text{tot}}$ , is the total amount of charges. (b) The BMR coefficient deduced from BMR fits as shown in (a) at conditions close to the respective open circuit for all five blends.

### 4.5.3 Charge extraction

Since we establish BMR as the dominating NGR mechanism in this study, the current density that is lost due to NGR will increase quadratically with carrier density. Consequently, even small increases in the steady state charge carrier density will speed up recombination losses. Because the overall steady state carrier density is directly impacted by the charge carrier

mobilities, we performed a detailed study of the electron and hole mobility in all blends. Electron and hole mobility were measured separately with different techniques and these results are compiled in Figure 4.10. Interestingly, electron mobilities deduced from the photocurrent transients in TDCF and those from the space charge limited current (SCLC) of electron-only device compare very well. All five blends have similar values around  $5 \times 10^{-3} \text{ cm}^2/\text{V}\cdot\text{s}$ , which is quite typical for the electron mobility in well performing polymer:fullerene blends. In stark contrast, the SCLC hole mobility from the hole-only device varies by more than one order of magnitude, from  $0.17 \times 10^{-3} \text{ cm}^2/\text{V}\cdot\text{s}$  in the case of F00 blend to  $1.2 \times 10^{-3} \text{ cm}^2/\text{V}\cdot\text{s}$  for the F100 blend (see Figure 4.12 in the experimental section for more details).

To verify the impact of a lower hole mobility on the average steady state carrier density, we applied the bias enhanced charge extraction (BACE) technique recently introduced by the Neher lab.<sup>106,131</sup> BACE is very comparable to TDCF with the only difference being the illumination conditions. Within BACE, a laser diode is applied for milliseconds to realize steady state between generation, recombination, and extraction at each bias. Then the laser diode is switched off within 10 ns and the voltage is reversed to extract all charges without any loss during extraction. Therefore, BACE is able to measure the steady state carrier density present in the device. The results are presented in supplementary Figure 4.13 in the experimental section. In the operating regime, with the light intensity adjusted to give a short circuit current of  $14 \text{ mA}/\text{cm}^2$ , the steady state carrier density decreases steadily with increased fluorination (Figure 4.13). Therefore, though the coefficient for BMR is almost the same for the five blends, the lower carrier density in the more fluorinated polymer based devices slows down NGR, resulting in a significant increase of the fill factor.

In addition to providing the average steady state carrier density under virtually all bias and illumination conditions, BACE technique further offers the effective extraction mobility, which is a non-linear function of the hole and the electron mobility as shown recently.<sup>106</sup> In the working solar cell, charge carrier motion by drift or diffusion is driven by the gradient of the quasi Fermi level.<sup>132</sup> This gradient is calculated from the difference in voltage which is needed to establish a certain carrier density either at open circuit or in the operating regime. From this gradient, the overall carrier density and the generated current, the effective extraction mobility can be estimated, according to recently published methodology.<sup>106</sup> The data obtained from this analysis is presented in Figure 4.10, which clearly shows that more fluorination increases the effective extraction mobility. Additionally, the comparison of the effective extraction mobility with the hole mobility deduced from SCLC measurements reveals that the steady state carrier density is strongly determined by the hole mobility.

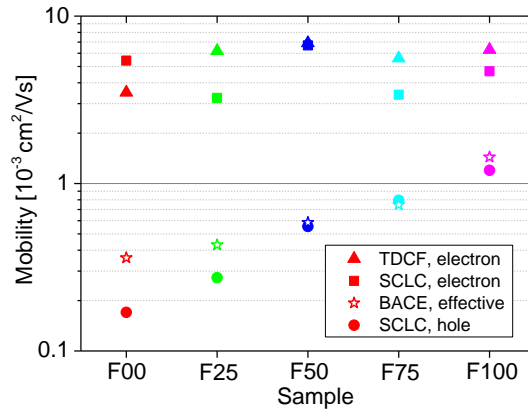


**Figure 4.10** Charge carrier mobilities of electrons and holes together with the effective extraction mobility as a function of fluorine substitution. The electron mobility is deduced from the transit time of TDCF transients and from electron only devices measured in the SCLC regime. The hole mobility is measured with hole only devices in the SCLC regime, and the effective extraction mobility is determined via BACE as described in the text.

## 4.6 Discussion

To summarize the results of the charge carrier dynamics experiments, we find that the generation of free charge is field-independent and that the overall generation efficiency is very comparable for all five blends. Furthermore, the BMR coefficient is equally moderate at ca.  $1 \times 10^{-17}$  m<sup>3</sup>/s and is not affected by fluorination. According to Langevin's recombination model, the recombination coefficient is directly proportional to the sum of electron and hole mobility.<sup>133</sup> Apparently, the BMR coefficient is determined by the faster type of carrier, the electrons, as the recombination coefficient and the electron mobilities are equally constant in our system. Calculating the Langevin recombination coefficient with the measured mobilities yields values around  $3 \times 10^{-15}$  m<sup>3</sup>/s for the studied blends, meaning that BMR recombination is suppressed by a factor of 300-400 for all five blends. In contrast, similar studies on P3HT:PC<sub>61</sub>BM in the Neher lab revealed hole and electron mobilities (from TDCF transient fits) of  $0.5 \times 10^{-3}$  and  $2 \times 10^{-3}$  cm<sup>2</sup>/Vs, respectively. Together with a BMR coefficient of  $0.5 \times 10^{-17}$  m<sup>3</sup>/s, this leads to a reduction factor of only ca. 150. Thus in relation to the electron and hole mobilities, recombination is even more suppressed in F100 blends. We surmise that this low BMR is related to the very low fullerene miscibility observed for F00 and F100; only ~4% PC<sub>61</sub>BM remains miscible in either polymer after solvent annealing in trichlorobenzene. Considering the amorphous or highly disordered nature of these polymers, such a residual fullerene concentration is one of the lowest observed for all donor polymers studied to date.<sup>87,119,134</sup> This reflects an inherently unfavorable molecular interaction between the fullerene and the polymers, thereby resulting in sufficiently pure domains in the corresponding BHJ blends. In short, the combination of the overall very high hole and electron mobilities and the strongly reduced recombination is the key aspect to achieve high fill factors (over 70%) at thick active layers of F100 based blends.



Several possible parameters such as morphology, backbone planarization, internal dipole moment change, etc. have been proposed to describe the effects of fluorination impacting the solar cell device performance. Given that the morphology is changing so little here, we have an ideal case to definitively investigate the impact of other parameters to further understand the “F effect”. The constancy of the UV-Vis spectra (Figure 4.2) directly suggests that backbone planarization is not an effect of fluorination in our system.<sup>110</sup> Similarly, the same field independent EGE and bimolecular recombination for all materials prove that the internal dipole moment change (between the ground state and the excited state)<sup>16</sup> has no significant impact on the charge generation or suppression of recombination. Similarly, molecular interactions and orbital overlap can be excluded as a cause here. We stress that such conclusions cannot be made if the only device data available or utilized are *J-V* characteristics; one should conduct comprehensive investigation on chemistry/materials, morphology and device physics with carefully designed and synthetically controlled set of materials.

After ruling out all other possible causes, we discover that a single parameter, the hole mobility, is responsible for the change of short circuit current and fill factor in thick polymer solar cells (over 300 nm) of the studied copolymers. Our results show that the most important parameter that determines the fill factor in this series of polymer:fullerene blends is the charge extraction efficiency, which we find is limited by the hole mobility. The strong increase of hole mobility with fluorination enables more rapid charge extraction to the electrodes, thereby reducing the overall steady state carrier density present in the device. As a result, the fill factor steadily increases from F00 to F100. Reduced recombination is also shown to be beneficial for high  $J_{sc}$  which is significantly enhanced when going from F00 to F25. The high electron and hole mobilities in combination with the strongly reduced bimolecular recombination coefficient

(relative to Langevin's limit) for F100 (i.e., PBnDT-FTAZ) sample are the key reason for the high fill factor of up to 72.9 % for its devices with a thick active layer (over 300 nm), even for thickness about 1  $\mu\text{m}$ .<sup>25</sup>

Our results clearly indicate that the increased fluorination on the conjugated backbone benefits the hole carrier mobility – with a strikingly monotonic correlation observed in this series (Figure 4.10). Because similar morphologies, probed by P-SoXS, have been observed for all five BHJ blends, the increased hole mobility with further fluorination is likely due to improved inter-chain transport, supported by the improved (010)  $\pi$ - $\pi$  stacking and face-on orientation observed by GIWAXS. Furthermore, because of the random nature of these three copolymers (i.e., F25, F50 and F75), our results indicate that the “fluorine” effect is not limited to structurally well-defined alternating copolymers such as PBnDT-FTAZ and other F-containing polymers. Strategically incorporating F substitution could be an important or sufficient design rationale one should consider in future molecular design of conjugated polymers for BHJ solar cells.

## 4.7 Conclusion

A few important conclusions emerge from this unequivocal mobility-controlled performance of BHJ solar cells with thick films. First, given the fact that typically electron mobility in polymer:fullerene BHJ solar cells is relatively high (e.g.,  $\sim 5 \times 10^{-3} \text{ cm}^2/\text{V}\cdot\text{s}$  in this study via both SCLC and TDCF), a comparably high hole mobility is needed to guarantee efficient charge extraction at low internal fields, which helps to reduce the NGR and improve the fill factor<sup>125</sup> (and the short circuit current). For example, the obtained SCLC hole mobility of  $1.2 \times 10^{-3} \text{ cm}^2/\text{V}\cdot\text{s}$  and the strongly reduced BMR coefficient for F100 based device is sufficient

to sustain a high fill factor of over 70% with a thick active layer over 300 nm. However, given this hole mobility value is still lower than that of electron, further enhancing the hole mobility could in principle increase the fill factor to over 80%<sup>135</sup> also for thicker active layers, a value on par with that of inorganic solar cells (e.g., Si, GaAs, etc.). Second, a high hole mobility is even more important for the more popular small band gap donors based BHJ devices. With more solar light absorbed due to their small band gap, these materials based devices can generate more charge carriers than the polymers (band gap of ~2.0 eV) in this study. Therefore they are more susceptible to the current loss due to NGR, which scales with the product between the recombination coefficient times the charge density squared (*vide supra*). Unfortunately, these small band gap polymers typically have low hole mobilities which cannot reconcile the conflict between the light absorption (mandating a thick film) and fast charge extraction (requiring thinner film if low hole mobility). With only few exceptions,<sup>136,137</sup> these small band gap polymers based solar cells typically reach their performance maximum at ~ 100 nm,<sup>98,99,108,119</sup> since a thicker film would lead to significantly reduced fill factor (and also current) due to recombination. Therefore, optimizing charge carrier extraction while maintaining efficient generation and strongly suppressed non-geminate recombination at relatively thick layers (over 300 nm) should remain key challenges for future material design and device optimization. These challenges also apply to the ongoing efforts to find fullerene replacements, where mobility measurements could be used as a screening tool. Finally, the “ideal” polymer solar cells should not only have a small band gap to maximize the light absorption (i.e., a potentially high  $J_{sc}$ ) and balanced energy level (i.e., a high  $V_{oc}$ ); they should also have comparably high electron/hole mobilities for fast charge extraction (i.e., reducing the carrier density) and good morphologies to reduce the recombination coefficient to achieve high a high fill factor. All these should be

achieved with thick films for maximizing the efficiency and more importantly, for the future roll-to-roll manufacturing such polymer solar cells.

#### 4.8 Experimental Section

TDCF<sup>124</sup> was measured with pulsed excitation from a diode-pumped, Q-switched Nd:YAG laser (NT242,EKSPLA) with 5,5 ns pulse duration and 500 Hz repetition rate. An Agilent 81150A pulse generator was used to apply the pre- and collection bias to the sample in combination with a home build amplifier. The current through the device was measured via a 50  $\Omega$  resistor in series recorded with a Yokogawa DL9140 oscilloscope. The pulse generator was triggered via a fast photodiode (EOT, ET-2030TTL). To compensate the internal latency of the pulse generator, the laser pulses were delayed multimode fiber (LEONI, 85m). The pulse fluence was measured with a Ophir Vega power meter equipped with a photodiode sensor PD300-UV.

BACE<sup>106</sup> was measured with the same set-up as TDCF except for the illumination source. In BACE a high power 1W, 445 nm laser diode (insaneware) with  $\sim 10$  ns light switch-off time is used. The LED is operated at 100 Hz repetition rate with applying the light for 9 ms to the sample to reach steady state conditions. The light is coupled into a fiber (LEONI, 60 m) for high homogeneity of the light profile. After the light is off, the voltage is reversed to extract all carriers without recombination losses being the same as in TDCF.

Samples for TDCF and BACE were prepared identical to those used in solar cell devices despite a smaller active area that ensured low RC time constants in the transient experiments. Devices have been encapsulated with 2 component epoxy resin and a glass lid prior to air exposure.

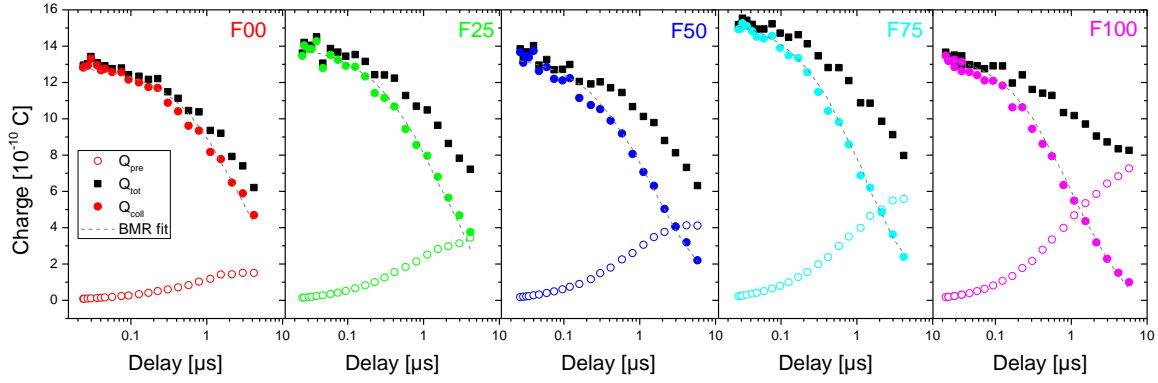


**Figure 4.11 BMR coefficient.** Time delay dependent charges extracted from TDCF measured at 0.7 V pre-bias for each blend with BMR fits as indicated by the dashed lines.  $Q_{\text{pre}}$  is the charge that can be extracted at the low internal field of the pre-bias.  $Q_{\text{coll}}$  is the charge that can be collected after the delay time and  $Q_{\text{tot}}$  is the sum of both.

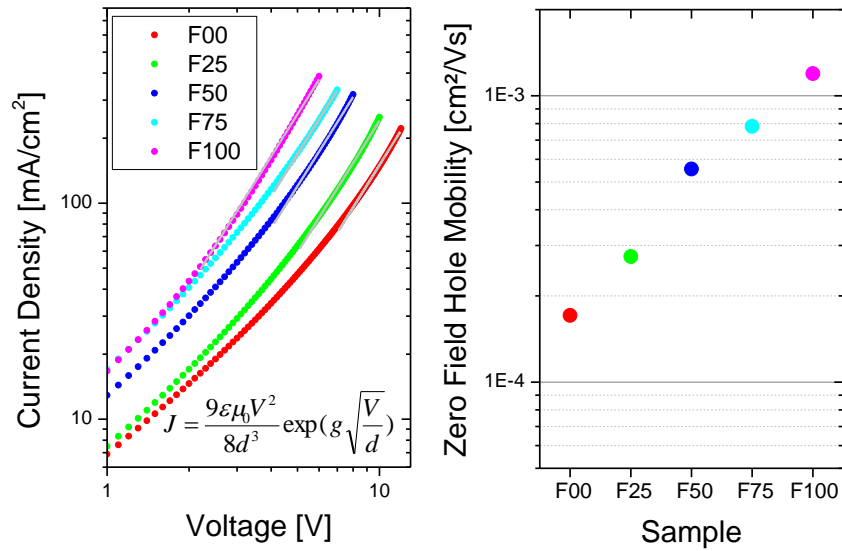


**Figure 4.12 Hole mobility derived from the hole only devices.** Left: Space charge limited currents of hole only devices with the fits according to Mott-Gurneys law using a Poole-Frenkel-type field-dependence of mobility (equation indicated) with a weak Poole-Frenkel factor to be  $g=1 \cdot 10^{-4} (\text{cm/V})^{1/2}$ . Right: Zero field hole mobilities  $\mu_0$  deduced from the data in the left figure.

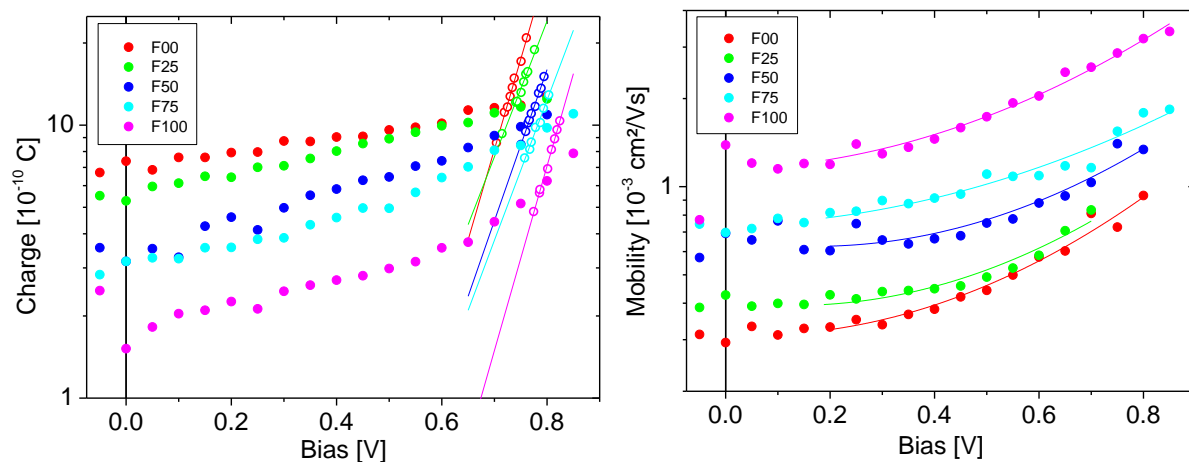


**Figure 4.13 Carrier density and effective extraction mobility measured with BACE.** Left: Carrier density measured with BACE with the intensity adjusted to give  $J_{sc}=14 \text{ mA/cm}^2$  for each blend (full circles) and the charge density at the respective open circuit voltage for each intensity (open circles) with linear fits for each blend. Right: effective extraction mobility as function of bias determined from the data in the left plot as described in the main text of the paper.

## CHAPTER 5

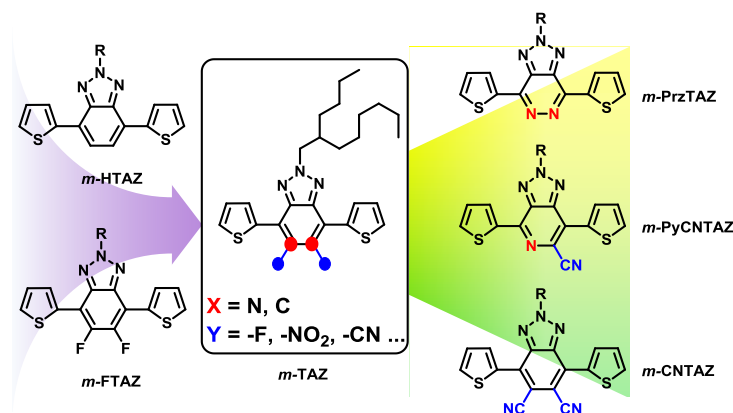
### A General Approach towards Electron Deficient Triazole Units to Construct Conjugated Polymers for Solar Cells

#### 5.1 Introduction

In our pursuit of novel polymeric materials for bulk heterojunction (BHJ) solar cells,<sup>6,68</sup> we discovered that benzotriazole is a unique building block with interesting structural and electronic features. Since the N-2 position of triazole can be selectively alkylated, a triazole based electron-accepting moiety (“acceptor”, e.g., benzotriazole) can host the side chain – required for the solubility of resulting conjugated polymers – in the triazole without introducing much steric hindrance in regard to the neighboring units. This desirable structural feature, also seen in other popular acceptors such as DPP (diketopyrrolopyrrole)<sup>138,139</sup> or isoindigo,<sup>140,141</sup> allows a more planar conjugated backbone with sufficient solubility in processing solvents. These properties lead to improved polymer packing/stacking and better charge transport. Indeed, in our initial attempt to incorporate these triazole based electron-accepting moieties into conjugated polymers,<sup>32</sup> the copolymer of fluorinated benzotriazole, PBnDT-FTAZ, achieved a high hole mobility on the order of  $10^{-3} \text{ cm}^2\text{V}^{-1}\text{s}^{-1}$  and a PCE over 7% in its BHJ solar cells with PC<sub>61</sub>BM. Even its non-fluorinated counterpart, PBnDT-HTAZ, containing benzotriazole (HTAZ), was also able to reach a device efficiency over 4%, comparable to that of P3HT based devices.

However, compared with DPP or isoindigo, benzotriazole is much less electron-deficient, manifested by the rather large band gap of  $\sim 2.0$  eV for PBnDT-F(H)TAZ, as opposed to the 1.4 eV or less for DPP based polymers.<sup>138,139</sup> In our previous attempt to lower the band gap of PBnDT-FTAZ, we replaced the flanking thiophenes in the repeat unit of PBnDT-FTAZ with selenophenes,<sup>142</sup> a well-documented approach to lower the band gap of thiophene based conjugated polymers.<sup>143-145</sup> The resulting polymer, PBnDT-SeFTAZ, indeed exhibited a smaller band gap of 1.8 eV due to its decreased LUMO, which resulted in a slightly higher  $J_{sc}$  of its BHJ device than that of PBnDT-FTAZ based ones. Unfortunately, the overall BHJ device efficiency of PBnDT-SeFTAZ was noticeably lower than that of PBnDT-FTAZ, largely due to the lower  $FF$ .<sup>142</sup> This low  $FF$  can be ascribed to the lower hole mobility of PBnDT-SeFTAZ, as we recently showed that a high mobility is crucial for fast charge extraction, a prerequisite for a high  $FF$ .<sup>20</sup>

**Chart 5.1.** General Structure of Triazole Based Acceptors



An alternative approach to lower the band gap of PBnDT-FTAZ would be strategically modify the benzotriazole core by introducing electron-withdrawing elements (e.g., pyridine, cyano, etc.). Similar strategies have been implemented for other “acceptors”.<sup>24,146-148</sup> For example, we have previously shown that replacing dithienyl benzothiadiazole (DTBT) with



dithienyl-thiadiazolopyridine (DTPyT) could lead to a lowered LUMO level (by  $\sim 0.3$  eV) and a narrowed band gap (by  $\sim 0.2$  eV) when copolymerized with BnDT.<sup>24</sup> Inspired by this successful precedent and others,<sup>146-148</sup> we envisioned a general modification strategy for the parent benzotriazole (TAZ) (Chart 5.1), aiming to enhance the electron withdrawing nature of the moiety *m*-TAZ while preserving its other beneficial structural features. However, building such a library of triazole acceptors would be very challenging if one chose to painstakingly synthesize each proposed structural modification of *m*-TAZ from individual starting materials, though we and others have taken such individualized syntheses for other structurally related acceptors (Scheme 5.1). Recognizing the high degree of structural similarity of these *m*-TAZ analogs, we decided to pursue a synthetic strategy that generates these analogous molecules more efficiently.

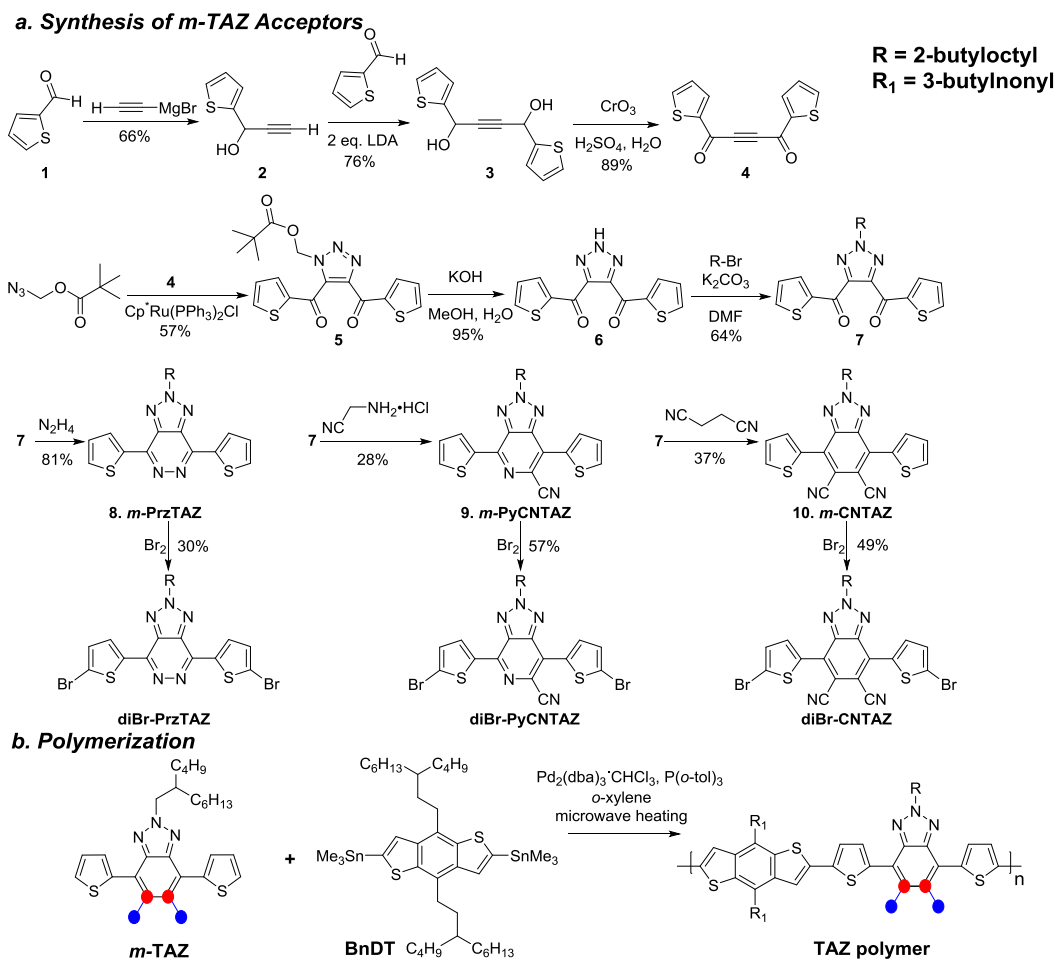
Herein, we report a general yet versatile synthetic approach towards a diverse set of *m*-TAZ acceptors (Scheme 5.2). The key intermediate to this general approach is the triazole fused 1,4-diketone with flanking thiophenes (**7** in Scheme 5.2), which can be easily converted into a specific triazole based acceptor through an one-step, Paal-Knorr-like condensation reaction with an appropriate nucleophilic reagent. The versatility of this synthetic strategy is demonstrated by the syntheses of three representative *m*-TAZ analogs in Chart 5.1, i.e., the pyridazine-fused triazole (*m*-PrzTAZ), the cyano substituted pyridine-fused triazole (*m*-PyCNTAZ), and the dicyano benzotriazole (*m*-CNTAZ). Three structurally related polymers, new additions to the family of PBnDT-TAZ, were then prepared. Our investigation of these polymers reveals that these *m*-TAZ analogs, bearing stronger electron withdrawing abilities, can indeed decrease the HOMO/LUMO levels and the band gap of resulting polymers, leading to improved BHJ device characteristics. Compared with PBnDT-FTAZ that typically gives a  $V_{oc}$  of 0.8 V in its BHJ devices, all three polymers exhibit higher values of  $V_{oc}$  ( $\sim 1$  V) in their corresponding BHJ

devices. Notably, one of these polymers, PBnDT-PyCNTAZ, demonstrates a high device efficiency around 8.4% with an active layer thickness of  $\sim 300$  nm, higher than that of PBnDT-FTAZ at a similar thickness.

**Scheme 5.1.** Synthetic strategies of popular acceptor units for organic photovoltaics

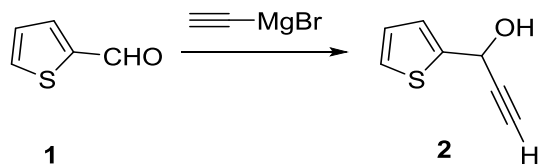
[illegible]

**Scheme 5.2** Syntheses of three *m*-TAZ acceptors from a 1,4-diketone intermediate and related PBnDT-TAZ polymers



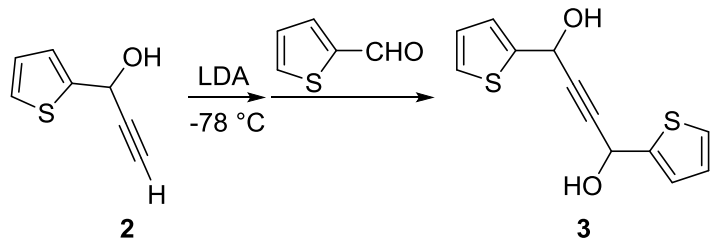
## 5.2 Synthesis and discussion

### 1-(thiophen-2-yl)prop-2-yn-1-ol (2)



10.15 g of thiophene-2-carbaldehyde (90.5 mmol) (**1**) was dissolved in 150 mL of anhydrous THF in an oven-dried 500 mL round bottom flask. 190 mL of ethynylmagnesium bromide solution in THF (0.5 M) was gently added at 0 °C under Argon. The reaction was stirred at r.t. under Argon overnight before being quenched by saturated ammonium chloride solution. The crude product was dissolved in ethyl acetate, washed with distilled water for three times and dried over MgSO<sub>4</sub>. Column chromatography with dichloromethane (R<sub>f</sub> ~ 0.3) yielded 8.26 g of **2** (59.8 mmol, 66%) as a yellow oil. **<sup>1</sup>H NMR** (400 MHz, CDCl<sub>3</sub>), δ: 7.32 (dd, *J* = 5.2, 1.6 Hz, 1H), 7.20 (dd, *J* = 3.6, 1.6 Hz, 1H), 6.98 (dd, *J* = 5.2, 3.6 Hz, 1H), 5.66 (m, 1H), 2.69 (d, *J* = 2.4 Hz, 1H), 2.45 (d, *J* = 7.2 Hz, 1H); **<sup>13</sup>C NMR** (100 MHz, CDCl<sub>3</sub>), δ: 144.1, 126.5, 125.8, 125.3, 83.0, 73.8, 59.5, 25.3.

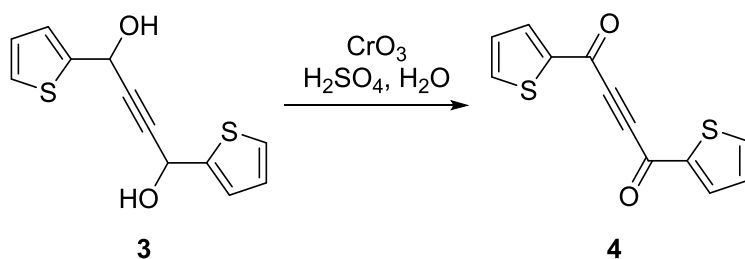
#### 1,4-di(thiophen-2-yl)but-2-yne-1,4-diol (**3**)



In an oven-dried 250 mL flask, 18.6 mL of freshly distilled diisopropylamine was dissolved in ~125 mL of anhydrous THF. (Note: the amount of THF must be sufficient to prevent the formation of a too viscous LDA solution.) 50.2 mL of *n*-BuLi in hexane (2.5 M) was slowly added at 0 °C and stirred for 30 minutes. 8.26 g of **2** (59.8 mmol) was dissolved in 200 mL of anhydrous THF in an oven-dried 500 mL round bottom flask. The freshly prepared LDA solution was slowly added and stirred at -78 °C for 1 hour. 7.38 g of **1** (65.8 mmol) was then added in one portion. The reaction was further stirred at -78 °C for 1 hour and slowly warmed up

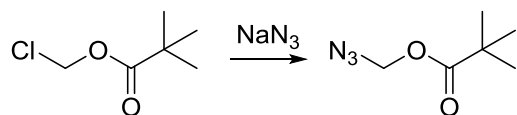
to r.t. After overnight reaction, the reaction was quenched by saturated ammonium chloride aqueous solution. The crude product was dissolved in ethyl acetate, washed with brine for three times and dried over  $\text{MgSO}_4$ . Column chromatography with hexane/ethyl acetate (v:v=2:1,  $R_f \sim 0.5$ ) yielded 11.35 g of **3** (45.3 mmol, 76%) as a yellow oil.  $^1\text{H NMR}$  (400 MHz,  $\text{CDCl}_3$ ),  $\delta$ : 7.32 (dd,  $J = 5.2, 1.2$  Hz, 1H), 7.21 (t,  $J = 1.6$  Hz, 1H), 6.99 (dd,  $J = 4.8, 3.6$  Hz, 1H), 5.77 (m, 1H), 2.41 (d,  $J = 7.2$  Hz, 1H);  $^{13}\text{C NMR}$  (100 MHz,  $\text{CDCl}_3$ ),  $\delta$ : 143.8, 126.8, 126.2, 125.8, 85.1, 60.2.

#### 1,4-di(thiophen-2-yl)but-2-yne-1,4-dione (**4**)



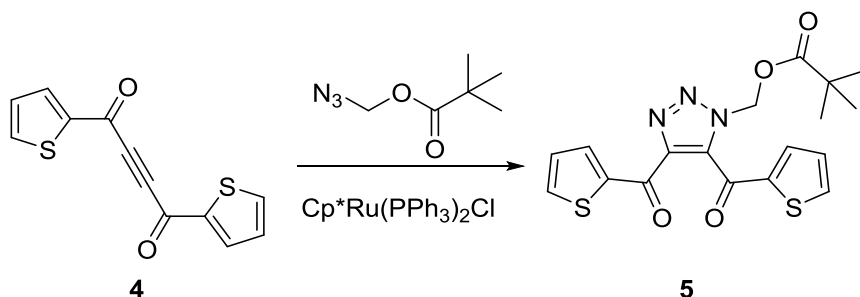
Jone's reagent was prepared by dissolving 9.52 g of  $\text{CrO}_3$  (95.2 mmol) in a diluted sulfuric acid (10.6 mL of concentrated sulfuric acid (98%) in 25.0 mL of distilled water). 11.35 g of **3** (45.3 mmol) was dissolved in 150 mL of acetone, and Jone's reagent was added dropwise at 0 °C until TLC showed complete conversion. Excess Jone's reagent was quenched by *i*-propanol. The reaction mixture was extracted by ethyl acetate and dried over  $\text{MgSO}_4$ . The crude product **4** (9.9 g, 40.2 mmol, yield = 89%) was directly used for next step without further purification.  $^1\text{H NMR}$  (400 MHz,  $\text{CDCl}_3$ ),  $\delta$ : 8.04 (dd,  $J = 3.6, 1.2$  Hz, 1H), 7.83 (dd,  $J = 4.8, 1.6$  Hz, 1H), 7.22 (dd,  $J = 4.8, 4.0$  Hz, 1H);  $^{13}\text{C NMR}$  (100 MHz,  $\text{CDCl}_3$ ),  $\delta$ : 167.9, 143.6, 137.0, 136.8, 128.8, 83.3.

#### Azidomethyl pivalate



(Note: Sodium azide and alkyl azide are **explosive!** and **shock-sensitive!** Caution must be used during reaction set-up, work-up and rot-vap.) The procedure is adapted from Synlett, 2005, No. 18, 2847 (doi: 10.1055/s-2005-918944). 7.53 g of chloromethyl pivalate (50.0 mmol) was dissolved in 100 mL of DMF, and 4.88 g of sodium azide (75.0 mmol) was carefully added. The reaction was stirred at 90 °C overnight, then water was carefully added. The reaction mixture was divided into three smaller portions, and each portion was extracted by ethyl acetate for three times. The organic portion was roughly concentrated on rot-vap, leaving sufficient amount of DMF (~ 50 mL in total) to dissolve azidomethyl pivalate and to avoid explosion. This crude product solution in DMF was directly used for next step without further purification.

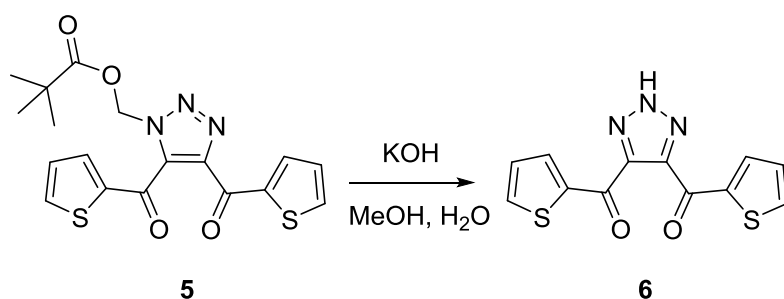
**(4,5-di(thiophene-2-carbonyl)-1H-1,2,3-triazol-1-yl)methyl pivalate (5)**



Crude product **4** (9.9 g, 40.2 mmol) and the crude azidomethyl pivalate were dissolved in a total volume of 150 mL of DMF in a 250 mL flask equipped with condenser. The solution was purged with Argon for 20 minutes and 0.35 g of  $\text{Cp}^*\text{Ru}(\text{PPh}_3)_2\text{Cl}$  was added. The reaction was heated at 90 °C for 20 hours. The crude product after ethyl acetate extraction was column purified with hexane/ethyl acetate (v/v = 4:1) as eluent ( $R_f \sim 0.4$ ), and then recrystallized in

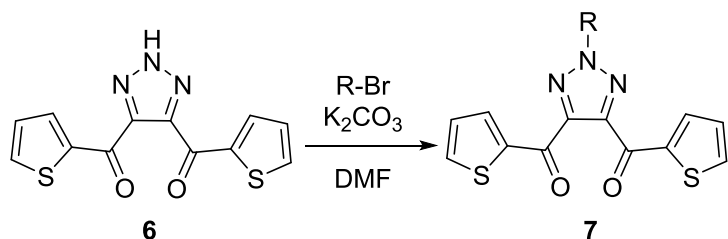
ethanol or methanol to yield 9.2 g of an off-white solid (overall yield after recrystallization: 57%). **<sup>1</sup>H NMR** (400 MHz, CDCl<sub>3</sub>), δ: 8.68 (dd, *J* = 3.2, 0.8 Hz, 1H), 7.81 (dd, *J* = 4.0, 0.8 Hz, 1H), 7.78 (dd, *J* = 4.0, 0.4 Hz, 1H), 7.47 (dd, *J* = 3.2, 0.8 Hz, 1H), 7.24 (dd, *J* = 3.6, 3.2 Hz, 1H), 7.11 (dd, *J* = 3.6, 3.2 Hz, 1H), 6.36 (s, 2H), 1.02 (s, 9H); **<sup>13</sup>C NMR** (100 MHz, CDCl<sub>3</sub>), δ: 177.1, 176.2, 176.2, 145.6, 142.4, 141.8, 137.6, 137.0, 135.9, 135.7, 128.7, 128.6, 69.6, 38.6, 26.5.

**(2H-1,2,3-triazole-4,5-diyl)bis(thiophen-2-ylmethanone) (6)**



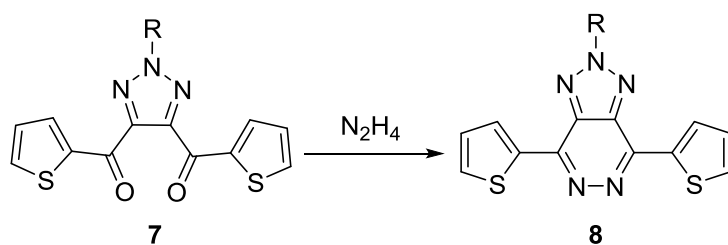
The deprotection procedure is adapted from Synlett, 2005, No. 18, 2847 (doi: 10.1055/s-2005-918944). 7.0 g of **5** (17.3 mmol) was dispersed in 150 mL of methanol, and 2.1 g of potassium hydroxide (38.2 mmol) was dissolved in 100 mL of water. The latter was poured into the former at r.t. under stirring. The reaction approached completion when the mixture turned into a clear solution, but overnight reaction would ensure fully deprotection. Excess amount of 1 M hydrochloric acid solution was then poured into the reaction, and the white precipitation was collected by filtration and dried in an oven at 90 °C to yield pure product **6** (4.8 g, 16.6 mmol, yield = 95%). **<sup>1</sup>H NMR** (400 MHz, MeOD), δ: 8.09 (d, *J* = 3.6 Hz, 1H), 8.00 (dd, *J* = 4.8 Hz, 1H), 7.26 (d, *J* = 4.0 Hz, 1H); **<sup>13</sup>C NMR** (100 MHz, MeOD), δ: 180.2, 146.3, 143.9, 137.7, 137.5, 129.8.

**(2-(2-butyloctyl)-2H-1,2,3-triazole-4,5-diyl)bis(thiophen-2-ylmethanone) (7)**



2.89 g of oven-dried **6** (10.0 mmol), 2.76 g of potassium carbonate (20.0 mmol) and 2.99 g of 2-butyl-1-octyl bromide (12.0 mmol) were combined in 50 mL of DMF and the reaction was stirred at r.t. overnight. The crude product after ethyl acetate extraction was dried over  $\text{MgSO}_4$ , filtered, concentrated, and column purified with hexane and dichloromethane (v/v = 1:3) as eluent to yield 2.93 g (6.4 mmol, 64%) of the common 1,4-diketone intermediate **7** as a colorless oil.  $^1\text{H NMR}$  (400 MHz,  $\text{CDCl}_3$ ),  $\delta$ : 8.00 (dd,  $J = 4.0, 1.2$  Hz, 2H), 7.75 (dd,  $J = 4.8, 1.2$  Hz, 2H), 7.78 (dd,  $J = 4.8, 3.6$  Hz, 1H), 4.51 (d,  $J = 6.8$  Hz, 2H), 2.19 (br, 1H), 1.36-1.28 (br, 16H), 0.93-0.85 (br, 6H);  $^{13}\text{C NMR}$  (100 MHz,  $\text{CDCl}_3$ ),  $\delta$ : 179.3, 146.5, 140.8, 135.7, 128.0, 126.1, 59.3, 38.8, 31.7, 31.4, 31.1, 29.5, 28.4, 26.2, 22.9, 22.6, 14.0, 14.0.

### 2-(2-butyloctyl)-4,7-di(thiophen-2-yl)-2H-[1,2,3]triazolo[4,5-*d*]pyridazine (**8**, PrzTAZ)

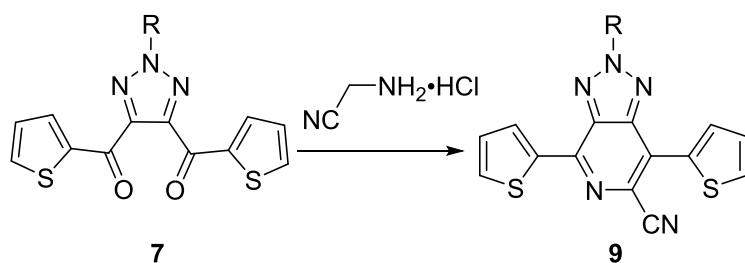


0.14 g of 1,4-diketone **7** (0.31 mmol), 3.1 g of hydrazine monohydrate (61 mmol) and two drops of acetic acid were dissolved in 50 mL of ethanol and refluxed overnight. 100 mL distilled water was added and the reaction was extracted by ethyl acetate for three times. The organic phase was dried and purified by column chromatography with hexane/dichloromethane



(v:v=1:1) as eluent, yielding 0.11 g of **7** (0.24 mmol, 81%) as a light yellow solid. **<sup>1</sup>H NMR** (400 MHz, CDCl<sub>3</sub>), δ: 8.49 (dd, *J* = 3.6, 0.4 Hz, 2H), 7.60 (dd, *J* = 4.8, 0.4 Hz, 2H), 7.25 (m, 2H), 4.85 (d, *J* = 6.4 Hz, 2H), 2.34 (br, 1H), 1.42-1.27 (br, 16H), 0.92-0.86 (br, 6H); **<sup>13</sup>C NMR** (100 MHz, CDCl<sub>3</sub>), δ: 146.7, 138.5, 138.0, 131.3, 130.3, 128.3, 60.9, 39.3, 31.7, 31.3, 31.0, 29.4, 28.4, 26.1, 22.8, 22.6, 14.0, 14.0.

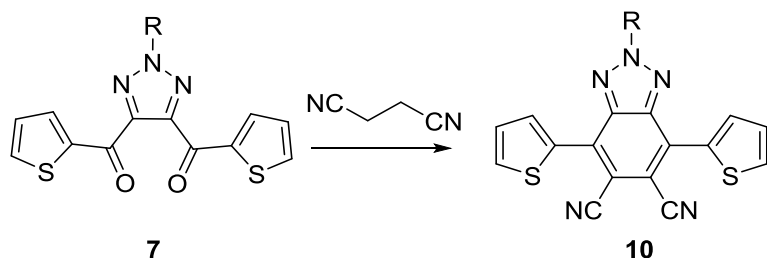
**2-(2-butyloctyl)-4,7-di(thiophen-2-yl)-2*H*-[1,2,3]triazolo[4,5-*c*]pyridine-6-carbonitrile (9, PyCNTAZ)**



0.61 g of potassium hydroxide (10.9 mmol) was dissolved in 50 mL of ethanol. 0.84 g of 1,4-diketone **7** (1.82 mmol) and 3.37 g of aminoacetonitrile hydrochloride (22.1 mmol) were dissolved in this basic solution and refluxed overnight. Reaction progress was monitored by taking NMR of an aliquot of reaction mixture. Excess aminoacetonitrile hydrochloride was supplemented until reaction conversion stopped increasing. The crude product was washed, extracted, dried, concentrated, and column purified by hexane/dichloromethane (v:v=1:1) to yield 0.43 g of **8** (0.9 mmol, 50%) as a yellow solid, which can be further recrystallized from ethanol to yield 0.23 g (0.47 mmol) bright yellow needle-like crystals. **<sup>1</sup>H NMR** (400 MHz, CDCl<sub>3</sub>), δ: 8.48 (br, 1H), 8.23 (d, *J* = 3.6 Hz, 1H), 7.61 (d, *J* = 5.2 Hz, 1H), 7.60 (m, 1H), 7.26 (m, 1H), 7.22 (m, 1H), 4.80 (d, *J* = 6.4 Hz, 2H), 2.29 (br, 1H), 1.43-1.27 (br, 16H), 0.92-0.88 (br, 6H); **<sup>13</sup>C NMR** (100 MHz, CDCl<sub>3</sub>), δ: 145.5, 145.1, 140.1, 138.5, 132.5, 131.5, 130.9, 130.9,

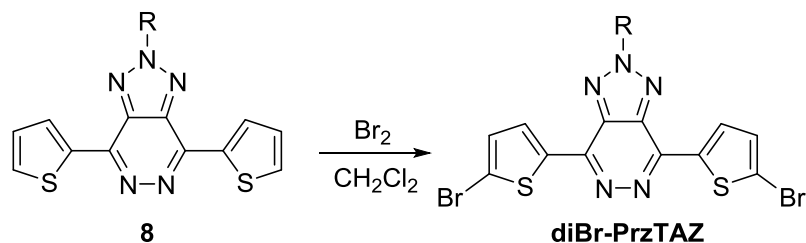
130.0, 128.5, 127.8, 124.5, 120.9, 118.5, 60.8, 39.1, 31.7, 31.3, 31.0, 29.4, 28.3, 26.1, 22.8, 22.6, 14.0, 14.0.

**2-(2-butyloctyl)-4,7-di(thiophen-2-yl)-2*H*-benzo[*d*][1,2,3]triazole-5,6-dicarbonitrile (10, CNTAZ)**



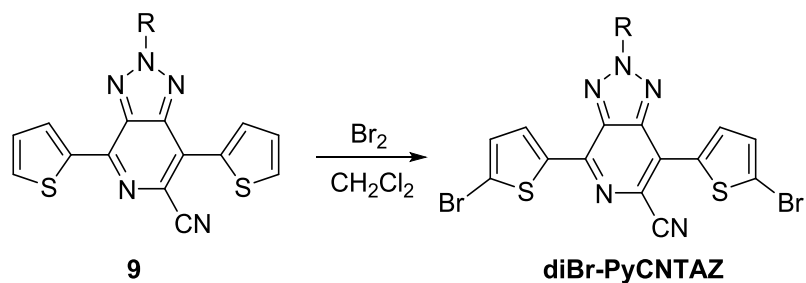
0.25 g of 1,4-diketone **7** (0.54 mmol), 61 mg of succinonitrile (0.75 mmol) and 0.75 g of potassium carbonate (5.4 mmol) were dispersed in 10 mL of DMF and stirred at 70 °C. Reaction progress was monitored by taking NMR of an aliquot of reaction mixture. Excess succinonitrile was supplemented over 24 hours until reaction conversion stopped increasing. The crude product was washed, extracted, dried, concentrated, and column purified by chloroform, yielding 100 mg of **9** (0.2 mmol, 37%) as a yellow solid. <sup>1</sup>H NMR (400 MHz, CDCl<sub>3</sub>), δ: 8.24 (d, *J* = 3.6 Hz, 2H), 7.70 (d, *J* = 5.2 Hz, 2H), 7.28 (t, *J* = 4.4 Hz, 2H), 4.7 (d, *J* = 6.4 Hz, 2H), 2.27 (br, 1H), 1.37-1.26 (br, 16H), 0.91-0.85 (br, 6H); <sup>13</sup>C NMR (100 MHz, CDCl<sub>3</sub>), δ: 142.8, 133.2, 131.8, 131.0, 130.9, 127.8, 116.9, 107.8, 60.9, 39.2, 31.7, 31.3, 31.0, 29.4, 28.4, 26.1, 22.8, 22.6, 14.0, 14.0.

**4,7-bis(5-bromothiophen-2-yl)-2-(2-butyloctyl)-2*H*-[1,2,3]triazolo[4,5-*d*]pyridazine (monomer diBr-PrzTAZ)**



0.20 g of molecule **8** (0.44 mmol) was dissolved in dichloromethane, and  $\text{Br}_2$ /dichloromethane solution was added dropwise. Reaction progress was tracked by TLC until no starting material was present. The reaction mixture was then concentrated and purified by column chromatography with chloroform as eluent, yielding 80 mg of monomer **diBr-PyCNTAZ** (0.13 mmol, 30%) as a yellow solid after recrystallization from ethanol.  $^1\text{H}$  NMR (400 MHz,  $\text{CDCl}_3$ ),  $\delta$ : 8.20 (d,  $J = 4.0$  Hz, 2H), 7.21 (d,  $J = 4.0$  Hz, 2H), 4.82 (d,  $J = 6.8$  Hz, 2H), 2.32 (br, 1H), 1.42-1.26 (br, 16H), 0.92-0.85 (br, 6H);  $^{13}\text{C}$  NMR (100 MHz,  $\text{CDCl}_3$ ),  $\delta$ : 145.9, 139.7, 137.5, 131.7, 131.4, 118.9, 60.9, 39.2, 31.7, 31.3, 31.0, 29.4, 28.4, 26.1, 22.8, 22.6, 14.0.

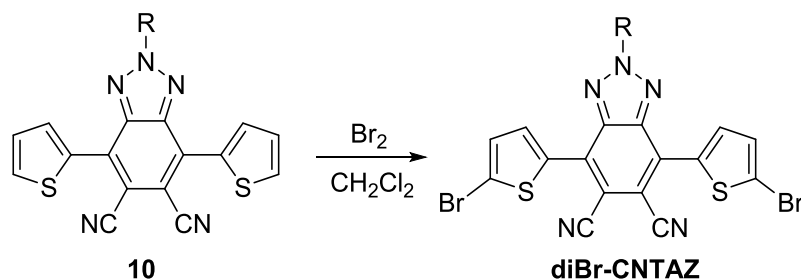
**4,7-bis(5-bromothiophen-2-yl)-2-(2-butyl-octyl)-2H-[1,2,3]triazolo[4,5-c]pyridine-6-carbonitrile (monomer diBr-PyCNTAZ)**



Similar to the synthesis of diBr-PrzTAZ. Yellow needle-like crystal. Yield after recrystallization in ethanol: 57%.  $^1\text{H}$  NMR (400 MHz,  $\text{CDCl}_3$ ),  $\delta$ : 8.18 (d,  $J = 4.0$  Hz, 1H), 8.05 (d,  $J = 4.0$  Hz, 1H), 7.21 (d,  $J = 4.0$  Hz, 1H), 7.16 (d,  $J = 4.0$  Hz, 1H), 4.80 (d,  $J = 6.4$  Hz, 2H),

2.27 (br, 1H), 1.57-1.26 (br, 16H), 0.93-0.85 (br, 6H);  $^{13}\text{C}$  NMR (100 MHz,  $\text{CDCl}_3$ ),  $\delta$ : 144.4, 144.1, 141.1, 137.8, 134.0, 131.8, 131.5, 131.1, 130.7, 123.3, 119.8, 119.6, 118.4, 118.1, 60.8, 39.1, 31.7, 31.3, 31.0, 29.4, 28.4, 26.1, 22.8, 22.6, 14.0, 14.0.

**4,7-bis(5-bromothiophen-2-yl)-2-(2-butyl-octyl)-2H-benzo[d][1,2,3]triazole-5,6-dicarbonitrile (monomer diBr-CNTAZ)**



Similar to the synthesis of diBr-PrzTAZ. Yellow needle-like crystal. Yield after recrystallization in ethanol: 49%.  $^1\text{H}$  NMR (400 MHz,  $\text{CDCl}_3$ ),  $\delta$ : 8.07 (d,  $J = 4.4$  Hz, 2H), 7.24 (d,  $J = 4.4$  Hz, 2H), 4.78 (d,  $J = 6.4$  Hz, 2H), 2.26 (br, 1H), 1.41-1.28 (br, 16H), 0.94-0.86 (br, 6H);  $^{13}\text{C}$  NMR (100 MHz,  $\text{CDCl}_3$ ),  $\delta$ : 142.3, 134.6, 132.0, 130.8, 129.6, 119.7, 116.6, 107.2, 60.9, 39.3, 31.7, 31.3, 31.0, 29.4, 28.4, 26.1, 22.8, 22.6, 14.0, 14.0.

**Synthesis of triazole-based polymers (PBnDT-PrzTAZ, PBnDT-PyCNTAZ, PBnDT-CNTAZ)**

0.1 mmol of dibromo triazole acceptor (61.1 mg for diBr-PrzTAZ, 63.5 mg for diBr-PyCNTAZ, 70.0 mg for diBr-CNTAZ), 0.102 mmol of distannylated benzodithiophene (89.8 mg), 2.0 mg of  $\text{Pd}_2(\text{dba})_3$   $\text{CHCl}_3$ , 4.8 mg of  $\text{P}(o\text{-tol})_3$  were sealed in a microwave reaction tube and went through three vacuum-Argon refilling cycles. Anhydrous *o*-xylene (0.7 mL) was added

into the tube to dissolve the monomers, catalyst and ligand. The reaction tube was irradiated under microwave with following parameters: maximum power: 300 W; temperature: 200 °C; ramp time: 10 minutes; heating time: 10 minutes. The crude polymer was dissolved in hot dichlorobenzene and precipitated in methanol. The precipitate was washed by hexane, ethyl acetate, tetrahydrofuran and chloroform subsequently in a Soxhlet extractor. The chloroform portion was collected, concentrated, and precipitated in methanol again to yield the targeted polymer. **PBnDT-PrzTAZ**:  $^1\text{H}$  NMR (500 MHz,  $\text{C}_2\text{D}_4\text{Cl}_2$ , 393K),  $\delta$ : 8.45, 7.72, 7.51, 4.93, 3.24, 2.44, 1.95, 1.67, 1.53, 1.45, 1.40, 1.36, 1.07, 1.00, 0.98. **Elemental analysis**: calculated: C: 71.59%, H: 8.71%, N: 6.96%, S: 12.74%. Found: C: 71.63%, H: 8.74%, N: 6.98%, S: 12.64%. **PBnDT-PyTAZ**:  $^1\text{H}$  NMR (500 MHz,  $\text{C}_2\text{D}_4\text{Cl}_2$ , 393K),  $\delta$ : 8.37, 7.38, 7.51, 4.92, 3.26, 2.52, 1.90, 1.54, 1.49, 1.40, 1.36, 1.10, 1.03, 0.98. **Elemental analysis**: calculated: C: 72.25%, H: 8.51%, N: 6.80%, S: 12.44%. Found: C: 72.35%, H: 8.67%, N: 6.67%, S: 12.20%. **PBnDT-CNTAZ**:  $^1\text{H}$  NMR (500 MHz,  $\text{C}_2\text{D}_4\text{Cl}_2$ , 393K),  $\delta$ : 8.42, 7.36, 5.06, 3.15, 2.49, 1.83, 1.49, 1.40, 1.11, 1.07, 1.01, 0.95. **Elemental analysis**: calculated: C: 72.89%, H: 8.31%, N: 6.64%, S: 12.16%. Found: C: 73.09, H: 8.49, N: 6.45%, S: 11.88%

Several points are worth noting for this general and versatile synthetic scheme. First, due to the unfavorable electronic structure of azide anion, our initial attempt to create the “free” triazole (**6**) via Huisgen cycloaddition of compound (**4**) by sodium azide only offered the target molecule with a miserable yield of 4%. On the other hand, the direct conversion of (**4**) to the target intermediate (**7**) with the appropriate alkyl azide, though high-yielding, only led to the undesirable *N*-1 alkylation. As shown in Scheme 5.2, this dilemma was resolved by applying a special alkylated azide, azidomethyl pivalate, first reported by Sharpless et al.,<sup>149</sup> to create the triazole protected by *N*-methyl pivalate, which can be readily removed to yield the *NH*-1,2,3-

triazole of high yield. Second, the alkylation of unsubstituted triazole usually generates appreciable amount of the *N*-1 alkylated isomer (~ 33% of the two alkylated isomers); interestingly, the *N*-2 alkylation selectivity can be significantly enhanced to above 90% when electron-withdrawing groups are attached to these two carbons in the triazole.<sup>150,151</sup> This helps to explain the high *N*-2 selectivity (91%, Figure 5.1) of the alkylation of the NH-1,2,3-triazole in our case (**6** to **7**), since this undecorated triazole (**6**) has carbonyls on the 4 and 5 positions. Lastly, though *N*-bromosuccinimide (NBS) was successfully used to brominate *m*-HTAZ and *m*-FTAZ,<sup>32</sup> it was not able to brominate these highly electron deficient *m*-TAZ analogs. Instead, molecular bromine had to be used to convert these *m*-TAZ acceptors into monomers for polymerizations; however, caution must be taken to avoid the possible over-bromination.

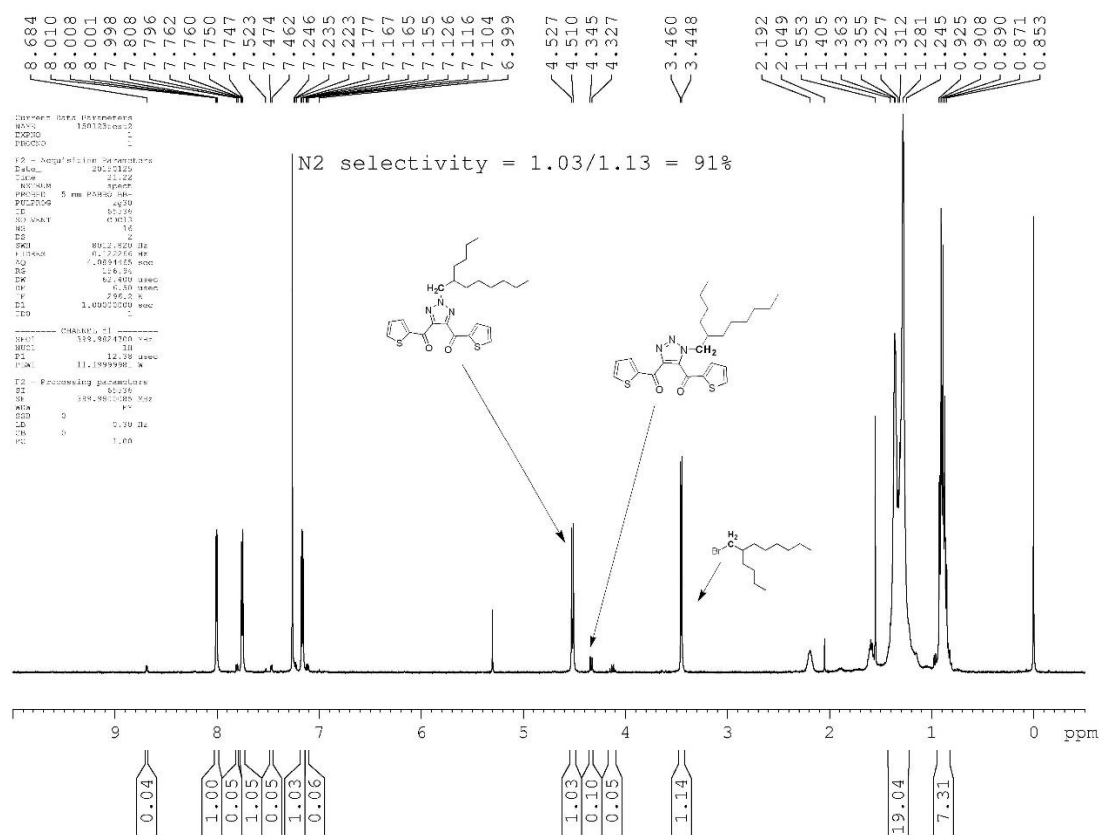


**Figure 5.1** High *N*-2 selectivity shown in <sup>1</sup>H-NMR of crude product of NH-1,2,3-triazole (**6**) alkylation. Methylene peaks are assigned to marked *N*-alkyl isomers and starting material.

### 5.3 Optical and electrochemical properties

These new *m*-TAZ monomers, together with the original *m*-FTAZ monomer, were carefully purified and submitted to the polymerization with distannylated BnDT (Scheme 5.2) to obtain four PBnDT-TAZ polymers of sufficiently high molecular weights (Table 5.1), following our previously reported procedure.<sup>152</sup> For simplicity, these polymers are named based on their unique acceptors, i.e., PrzTAZ for PBnDT-PrzTAZ, in following discussion. Assessing optical properties of these four polymers as thin films via UV-Vis (Figure 5.2) reveals a gradual red-shift of the absorption edge from FTAZ (619 nm) to PrzTZ (641 nm), then to PyCNTAZ (673 nm) and finally to CNTAZ (710 nm). The band gaps of these polymers are then estimated and compared in Table 5.1, which offer a rich set of data to evaluate the impact of structural modifications to the original PBnDT-HTAZ. As we previously discovered, fluorine substitutions on the benzotriazole (i.e., from HTAZ to FTAZ) do not noticeably change the band gap of the resulting polymer; HTAZ and FTAZ polymers have a similar band gap of  $\sim 2.0$  eV. However, these strongly electron withdrawing cyano substituents on the benzotriazole lead to a 0.23 eV reduction of the band gap of the resulting polymer CNTAZ. On the other hand, replacing the two  $sp^2$  C in the benzotriazole with two  $sp^2$  N, i.e., from HTAZ to PrzTAZ, only reduces the band gap by a marginal amount ( $\sim 0.07$  eV). Combining these two strategies,  $sp^2$  N and cyano substituent, results in a polymer (PyCNTAZ) of a moderate band gap reduction ( $\sim 0.16$  eV) when compared with that of the HTAZ polymer. These results indicate that though both  $sp^2$  N and cyano substituents can reduce the band gap beyond fluorine substitution, the cyano substituent is more effective. Similar results were recently reported by Heeney et al. in comparing the fluorine substituted benzothiadiazole and the cyano substituted one.<sup>147</sup>

We next investigated the impact of these structural modifications on the energy levels of PBnDT-TAZ polymers. While the HOMO energy level can be estimated from the oxidation onset of the polymer, measured by cyclic voltammetry, the LUMO level was calculated by  $E_{\text{LUMO}} = E_{\text{HOMO}} + E_{\text{gap}}$  (optical). Having obtained the energy levels of all four polymers (Table 5.1), we then compare them in an energy diagram (Figure 5.3) which shows an interesting “staircase” behavior. Specifically, the HOMO energy level of the PBnDT-TAZ polymer gradually decreases, following the order of FTAZ, PrzTAZ, PyCNTAZ, and finally CNTAZ. This can be ascribed to the unique structural feature of these TAZ acceptors where the solubilizing alkyl chains are anchored on the center nitrogen of the triazole (rather than on these flanking thiophenes). This desirable structural feature would minimize the steric hindrance between the “donor” (BnDT) and the acceptor (TAZ), thereby promoting the molecular orbital delocalization over the entire repeat unit (consisting of a donor and an acceptor). Thus the structural modification of the TAZ acceptor can also have strong influence on the HOMO level of the PBnDT-TAZ polymer, though to a lesser degree than it does to the LUMO level, evidenced by the band gap decreasing from FTAZ to CNTAZ (as discussed earlier).

**Table 5.1** Molecular weight and dispersity, absorption and energy levels of PBnDT-TAZ polymers

Polymer	$M_n^a$ (kg/mol)	$\bar{D}^a$	Abs. onset (nm)	$E_{\text{gap}}$ (eV)	HOMO <sup>b</sup> (eV)	LUMO <sup>c</sup> (eV)
FTAZ	81	1.84	619	2.00	− 5.45	− 3.45
PrzTAZ	53	1.48	641	1.93	− 5.66	− 3.73
PyCNTAZ	53	2.52	673	1.84	− 5.67	− 3.83
CNTAZ	102	2.35	701	1.77	− 5.73	− 3.96

<sup>a</sup>Measured by GPC in 1,2,4-trichlorobenzene at 150 °C.

<sup>b</sup>Measured by cyclic voltammetry.

<sup>c</sup>Calculated from measured HOMO level and optical band gap.



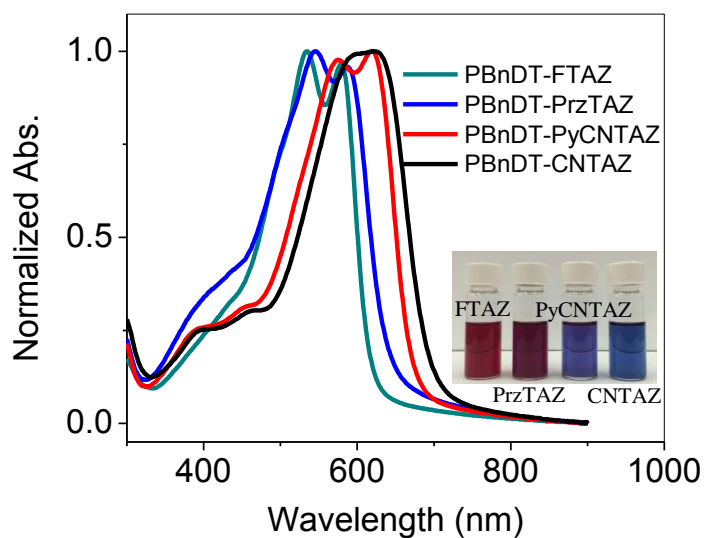


**Figure 5.2** Normalized film absorptions of PBnDT-TAZ polymers spun cast from their *o*-dichlorobenzene (ODCB) solution; inset shows the color variations of their ODCB solution (0.15 mg/mL).

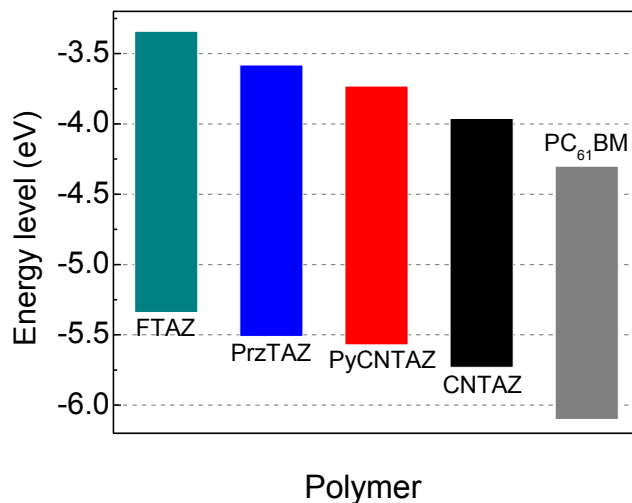


**Figure 5.3** Energy level diagram of PBnDT-TAZ polymers and PC<sub>61</sub>BM. While the HOMO of each polymer was determined by cyclic voltammetry, LUMO was derived by  $E_{\text{LUMO}} = E_{\text{HOMO}} + E_{\text{gap}}$  (optical).

## 5.4 Photovoltaic Device Performance

To correlate these structural changes of PBnDT-TAZ with photovoltaic properties, BHJ photovoltaic devices of a normal architecture were fabricated and tested (ITO/hole transport layer/PBnDT-TAZ:PC<sub>61</sub>BM/Ca/Al). We initially applied the ubiquitous PEDOT:PSS as the hole transport layer (HTL); however, only a moderate increase of  $V_{oc}$  of  $\sim 0.06$  V was observed for the CNTAZ device when compared with the FTAZ device, though the HOMO level of CNTAZ is significantly lower (by  $\sim 0.3$  eV) than that of FTAZ (Table 5.2). We thus realized that PEDOT:PSS, typically having a work function of  $-5.0$  eV, was not an ideal HTL for these polymers with very low HOMO levels. For better matching these deep-lying HOMO energy levels and enabling more efficient charge transport, we selected copper(I) thiocyanate (CuSCN) with a high ionization potential (IP) of  $-5.5$  eV as the HTL.<sup>153</sup> Indeed, for these three new PBnDT-TAZ polymers (PrzTAZ, PyCNTAZ and CNTAZ), devices with CuSCN as the HTL show noticeably improved performance when compared with the PEDOT:PSS counterparts; in particular, over 30% increase of the overall efficiency was observed for the PyCNTAZ device (from 5.21% in Table 5.2 to 6.95% in Table 5.3). The reference polymer, PBnDT-FTAZ, on the other hand, does not show much performance improvement upon adopting CuSCN as the HTL in its device. It seems that the relatively high HOMO level of FTAZ (among the four polymers) does not require a HTL of high IP; PEDOT:PSS is sufficient as the HTL for the FTAZ devices. Figure 5.4 consolidates representative J-V curve from these BHJ devices with CuSCN as the HTL, while Figure 5.5 compares corresponding EQE spectra.

**Table 5.2** Highest performance of four triazole-based polymers with PEDOT:PSS as hole transport layer

Polymer	Thickness (nm)	$J_{sc}$ (mA/cm <sup>2</sup> )	$V_{oc}$ (V)	$FF$ (%)	$\eta$ (%)
PBnDT-FTAZ	123	8.65±0.28	0.825±0.006	75.7±0.8	5.40±0.24
PBnDT-PrzTAZ	136	7.47±0.30	0.890±0.011	47.7±0.7	3.17±0.17
PBnDT-PyCNTAZ	112	8.66±0.73	0.914±0.004	65.8±0.8	5.21±0.42
PBnDT-CNTAZ	143	8.28±0.45	0.884±0.017	56.5±1.0	4.14±0.25

**Table 5.3** Active Layer thickness, photovoltaic performance and hole mobility of TAZ polymers.

Polymer	Thickness (nm)	$J_{sc}^a$ (mA/cm <sup>2</sup> )	$V_{oc}^a$ (V)	$FF^a$ (%)	$\eta^a$ (%)	Hole mobility <sup>b</sup> (cm <sup>2</sup> V <sup>-1</sup> s <sup>-1</sup> )
FTAZ	125	8.89±0.24	0.853±0.004	75.9±1.0	5.75±0.18	$1.78 \times 10^{-3}$
PrzTAZ	131	8.33±0.22	0.955±0.010	59.7±2.1	4.75±0.25	$4.47 \times 10^{-5}$
PyCNTAZ	117	10.58±0.42	0.964±0.003	68.2±0.9	6.95±0.34	$7.02 \times 10^{-4}$
CNTAZ	140	9.41±0.49	1.023±0.002	63.7±1.4	6.13±0.19	$4.92 \times 10^{-4}$

<sup>a</sup>Measured under 1 sun, AM 1.5G condition with CuSCN as hole transport layer with a normal device structure.

<sup>b</sup>Measured by space charge limited current (SCLC) method.

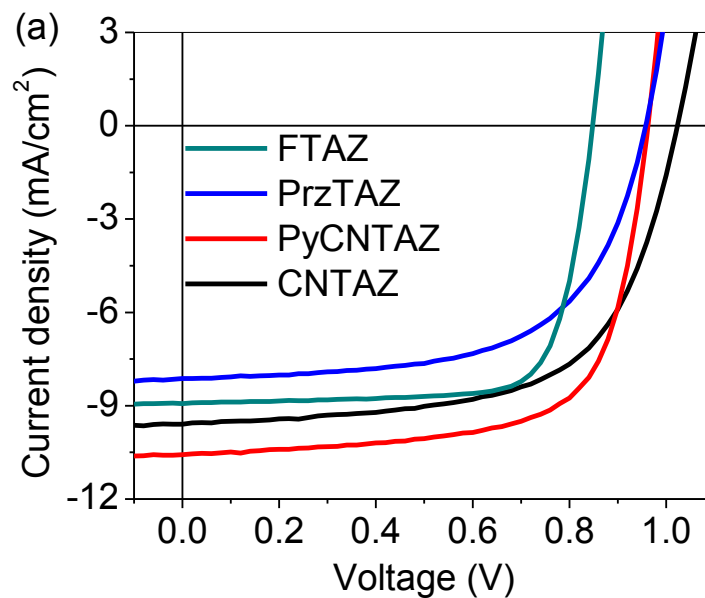


**Figure 5.4** *J-V* curves of BHJ device based on four TAZ polymers with CuSCN as hole transport layer under 1 sun, AM 1.5G condition.

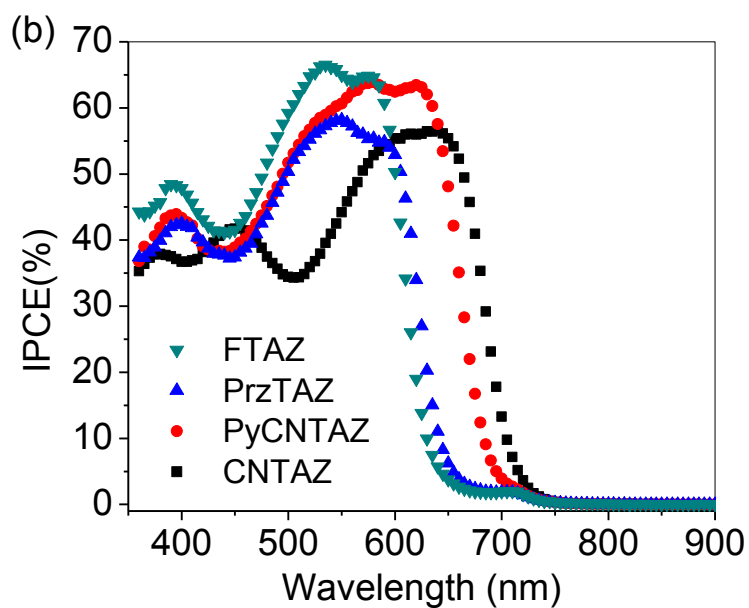


**Figure 5.5** Incident photon to current efficiency (IPCE) of BHJ device based on four TAZ polymers with CuSCN as hole transport layer under 1 sun, AM 1.5G condition.

With the appropriate HTL (i.e., CuSCN), these three new PBnDT-TAZ polymers based devices demonstrate impressive  $V_{oc}$  values around 1 V (Table 5.3), tracing the HOMO energy levels very well, with the highest  $V_{oc}$  observed from the device based on CNTAZ that has the lowest HOMO level. On the other hand, the  $J_{sc}$  values do not show a clear trend. For example, PyCNTAZ, having a larger band gap than that of CNTAZ, in fact produces a higher  $J_{sc}$  value in its BHJ device than that of the CNTAZ device (Table 5.3). Together with a decent  $FF$  of 68% and a high  $V_{oc}$  of 0.96 V, the BHJ device based on PyCNTAZ exhibits the highest efficiency of ~ 7% in this series of four PBnDT-TAZ polymers, a 20% increase over the reference FTAZ device at similar thicknesses (~ 120 nm).

It is also interesting to note that the FTAZ device still boasts the highest  $FF$  in Table 5.3, ascribed to its highest hole mobility in this series of PBnDT-TAZ polymers. Furthermore, the trend in  $FF$  in this series of devices traces the hole mobility well, with PrzTAZ based device showing the lowest  $FF$  and the lowest hole mobility. In general, as Chapter 4 pointed out, a high hole mobility is required for efficient charge transport and extraction, thereby reducing the steady state carrier density and the directly related nongeminate recombination loss, benefiting a high  $J_{sc}$  and a high  $FF$ .<sup>20,154</sup> A low hole mobility, on the other hand, would lead to charge buildup and significant recombination; such a situation would be exacerbated by applying smaller band gap materials and/or thick active layers. Indeed, the high mobility of the original FTAZ achieved its highest device performance (over 7%) at an active layer thickness of ~ 300 nm, with a respectable  $FF$  of ~ 70%.<sup>20</sup> Interestingly, PyCNTAZ, whose hole mobility is noticeably lower than that of FTAZ (Table 5.3), exhibits much higher device efficiency (8.4%) at the similar film thickness (Table 5.4), albeit with a lower  $FF$  of 62% as expected from its lower mobility. In this case, the further enhancement of  $J_{sc}$  and in particular,  $V_{oc}$ , outweighs the decrease of  $FF$ . Further

increasing the active layer thickness of PyCNTAZ devices does not improve  $J_{sc}$  much, and the  $FF$  decreases even faster, leading to the efficiency drop (Table 5.4). This comparison on device performance between the FTAZ and PyCNTAZ exemplifies the significance of balancing both energy levels and charge transport properties in low band gap polymers. Further study is required to understand the underlying mechanism on what determines the hole mobility, and draw a clear correlation between the chemical structure and the mobility. It is very likely that the morphology of the active layer would play an important role, as we previously disclosed.<sup>20</sup>

**Table 5.4** Thickness dependence of PBnDT-PyCNTAZ device performance

Thickness (nm)	$J_{sc}$ (mA/cm <sup>2</sup> )	$V_{oc}$ (V)	$FF$ (%)	$\eta$ (%)
527	14.02±0.51	0.948±0.002	48.4±1.4	6.44±0.38
421	14.38±0.45	0.957±0.001	52.2±1.3	7.18±0.36
394	13.64±0.34	0.957±0.003	48.1±1.1	6.28±0.18
300	14.07±0.50	0.959±0.002	62.0±1.9	8.37±0.31
230	12.74±0.50	0.966±0.001	63.0±0.6	7.75±0.35
202	11.69±0.47	0.970±0.002	59.6±1.1	6.75±0.21
158	11.18±0.39	0.957±0.007	68.5±3.2	7.32±0.35
122	10.92±0.29	0.965±0.002	71.4±1.3	7.52±0.26
104	10.58±0.24	0.974±0.001	69.4±0.4	7.15±0.19

## 5.5 Conclusion

In summary, we designed a unique synthetic approach to allow easy access to a diverse set of triazole based conjugated molecules, and experimentally demonstrated its efficacy by creating three representative *m*-TAZ molecules of different electron-accepting abilities. The generality and versatility featured by our synthetic strategy of *m*-TAZ distinguishes it from the

syntheses of many popular electron-accepting conjugated moieties, i.e., “acceptors” (see Scheme 5.1 for a detailed comparison). For some of these acceptors, the synthesis starts with the electron-deficient core, followed by adding peripheral units (e.g., from benzodithiazole to DTBT). This divergent approach mandates a *de novo* synthesis if one changes the chemical structure of the core (e.g., comparing DTBT with DTPyT or DTffBT). For other acceptors, the synthetic approach can be convergent (e.g., DPP<sup>155</sup> and isoindigo<sup>156</sup>); however, there are very few (if any) structural variations that could change the electronic property of the core, since these cores are already highly fused heterocycles (thus lacking substitution positions). In contrast, our novel synthetic approach of TAZ derivatives maximizes synthetic degeneracy by picking both a suitable acceptor and a convergent strategy. More importantly, our synthesis opens the door to a great variety of TAZ derivatives; new design of triazole acceptors is now solely limited by the availability of appropriate condensation reagents in the last step.

These structural changes on the TAZ molecule have a great influence on the electronic and optical properties of related conjugated polymers. When applied in BHJ solar cells, these PBnDT-TAZ polymers, all having deep-lying HOMO levels, exhibited noticeably higher  $V_{oc}$  (around 1 V) than that of the original FTAZ based devices. At comparable active layer thicknesses, PyCNTAZ based devices exhibited the highest efficiency of 7.5%. Considering its medium band gap of 1.85 eV and high  $V_{oc}$  (~ 1 V), PyCNTAZ could be an ideal material for tandem cells to maximize the solar light utilization

## Chapter 6

### Conclusions and future directions

#### 6.1 Conclusions

In the field of organic photovoltaics, PBnDT-FTAZ has remained attractive since its first appearance. Contradicting the conventional design principles for high-performing D-A polymers, PBnDT-FTAZ exhibits an exceedingly effective utilization of incident photons within its narrow absorption range. Its large band gap and high efficiency in thick films make it appealing for both tandem solar cells and scalable roll-to-roll fabrication. This dissertation is dedicated to revealing the fundamental reasons behind the unexpectedly high performance of PBnDT-FTAZ, and to designing better polymers based on these underlying principles. Specifically, this dissertation reaches six important conclusions regarding the synthesis, morphology, and molecular design of triazole-based conjugated polymers.

- 1) The selectivity and conversion of either benzotriazole *N*-alkylation isomer can be improved by a properly chosen solvent or solvent mixture.
- 2) The molecular weight of PBnDT-FTAZ can be actively controlled by stoichiometry to reproducibly yield high performing polymers.
- 3) Molecular weight of PBnDT-FTAZ shapes the domain spacing in a BHJ with PC<sub>61</sub>BM. An optimal number average molecular weight of 40 kg/mol produces a small domain size of about 20-30 nm, and leads to the optimal  $J_{sc}$  and power conversion efficiency.



- 4) Fluorination on the PBnDT-FTAZ backbone improves hole mobility by two orders of magnitude, significantly reduces bimolecular recombination, and thus enhances *FF* and PCE.
- 5) A general synthetic strategy for developing diverse triazole-based acceptors is introduced. Nitrogen hetero atom and cyano substituent can be readily incorporated into the conjugated backbone by versatile condensation reactions of 1,4-diketone.
- 6) PBnDT-PyCNTAZ improves the power conversion efficiency by extending the absorption range of the original PBnDT-FTAZ, although at the cost of hole mobility.

In summary, the favorable BHJ morphology of PBnDT-FTAZ:PC<sub>61</sub>BM in active layer suggests how this polymer is able to utilize solar energy effectively. In the amorphous region, a proper molecular weight of approximately 40 kg/mol leads to a small domain size, which is comparable to the diffusion length of exciton. As a result, the charge separation step benefits as more excitons survive to reach the D:A interface, increasing the probability of exciton splitting at the D:A interface, and producing more free charge carriers. On the other hand, in the crystalline region, the  $\pi$ - $\pi$  stacking is strengthened by fluorine substituents, leading to an improved hole mobility. Thus, the generated free charges can be rapidly extracted out of the active layer, without accumulating near the interface and undergoing non-geminate recombination. While the proper domain size is favorable for charge separation, the high hole mobility facilitates the charge extraction. Consequently, although narrow absorption of PBnDT-FTAZ limits the exciton generation step, the generated excitons can be utilized more effectively in the two following steps as described above.

It is inspiring to see how improving only one or two steps of the four-step working mechanism (discussed in Chapter 1) could dramatically enhance the overall efficiency, even

though the other steps were not optimal. In the case of PBnDT-FTAZ, the fluorine substituents expedite the charge transport process and lead to a 7% efficiency; while in the case of PBnDT-PyCNTAZ, the gain in exciton generation exceeds the loss during the charge transport step, so the PBnDT-PyCNTAZ reaches an even higher efficiency than PBnDT-FTAZ. Considering the fact that the 7% efficiency of PBnDT-FTAZ was realized without any extensive device engineering, we are optimistic that there is still a great potential for organic solar cells to achieve an efficiency above 10% with the integration of multiple beneficial structural characteristics into one polymer backbone.

## **6.2 Future directions**

### **6.2.1 Effect of Polydispersity ( $\bar{D}$ )**

In our molecular weight study in Chapter 3, an artificial mixture of the 60 kg/mol polymer and 10 kg/mol polymer recovers the efficiency of the high performance 40 kg/mol polymer, but the morphology of this polymer blend does not directly explain the “recovered” device performance: although its domain spacing is substantially larger than that of the 40 kg/mol polymer, its  $J_{sc}$  is still very high. This indicates that a new morphology scenario other than phase separated domains might exist in this polymer blend. Two possible situations are hypothesized. In the first situation, the 60 kg/mol polymer governs the overall morphology, but the 10 kg/mol polymer works as “plasticizer” to improve processibility of the high molecular weight polymer, thus allowing better intermixing between polymer and PC<sub>61</sub>BM. In the second situation, the 10 kg/mol polymer dominates the formation of crystalline domains, and the 60 kg/mol polymer serves as connections between the crystalline regions to facilitate hole transport.

To accurately determine the actual situation requires a comprehensive investigation into how the active layer morphology and device physics change as a function of the weight percentage of the lower molecular weight portion (i.e.,  $D$ ). Practically, it is important for us to learn how to take advantage of the dispersity of polymeric materials instead of overcoming it, as a broad  $D$  is often encountered in step-growth polymerizations, especially on industrial scales. Effective utilization of both low molecular weight and high molecular weight polymers not only simplifies the synthetic control during polymerization, but also converts non-ideal polymers into useful products, thus further decreasing the cost of organic photovoltaic technology.

### **6.2.2 Further study on fluorination effect**

It is generally agreed upon in the OPV community that fluorine substitution is beneficial for device performance in many aspects: it strengthens  $\pi$ - $\pi$  stacking, improves morphological stability, enhances hole transport, and introduces a local dipole to partially separate excitons. In Chapter 4, we determined the reason for the high performance of PBnDT-FTAZ by correlating fluorine substituents to the improved hole mobility from better  $\pi$ - $\pi$  stacking in the crystalline region. However, many fundamental questions regarding fluorine impact still remain unclear. 1) How does fluorine substitution strengthen  $\pi$ - $\pi$  stacking? Do other strong electron withdrawing substituents, such as cyano and nitro groups, have a similar effect? These questions demand a deeper understanding of the essence of the so called “ $\pi$ - $\pi$  stacking” and more experimental comparisons. 2) How does fluorine substitution affect BHJ morphology, in both crystalline and amorphous regions? It is well known that perfluorinated alkanes are neither hydrophilic nor oleophilic, but the molecular interaction between polymer and fullerene will be different from the interaction between polymer and water. 3) How would the position of fluorine substituents

affect the polymer performance? It has been proved that in PTB7, fluorination on the donor unit reduces the local dipole moment and leads to inferior charge separation;<sup>16,17</sup> however, in some other cases, fluorination on the donor unit worked synergistically with fluorine substituents on the acceptor to enhance the PCE.<sup>157</sup> A means of rationally fluorinating structure units which fully benefit from the fluorination remains to be elucidated.

### 6.2.3 Enriching triazole acceptor library

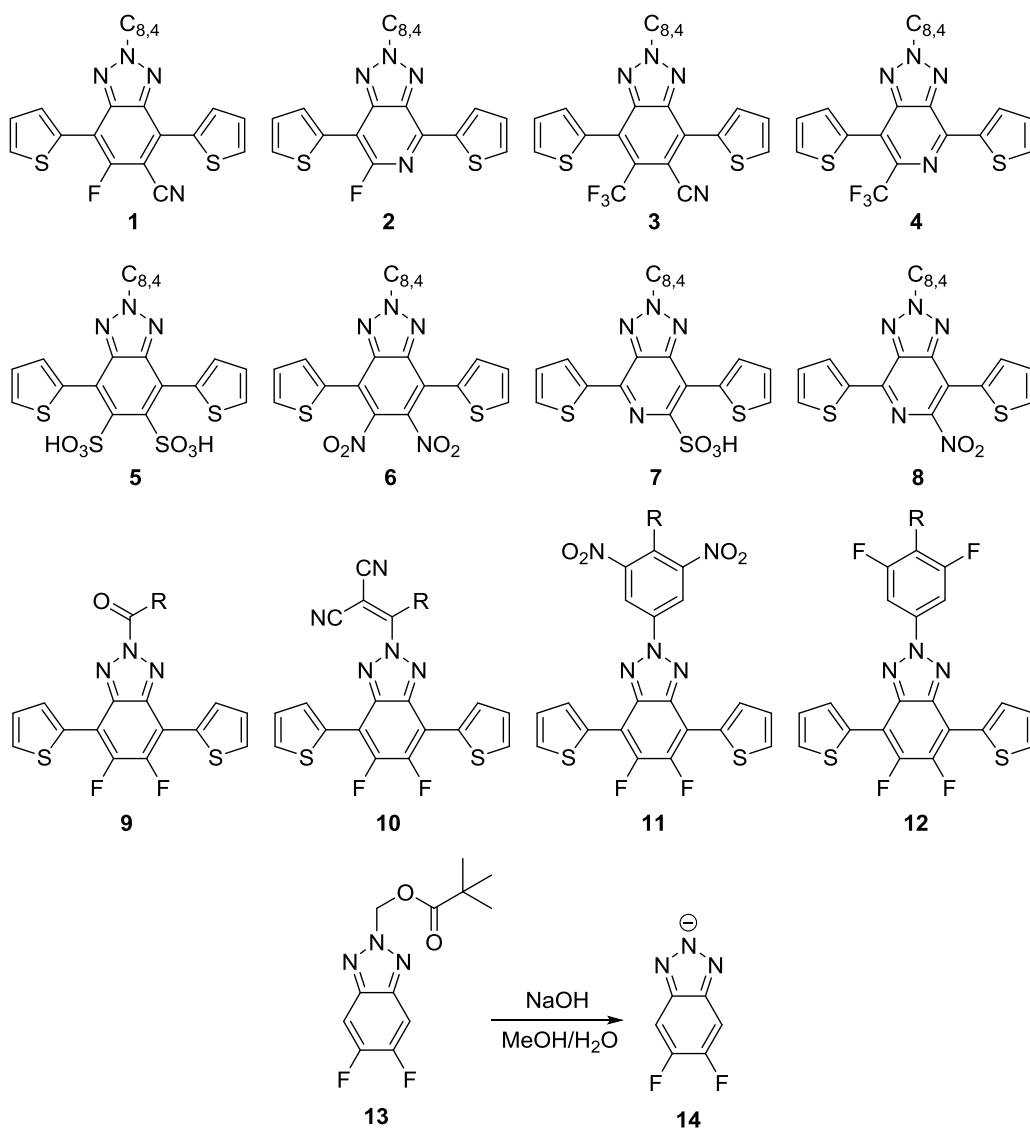
Although PBnDT-PyCNTAZ surpasses the efficiency of PBnDT-FTAZ (as shown in Chapter 5), it is at the cost of hole mobility and charge extraction. This suggests that the efficiency of triazole-based polymers can still be enhanced by introducing fluorine substituents onto the triazole acceptor. Molecule **1** to **4** in Scheme 6.1 are proposed to introduce both a smaller band gap and fluorine/trifluoromethyl substituents into benzotriazole via binary condensation reagents. Various fluorination methods should also be considered as an alternative to synthesize these proposed molecules.

Many other electron-withdrawing substituents, such as nitro and sulfonyl groups, are also proposed to gain fundamental insights into substituent effects (molecule **5** to **8** in Scheme 6.1). Different from other D-A polymers, the relatively high electron-density on benzotriazole is very tolerant to electron-deficient groups, which provides ample space for experimentation.

Some other acceptors have been proposed since the synthesis of original FTAZ. In these acceptors (molecule **9** - **12**), the fluorinated benzotriazole moiety is completely maintained, and structural changes are localized at the solubilizing alkyls on the triazole. The high LUMO of the triazole is mainly ascribed to the electron lone pair on the nitrogen. These molecules are

expected to directly reduce the  $\pi$  electron density of the triazole by withdrawing the electron long pair to the side chain.

Finally, the deprotection of the pivalate group in MeOH/H<sub>2</sub>O (Chapter 5) possibly opens a new route to triazole ionomers. After deprotection, the benzotriazole anion would be readily soluble in water (from molecule **13** to **14**). It would be interesting to examine the chemistry of the benzotriazole ionomer and whether its polymer would exhibit any aqueous solubility.



**Scheme 6.1** Proposed molecules to enrich triazole acceptor library.

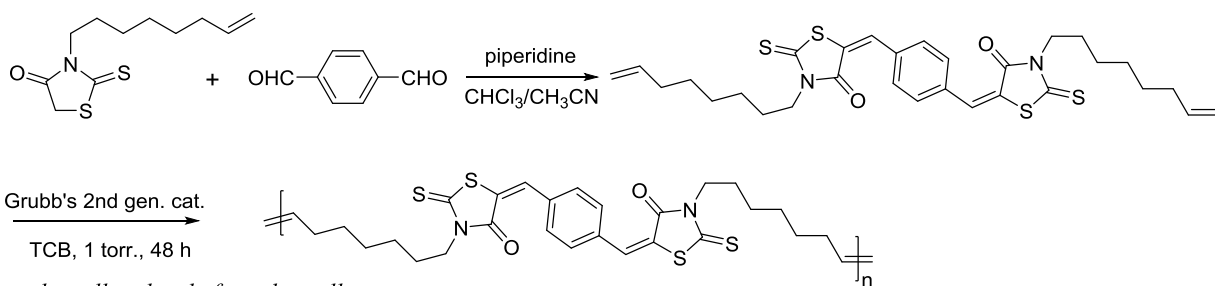
#### 6.2.4 Bridging the gap between small molecules and polymers

Although polymers are quite successful in organic photovoltaics, they also suffer from many disadvantages, including batch-to-batch variation, dispersity, and difficulty in purification. On the other hand, some small molecules have achieved high efficiencies comparable to those of polymers.<sup>158,159</sup> However, small molecules also have their own drawbacks, including poor film formation and poor morphology control.

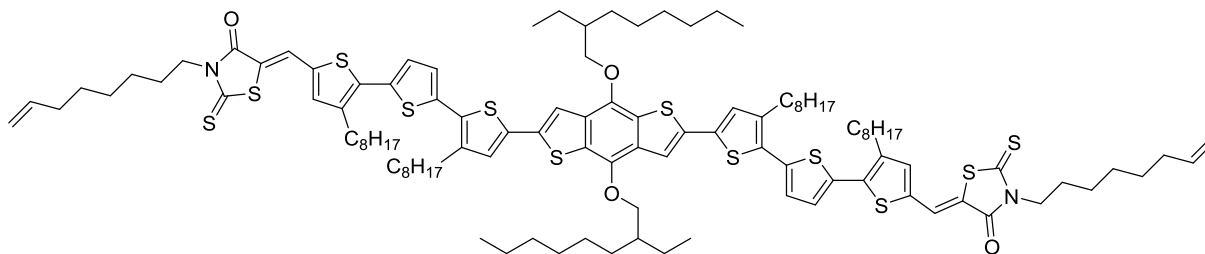
Aiming to combine the advantages of both polymers and small molecules, we propose to connect photovoltaic active small molecules via non-conjugated polymer chains. In this case, the functional moiety is mono-dispersed and can be sufficiently purified by column chromatography and recrystallization. After polymerization, the dispersity would not significantly affect the electrochemical/photovoltaic properties of the final product, and the polymer's viscosity would allow morphological control of the BHJ layer.

In our prototype polymer, we polymerized a model compound with two alkene side chains via acyclic diene metathesis (ADMET) (Scheme 6.2). Polymerization was run under vacuum for 2 days, and any remaining catalyst was then removed by refluxing with *in situ* generated  $P(OH)_3$  ligand. The future work will focus on polymerizing a high-performing small molecule via ADMET polymerization, and to then compare its performance with the original small molecules.<sup>160</sup>

#### Model ADMET Polymerization



#### Selected small molecule for solar cell



**Scheme 6.2** ADMET polymerization of small molecules with photovoltaic performance

### 6.2.5 Future directions in the OPV field

Last decade has witnessed a synthetic thrust for new polymers for organic photovoltaics and a rapid efficiency hike. Recently, device engineering has been playing a vital role in improving the OPV efficiency from 7% to 10%.<sup>161,162</sup> Promising as the OPV field is, many fundamental science questions are still waiting to be solved. For example, the four-step mechanism introduced in Chapter 1 neglects one important underlying process: exciton diffusion to the polymer:fullerene interface. Due to the lack of characterization methods, the existence and fate of excitons has been under constant debate. It is still uncertain whether exciton diffusion length determines the optimal domain size, although a smaller domain size around 40-50 nm does enhance OPV efficiency.<sup>12</sup>

Since the field of OPV research is highly interdisciplinary, involving organic chemistry, polymer chemistry, polymer physics both in solution and solid state, polymer composite morphology, semiconductor physics, device fabrication, and engineering, we are not able to summarize every possible aspect regarding future OPV research. Instead, from a synthetic chemist's point of view, we will briefly describe three future directions.

### **1) Green chemistry and scalable synthesis.**

Current syntheses of conjugated polymers often involve highly reactive reagents (such as *n*-BuLi or *t*-BuLi), toxic chemicals (such as trimethyltin chloride and halogenated solvents), and harsh conditions (such as concentrated sulfuric acid).<sup>163</sup> Being potentially dangerous and hazardous, these reagents and conditions greatly impede the industrial synthesis and commercial viability of conjugated polymers; the limited supply of polymers in turn slows down the research and development of OPV technology.

To promote large-scale synthesis of conjugated polymers, and to carry forward the low cost advantage of OPV technology, the synthesis of photovoltaic materials must be safer, cleaner, and easier. Recently, C-H activation has been applied to cross-coupling reactions, and leads to a new polymerization method, direct (hetero) arylation polymerization (DHAP), which eliminates the use of hazardous organotin reagents.<sup>164</sup> The industry is also actively seeking new polymerization methods with toluene as solvent to replace halogenated solvents. One of our future works, "bridging the gap between small molecules and polymers" (*vide supra*), provides another solution to scalable synthesis. The synthesis of functional chromophores could take advantage of successful pharmaceutical industry procedures to reduce hazardous waste, while the polymer chain could be a conventional polyester or polyether, both of which are common commercially available polymers.



## **2) Engineering the polymer:fullerene interface.**

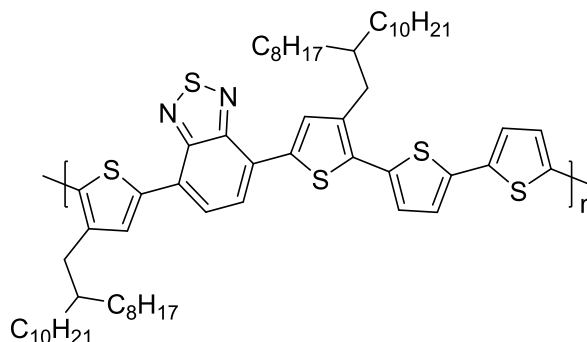
The significance of the polymer:fullerene interface will never be overstated, especially at current stage of OPV research where the other physical processes in the polymer domain and at the electrodes are mostly well understood. Several recent works have pointed out some important design rules for the polymer:fullerene interface. For example, a “face-on” orientation of polymer backbone relative to the fullerene is favorable for charge separation,<sup>13</sup> and docking the fullerene at the acceptor moiety in D-A polymers facilitates electron transfer of partially separated charges.<sup>18</sup>

As many precise characterization methods and accurate computational methodologies emerge, a clearer picture of a favorable polymer:fullerene molecular interface is gradually depicted, and the high-performance of many polymers will be explained. However, it remains challenging for chemists to actively realize these favorable interfaces through material chemistry. Taking the two examples in the last paragraph, a difficult question is what substituent or side chain would be favorable for “face-on” orientation or fullerene docking. To answer these questions, more comprehensive structure-property relationship studies and fundamental modelling of molecular interactions between polymer and fullerene are required.

## **3) Optimization of BHJ morphology by polymer chemical structure.**

Several representative high-performing polymers, especially the PTB7<sup>165</sup> and DPP<sup>166</sup> series of polymers, have been thoroughly studied and continuously optimized over the past few years. However, they are not the only promising polymers for future OPV technology. The first stage of D-A polymer design (see Chapter 1) provides us many promising candidates, but due to

various reasons, their great potential has yet to be exploited. One of the bottlenecks limiting their performance is the BHJ morphology.



**Scheme 6.3** A representative polymer displaying dramatically enhanced OPV performance from 1.6% to 10% upon morphology improvement

The pivotal role of BHJ morphology can be best described using two examples. In the first example, a high-performing polymer, PBnDT-FTAZ, suffered from large domain size and lost 80% of its efficiency (Chapter 3). Actually, many high-performing polymers have rigorous requirements for BHJ morphology, and often require morphology optimization to achieve high performance. In another example, without rational morphology optimization, the polymers in Scheme 6.3 exhibited inferior efficiency of around 1.6%.<sup>167</sup> However, recently Yan et al. discovered that 2-octyldecyl side chain introduced a significant change in polymer aggregation at different temperatures.<sup>12</sup> By selecting the proper temperature during film fabrication, the authors were able to achieve a domain size around 30-40 nm regardless of the fullerene derivative species, and the OPV efficiency greatly increased to ~10%, among the highest values reported.

It is well known to the OPV community that side chains affect backbone packing and lamellar spacing in the crystalline region.<sup>168</sup> Since the OPV community started to consider the morphology in non-crystalline region, Yan's work in the previous example is the first time that

the effect of side chains on the non-crystalline region morphology is reported. Thus, it is very interesting to revisit how those structural motifs that we used to shape the morphology in the crystalline region would affect the morphology in the non-crystalline region. Given the success in crystal engineering and controlling  $\pi$ - $\pi$  stacking in the crystalline domain, it is very likely that chemists will be able to tune the domain size in the non-crystalline region via structural modification.

## APPENDIX I: GENERAL METHODS

Anhydrous THF was obtained by distillation from sodium/benzophenone prior to use. Diisopropylamine was distilled from potassium hydroxide prior to use. 2-Butyl-1-octyl bromide was prepared according to literature procedures [Chem. Mater. 21 (13), 2789-2797 (2009)]. All other chemicals and reagents were purchased from commercial suppliers (Sigma Aldrich, Alfa Aesar, Matrix Scientific, etc.) and used without further purification. Microwave polymerization was carried out in a CEM Discover microwave reactor (Model number: 908005).

**UV-visible spectra** were acquired on a Shimadzu UV-2600 spectrophotometer. The thin films for UV-visible measurement were coated from *o*-dichlorobenzene (*o*-DCB) solution on pre-cleaned glass slides.

**Cyclic voltammetry** measurements were carried out using a Bioanalytical Systems (BAS) Epsilon potentiostat equipped with a standard three-electrode configuration, comprising a glassy carbon working electrode, a Ag/AgNO<sub>3</sub> (0.01 M in anhydrous acetonitrile) reference electrode, and a Pt wire counter electrode. The measurement was done in anhydrous acetonitrile with tetrabutylammonium hexafluorophosphate (0.1 M) as the supporting electrolyte under an argon atmosphere at a scan rate of 100 mV/s. Polymer films were drop cast onto the glassy carbon working electrode from a concentrated *o*-dichlorobenzene solution and dried under heat prior to measurements. The potential of Ag/AgNO<sub>3</sub> reference electrode was internally calibrated by using the ferrocene/ferrocenium redox couple (Fc/Fc<sup>+</sup>). The electrochemical onsets were determined at the position where the current starts to differ from the baseline. The HOMO in electron volts was calculated from the onset of the oxidation potential ( $E_{ox}$ ) according to the following equation:

$$HOMO = -[4.8eV + e(E_{ox} - E_{Fc/Fc^+})]$$

$$E_{LUMO} = E_{gap} (optical) - E_{HOMO}$$

**Gel permeation chromatography (GPC)** measurements were performed on a Polymer Laboratories PL-GPC 220 instrument, using 1,2,4-trichlorobenzene as the eluent (stabilized with 125 ppm BHT) at 135 °C. The obtained molecular weight is relative to polystyrene standards.

**<sup>1</sup>H nuclear magnetic resonance (NMR)** spectra were obtained at Bruker 400 MHz DRX spectrometer as solutions in CDCl<sub>3</sub>. Chemical shifts are reported in parts per million (ppm,  $\delta$ ) and referenced from tetramethylsilane.

**Elemental analysis** was done by Atlantic Microlab, Inc.

**SCLC hole mobility** was acquired through the hole-only devices with a configuration of ITO/PEDOT:PSS/polymer:PC<sub>61</sub>BM/Pd. The experimental dark current densities  $J$  of polymer:PC<sub>61</sub>BM blends were measured when applied with voltage from 0 V to 5 V. The applied voltage  $V$  was corrected from the voltage drop  $V_{rs}$  due to the series resistance and contact resistance from ITO/poly(3,4-ethylene-dioxythiophene):poly(styrenesulfonic acid) (ITO/PEDOT:PSS), which were found to be around 35  $\Omega$  from a reference device without the layer of polymer:PC<sub>61</sub>BM. From the plots of  $J^{0.5}$  vs  $V$ , hole mobilities of copolymers was deduced from the Mott-Gurneys law:

$$J = \frac{9}{8} \epsilon_r \epsilon_0 \mu_h \frac{V^2}{L^3}$$

where  $\epsilon_0$  is the permittivity of free space,  $\epsilon_r$  is the dielectric constant of the polymer which is assumed to be around 3,  $\mu_h$  is the hole mobility,  $V$  is the voltage drop across the device, and  $L$  is the film thickness of active layer.

**Device Fabrication:** Glass substrates coated with patterned indium doped tin oxide (ITO) were purchased from Thin Film Devices, Inc. The 150 nm sputtered ITO pattern had a resistivity of 20  $\Omega/\square$ . Prior to use, the substrates were ultrasonicated in deionized water, acetone, then 2-

proponal for 15 minutes each. The substrates were dried under a stream of nitrogen and subjected to the treatment of UV-Ozone for 15 min. A filtered dispersion of PEDOT:PSS in water (Clevios™ PH500 from Heraeus) was then spun cast onto cleaned ITO substrates at 4000 rpm for 60 s and then baked at 120 °C for 15 min in air to give a thin film with a thickness of 40 nm. For devices with CuSCN buffer layer, the CuSCN was dissolved in dipropylsulfide with a concentration of 20 mg/ml under stirring for 24 h. Then the saturated CuSCN solution was filtered by 1.0 µm poly(tetrafluoroethylene) (PTFE) filter and spun-cast onto the cleaned ITO substrates at 1000 rpm for 60 s and then baked at 80 °C for 15 min in a glovebox under nitrogen atmosphere to give a thin film with a thickness of 40 nm. Blends of polymer:PC<sub>61</sub>BM (1:2 w/w, 7 or 8 mg/mL for polymer) were dissolved in 1,2,4-trichlorobenzene with heating at 130 °C for 6h. All the solutions were filtered through a 5.0 µm PTFE filter and spun-cast at an optimized rpm for 60 seconds onto the PEDOT:PSS or CuSCN layer. The substrates were then transferred into vacuum chamber immediately after spin-coating and dried at 30 mmHg below atmosphere for 30 mins. The devices were finished for measurement after thermal deposition of a 30 nm film of calcium and a 80 nm aluminum film as the cathode at a base pressure of  $2 \times 10^{-6}$  mbar. There were 8 devices per substrate, with an active area of 13 mm<sup>2</sup> per device. Device characterization was carried out under AM 1.5G irradiation with the intensity of 100 mW/cm<sup>2</sup> (Oriel 91160, 300 W) calibrated by a NREL certified standard silicon cell. Current density versus voltage (J-V) curves were recorded with a Keithley 2400 digital source meter. External quantum efficiency (EQE) were detected under monochromatic illumination (OrielCornerstone 260 1/4 m monochromator equipped with Oriel 70613NS QTH lamp), and the calibration of the incident light was performed with a monocrystalline silicon diode (Model No.: Newport 71580). All

fabrication steps after adding the PEDOT:PSS layer onto ITO substrate, and characterizations were performed in gloveboxes under nitrogen atmosphere.

**X-Ray Characterization:** R-SoXS characterization was conducted at Beamline 11.0.1.2 of the Advanced Light Source (ALS) in the soft X-ray energy regime ( $\sim 280$  eV). A section of film was floated onto  $1.5\text{ mm} \times 1.5\text{ mm}$  silicon nitride windows. The 1D averaged intensity is multiplied by  $q^2$ , which then corresponds to an azimuthal integration of the 2D data. This more directly reflects the fractional distribution of domain spacing than the traditional 1D  $I(q)$  function as  $I(q) \cdot q^2$  resembles the power spectral density of the 2D data. GIWAXS was carried out at Beamline 7.3.3. of the ALS using a Dectris Pilatus 1M photon counting detector. Blend films were measured at an incident angle of  $\sim 0.14^\circ$ , above the critical angle so the X-ray beam penetrated to the substrate. The photon energy used for GIWAXS was 10 keV. Air scatter which provides a background signal was reduced using helium gas. Data was not corrected for the missing wedge in the out of plane direction. STXM was conducted at Beamline 5.3.2.2 of the ALS. A 10K blend films from the 10K device was floated onto a TEM grid for measurement. During measurement, the chamber was filled with  $1/3$  ATM He. The imaginary part of the index of refraction of pure materials was determined from STXM measurements and was then used to calculate the real part via a Kramers-Kronig transformation. Mass densities of  $1.1$  and  $1.3\text{ g/cm}^3$  for polymer and fullerene were assumed to calculate the complex indices of refraction.

## **APPENDIX II: DETERMINING N-ALKYLATION SELECTIVITY OF BENZOTRIAZOLE BY <sup>1</sup>H-NMR SPECTRA IN CHAPTER 2**

### **General Procedures**

1,2,3-benzotriazole and 1-bromohexane were purchased from Acros Organics. Potassium carbonate was purchased from Fisher Scientific. All the solvents were used as received from commercial sources. <sup>1</sup>H-NMR spectra were measured on either a Bruker Avance 300 MHz AMX or a Bruker 400 MHz DRX spectrometer with CDCl<sub>3</sub> as the solvent and tetramethylsilane (TMS) as the internal standard. Column chromatography was performed using 230-400 mesh silica gel from Silicycle.

Typically, 1.0 mmol of 1,2,3-benzotriazole and 1.2 mmol of alkyl halide were combined and dissolved in 40 mL solvent (or 50 mL for DMF/THF mixed solvent in Table 5). Then 2.0 mmol potassium carbonate was added to the solution under stirring. When the solvent was DMF/NMP/DMAc/DMSO/dioxane, the reaction was quenched by water after 24 h and extracted by ethyl acetate. The organic phase was dried with sodium sulfate and concentrated by rotary evaporation. When the solvent was MeOH/THF/DME/ethyl ether, the solvent was directly evaporated on a rotary evaporator. The crude product was then dissolved in CDCl<sub>3</sub> to be examined by <sup>1</sup>H-NMR spectrum. Column chromatography of crude product was conducted with hexane/methylene chloride (v/v=1:1) as eluent.

### **<sup>1</sup>H-NMR spectra of all alkylation products under different conditions in this work**

1. MeOH reflux
2. DMF 0 °C
3. DMF room temperature



4. DMF 60 °C
5. C6,2 bromide
6. C8,4 bromide
7. n-Butyl bromide
8. s-Butyl bromide
9. t-Butyl bromide
10. Hexyl chloride
11. Hexyl iodide
12. Methyl iodide
13. NMP
14. DMAc
15. DMSO
16. THF
17. Dioxane
18. DME
19. EE
20. 18-Crown-6 in DMF
21. 18-Crown-6 in THF

22. 100% THF

23. 95% THF and 5% DMF

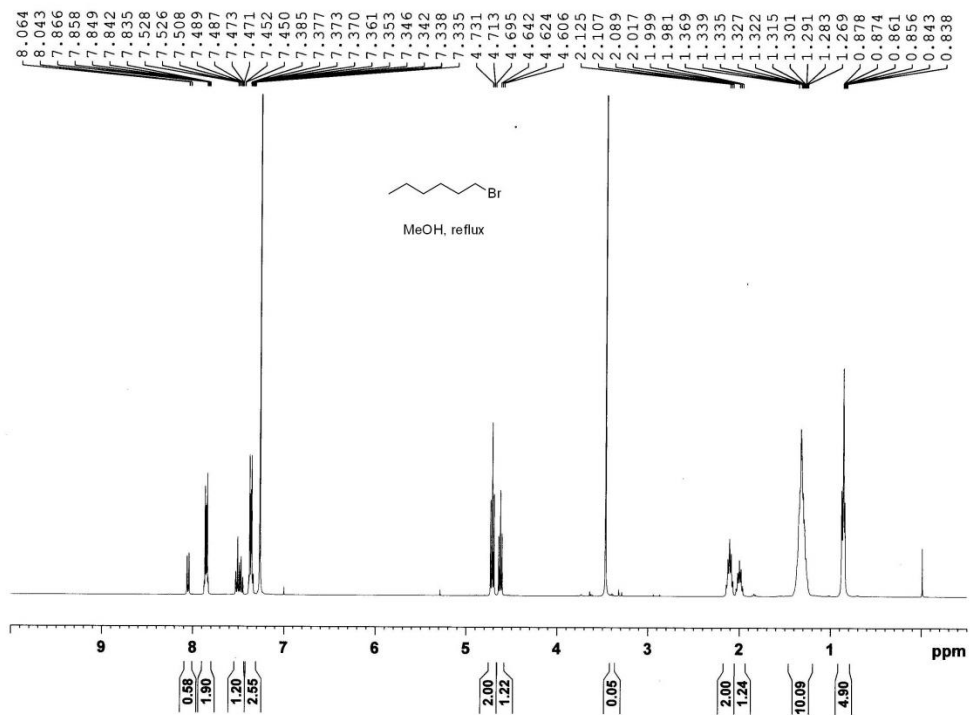
24. 80% THF and 20% DMF

25. 50% THF and 50% DMF

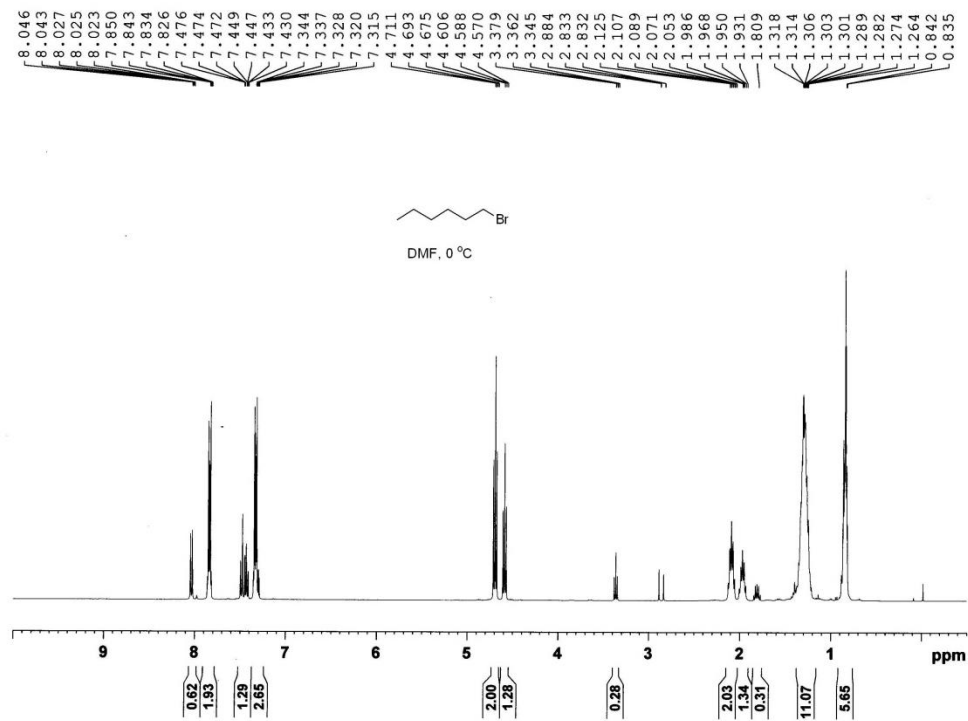
26. 20% THF and 80% DMF

27. 5% THF and 95% DMF

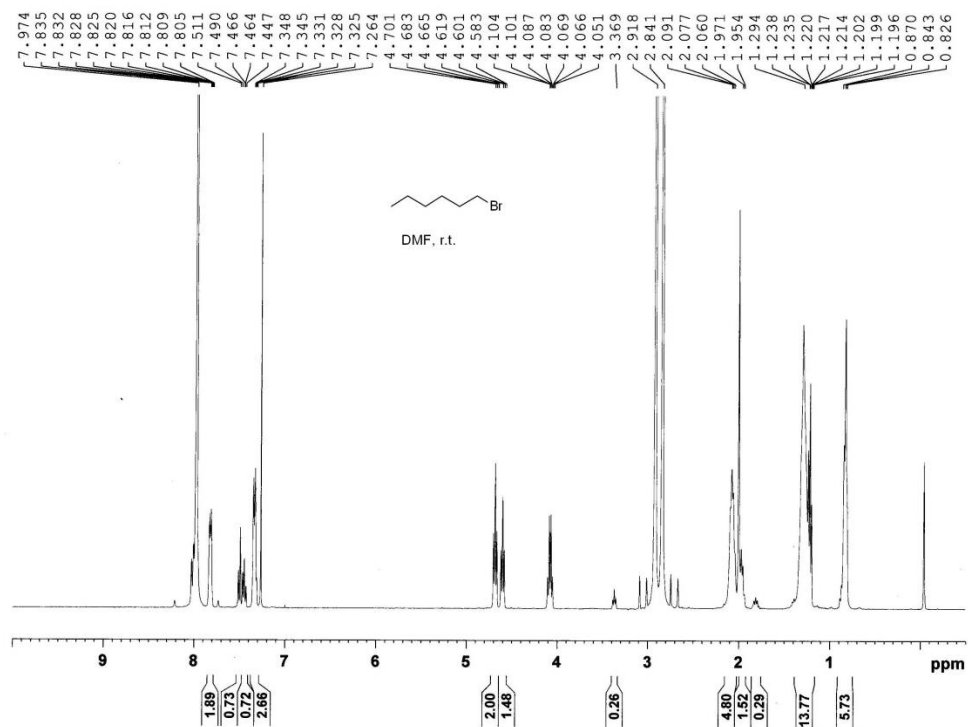
28. 100% DMF



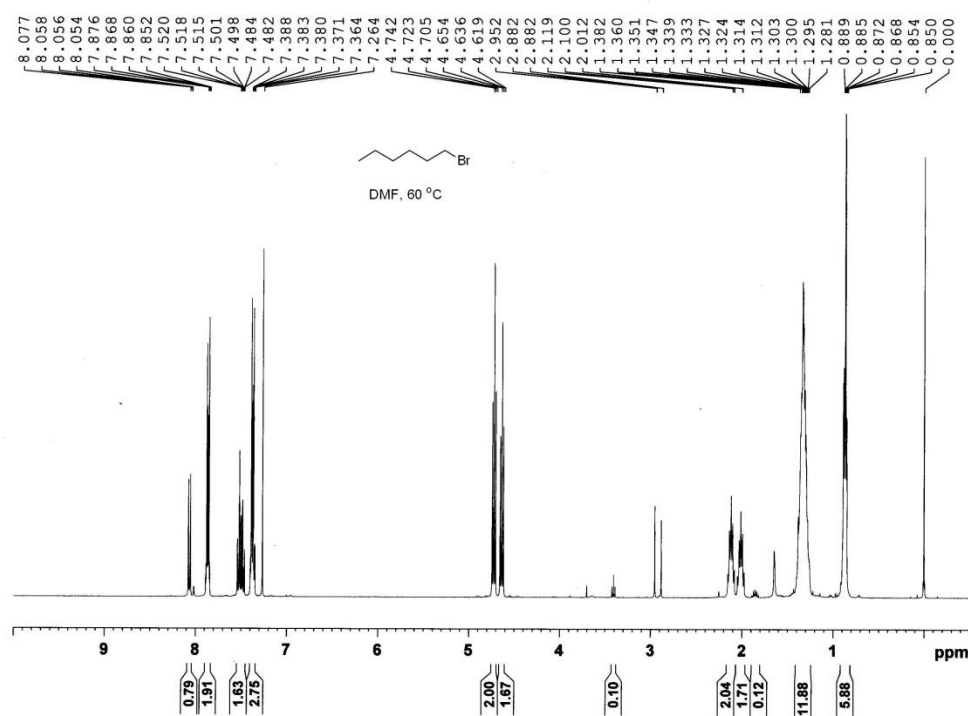
1



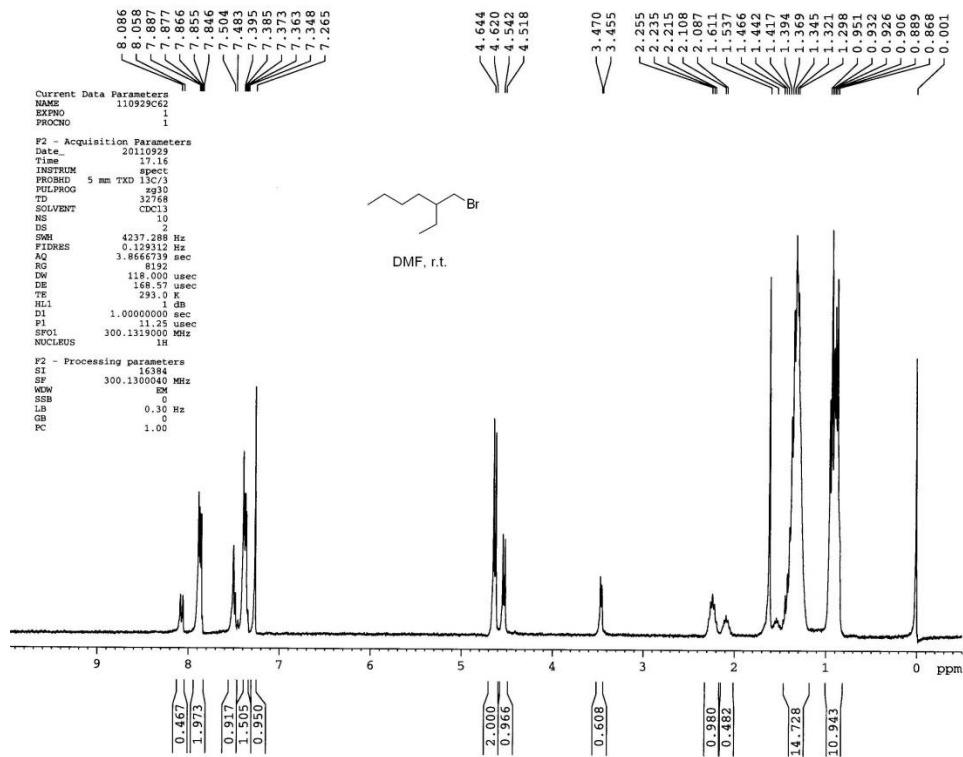
2



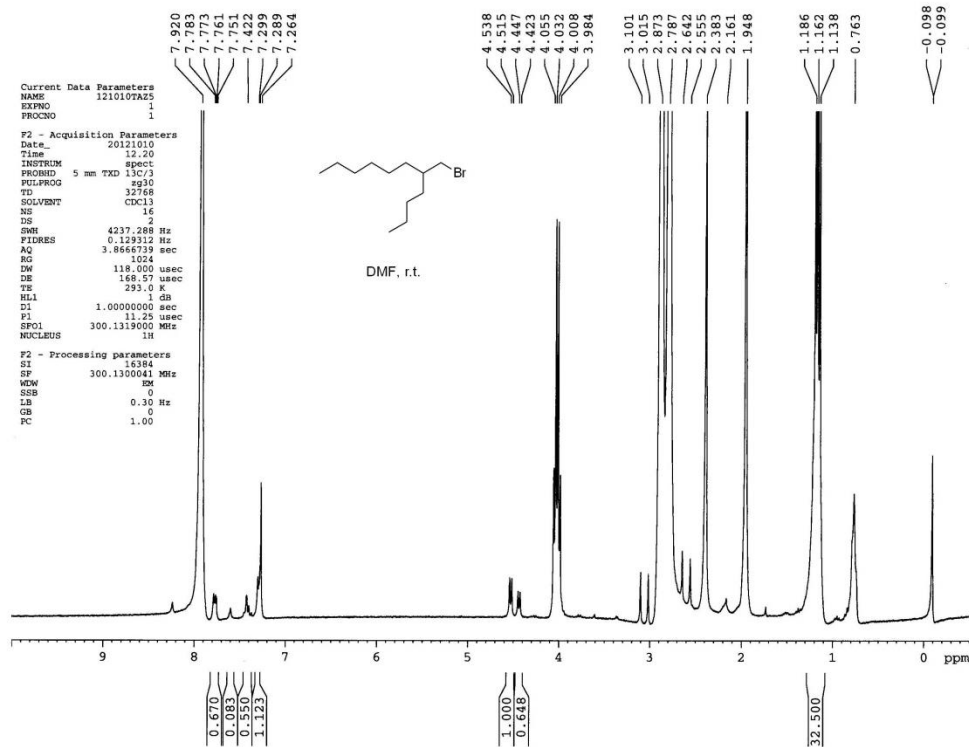
3



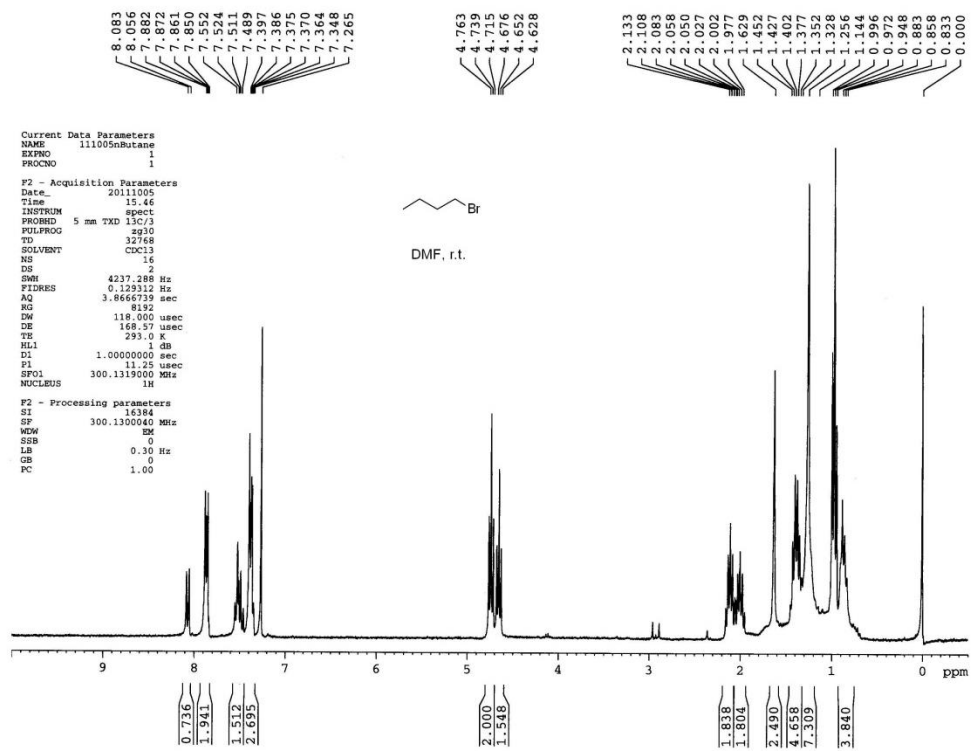
4



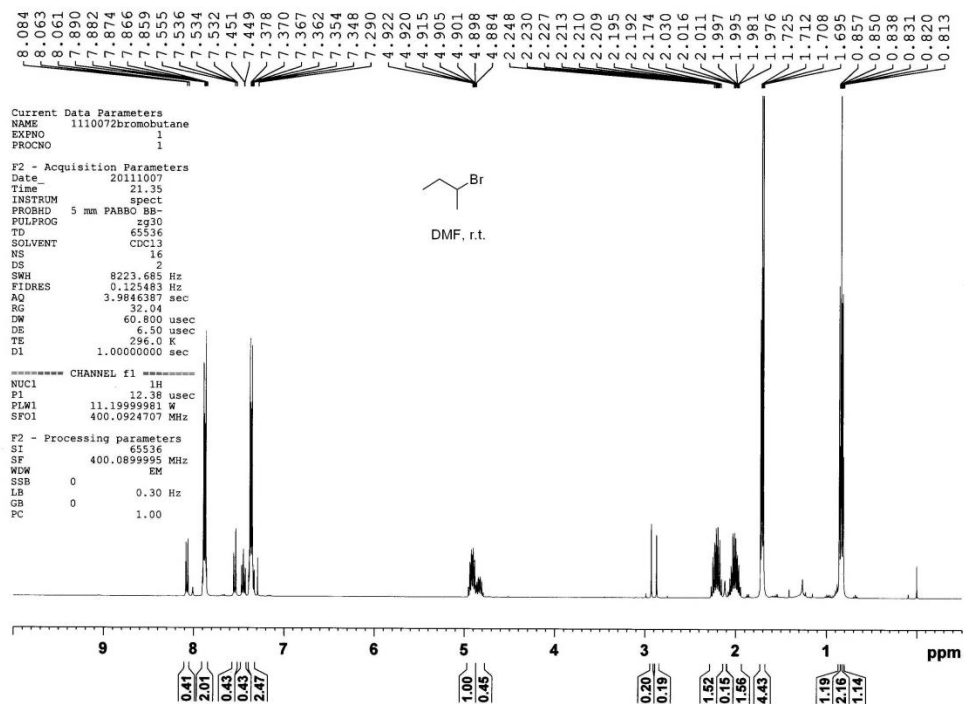
5



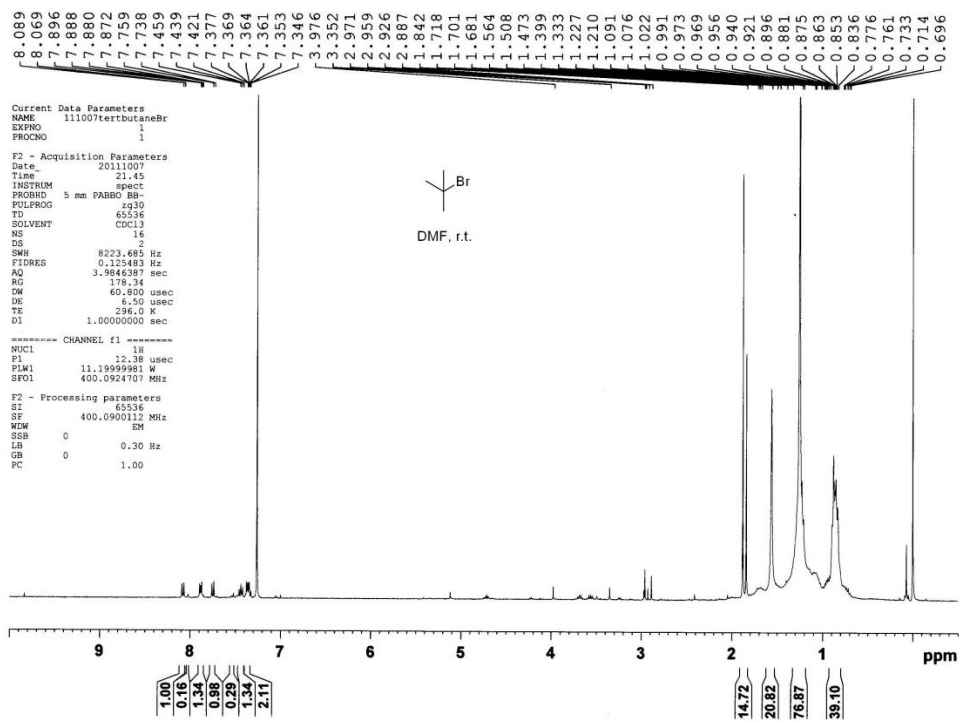
6



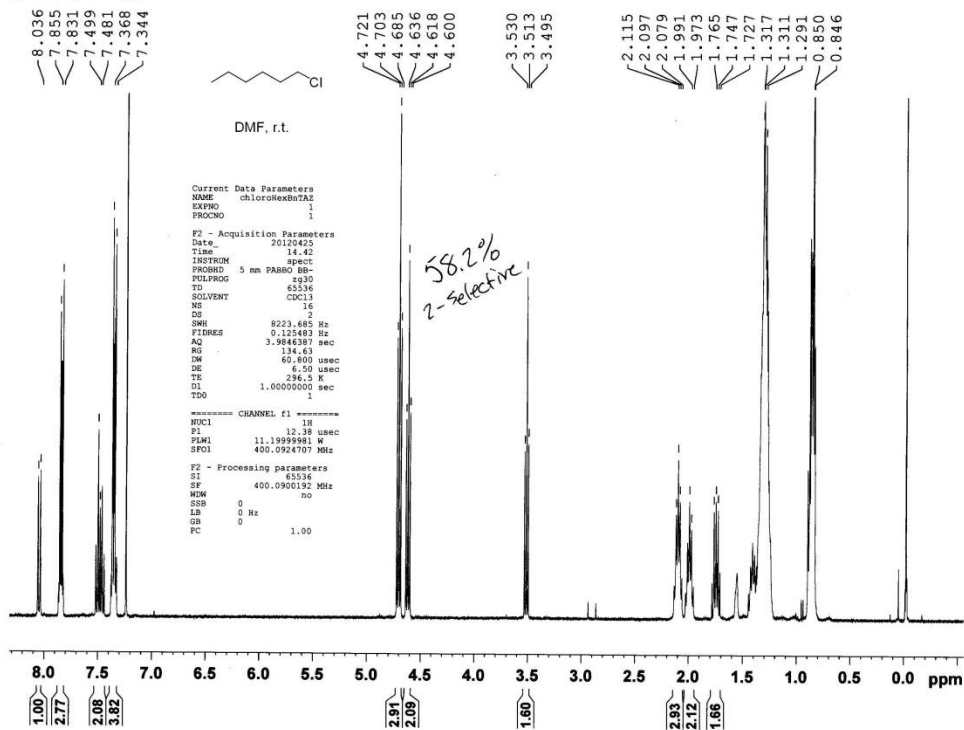
7



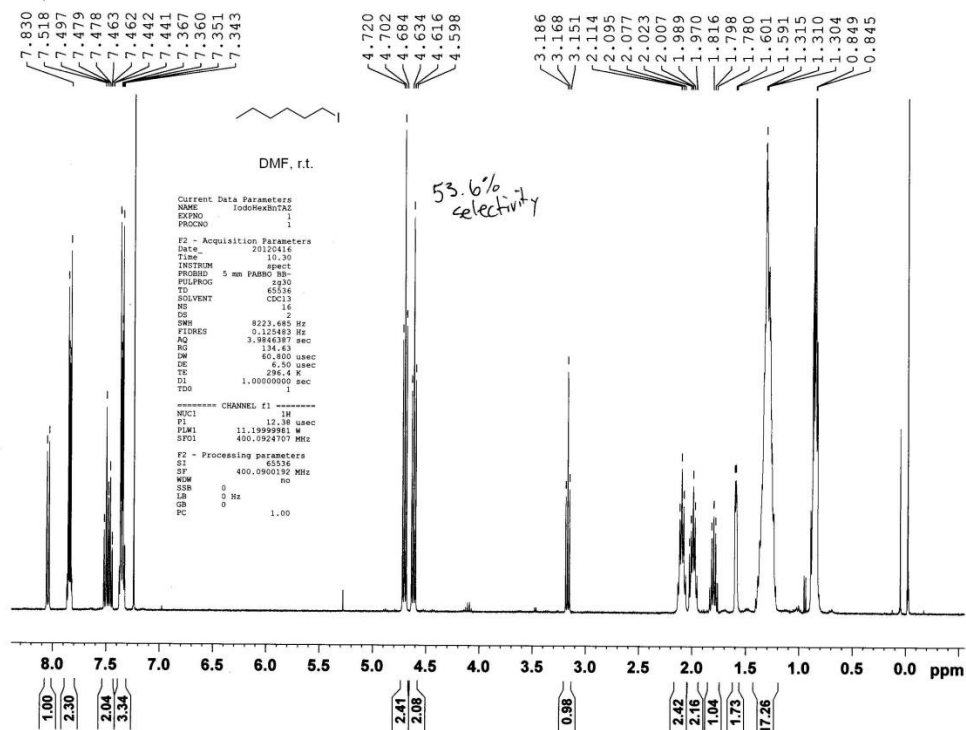
8



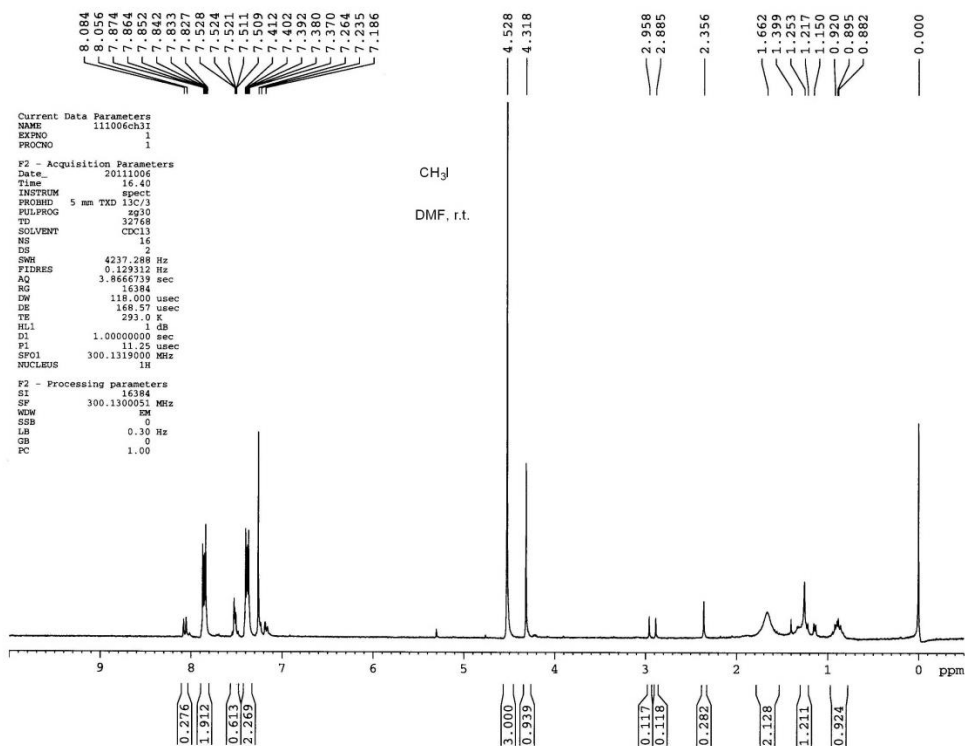
Chlorohexane



Iodobutane

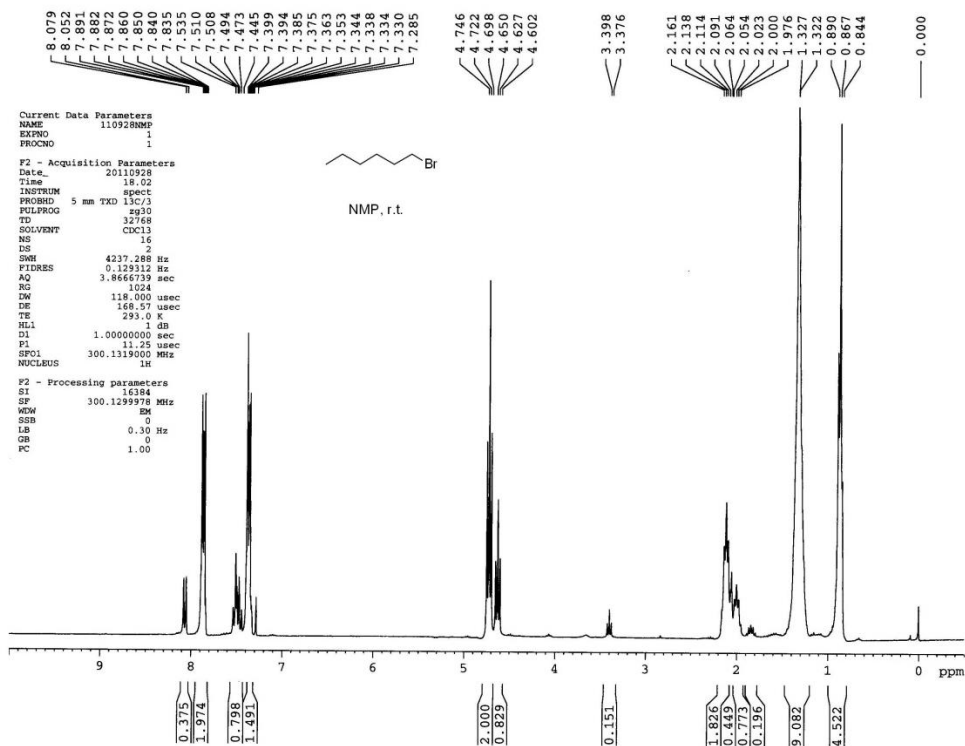


11

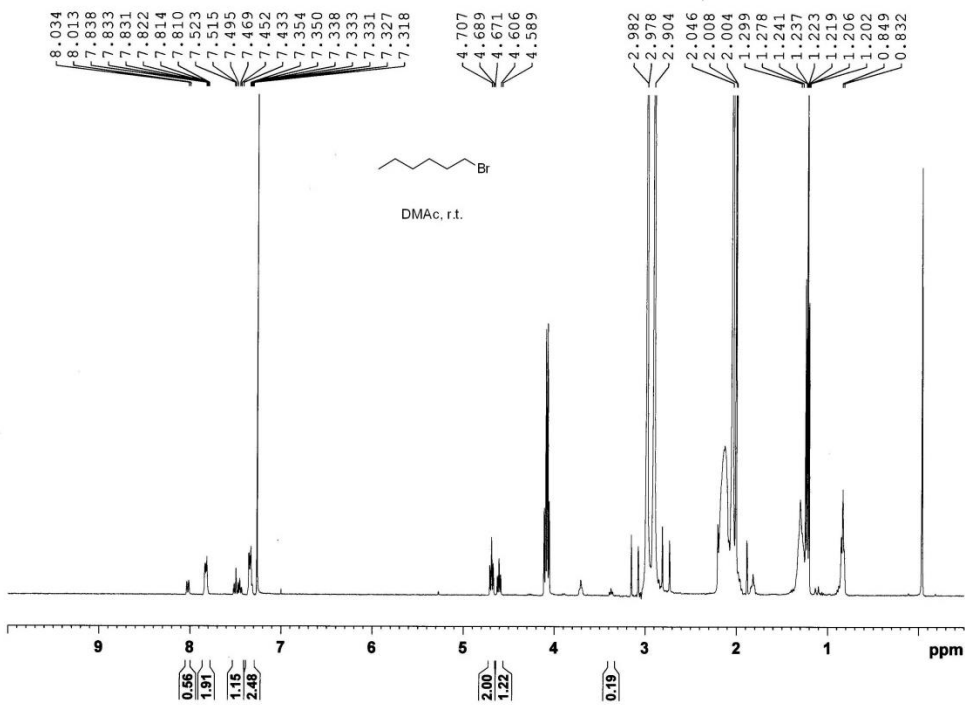


12

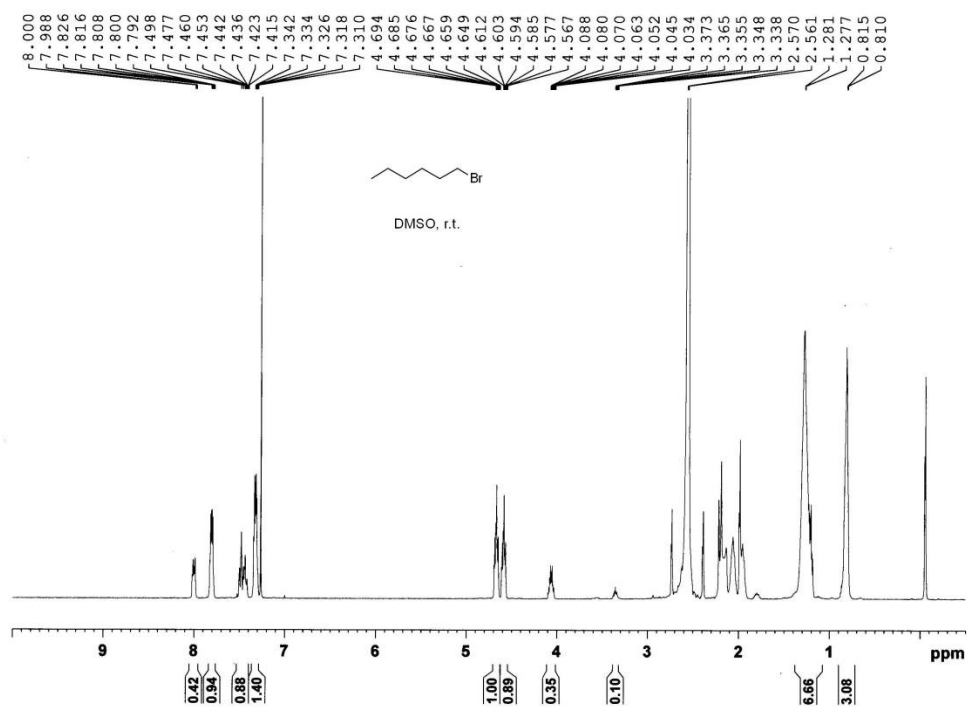




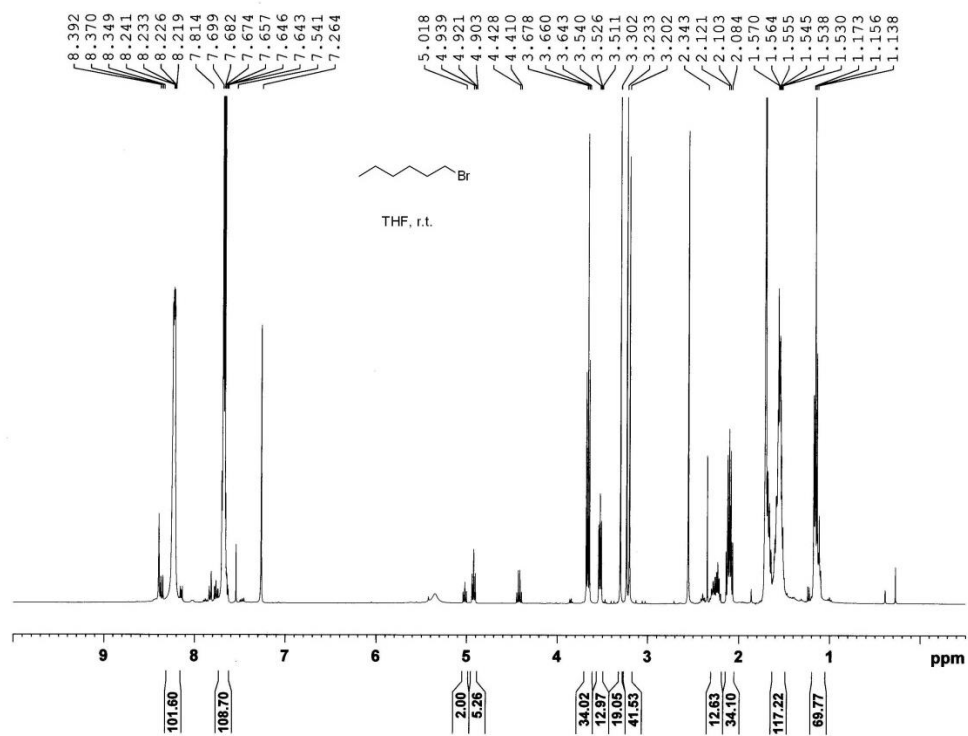
13



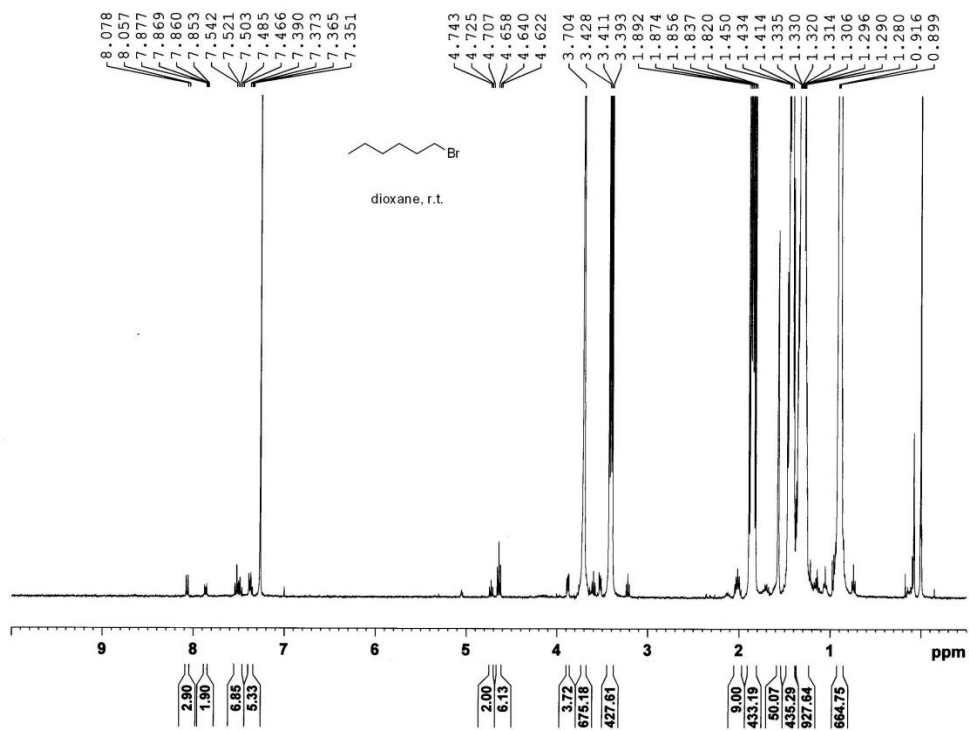
14



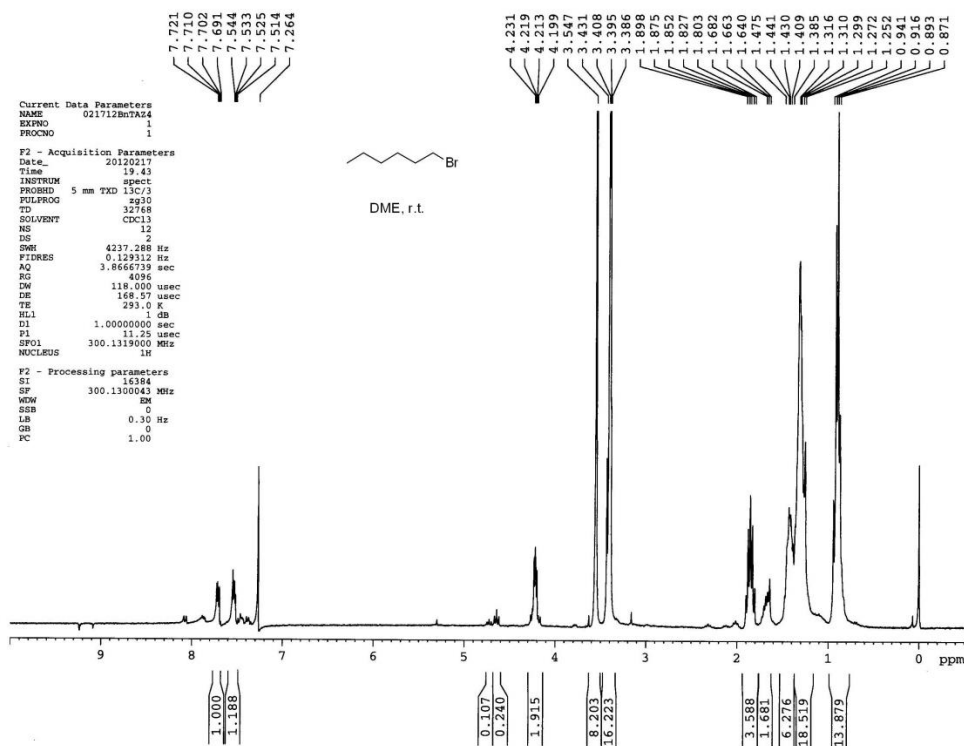
15



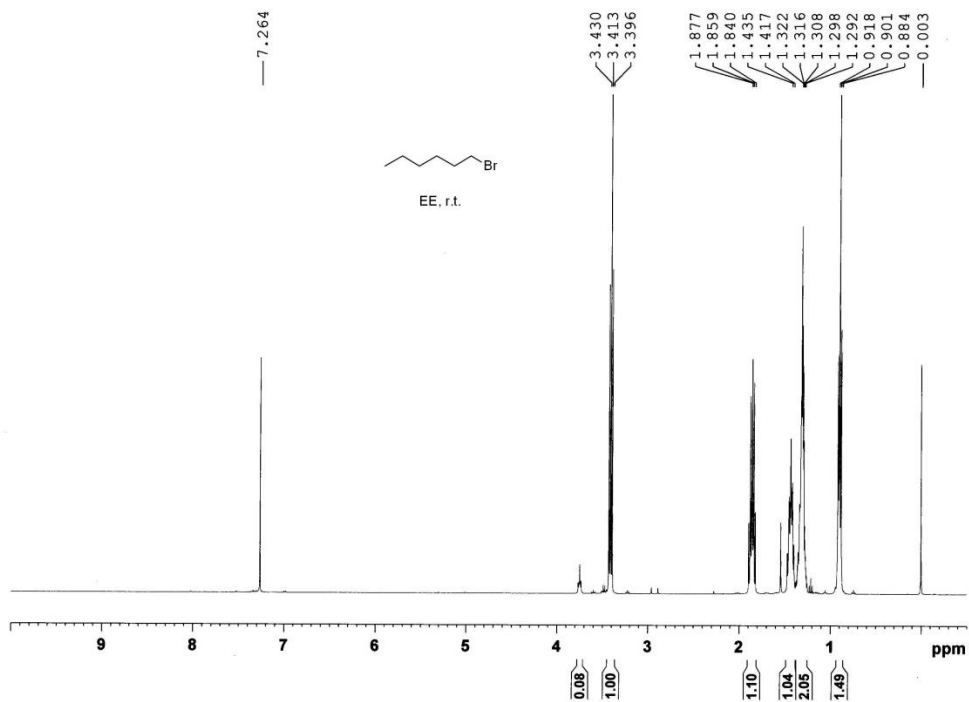
16



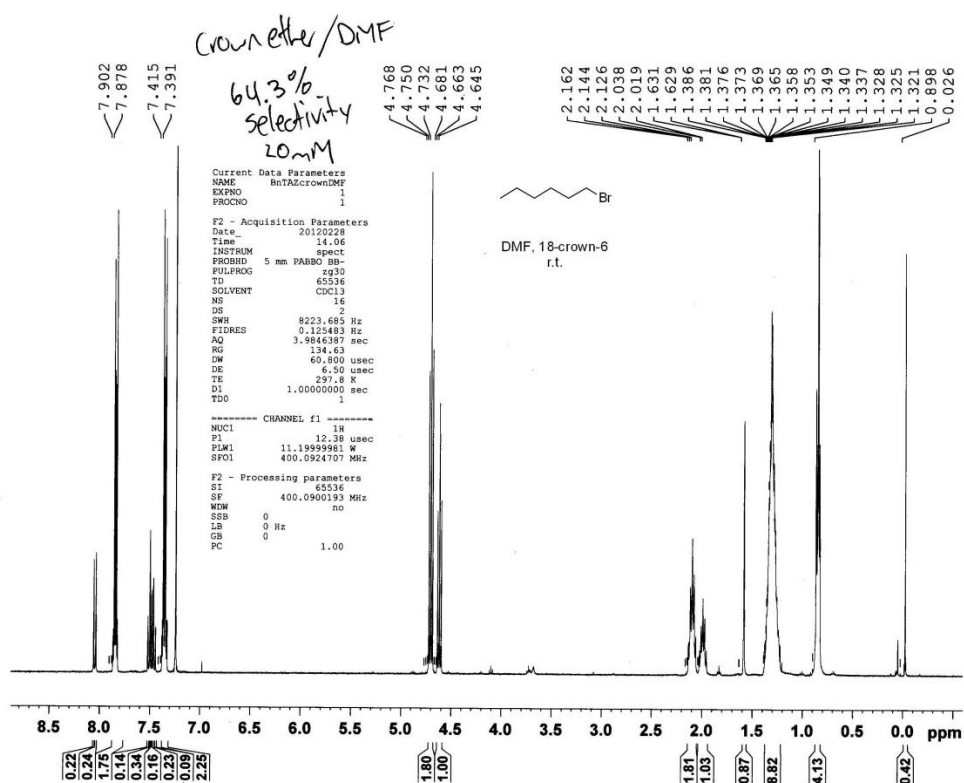
17



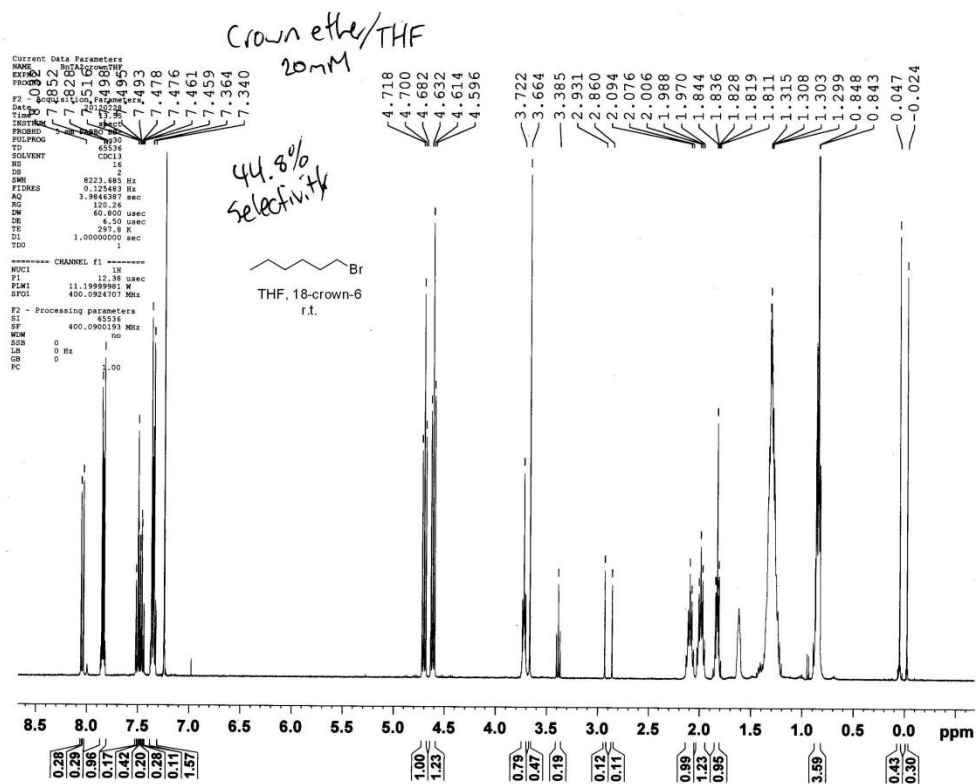
18



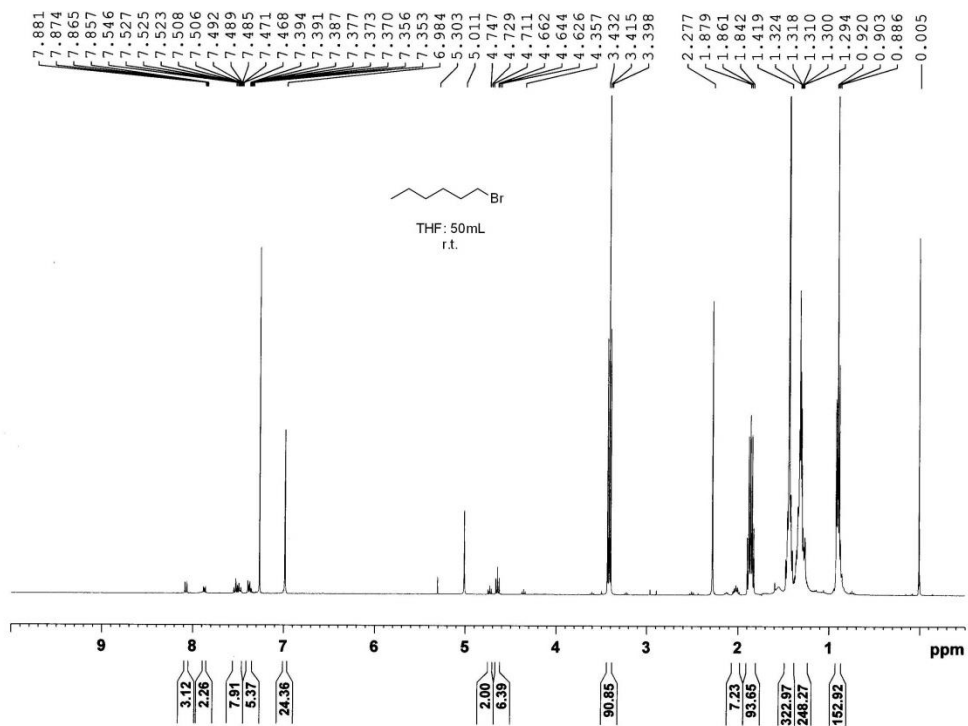
19



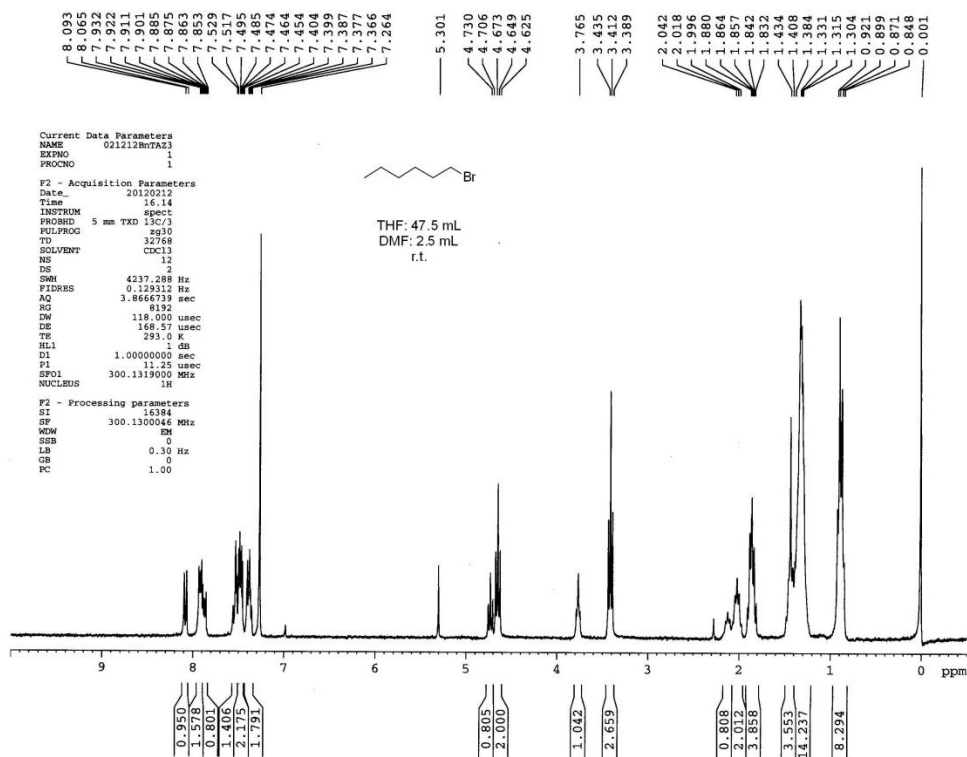
20



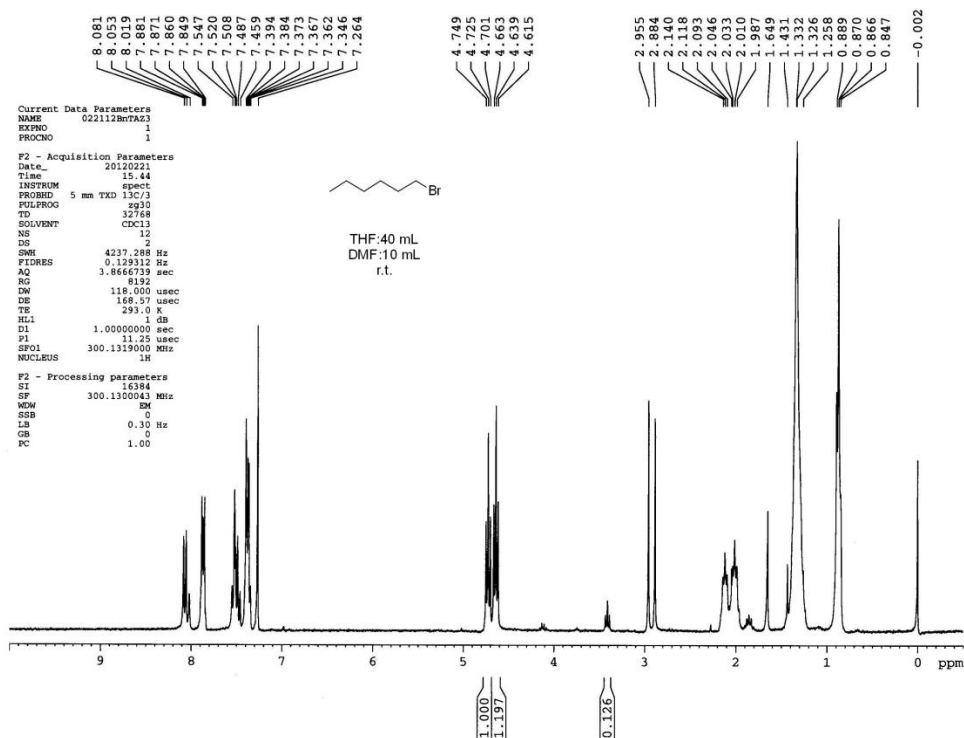
21



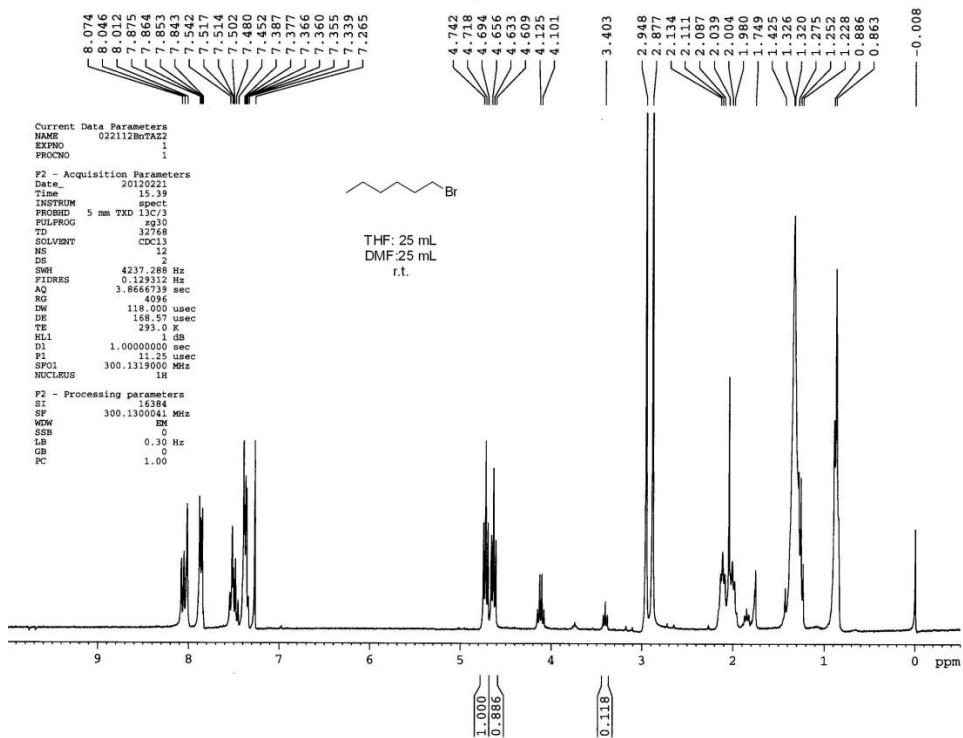
22



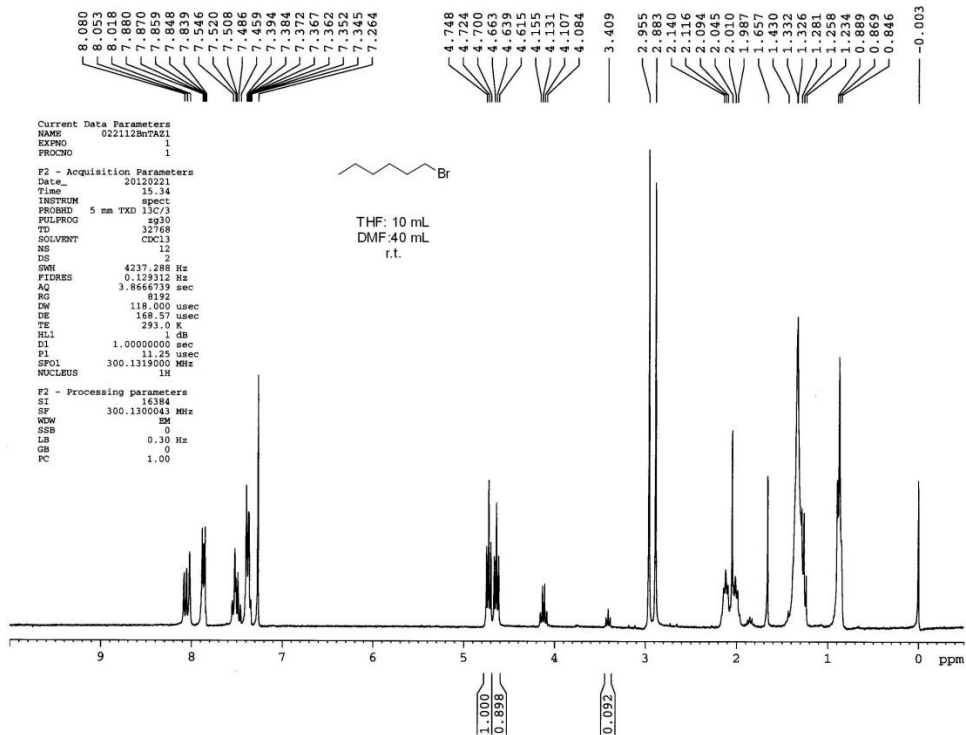
23



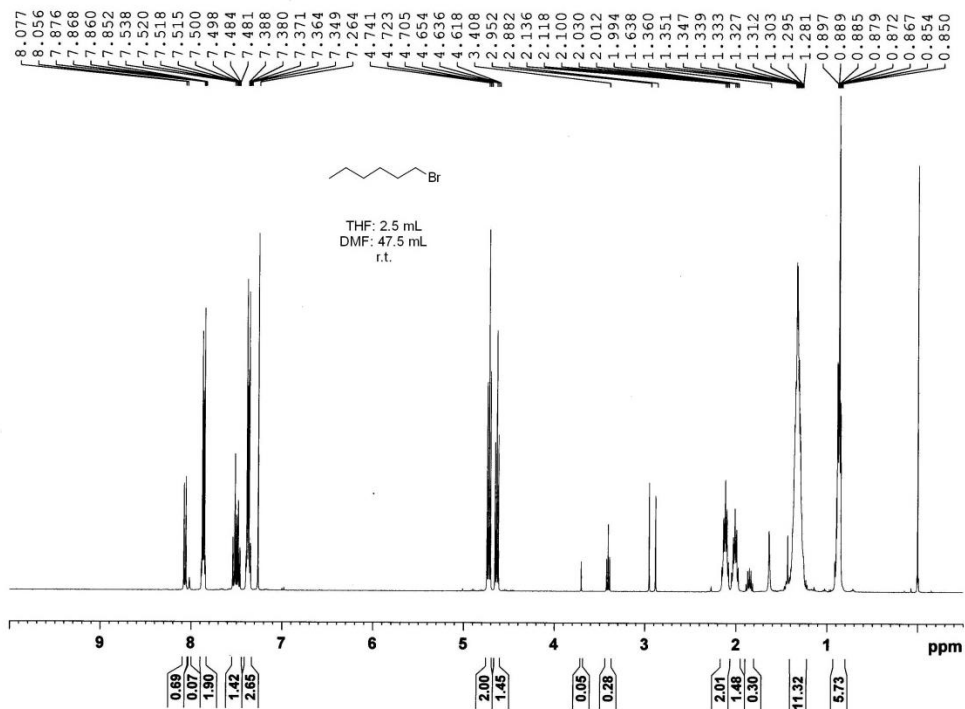
24



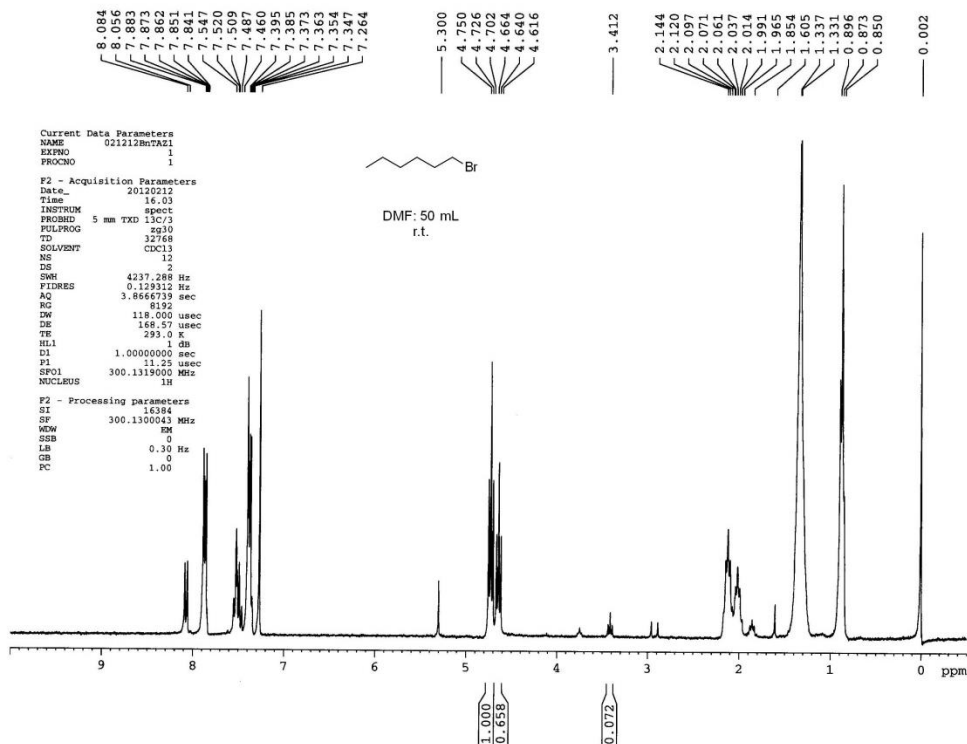
25



26



27

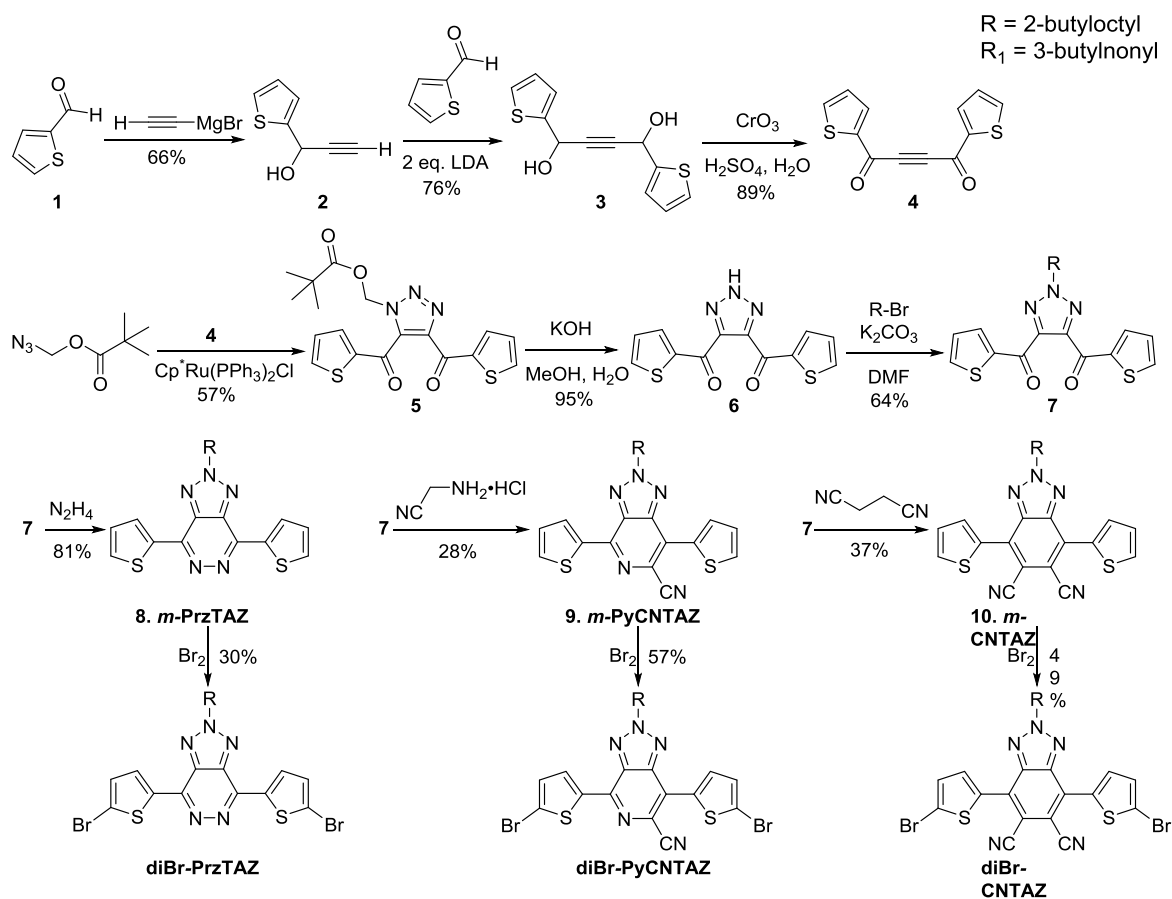


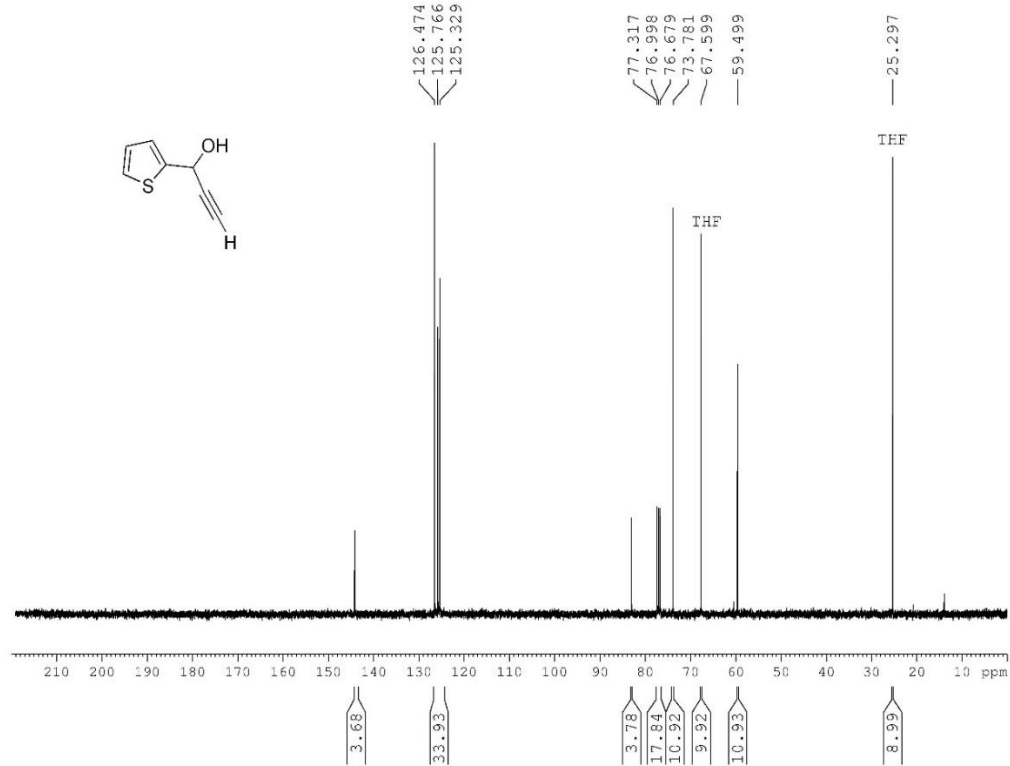
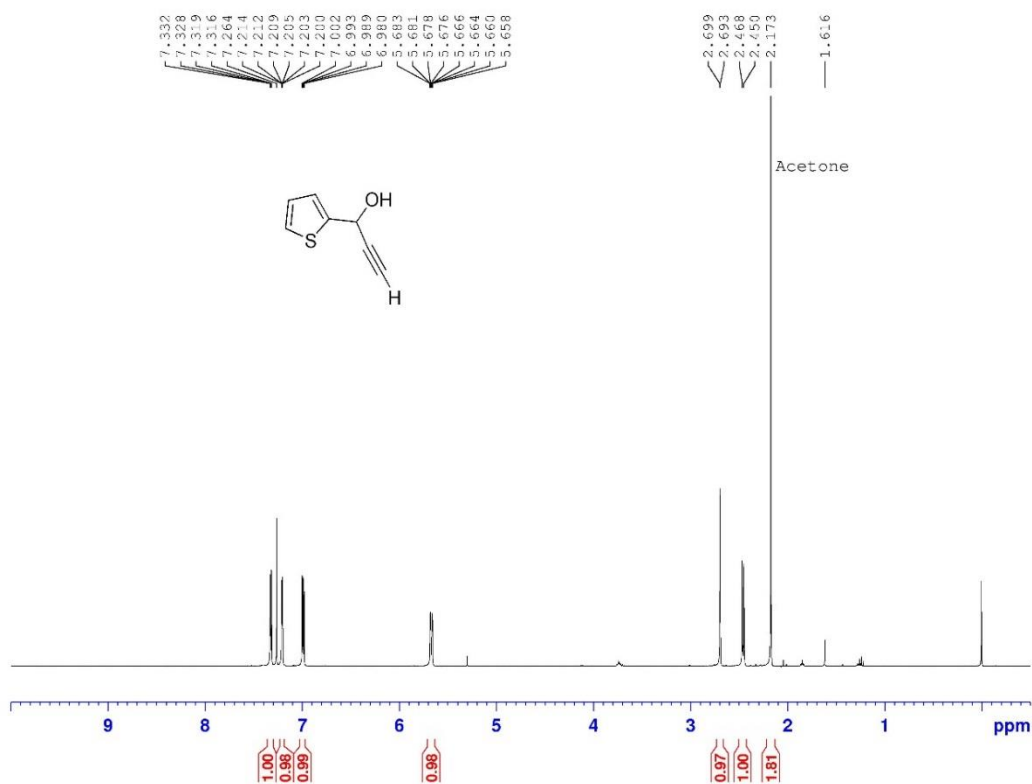
28

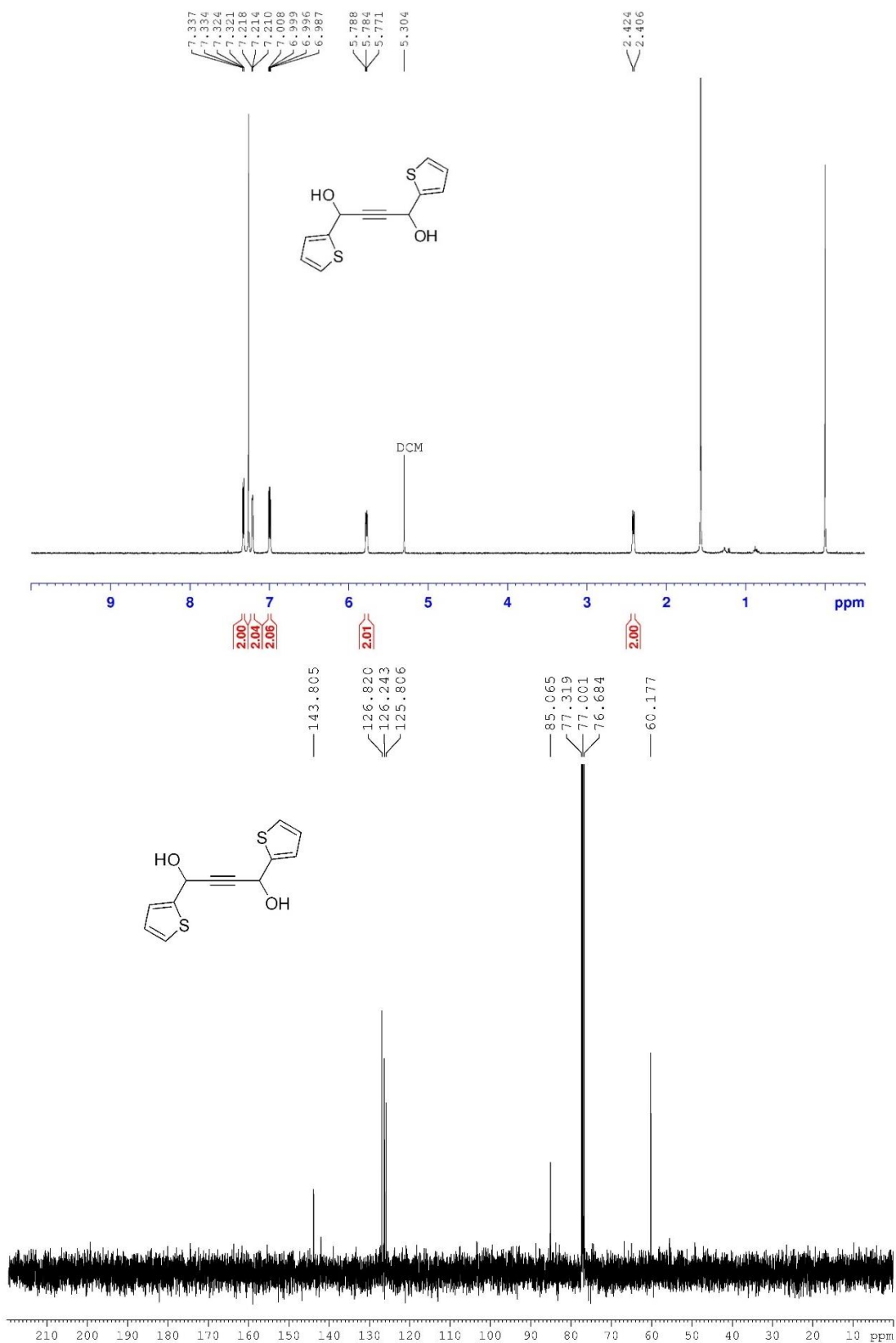


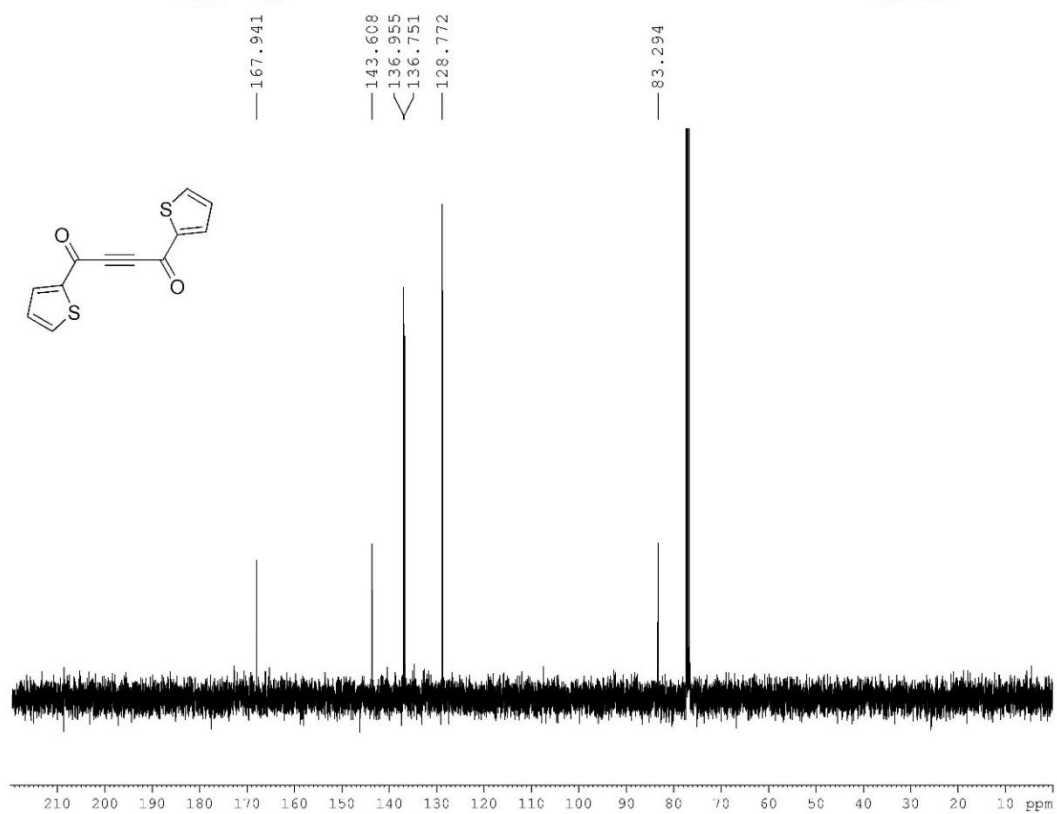
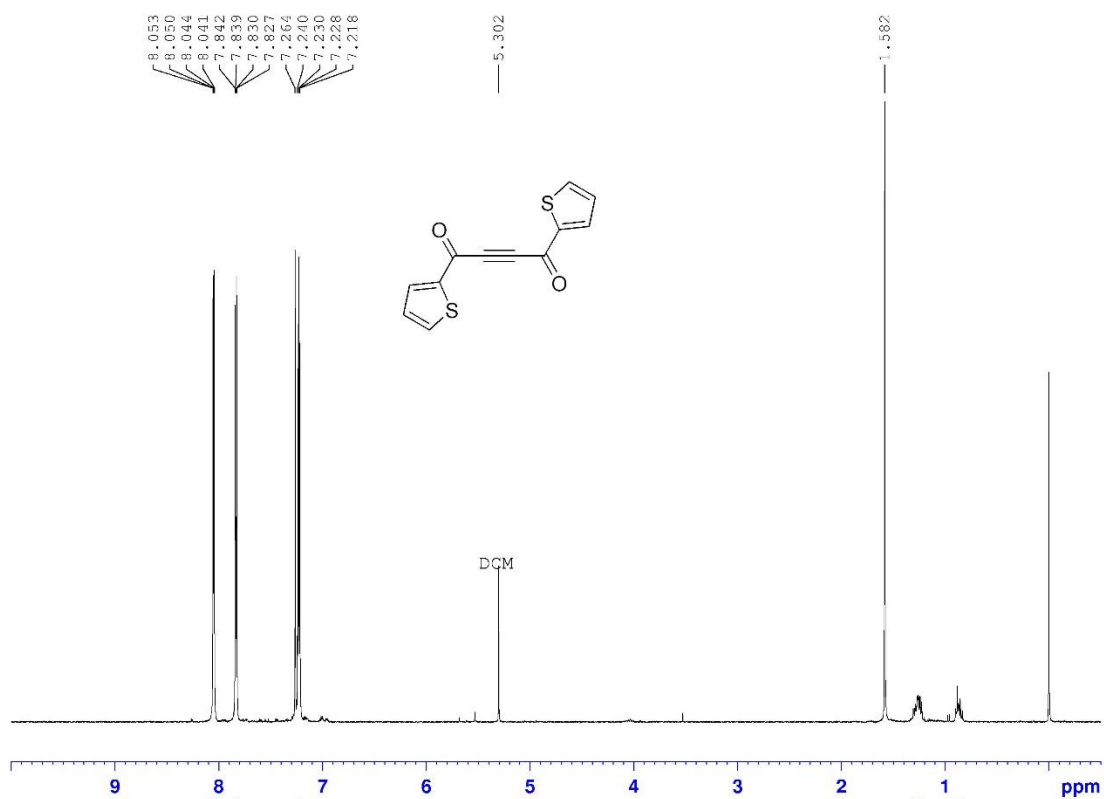
# APPENDIX III: NMR SPECTRA OF INTERMEDIATES, MONOMERS AND POLYMERS IN CHAPTER 5

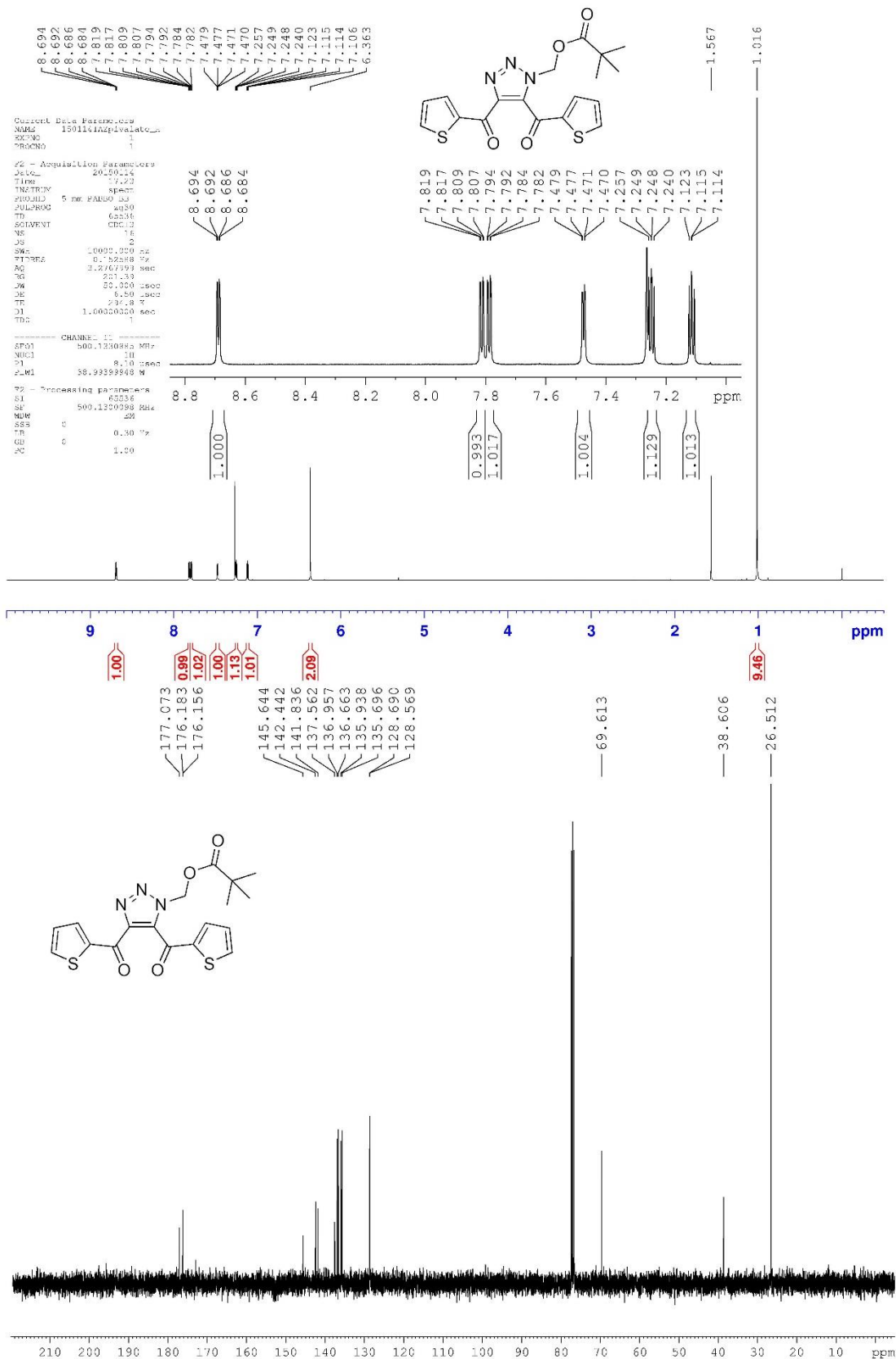
## Reaction Scheme

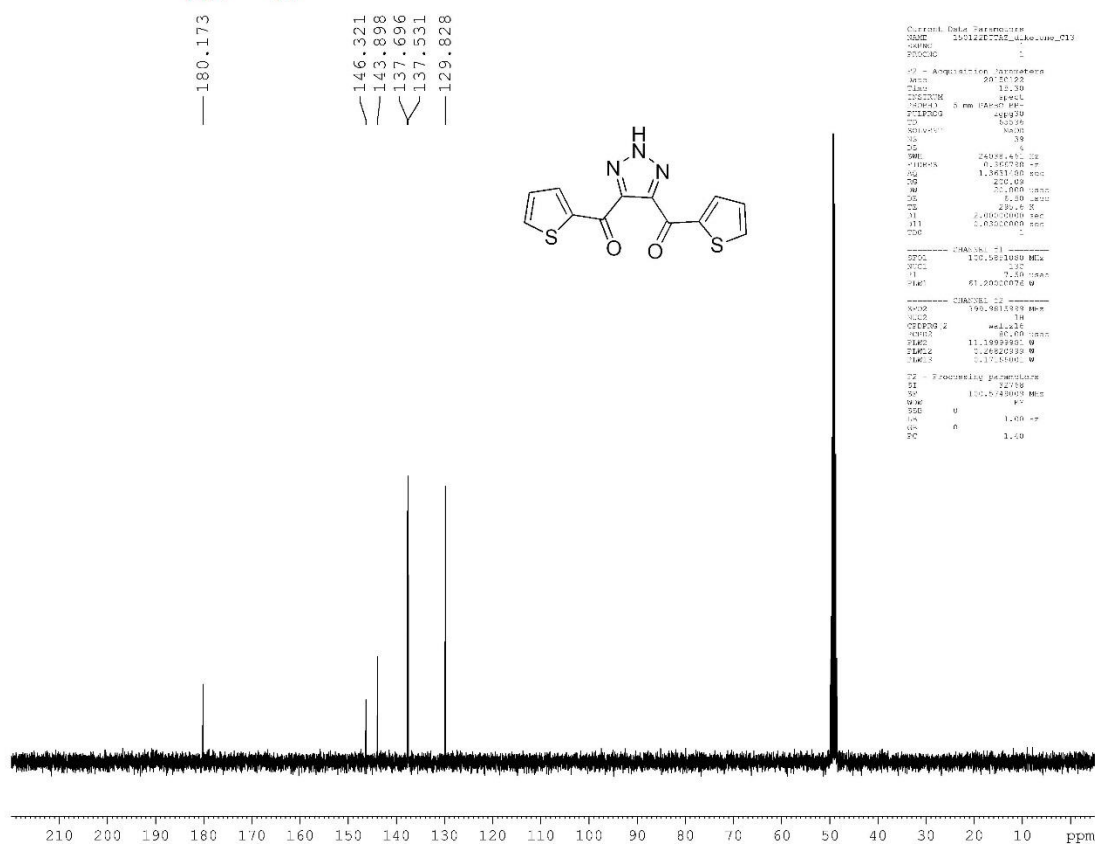
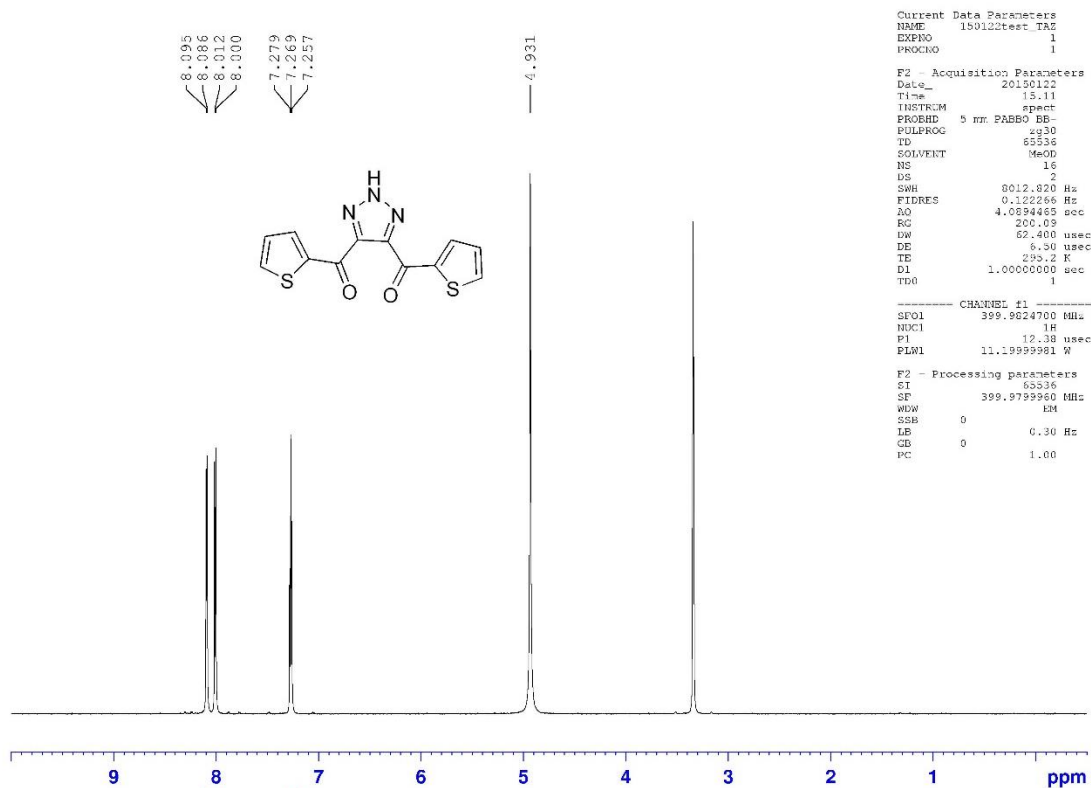


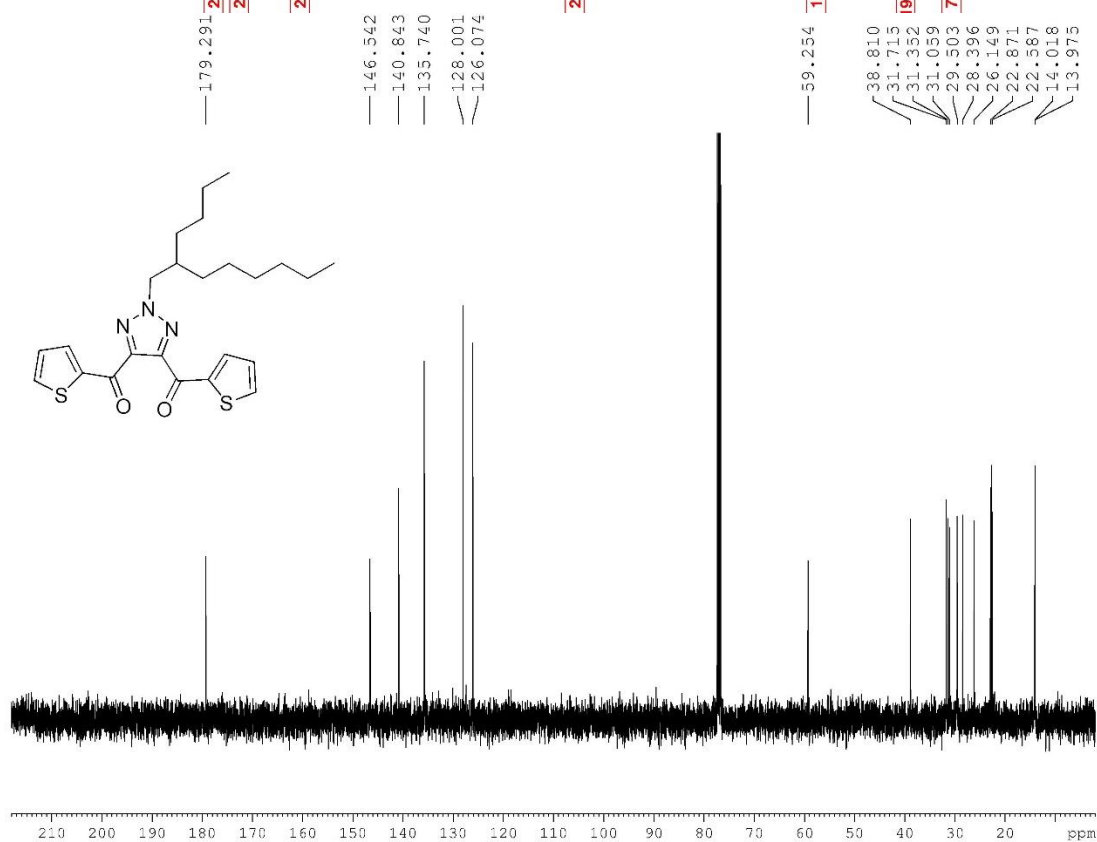
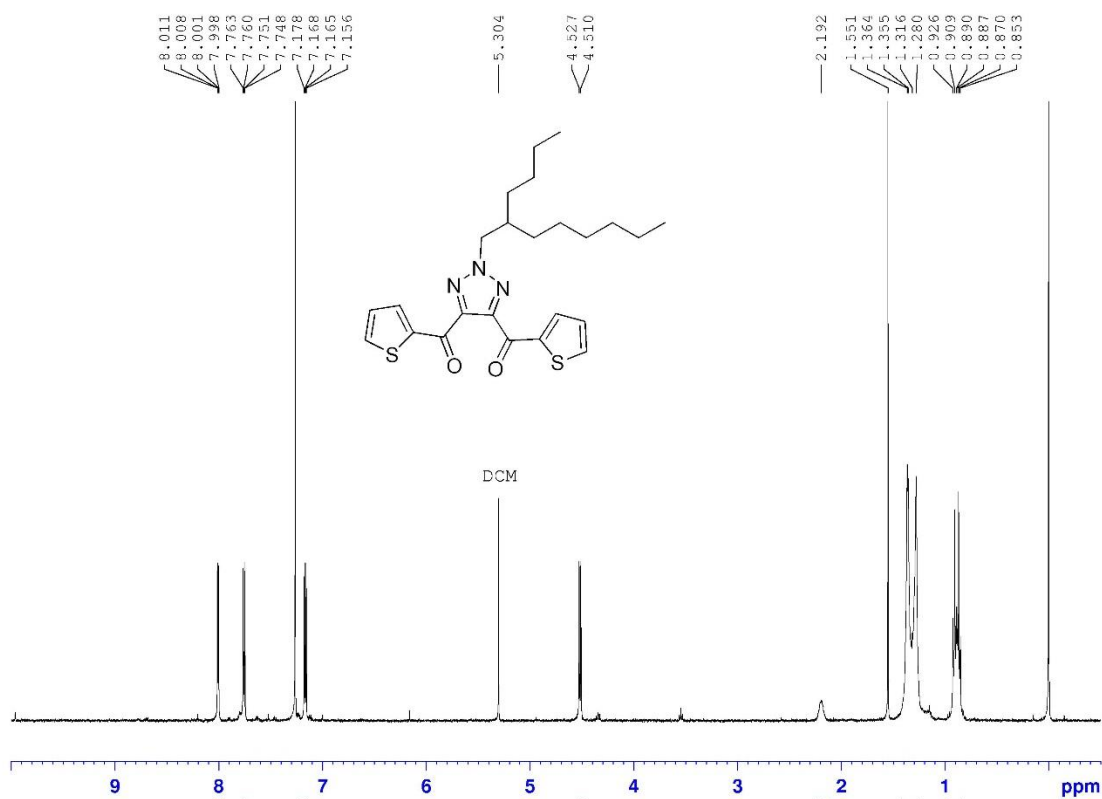


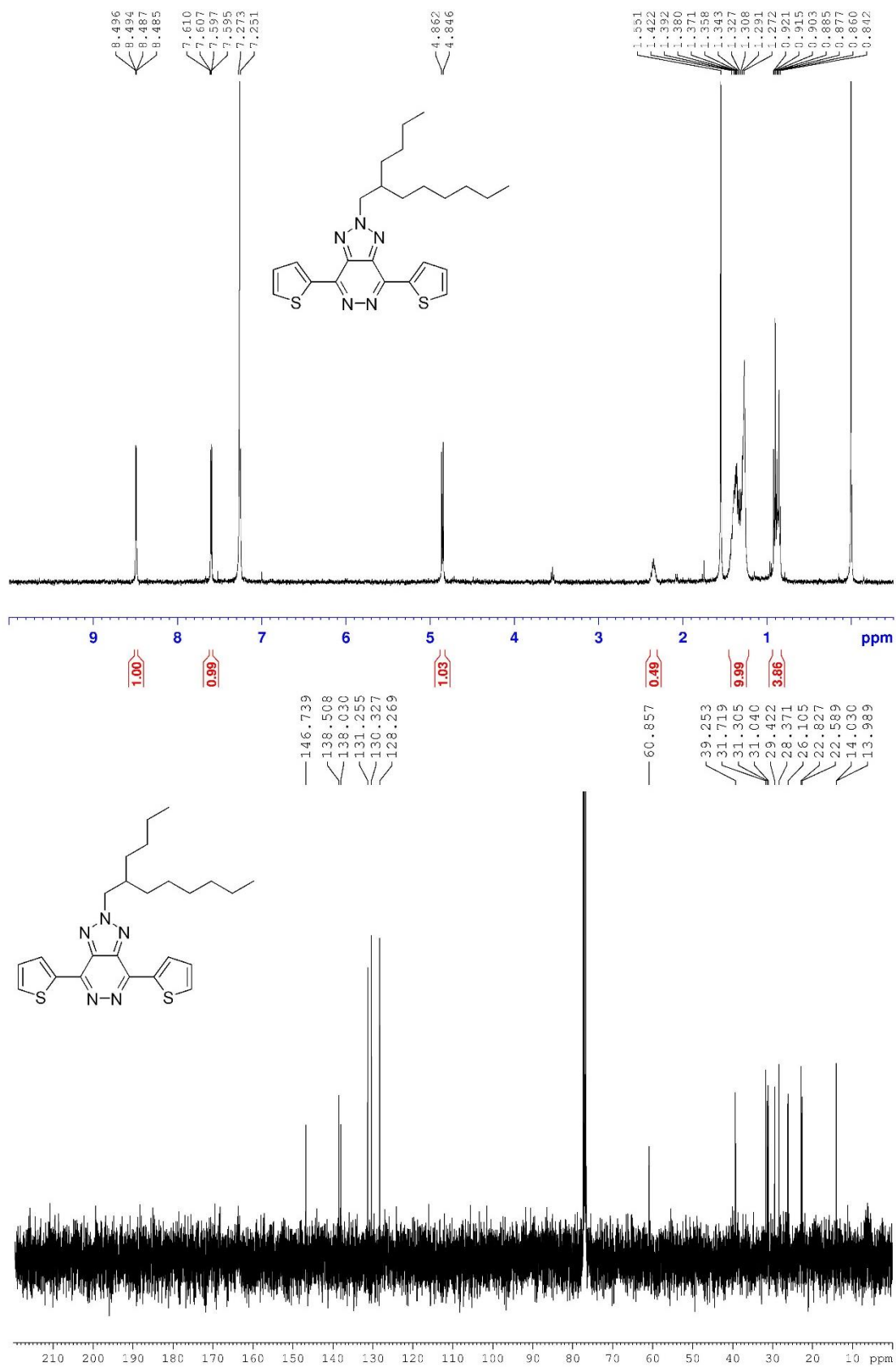




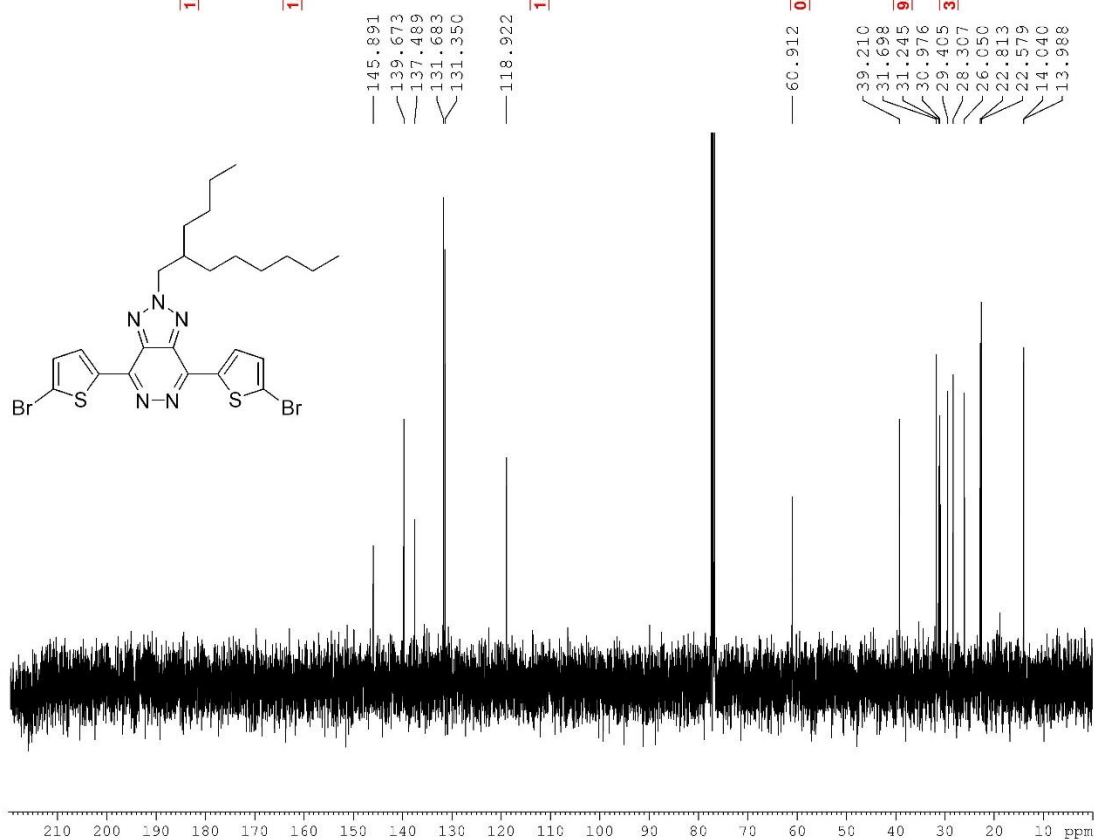
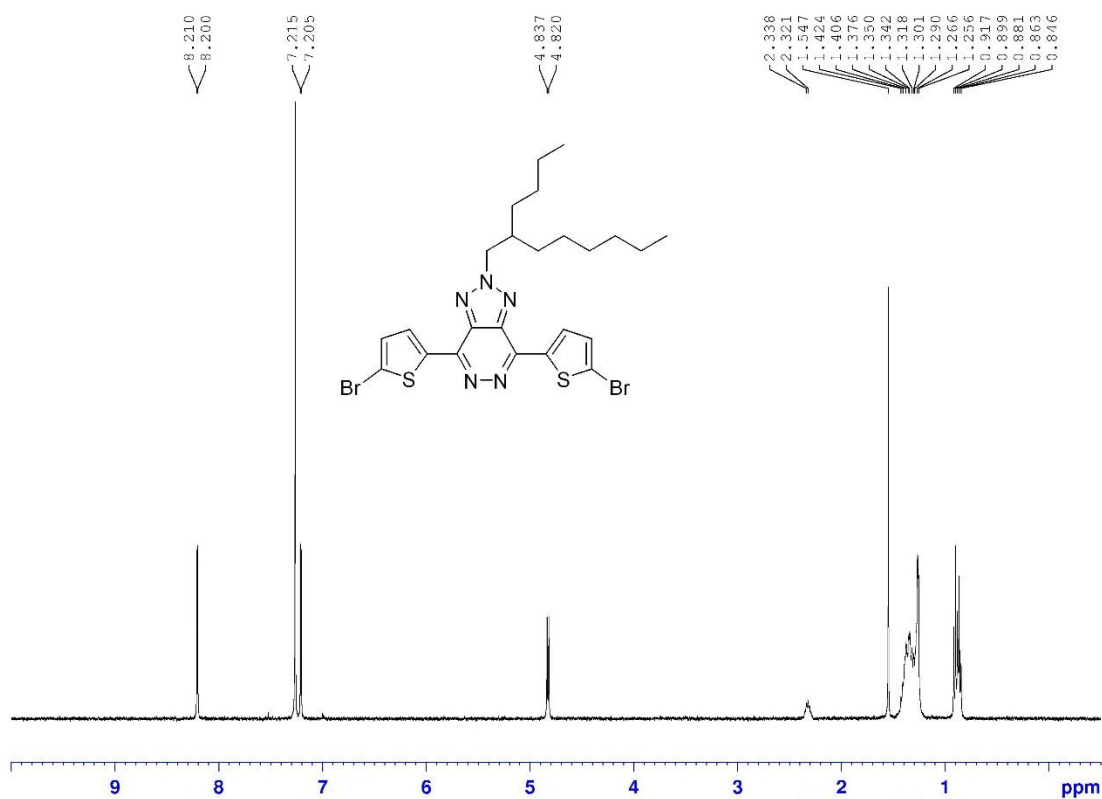


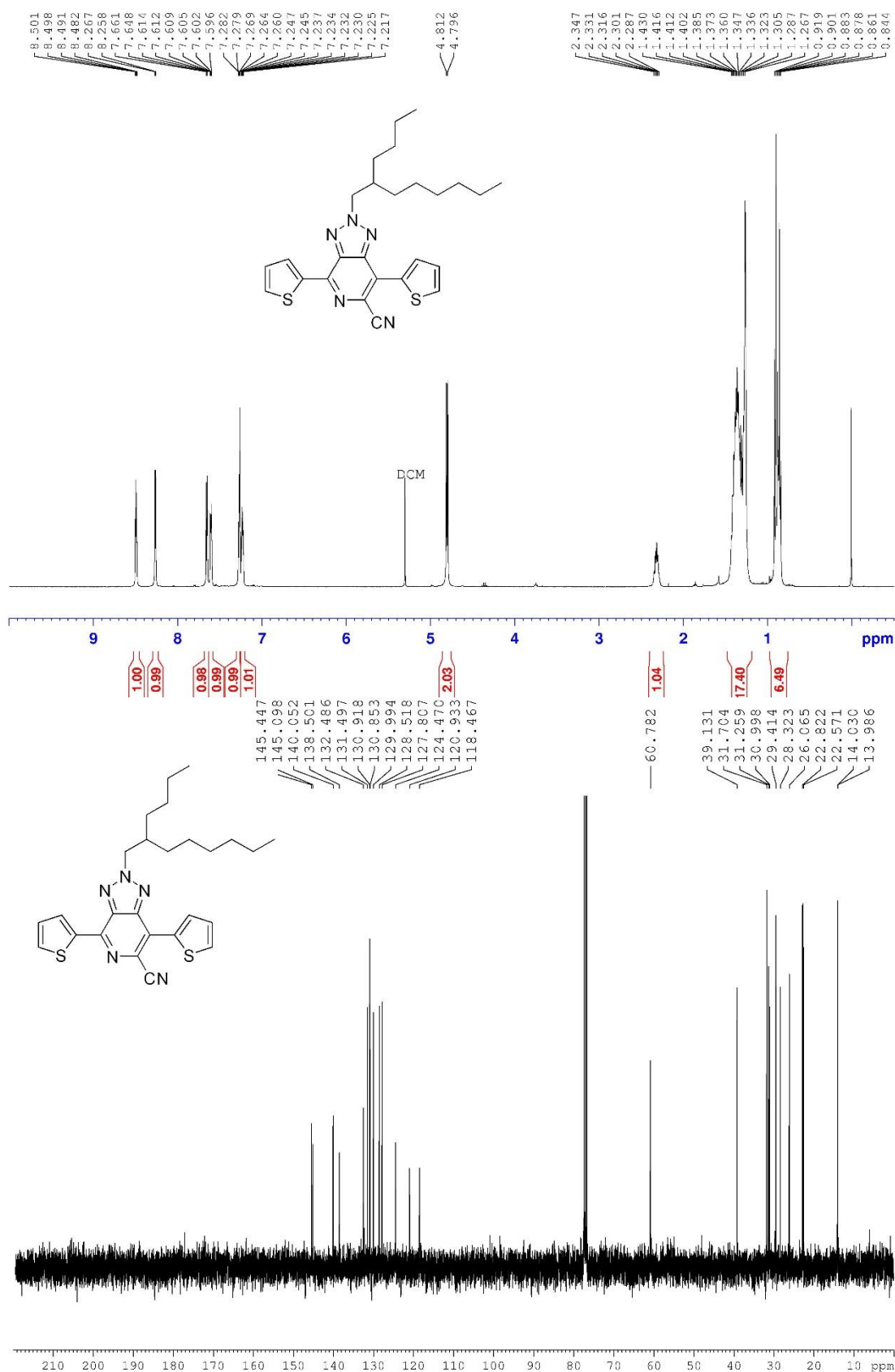


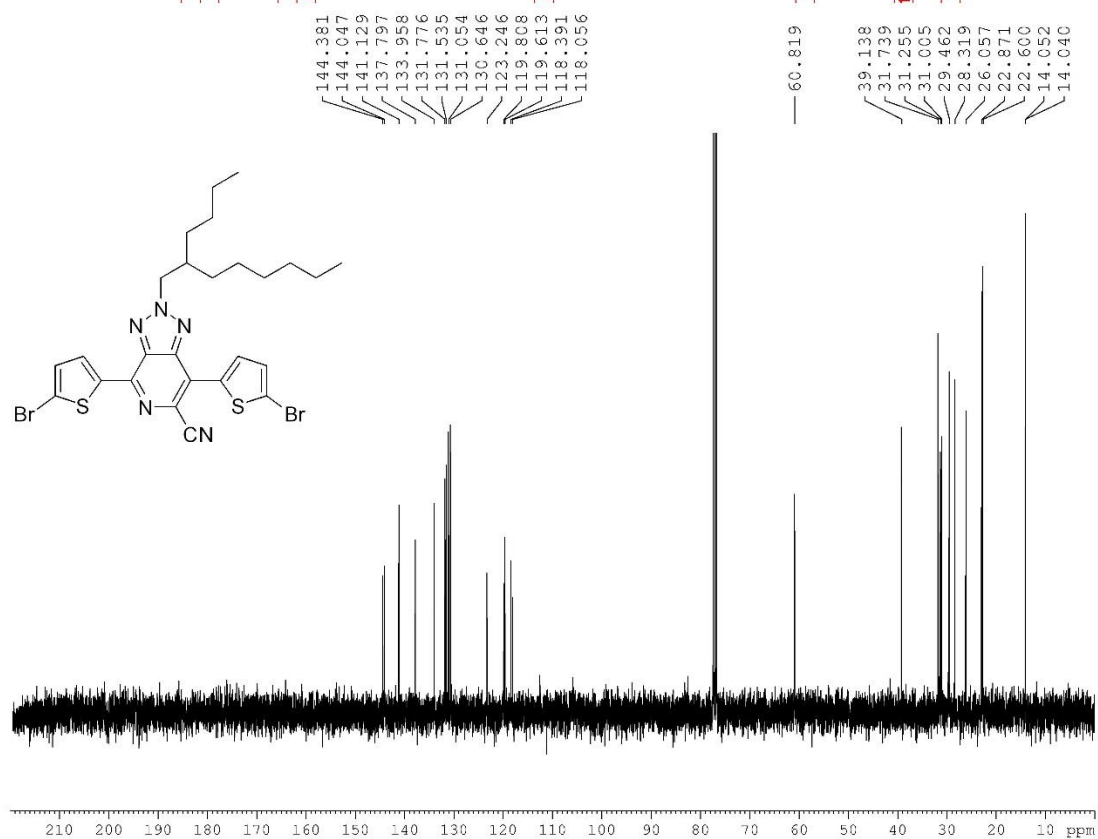
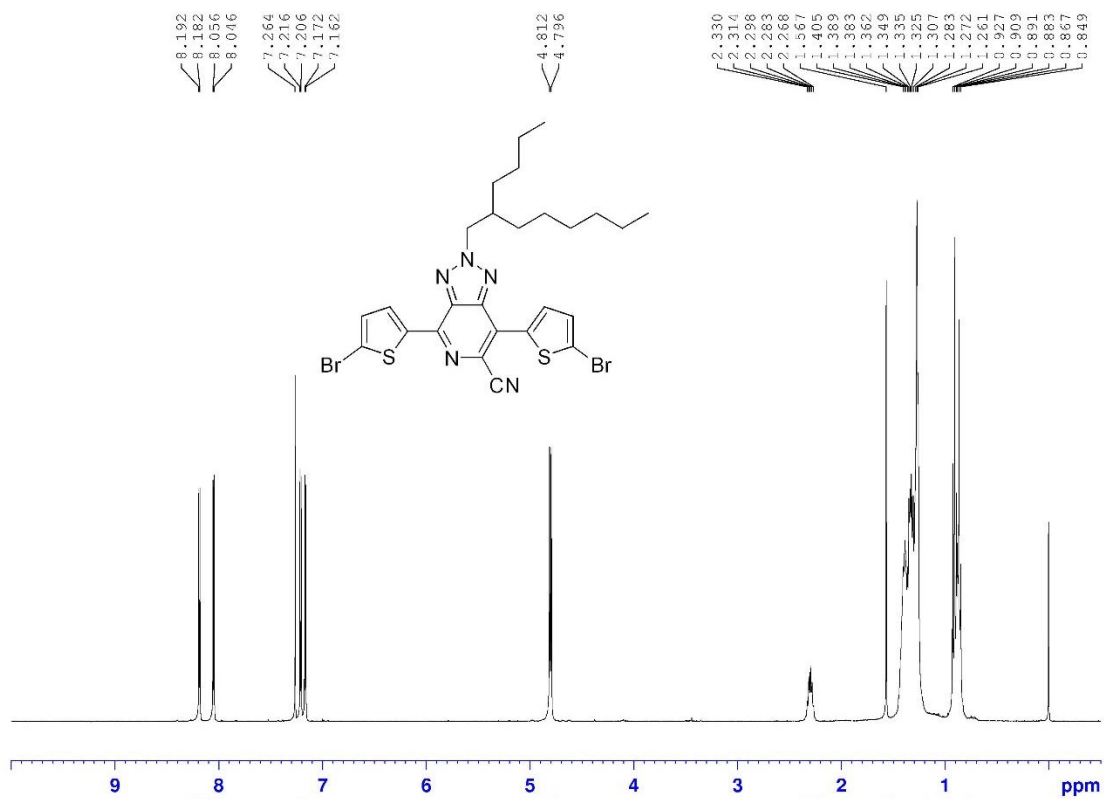


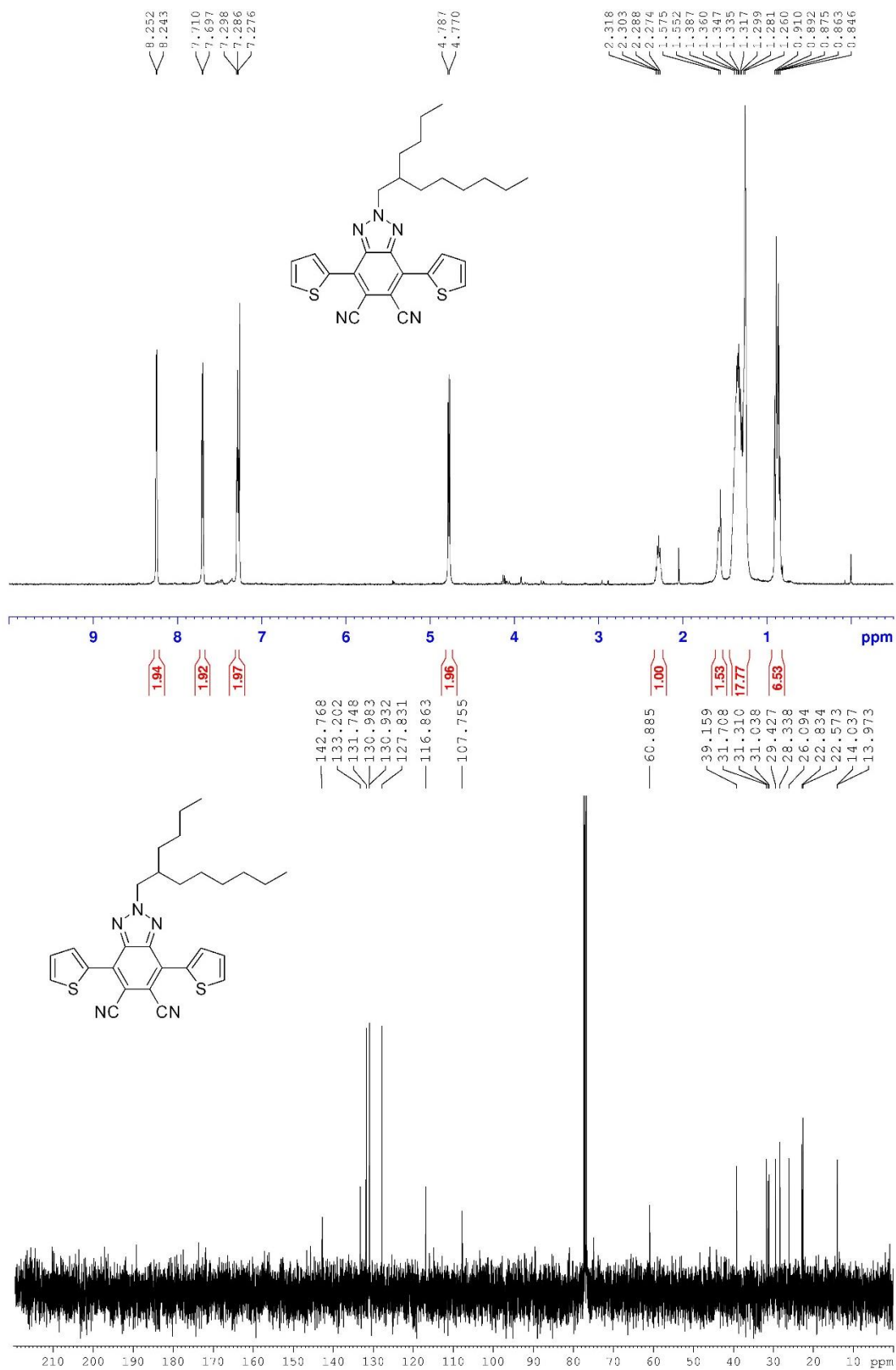


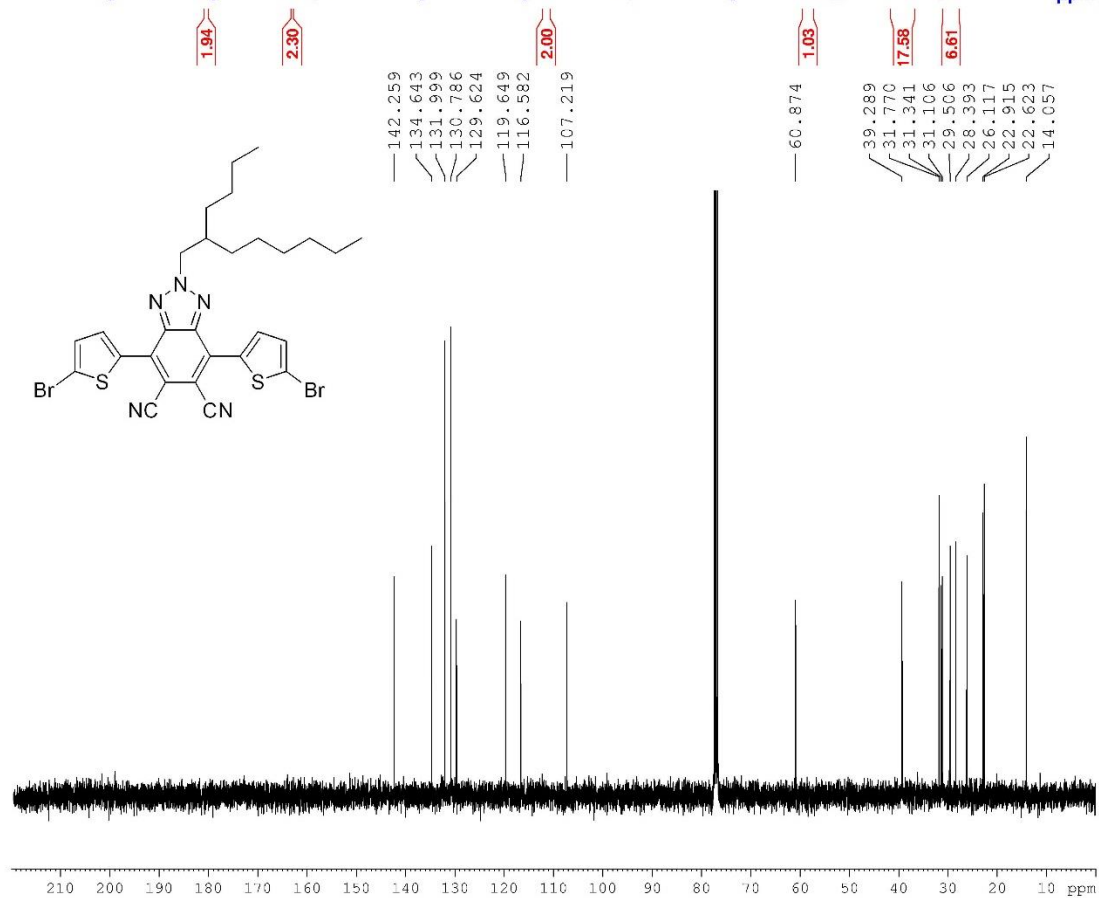
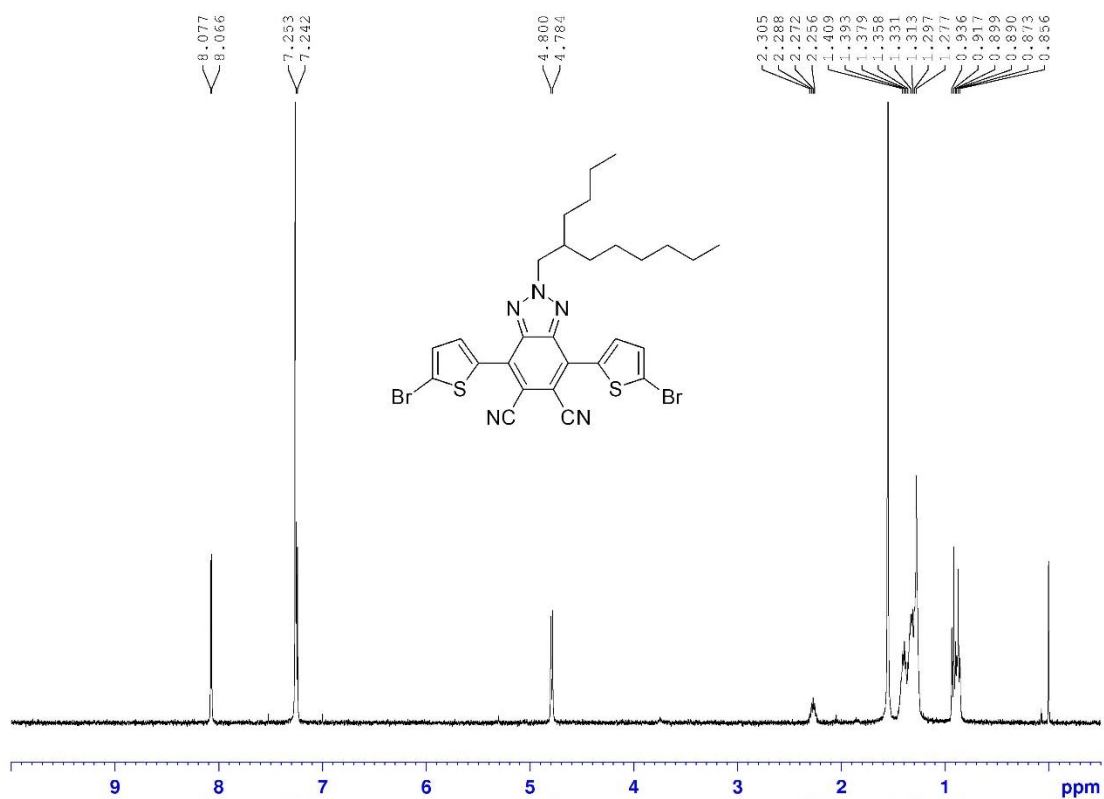


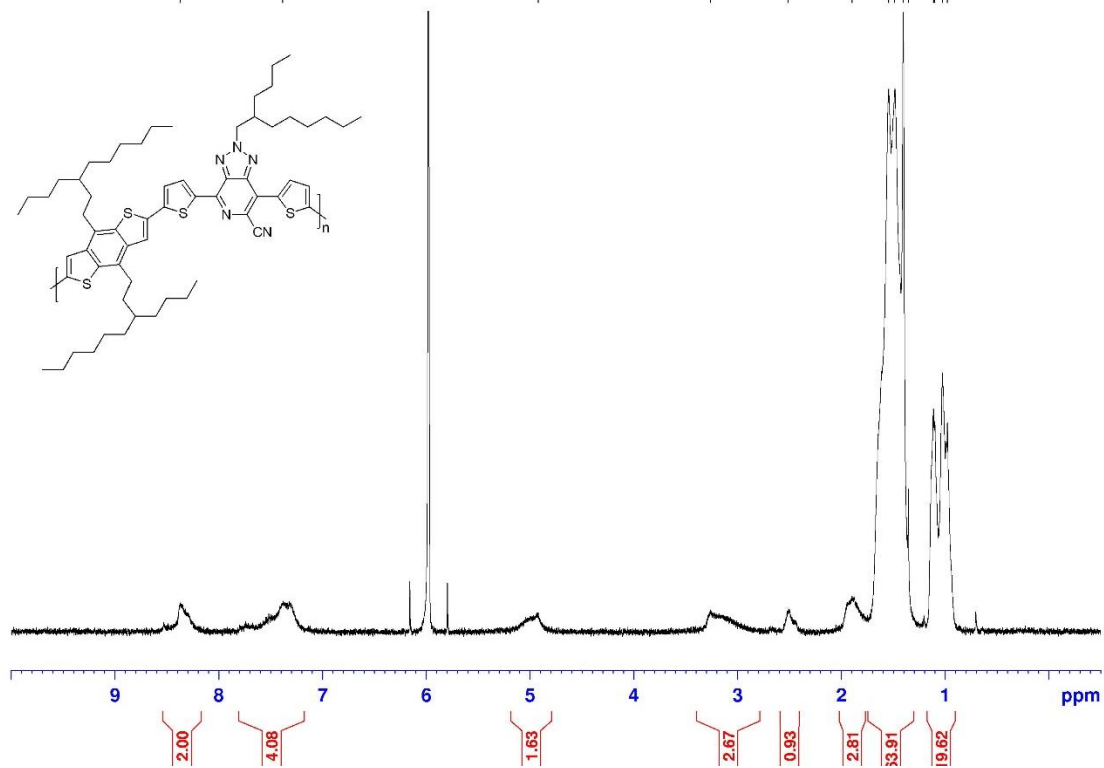
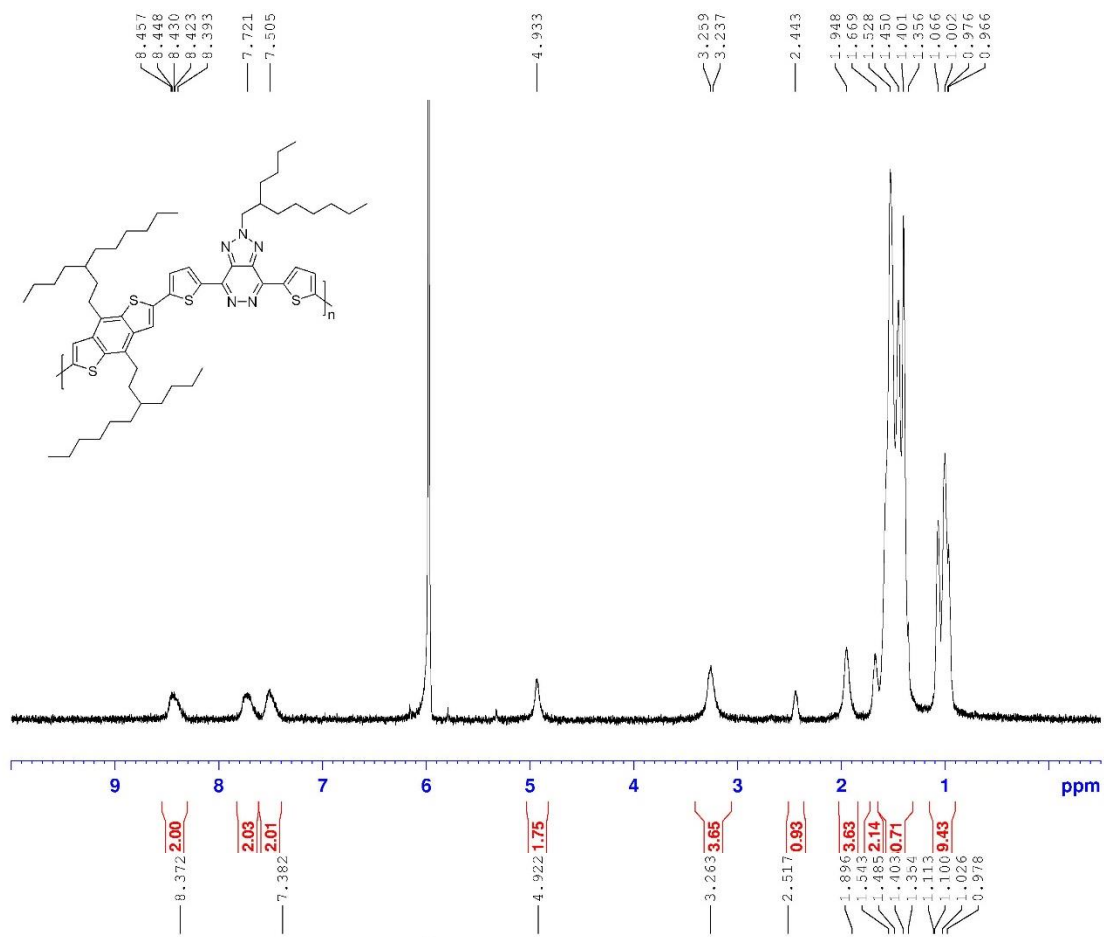


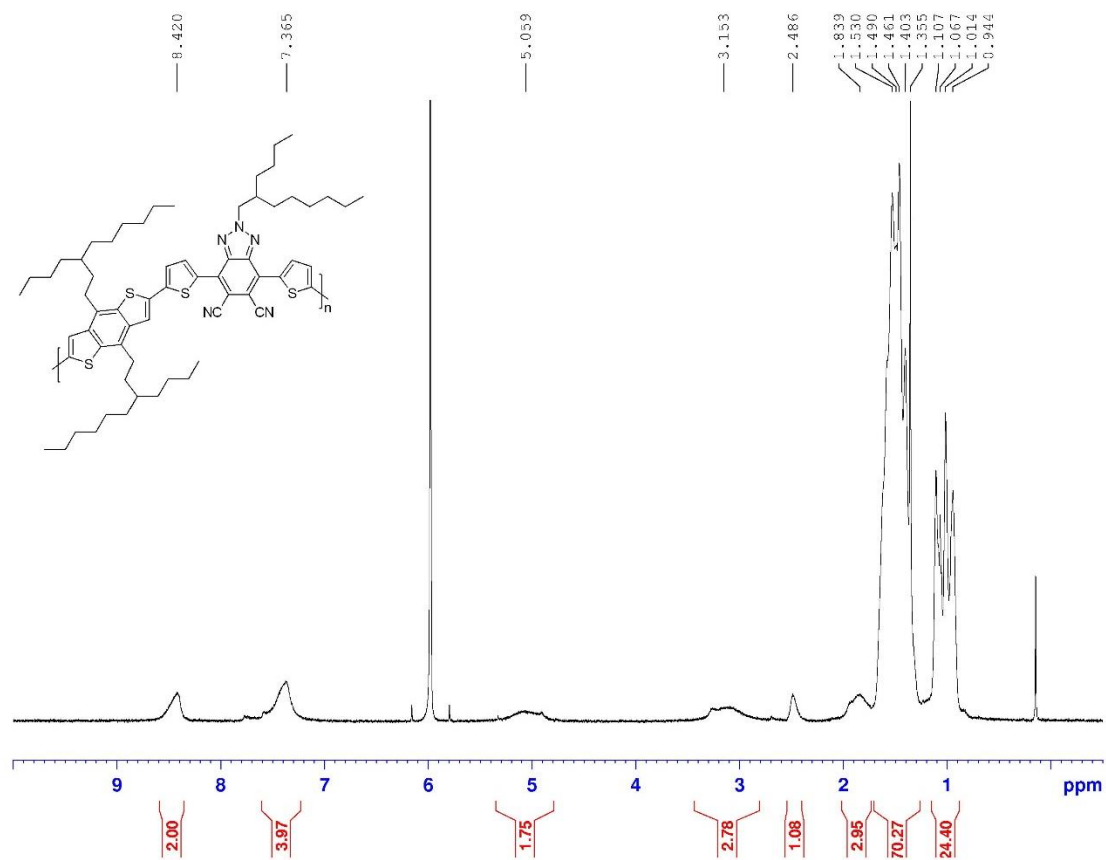












## REFERENCES

- (1) U.S. Energy Information Administration 2011.
- (2) Shafiee, S.; Topal, E. *Energy Policy* **2009**, *37*, 181.
- (3) Green, M. A.; Emery, K.; Hishikawa, Y.; Warta, W.; Dunlop, E. D. *Progress in Photovoltaics* **2015**, *23*, 1.
- (4) Lizin, S.; Van Passel, S.; De Schepper, E.; Maes, W.; Lutsen, L.; Manca, J.; Vanderzande, D. *Energy & Environmental Science* **2013**, *6*, 3136.
- (5) Thompson Research Group 2015.
- (6) Zhou, H. X.; Yang, L. Q.; You, W. *Macromolecules* **2012**, *45*, 607.
- (7) Sun, Y. M.; Seo, J. H.; Takacs, C. J.; Seifert, J.; Heeger, A. J. *Adv. Mater.* **2011**, *23*, 1679.
- (8) Yu, G.; Gao, J.; Hummelen, J. C.; Wudl, F.; Heeger, A. J. *Science* **1995**, *270*, 1789.
- (9) Brabec, C. J.; Durrant, J. R. *MRS Bull.* **2008**, *33*, 670.
- (10) Shockley, W.; Queisser, H. J. *J. Appl. Phys.* **1961**, *32*, 510.
- (11) Bruno, A.; Reynolds, L. X.; Dyer-Snaith, C.; Nelson, J.; Haque, S. A. *J. Phys. Chem. C* **2013**, *117*, 19832.
- (12) Liu, Y. H.; Zhao, J. B.; Li, Z. K.; Mu, C.; Ma, W.; Hu, H. W.; Jiang, K.; Lin, H. R.; Ade, H.; Yan, H. *Nat. Commun.* **2014**, *5*.
- (13) Tumbleston, J. R.; Collins, B. A.; Yang, L. Q.; Stuart, A. C.; Gann, E.; Ma, W.; You, W.; Ade, H. *Nat. Photonics* **2014**, *8*, 385.
- (14) Coffey, D. C.; Larson, B. W.; Hains, A. W.; Whitaker, J. B.; Kopidakis, N.; Boltalina, O. V.; Strauss, S. H.; Rumbles, G. *J. Phys. Chem. C* **2012**, *116*, 8916.
- (15) Scharber, M. C.; Wuhlbacher, D.; Koppe, M.; Denk, P.; Waldauf, C.; Heeger, A. J.; Brabec, C. L. *Adv. Mater.* **2006**, *18*, 789.
- (16) Carsten, B.; Szarko, J. M.; Son, H. J.; Wang, W.; Lu, L.; He, F.; Rolczynski, B. S.; Lou, S. J.; Chen, L. X.; Yu, L. *J Am Chem Soc* **2011**, *133*, 20468.
- (17) Rolczynski, B. S.; Szarko, J. M.; Son, H. J.; Liang, Y.; Yu, L.; Chen, L. X. *J Am Chem Soc* **2012**, *134*, 4142.
- (18) Graham, K. R.; Cabanetos, C.; Jahnke, J. P.; Idso, M. N.; El Labban, A.; Ndjawa, G. O. N.; Heum Mueller, T.; Vandewal, K.; Salleo, A.; Chmelka, B. F.; Amassian, A.; Beaujuge, P. M.; McGehee, M. D. *J Am Chem Soc* **2014**, *136*, 9608.
- (19) Foster, S.; Deledalle, F.; Mitani, A.; Kimura, T.; Kim, K.-B.; Okachi, T.; Kirchartz, T.; Oguma, J.; Miyake, K.; Durrant, J. R.; Doi, S.; Nelson, J. *Advanced Energy Materials* **2014**, *4*.



- (20) Li, W. T.; Abrecht, S.; Yang, L. Q.; Roland, S.; Tumbleston, J. R.; McAfee, T.; Yan, L.; Kelly, M. A.; Ade, H.; Neher, D.; You, W. *J. Am. Chem. Soc.* **2014**, *136*, 15566.
- (21) Osaka, I.; Saito, M.; Mori, H.; Koganezawa, T.; Takimiya, K. *Adv Mater* **2012**, *24*, 425.
- (22) Liang, Y.; Feng, D.; Wu, Y.; Tsai, S.-T.; Li, G.; Ray, C.; Yu, L. *J Am Chem Soc* **2009**, *131*, 7792.
- (23) Beaujuge, P. M.; Amb, C. M.; Reynolds, J. R. *Accounts of Chemical Research* **2010**, *43*, 1396.
- (24) Zhou, H. X.; Yang, L. Q.; Price, S. C.; Knight, K. J.; You, W. *Angewandte Chemie-International Edition* **2010**, *49*, 7992.
- (25) Price, S. C.; Stuart, A. C.; Yang, L.; Zhou, H.; You, W. *J. Am. Chem. Soc.* **2011**, *133*, 4625.
- (26) Zhou, H.; Yang, L.; Stuart, A. C.; Price, S. C.; Liu, S.; You, W. *Angewandte Chemie International Edition* **2011**, *50*, 2995.
- (27) Collins, B. A.; Cochran, J. E.; Yan, H.; Gann, E.; Hub, C.; Fink, R.; Wang, C.; Schuettfort, T.; McNeill, C. R.; Chabiny, M. L.; Ade, H. *Nature Materials* **2012**, *11*, 536.
- (28) Jailaubekov, A. E.; Willard, A. P.; Tritsch, J. R.; Chan, W.-L.; Sai, N.; Gearba, R.; Kaake, L. G.; Williams, K. J.; Leung, K.; Rossky, P. J.; Zhu, X. Y. *Nature Materials* **2013**, *12*, 66.
- (29) Couderc, E. *MRS Bull.* **2013**, *38*, 119.
- (30) Grancini, G.; Maiuri, M.; Fazzi, D.; Petrozza, A.; Egelhaaf, H. J.; Brida, D.; Cerullo, G.; Lanzani, G. *Nature Materials* **2013**, *12*, 29.
- (31) Lee, J.; Vandewal, K.; Yost, S. R.; Bahlke, M. E.; Goris, L.; Baldo, M. A.; Manca, J. V.; Van Voorhis, T. *J Am Chem Soc* **2010**, *132*, 11878.
- (32) Price, S. C.; Stuart, A. C.; Yang, L. Q.; Zhou, H. X.; You, W. *J Am Chem Soc* **2011**, *133*, 4625.
- (33) Tanimoto, A.; Yamamoto, T. *Adv Synth Catal* **2004**, *346*, 1818.
- (34) Tam, T. L.; Li, H. R.; Lam, Y. M.; Mhaisalkar, S. G.; Grimsdale, A. C. *Org Lett* **2011**, *13*, 4612.
- (35) Tam, T. L.; Tan, H. H. R.; Ye, W. T.; Mhaisalkar, S. G.; Grimsdale, A. C. *Org Lett* **2012**, *14*, 532.
- (36) Tam, T. L. D.; Ye, W. T.; Tan, H. H. R.; Zhou, F.; Su, H. B.; Mhaisalkar, S. G.; Grimsdale, A. C. *J Org Chem* **2012**, *77*, 10035.
- (37) Patel, D. G.; Feng, F. D.; Ohnishi, Y. Y.; Abboud, K. A.; Hirata, S.; Schanze, K. S.; Reynolds, J. R. *J Am Chem Soc* **2012**, *134*, 2599.
- (38) Balan, A.; Baran, D.; Toppare, L. *Polym Chem-Uk* **2011**, *2*, 1029.

- (39) Katritzky, A. R.; Manju, K.; Singh, S. K.; Meher, N. K. *Tetrahedron* **2005**, *61*, 2555.
- (40) Katritzky, A. R.; Rachwal, S. *Chem Rev* **2010**, *110*, 1564.
- (41) Katritzky, A. R.; Rachwal, S. *Chem Rev* **2011**, *111*, 7063.
- (42) Zhang, L. J.; He, C.; Chen, J. W.; Yuan, P.; Huang, L. A.; Zhang, C.; Cai, W. Z.; Liu, Z. T.; Cao, Y. *Macromolecules* **2010**, *43*, 9771.
- (43) Baran, D.; Balan, A.; Celebi, S.; Esteban, B. M.; Neugebauer, H.; Sariciftci, N. S.; Toppare, L. *Chem Mater* **2010**, *22*, 2978.
- (44) Zhang, Z. H.; Peng, B.; Liu, B.; Pan, C. Y.; Li, Y. F.; He, Y. H.; Zhou, K. C.; Zou, Y. P. *Polym Chem-Uk* **2010**, *1*, 1441.
- (45) Katritzky, A. R.; Kuzmierkiewicz, W.; Greenhill, J. V. *Recl Trav Chim Pay B* **1991**, *110*, 369.
- (46) Yan, W. M.; Liao, T.; Tuguldur, O.; Zhong, C.; Petersen, J. L.; Shi, X. D. *Chem-Asian J* **2011**, *6*, 2720.
- (47) Kurts, A. L.; Masias, A.; Genkina, N. K.; Beletskaya, I. P.; Reutov, O. A. *Dokl Akad Nauk Sssr+* **1969**, *187*, 807.
- (48) Krom, J. A.; Streitwieser, A. *J Am Chem Soc* **1992**, *114*, 8747.
- (49) Streitwieser, A.; Krom, J. A.; Kilway, K. V.; Abbotto, A. *J Am Chem Soc* **1998**, *120*, 10801.
- (50) Streitwieser, A.; Wang, D. Z. R. *J Am Chem Soc* **1999**, *121*, 6213.
- (51) Streitwieser, A.; Wang, D. Z. R.; Stratakis, M. *J Org Chem* **1999**, *64*, 4860.
- (52) Streitwieser, A.; Juaristi, E.; Kim, Y. J.; Pugh, J. K. *Org Lett* **2000**, *2*, 3739.
- (53) Streitwieser, A. *J Mol Model* **2006**, *12*, 673.
- (54) Williard, P. G.; Carpenter, G. B. *J Am Chem Soc* **1985**, *107*, 3345.
- (55) Williard, P. G.; Salvino, J. M. *Tetrahedron Lett* **1985**, *26*, 3931.
- (56) Williard, P. G.; Carpenter, G. B. *J Am Chem Soc* **1986**, *108*, 462.
- (57) Williard, P. G.; Liu, Q. Y. *J Am Chem Soc* **1993**, *115*, 3380.
- (58) Williard, P. G.; Hintze, M. J. *J Am Chem Soc* **1987**, *109*, 5539.
- (59) Williard, P. G.; Salvino, J. M. *J Org Chem* **1993**, *58*, 1.
- (60) Henderson, K. W.; Williard, P. G.; Bernstein, P. R. *Angew Chem Int Edit* **1995**, *34*, 1117.
- (61) Henderson, K. W.; Dorigo, A. E.; Williard, P. G.; Bernstein, P. R. *Angew Chem Int Edit* **1996**, *35*, 1322.
- (62) Gareyev, R.; Streitwieser, A. *J Org Chem* **1996**, *61*, 1742.

- (63) Andrews, P. C.; Deacon, G. B.; Forsyth, C. M.; Scott, N. M. *Angewandte Chemie-International Edition* **2001**, 40, 2108.
- (64) Henze, W.; Vyater, A.; Krause, N.; Gschwind, R. M. *J Am Chem Soc* **2005**, 127, 17335.
- (65) Albert, A.; Taylor, P. J. *J Chem Soc Perk T 2* **1989**, 1903.
- (66) Service, R. F. *Science* **2011**, 332, 293.
- (67) Tumbleston, J. R.; Stuart, A. C.; Gann, E.; You, W.; Ade, H. *Advanced Functional Materials* **2013**.
- (68) Uy, R. L.; Price, S. C.; You, W. *Macromol. Rapid Commun.* **2012**, 33, 1162.
- (69) Zhou, H. X.; Yang, L. Q.; Stoneking, S.; You, W. *ACS Appl. Mater. Interfaces* **2010**, 2, 1377.
- (70) Koppe, M.; Brabec, C. J.; Heiml, S.; Schausberger, A.; Duffy, W.; Heeney, M.; McCulloch, I. *Macromolecules* **2009**, 42, 4661.
- (71) Schilinsky, P.; Asawapirom, U.; Scherf, U.; Biele, M.; Brabec, C. J. *Chem Mater* **2005**, 17, 2175.
- (72) Ma, W.; Kim, J. Y.; Lee, K.; Heeger, A. J. *Macromol. Rapid Commun.* **2007**, 28, 1776.
- (73) Coffin, R. C.; Peet, J.; Rogers, J.; Bazan, G. C. *Nat Chem* **2009**, 1, 657.
- (74) Tong, M. H.; Cho, S.; Rogers, J. T.; Schmidt, K.; Hsu, B. B. Y.; Moses, D.; Coffin, R. C.; Kramer, E. J.; Bazan, G. C.; Heeger, A. J. *Advanced Functional Materials* **2010**, 20, 3959.
- (75) Zhou, H. X.; Yang, L. Q.; Xiao, S. Q.; Liu, S. B.; You, W. *Macromolecules* **2010**, 43, 811.
- (76) Chu, T. Y.; Lu, J. P.; Beaupre, S.; Zhang, Y. G.; Pouliot, J. R.; Zhou, J. Y.; Najari, A.; Leclerc, M.; Tao, Y. *Advanced Functional Materials* **2012**, 22, 2345.
- (77) Odian, G. In *Principles of Polymerization, 4th edition*; 2004 ed.; Wiley: Hoboken, 2004.
- (78) Zaleskiy, S. S.; Ananikov, V. P. *Organometallics* **2012**, 31, 2302.
- (79) Izumi, T.; Kobashi, S.; Takimiya, K.; Aso, Y.; Otsubo, T. *J Am Chem Soc* **2003**, 125, 5286.
- (80) Koch, F. P. V.; Smith, P.; Heeney, M. *Journal of American Chemical Society* **2013**.
- (81) Stuart, A. C.; Tumbleston, J. R.; Zhou, H. X.; Li, W. T.; Liu, S. B.; Ade, H.; You, W. *J Am Chem Soc* **2013**, 135, 1806.
- (82) Gann, E.; Young, A. T.; Collins, B. A.; Yan, H.; Nasiatka, J.; Padmore, H. A.; Ade, H.; Hexemer, A.; Wang, C. *Rev. Sci. Instrum.* **2012**, 83.
- (83) Ma, W.; Tumbleston, J. R.; Wang, M.; Huang, F.; Ade, H. *Advanced Energy Materials* **2013**, 3, 864.

- (84) Treat, N. D.; Varotto, A.; Takacs, C. J.; Batara, N.; Al-Hashimi, M.; Heeney, M. J.; Heeger, A. J.; Wudl, F.; Hawker, C. J.; Chabinyc, M. L. *J Am Chem Soc* **2012**, *134*, 15869.
- (85) Treat, N. D.; Brady, M. A.; Smith, G.; Toney, M. F.; Kramer, E. J.; Hawker, C. J.; Chabinyc, M. L. *Advanced Energy Materials* **2011**, *1*, 82.
- (86) Collins, B. A.; Li, Z.; McNeill, C. R.; Ade, H. *Macromolecules* **2011**, *44*, 9747.
- (87) Collins, B. A.; Li, Z.; Tumbleston, J. R.; Gann, E.; McNeill, C. R.; Ade, H. *Adv. Energy Mater.* **2013**, *3*, 65.
- (88) He, X. X.; Collins, B. A.; Watts, B.; Ade, H.; McNeill, C. R. *Small* **2012**, *8*, 1920.
- (89) Ma, W.; Ye, L.; Zhang, S. Q.; Hou, J. H.; Ade, H. *J. Mater. Chem. C* **2013**, *1*, 5023.
- (90) Rand, B. P.; Cheyns, D.; Vasseur, K.; Giebink, N. C.; Mothy, S.; Yi, Y. P.; Coropceanu, V.; Beljonne, D.; Cornil, J.; Bredas, J. L.; Genoe, J. *Advanced Functional Materials* **2012**, *22*, 2987.
- (91) Bartelt, J. A.; Beiley, Z. M.; Hoke, E. T.; Mateker, W. R.; Douglas, J. D.; Collins, B. A.; Tumbleston, J. R.; Graham, K. R.; Amassian, A.; Ade, H.; Frechet, J. M. J.; Toney, M. F.; McGehee, M. D. *Advanced Energy Materials* **2013**, *3*, 364.
- (92) Westacott, P.; Tumbleston, J. R.; Shoaee, S.; Fearn, S.; Bannock, J. H.; Gilchrist, J. B.; Heutz, S.; deMello, J.; Heeney, M.; Ade, H.; Durrant, J.; McPhail, D. S.; Stingelin, N. *Energy Environ. Sci.* **2013**, *6*, 2756.
- (93) Bhatt, M. P.; Magurudeniya, H. D.; Sista, P.; Sheina, E. E.; Jeffries-EL, M.; Janesko, B. G.; McCullough, R. D.; Stefan, M. C. *Journal of Materials Chemistry A* **2013**, *1*, 12841.
- (94) Bryan, Z. J.; McNeil, A. J. *Macromolecules* **2013**.
- (95) Yokozawa, T.; Nanashima, Y.; Ohta, Y. *ACS Macro Lett.* **2012**, *1*, 862.
- (96) Bridges, C. R.; McCormick, T. M.; Gibson, G. L.; Hollinger, J.; Seferos, D. S. *J Am Chem Soc* **2013**, *135*, 13212.
- (97) Liao, S.-H.; Jhuo, H.-J.; Cheng, Y.-S.; Chen, S.-A. *Adv. Mater.* **2013**, *25*, 4766.
- (98) Cabanetos, C.; El Labban, A.; Bartelt, J. A.; Douglas, J. D.; Mateker, W. R.; Fréchet, J. M. J.; McGehee, M. D.; Beaujuge, P. M. *J. Am. Chem. Soc.* **2013**, *135*, 4656.
- (99) Chen, H.-Y.; Hou, J.; Zhang, S.; Liang, Y.; Yang, G.; Yang, Y.; Yu, L.; Wu, Y.; Li, G. *Nature Photon.* **2009**, *3*, 649.
- (100) Zhou, H.; Yang, L.; You, W. *Macromolecules* **2012**, *45*, 607.
- (101) Hedley, G. J.; Ward, A. J.; Alekseev, A.; Howells, C. T.; Martins, E. R.; Serrano, L. A.; Cooke, G.; Ruseckas, A.; Samuel, I. D. W. *Nat. Commun.* **2013**, *4*, 2867.
- (102) Tumbleston, J. R.; Collins, B. A.; Yang, L.; Stuart, A. C.; Gann, E.; Ma, W.; You, W.; Ade, H. *Nature Photon.* **2014**, *8*, 385.

- (103) Hoke, E. T.; Vandewal, K.; Bartelt, J. A.; Mateker, W. R.; Douglas, J. D.; Noriega, R.; Graham, K. R.; Frechet, J. M. J.; Salleo, A.; McGehee, M. D. *Adv. Energy Mater.* **2013**, *3*, 220.
- (104) Proctor, C. M.; Albrecht, S.; Neher, D.; Nguyen, T. Q. *Adv. Energy Mater.* **2014**.
- (105) Shoaee, S.; Subramaniyan, S.; Xin, H.; Keiderling, C.; Tuladhar, P. S.; Jamieson, F.; Jenekhe, S. A.; Durrant, J. R. *Adv. Funct. Mater.* **2013**, *23*, 3286.
- (106) Albrecht, S.; Tumbleston, J. R.; Janietz, S.; Dumsch, I.; Allard, S.; Scherf, U.; Ade, H.; Neher, D. *J. Phys. Chem. Lett.* **2014**, *5*, 1131.
- (107) Collins, B. A.; Tumbleston, J. R.; Ade, H. *J. Phys. Chem. Lett.* **2011**, *2*, 3135.
- (108) Dou, L.; Chen, C.-C.; Yoshimura, K.; Ohya, K.; Chang, W.-H.; Gao, J.; Liu, Y.; Richard, E.; Yang, Y. *Macromolecules* **2013**, *46*, 3384.
- (109) Stuart, A. C.; Tumbleston, J. R.; Zhou, H.; Li, W.; Liu, S.; Ade, H.; You, W. *J. Am. Chem. Soc.* **2013**, *135*, 1806.
- (110) Schroeder, B. C.; Huang, Z.; Ashraf, R. S.; Smith, J.; D'Angelo, P.; Watkins, S. E.; Anthopoulos, T. D.; Durrant, J. R.; McCulloch, I. *Adv. Funct. Mater.* **2012**, *22*, 1663.
- (111) Albrecht, S.; Janietz, S.; Schindler, W.; Frisch, J.; Kurpiers, J.; Kniepert, J.; Inal, S.; Pingel, P.; Fostiropoulos, K.; Koch, N.; Neher, D. *J. Am. Chem. Soc.* **2012**, *134*, 14932.
- (112) Zhang, M.; Guo, X.; Zhang, S.; Hou, J. *Adv. Mater.* **2014**, *26*, 1118.
- (113) Son, H. J.; Wang, W.; Xu, T.; Liang, Y.; Wu, Y.; Li, G.; Yu, L. *J. Am. Chem. Soc.* **2011**, *133*, 1885.
- (114) Li, W.; Yang, L.; Tumbleston, J. R.; Yan, L.; Ade, H.; You, W. *Adv. Mater.* **2014**.
- (115) He, X.; Mukherjee, S.; Watkins, S.; Chen, M.; Qin, T.; Thomsen, L.; Ade, H.; McNeill, C. R. *J. Phys. Chem. C* **2014**, *118*, 9918.
- (116) Liu, P.; Zhang, K.; Liu, F.; Jin, Y.; Liu, S.; Russell, T. P.; Yip, H.-L.; Huang, F.; Cao, Y. *Chem. Mater.* **2014**, *26*, 3009.
- (117) Wang, H.; Yu, X.; Yi, C.; Ren, H.; Liu, C.; Yang, Y.; Xiao, S.; Zheng, J.; Karim, A.; Cheng, S. Z. D.; Gong, X. *J. Phys. Chem. C* **2013**, *117*, 4358.
- (118) Beiley, Z. M.; Hoke, E. T.; Noriega, R.; Dacuna, J.; Burkhard, G. F.; Bartelt, J. A.; Salleo, A.; Toney, M. F.; McGehee, M. D. *Adv. Energy Mater.* **2011**, *1*, 954.
- (119) Bartelt, J. A.; Beiley, Z. M.; Hoke, E. T.; Mateker, W. R.; Douglas, J. D.; Collins, B. A.; Tumbleston, J. R.; Graham, K. R.; Amassian, A.; Ade, H.; Fréchet, J. M. J.; Toney, M. F.; McGehee, M. D. *Adv. Energy Mater.* **2013**, *3*, 364.
- (120) Peet, J.; Wen, L.; Byrne, P.; Rodman, S.; Forberich, K.; Shao, Y.; Drolet, N.; Gaudiana, R.; Demmler, G.; Waller, D. *Appl. Phys. Lett.* **2011**, *98*, 043301.
- (121) Tumbleston, J. R.; Stuart, A. C.; Gann, E.; You, W.; Ade, H. *Adv. Funct. Mater.* **2013**, *23*, 3463.

- (122) Rivnay, J.; Mannsfeld, S. C. B.; Miller, C. E.; Salleo, A.; Toney, M. F. *Chem. Rev.* **2012**, *112*, 5488.
- (123) Credgington, D.; Jamieson, F. C.; Walker, B.; Nguyen, T.-Q.; Durrant, J. R. *Adv. Mater.* **2012**, *24*, 2135.
- (124) Albrecht, S.; Schindler, W.; Kurpiers, J.; Kniepert, J.; Blakesley, J. C.; Dumsch, I.; Allard, S.; Fostiropoulos, K.; Scherf, U.; Neher, D. *J. Phys. Chem. Lett.* **2012**, *3*, 640.
- (125) Proctor, C. M.; Kuik, M.; Nguyen, T.-Q. *Prog. Polym. Sci.* **2013**, *38*, 1941.
- (126) Vandewal, K.; Albrecht, S.; Hoke, E. T.; Graham, K. R.; Widmer, J.; Douglas, J. D.; Schubert, M.; Mateker, W. R.; Bloking, J. T.; Burkhard, G. F.; Sellinger, A.; Fréchet, J. M. J.; Amassian, A.; Riede, M. K.; McGehee, M. D.; Neher, D.; Salleo, A. *Nat. Mater.* **2014**, *13*, 63.
- (127) Gđinas, S.; Rao, A.; Kumar, A.; Smith, S. L.; Chin, A. W.; Clark, J.; van der Poll, T. S.; Bazan, G. C.; Friend, R. H. *Science* **2014**, *343*, 512.
- (128) Yost, S. R.; Van Voorhis, T. *J. Phys. Chem. C* **2013**, *117*, 5617.
- (129) Hamilton, R.; Shuttle, C. G.; O'Regan, B.; Hammant, T. C.; Nelson, J.; Durrant, J. R. *J. Phys. Chem. Lett.* **2010**, *1*, 1432.
- (130) Groves, C.; Greenham, N. C. *Phys. Rev. B* **2008**, *78*, 155205.
- (131) Lange, I.; Kniepert, J.; Pingel, P.; Dumsch, I.; Allard, S.; Janietz, S.; Scherf, U.; Neher, D. *J. Phys. Chem. Lett.* **2013**, *4*, 3865.
- (132) Wřfel, P. *Physics of Solar Cells: From Principles to New Concepts*; WILEY-VCH Verlag ed., 2008.
- (133) Lakhwani, G.; Rao, A.; Friend, R. H. *Annu. Rev. Phys. Chem.* **2014**, *65*, 557.
- (134) Ma, W.; Tumbleston, J. R.; Wang, M.; Gann, E.; Huang, F.; Ade, H. *Adv. Energy Mater.* **2013**, *3*, 864.
- (135) Guo, X.; Zhou, N.; Lou, S. J.; Smith, J.; Tice, D. B.; Hennek, J. W.; Ortiz, R. P.; Navarrete, J. T. L.; Li, S.; Strzalka, J.; Chen, L. X.; Chang, R. P. H.; Facchetti, A.; Marks, T. J. *Nature Photon.* **2013**, *7*, 825.
- (136) Hu, X.; Yi, C.; Wang, M.; Hsu, C.-H.; Liu, S.; Zhang, K.; Zhong, C.; Huang, F.; Gong, X.; Cao, Y. *Adv. Energy Mater.* **2014**.
- (137) Li, W.; Hendriks, K. H.; Roelofs, W. S. C.; Kim, Y.; Wienk, M. M.; Janssen, R. A. J. *Adv. Mater.* **2013**, *25*, 3182.
- (138) Qu, S. Y.; Tian, H. *Chem. Commun.* **2012**, *48*, 3039.
- (139) Bijleveld, J. C.; Zoombelt, A. P.; Mathijssen, S. G. J.; Wienk, M. M.; Turbiez, M.; de Leeuw, D. M.; Janssen, R. A. J. *J. Am. Chem. Soc.* **2009**, *131*, 16616.
- (140) Lei, T.; Wang, J. Y.; Pei, J. *Accounts Chem. Res.* **2014**, *47*, 1117.

- (141) Wang, E. G.; Mammo, W.; Andersson, M. R. *Adv. Mater.* **2014**, *26*, 1801.
- (142) Uy, R. L.; Yan, L.; Li, W. T.; You, W. *Macromolecules* **2014**, *47*, 2289.
- (143) Planells, M.; Schroeder, B. C.; McCulloch, I. *Macromolecules* **2014**, *47*, 5889.
- (144) Lee, J.; Han, A. R.; Kim, J.; Kim, Y.; Oh, J. H.; Yang, C. *J. Am. Chem. Soc.* **2012**, *134*, 20713.
- (145) Shahid, M.; Ashraf, R. S.; Huang, Z. G.; Kronemeijer, A. J.; McCarthy-Ward, T.; McCulloch, I.; Durrant, J. R.; Sirringhaus, H.; Heeney, M. *J. Mater. Chem.* **2012**, *22*, 12817.
- (146) Blouin, N.; Michaud, A.; Gendron, D.; Wakim, S.; Blair, E.; Neagu-Plesu, R.; Belletete, M.; Durocher, G.; Tao, Y.; Leclerc, M. *J. Am. Chem. Soc.* **2008**, *130*, 732.
- (147) Casey, A.; Han, Y.; Fei, Z. P.; White, A. J. P.; Anthopoulos, T. D.; Heeney, M. *J. Mater. Chem. C* **2015**, *3*, 265.
- (148) Cha, H.; Kim, H. N.; An, T. K.; Kang, M. S.; Kwon, S. K.; Kim, Y. H.; Park, C. E. *ACS Appl. Mater. Interfaces* **2014**, *6*, 15774.
- (149) Loren, J. C.; Krasinski, A.; Fokin, V. V.; Sharpless, K. B. *Synlett* **2005**, 2847.
- (150) Wang, X. J.; Zhang, L.; Krishnamurthy, D.; Senanayake, C. H.; Wipf, P. *Org. Lett.* **2010**, *12*, 4632.
- (151) Wang, X. J.; Zhang, L.; Lee, H.; Haddad, N.; Krishnamurthy, D.; Senanayake, C. H. *Org. Lett.* **2009**, *11*, 5026.
- (152) Li, W. T.; Yang, L. Q.; Tumbleston, J. R.; Yan, L.; Ade, H.; You, W. *Adv. Mater.* **2014**, *26*, 4456.
- (153) Pattanasattayavong, P.; Yaacobi-Gross, N.; Zhao, K.; Ndjawa, G. O. N.; Li, J. H.; Yan, F.; O'Regan, B. C.; Amassian, A.; Anthopoulos, T. D. *Adv. Mater.* **2013**, *25*, 1504.
- (154) Proctor, C. M.; Love, J. A.; Nguyen, T. Q. *Adv. Mater.* **2014**, *26*, 5957.
- (155) Bronstein, H.; Chen, Z. Y.; Ashraf, R. S.; Zhang, W. M.; Du, J. P.; Durrant, J. R.; Tuladhar, P. S.; Song, K.; Watkins, S. E.; Geerts, Y.; Wienk, M. M.; Janssen, R. A. J.; Anthopoulos, T.; Sirringhaus, H.; Heeney, M.; McCulloch, I. *J. Am. Chem. Soc.* **2011**, *133*, 3272.
- (156) Wang, E. G.; Ma, Z. F.; Zhang, Z.; Vandewal, K.; Henriksson, P.; Inganäs, O.; Zhang, F. L.; Andersson, M. R. *J. Am. Chem. Soc.* **2011**, *133*, 14244.
- (157) Zhang, M.; Guo, X.; Zhang, S.; Hou, J. *Adv. Mater.* **2014**, *26*, 1118.
- (158) Kan, B.; Li, M.; Zhang, Q.; Liu, F.; Wan, X.; Wang, Y.; Ni, W.; Long, G.; Yang, X.; Feng, H.; Zuo, Y.; Zhang, M.; Huang, F.; Cao, Y.; Russell, T. P.; Chen, Y. *J Am Chem Soc* **2015**, *137*, 3886.

- (159) Zhang, Q.; Kan, B.; Liu, F.; Long, G.; Wan, X.; Chen, X.; Zuo, Y.; Ni, W.; Zhang, H.; Li, M.; Hu, Z.; Huang, F.; Cao, Y.; Liang, Z.; Zhang, M.; Russell, T. P.; Chen, Y. *Nat. Photonics* **2015**, 9, 35.
- (160) Zhou, J.; Wan, X.; Liu, Y.; Zuo, Y.; Li, Z.; He, G.; Long, G.; Ni, W.; Li, C.; Su, X.; Chen, Y. *J Am Chem Soc* **2012**, 134, 16345.
- (161) Chen, J. D.; Cui, C. H.; Li, Y. Q.; Zhou, L.; Ou, Q. D.; Li, C.; Li, Y. F.; Tang, J. X. *Adv. Mater.* **2015**, 27, 1035.
- (162) Liu, C.; Yi, C.; Wang, K.; Yang, Y.; Bhatta, R. S.; Tsige, M.; Xiao, S.; Gong, X. *Acs Applied Materials & Interfaces* **2015**, 7, 4928.
- (163) Po, R.; Bianchi, G.; Carbonera, C.; Pellegrino, A. *Macromolecules* **2015**, 48, 453.
- (164) Mercier, L. G.; Leclerc, M. *Accounts of Chemical Research* **2013**, 46, 1597.
- (165) Lu, L.; Yu, L. *Adv. Mater.* **2014**, 26, 4413.
- (166) Choi, H.; Ko, S.-J.; Kim, T.; Morin, P.-O.; Walker, B.; Lee, B. H.; Leclerc, M.; Kim, J. Y.; Heeger, A. J. *Adv. Mater.* **2015**.
- (167) Jo, J. W.; Bae, S.; Liu, F.; Russell, T. P.; Jo, W. H. *Advanced Functional Materials* **2014**, 25, 120.
- (168) Yang, L.; Zhou, H.; You, W. *J. Phys. Chem. C* **2010**, 114, 16793.